PhD Thesis in Materials Science

Atomic and electronic structure of self-organized defects in epitaxial films of functional perovskite-type oxides

Núria Bagués Salguero

Supervisors:

Dr. Felip Sandiumenge Ortíz
Dr. José Santiso López

Tutor:

Prof. Javier Rodríguez Viejo

Institut Català de Nanociència i Nanotecnologia (ICN$_2$-CISC)
Institut de Ciències de Materials de Barcelona (ICMAB-CSIC)
Department de Física, Universitat Autònoma de Barcelona (UAB)

April 2017

Dr. José Santiso Lopez, Científic titular del CSIC a l'Institut Català de Nanociència i Nanotecnologia, **Dr. Felip Sandiumenge Ortíz**, Investigador científic del CSIC a l'Institut de Ciència de Materials de Barcelona i **Prof. Javier Rodríguez Viejo,** Catedràtic de la Universitat Autònoma de Barcelona.

CERTIFIQUEN

que **Núria Bagués Salguero**, llicenciada en Geologia per la Universitat Autònoma de Barcelona, ha dut a terme sota la seva direcció el treball que porta per títol "Atomic and electronic structure of self-organized defects in epitaxial films of functional perovskite-type oxides", i queda recollit en aquesta memòria per optar al grau de Doctor en Ciència de Materials.

I per que així consti, signen el present certificat.

Núria Bagués Salguero   Dr. José Santiso López   Dr. Felip Sandiumenge Ortíz   Prof. Javier Rodríguez Viejo

Bellaterra, Abril de 2017

Als meus pares, Marina i Albert

Contents

Acknowledgments

Voldria escriure unes paraules d'agraïment a totes les persones que han contribuït en el desenvolupament d'aquesta Tesi Doctoral, tan les que m'han assessorat des d'un punt de vista professional com les que m'han acompanyat a nivell personal. Gràcies a la contribució de totes elles, el treball realitzat durant els darrers anys ha donat fruit a la present Tesi Doctoral.

En primer lloc, agrair l'oportunitat que m'han donat els meus directors de Tesi, Dr. Jose Santiso i Dr. Felip Sandiumenge, de descobrir el món de la recerca en la Ciència de Materials. Especialment, tot el coneixement transmès i que ha resultat essencial per al desenvolupament d'aquesta Tesi. Gràcies Santi per la constància i l'acolliment. Gràcies Felip per les idees i el suport mostrat. Com a supervisors us heu complementat en tot moment aportant guiatge i assessorament. Agrair-vos doncs, el gran creixement professional i personal al vostre costat.

A tots els companys del grup de Nanomaterials Growth Division de l'Institut Català de Nanociència i Nanotecnologia (ICN$_2$-CSIC), prèviament a Jaume Roqueta, James Arturo Zapata i Roberto Moreno, i especialment als actuals companys de despatx: Dra**.** Anna Magrasó, Laura Rodríguez, Dr. José Manuel Caicedo (Roque) i Arindom Chatterje. Gràcies per l'entusiasme, l'alegria del dia a dia i les converses de despatx.

També als companys del grup Advanced Characterization and Nanostructured Materials de l'Institut de Ciències de Materials de Barcelona (ICMAB) – CSIC. Al Prof. Benjamin Martínez, Dr. Lluís Balcells, Dr. Carles Frontera, Dr. Alberto Pomar, Dra. Zorica Konstantinovic i Dr. Bernat Bozzo, per la meravellosa acollida a l'inici d'aquest projecte i per tot l'aprenentatge al vostre costat. Especialment a la Laura, la Regina i al José, per les alegries i les preocupacions del dia a dia i per les aventures viscudes a Berlín.

A tots els altres col·laboradors de l'ICMAB i de l'ICN$_2$ que han participat d'alguna manera o altra en aquesta Tesi. La Dra. Neus Domingo del grup Oxide Nanophysics del ICN$_2$, per la col·laboració en les mesures de Magnetic Force Microscopy. La Prof. Carmen Ocal del Group of Physical Chemistry of Surfaces and Interfaces de l'ICMAB i al Dr. Marcos Paradinas per les mesures de Conducting Atomic Force Microscopy.

Als membres del grup de Electron Microscopy Division del ICN$_2$, especialment a la Belén Ballesteros per l'acompanyament i el suport amb el microscopi, el TEM. Al Francisco Belarre, per fer-me descobrir el món de la preparació de mostres i per totes les hores compartides i batallades perquè sortissin correctament.

A tots els companys i companyes de l'ICMAB, Bernat, Blai, Carlos, Jaume, etc., i de l'ICN$_2$, Alba, Rocío, Ela, Marcos, Federico, Marc, Jessica, etc., amb qui hem compartit congressos, cursos, discussions, preocupacions, cafès i festes.

I would like thank Prof. Michael Walls for the collaboration with the ESTEEM2 project.

Merci au personnal du Centre d'Élaboration des Matériaux et d'Etudes Structurales (CEMES) - CNRS et en particulier au Prof. Marie-Jo Casanove pour m'accueillir, me donner la bienvenue et me donner l'opportunité de travailler au sein de son groupe. Merci aussi à tous les collègues du CEMES, David, Juan Carlos, Zofia, Caroline, etc., pour rendre mon séjour en France très agréable et fructueuse.

I would also like to thank Prof. Dave McComb for giving me the opportunity to work with his group at the Center for Electron Microscopy and Analysis (CEMAS) of the Ohio State University. Many thanks also to Robert for teaching and helping me in the use of the TEMs. I would like to especially acknowledge Bryan, for helping me, as well as for the good moments shared in front of the microscope and outside of lab. Thanks also to all those who made my stay in Ohio comfortable and enjoyable, especially to Molly, Sushi, Ally, Stephen, etc., thanks for showing me your country and traditions, such as the Thanksgiving day, our "*Day of the big chicken*".

Agrair el suport econòmic al Ministeri d'Espanya (Ministerio de Economía y Competitividad - MINECO) proporcionat mitjançant la beca FPI (BSE-2012-055421 dins del projecte MAT2011-29081-C02-01), sense la qual no hauria estat possible realitzar l'activitat de recerca presentada en aquesta Tesi. També vull donar les gràcies als fons proporcionats per European Union Seventh Framework Programme (312483-ESTEEM2) que m'han permès l'accés a microscopis amb corrector d'aberracions al CEMES i Laboratoire de Physique des Solides (LPS)-CNRS.

I would like thank Andrew Hudson for his comments and suggestions regarding written English.

Per acabar, m'agradaria agrair el suport d'*aquellagent,* els amics que et treuen de casa perquè et toqui l'aire, per distreure't i animar-te, sobretot en la recta final d'aquest repte personal que ha estat la Tesi Doctoral. Moltes gràcies per ser sempre al meu costat!

Al Xavier Bolós: tot i que ara siguis lluny de la nostra terra, ets al meu costat per animar-me a seguir endavant, i com no, per dibuixar-me un somriure sempre. Moltes gràcies per la gran paciència i el suport incondicional! Ara sí, la següent aventura ens espera.

I finalment, vull dedicar aquesta Tesi Doctoral a la meva mare Marina Salguero, al meu pare Albert Bagués i a la meva germana Anna, sense ells res d'això hauria estat possible. Moltes gràcies per cuidar-me i recolzar-me, i per ajudar-me sempre a seguir endavant. Moltíssimes gràcies per la paciència, el suport i la comprensió. Aquesta Tesi és per a vosaltres.

Moltes gràcies!

Núria

Barcelona, 27 d'abril de 2017

Abstract

The epitaxial thin films of functional perovskite-type oxides (ABO_3) present interfacial coupling and misfit relaxation mechanisms governed by a complex interplay of chemical, electronic and structural degrees of freedom. The relaxation mechanisms of strained films may accommodate defects, such as misfit dislocations or twin walls, which exhibit a strong tendency towards self-organization with characteristic length scales of tens of nanometres. The core lattice structure of these defects is different from the bulk of the material and thus may be considered as a nano-phase with likely different physical properties, leading to the formation of functional nanostructures. The correlation between defect structure and functionality, together with the capacity of these defects to self-organize, offers a unique opportunity for the bottom-up elaboration of functional complex oxides nanodevices.

This thesis focuses on the characterization of the microstructure, interface and self-organized defects of epitaxial films and functional nanostructures of oxide materials by using advanced transmission electron microscopy. Special emphasis is put on the atomic and chemical structure of the interfaces and generated defects, such as dislocations, twin walls and phase segregations, as well as on the strain fields and their correlation with chemical heterogeneities. In this regard, two different systems composed of *lanthanum manganites* are considered: $LaMnO_3$:MnO_x nanocomposite grown on (001)$SrTiO_3$ and on (001)$LaAlO_3$ substrates; and $La_{0.7}Sr_{0.3}MnO_3$ films with self-organized defects grown on (001)$SrTiO_3$ and on (001)$LaAlO_3$. The materials studied in this work may be regarded as nanostructured films resulting from the self-organization of misfit relieving defects as follows: nanoinclusions of a MnO_x phase (volume defects) in $LaMnO_3$; twin walls between twin domains (planar defects) in $La_{0.7}Sr_{0.3}MnO_3$ on $SrTiO_3$; and misfit dislocations (line defects) in $La_{0.7}Sr_{0.3}MnO_3$ on $LaAlO_3$.

In the $LaMnO_3$:MnO_x nanocomposite, the formation of regular vertically aligned nanoinclusions of a manganese oxide (MnO_x) embedded in an $LaMnO_3$ film is analysed via microstructural characterization. This analysis includes the determination of the $LaMnO_3$ matrix microstructure with respect to the substrate together with the identification of the manganese oxide phase and a secondary phase: a La-rich layer close to $LaMnO_3$-substrate interface. In the case of $La_{0.7}Sr_{0.3}MnO_3$ on (001)$SrTiO_3$ substrates, a detailed analysis of twin walls and their implications on the functional properties is performed. Local changes in the physical and structural properties of the TWs lead to the view of a twinned film as a self-organized nanostructure consisting of vertical nano-sheets of strongly compressed $La_{0.7}Sr_{0.3}MnO_3$ embedded in a matrix of tensile strained $La_{0.7}Sr_{0.3}MnO_3$. In the case of $La_{0.7}Sr_{0.3}MnO_3$ ultrathin films grown on (001)$LaAlO_3$, the relaxation mechanism of this films is analysed. These films relieve the misfit strain by the formation of misfit dislocations above a critical film thickness of 2.5 nm. A detailed study of structural, chemical and electronic changes associated with the dislocation is also performed paying particular attention to the influence of strain fields on chemical composition at the nanoscale. A chemical reorganization occurs to accommodate the strain at the dislocations core region. The dependence of the degree of order of the dislocation

pattern on film thickness is also explored. Finally, the implications of the dislocation strain field on surface topography and electrical transport are analysed, demonstrating that the multiscale nature of dislocations holds great promise for the creation of spontaneous surface ordered functional nanostructures in complex oxide thin films.

The results and main conclusions obtained in this work open new perspectives for the development of functional self-organized nanostructures based on strain relieving defects.

Resum

Les capes fines epitaxials d'òxids funcionals tipus perovskita (ABO_3) presenten mecanismes d'acoblament d'intercara i de relaxació del desajust governats per un joc complex de graus de llibertat químics, electrònics i estructurals. Aquests mecanismes poden acomodar defectes, tals com dislocacions de desajust i parets de macla, que presenten una gran tendència a l'auto-organització amb escales característiques de desenes de nanòmetres. L'estructura de la xarxa en el nucli d'aquests defectes és diferent de la major part del material, i per tant pot ser considerat com una nano-fase amb propietats físiques probablement diferents, portant a la formació de nano-estructures funcionals. La correlació entre l'estructura del defecte i la funcionalitat, juntament amb la capacitat d'aquests defectes per auto-organitzar-se, ofereix una oportunitat única per l'elaboració *bottom-up* de nano-dispositius d'òxids funcionals complexes.

Aquesta Tesi es centra en la caracterització de la microestructura, l'intercara i els defectes auto-organitzats de capes epitaxials i nanoestructures funcionals de materials d'òxids mitjançant l'ús de Microscòpia Electrònica de Transmissió. Es presta especial atenció a l'estructura atòmica i electrònica de les intercares i defectes generats, tals com dislocacions, parets de macla i segregacions de fases, així com als camps de deformació i la seva relació amb les homogeneïtats químiques. En aquesta direcció, dos sistemes diferents compostos per manganites de Lantà són considerats: nanocompost de $LaMnO_3$:MnO_x crescut sobre substrats de $(001)SrTiO_3$ i de $(001)LaAlO_3$; i capes de $La_{0.7}Sr_{0.3}MnO_3$ amb defectes auto-organitzats crescudes sobre substrats de $(001)SrTiO_3$ i de $(001)LaAlO_3$. Els materials estudiats en aquest treball poden ser considerats com capes nanoestructurades resultants de l'autoorganització de defectes que relaxen el desajust: nanoinclusions de MnO_x (defectes de volum) en el $LaMnO_3$; parets de macla entre dominis de macla (defectes planars) en $La_{0.7}Sr_{0.3}MnO_3$/$SrTiO_3$ i dislocacions de desajust (defectes lineals) en $La_{0.7}Sr_{0.3}MnO_3$/$LaAlO_3$.

En el nanocompost de $LaMnO_3$:MnO_x, s'analitza la formació regular de nanoinclusions d'òxid de manganès verticalment alienades dins d'una capa de $LaMnO_3$ a través d'una caracterització microestructural. Aquestes anàlisis inclouen la determinació de la microestructura del $LaMnO_3$ respecte el substrat conjuntament amb la identificació de la fase de l'òxid de manganès i d'una fase secundària, una capa rica en La a prop de l'intercara $LaMnO_3$-$SrTiO_3$. En el cas del $La_{0.7}Sr_{0.3}MnO_3$/$SrTiO_3$, es realitza una anàlisi detallada de les parets de macla i de les implicacions d'aquestes en les propietats funcionals. Els canvis locals en les propietats físiques i estructurals de les parets de macla permeten veure una capa amb macles com a una estructura auto-organitzada consistint en nano-làmines verticals de $La_{0.7}Sr_{0.3}MnO_3$ fortament comprimides dins d'una matriu tensionada de $La_{0.7}Sr_{0.3}MnO_3$. En el cas de les capes ultrafines de $La_{0.7}Sr_{0.3}MnO_3$/$LaAlO_3$, s'analitza el mecanisme de relaxament d'aquestes capes, les quals alleugen la tensió de desajust a través de la formació de dislocacions per sobre d'un gruix de crític de capa de 2.5nm. Es realitza un estudi detallat dels canvis estructurals, químics i electrònics associats amb les dislocacions, posant especial

atenció a la influència dels camps de deformació en la composició química a la nanoescala. En aquesta direcció, s'observa una reorganització química a la regió del nucli de la dislocació, la qual té lloc per acomodar la deformació. També s'explora la dependència de l'organització de les dislocacions amb el gruix de les capes. Finalment, són analitzades les implicacions del camp de deformació de les dislocacions en la topografia i el transport elèctric a la superfície de les capes, demostrant que la naturalesa multi-escala de les dislocacions és de gran potencial per la creació de nanoestructures funcionals organitzades espontàniament en la superfície de capes fines d'òxids complexes.

Els principals resultats i conclusions obtinguts en aquesta Tesis obren una nova perspectiva per al desenvolupament d'estructures funcionals auto-organitzades basades en defectes que relaxen tensions.

Abbreviations List

ADF – Annular dark field

AFM – Atomic force microscopy

AMCSD – American Mineralogist Crystal Structure Database

BF – Bright field

BSE – Backscattered electrons

C-AFM – Conducting - atomic force microscopy

DF – Dark field

ED – Electron diffraction

EDS – Energy dispersive X-ray spectroscopy

FEG – Field emission gun

EELS – Electron energy loss spectroscopy

FFT – Fast Fourier transform

FWHM – Full width half maximum

FT – Fourier transform

FMM – Force modulation microscopy

GP – Glide Plane

HAADF – High angle annular dark field

HP – Half planes

HR – High resolution

ICMAB – Institut de Ciència de Materials de Barcelona

ICN_2 – Institut Català de Nanociència i Nanotecnologia

LAADF – Low angle annular dark field

LAO – $LaAlO_3$

LMO – LaMnO$_3$

LSMO – La$_{0.7}$Sr$_{0.3}$MnO$_3$

MAADF – Medium angle annular dark field

MD – Misfit dislocations

MFM – Magnetic force microscopy

OC – Orientation contrast

PIPS – Precision Ion Polishing System

PCA – Principal component analysis

PLD – Pulsed laser deposition

RF – Radio frequency

SAED –Selected area electron diffraction

SE – Secondary electrons

SEM – Scanning electron microscopy

SI – Spectrum images

SPM – Scanning probe microscopy

STEM – Scanning transmission electron microscopy

STO – SrTiO$_3$

TEM – Transmission electron microscopy

TD – Twin domain

TW – Twin wall

VHN – Vertical heteroepitaxial nanocomposites

XRD – X-ray diffraction

ZLP – Zero-loss peak

Chapter 1

Thesis rationale

Most of the functionalities of perovskite-type oxides are based on the presence of transition metal cations. Transition metal oxides present strong lattice-electron, electron-spin and spin-orbit couplings due to the competition between various interactions, such as Coulomb repulsion, strain, orbital bandwidths and Hund's exchange, which have energies with similar magnitudes [1]. This interplay between competing energy scales results in a variety of orderings of spin, charge, and orbital degrees of freedom, giving a wide variety of functional properties to these materials [2], including ferroelectricity, ferromagnetism, antiferromagnetism, metallicity, superconductivity, and optical properties.

Thin film epitaxy of complex transition metal oxides has been used to manipulate the properties of these materials by altering the subtle energy landscape of the competing interactions through the epitaxial strain and dissimilarities between the substrate and the grown material [3]. In the early stages of epitaxial growth of heterostructures, the film structure tends to adapt to the substrate in-plane cell parameters. Perovskite-type oxides are capable of accommodating strain in a rich variety of ways that can have various effects on the physical properties of the material. Furthermore, fascinating interfacial behaviour arises due the complex interplay of strongly correlated degrees of freedom, which in turn manifests a strong sensitivity to external perturbations [3]. The formation of highly conducting electron gases between two insulating materials [4], interfacial superconductivity [5, 6], or polarization-dependent spin transfer [7], are examples of these unexpected interfacial phenomena. The misfit relaxation mechanisms and interfacial coupling of these heteroepitaxial thin films are connected with thin film growth mechanism, tridimensional nanostructure generation and physical properties.

The next generation of nanodevices will demand further miniaturization requiring strategies to control and manipulate the lateral modulation of atomic length scales. Such strategies can take advantage of the fact that the relaxation mechanisms of strained films may accommodate defects, such as misfit dislocations or twin walls, which exhibit a strong tendency towards self-organization with characteristic length scales of 10 to 30 nm. Since the core structure of these defects is different from the bulk, they may be considered nano-phases with different physical properties, leading to the

formation of functional nanostructures. Thus, the formation of these self-organized defects offers a unique opportunity for the bottom-up elaboration of functional complex oxide devices.

Transmission electron microscopy is a useful technique for studying the interface microstructure and the associated defects that relieve the misfit strain of these heterostructures. The combination of the different image modes and spectroscopies permits to obtain structural and chemical information of the microstructure, the interface and the defects with atomic resolution.

The aim of this thesis is to characterize the microstructure and interface features of heteroepitaxial films and functional nanostructures of oxide materials by transmission electron microscopy. Special emphasis is given to the atomic and chemical structure of the interfaces and generated defects, such as dislocations, twin walls and phase segregations; as well as to the strain fields and their correlation with chemical heterogeneities. In this regard, two different systems are considered: $LaMnO_3:MnO_x$ nanocomposite grown on $(001)SrTiO_3$ and on $(001)LaAlO_3$substrates; and $La_{0.7}Sr_{0.3}MnO_3$ films with self-organized defects (twins or dislocations) grown on $(001)SrTiO_3$ and on $(001)LaAlO_3$. From this point of view, the materials studied in these work may be regarded as nanostructured films resulting from self-arrangement of misfit relieving defects as follows: phase segregations of MnO_x (volume defects) in $LaMnO_3$, twin walls between the twin domains (planar defects) in $La_{0.7}Sr_{0.3}MnO_3$ /$SrTiO_3$ and misfit dislocations (line defects) in $La_{0.7}Sr_{0.3}MnO_3$ /$LaAlO_3$.

1.1. Outline of the thesis

This thesis is organized as follows:

Chapter 2 discusses the basic concepts regarding epitaxial thin films derived from functional perovskite-type oxides. These concepts include the main structural, electronic and physical properties of transition metal perovskite oxides; the epitaxial growth of thin films; relaxation and interfacial accommodation mechanisms; and the main defects in the materials.

Chapter 3 describes the experimental techniques used to grow and characterize the thin films studied in this work. Special attention is given to transmission electron microscopy, which has been the principal methodology used to characterize the thin films studied in this thesis.

Chapter 4 analyses the spontaneous formation of regular vertically aligned nanoinclusions of a manganese oxide (MnO_x) embedded in an antiferromagnetic $LaMnO_3$ film via a microstructural characterization of a $LaMnO_3:MnO_x$ nanocomposite. This analysis includes the determination of $LaMnO_3$ matrix microstructure with respect to the substrate together with the identification of the manganese oxide phase and a secondary phase La-rich layer close to $LaMnO_3$-substrate interface. Finally, the formation mechanisms of the $LaMnO_3:MnO_x$ nanocomposite are discussed.

Chapter 5 contains a microstructural study of $La_{0.7}Sr_{0.3}MnO$ films on $(001)SrTiO_3$ with a detailed analysis of twin walls and their implications on the functional properties.

Chapter 6 analyses the microstructure, interface and defects present in $La_{0.7}Sr_{0.3}MnO_3$ ultrathin films grown on (001)$LaAlO_3$ substrates. This chapter also discusses the structural, chemical and electronic changes associated with the core of edge dislocations at the $La_{0.7}Sr_{0.3}MnO_3$-$LaAlO_3$ interface. It is also discussed dependence of the degree of order of the dislocation pattern on film thickness and the implications of the strain field of dislocations on surface topography and electrical transport.

Chapter 7 contains general conclusions and recommendations for further research.

Chapter 2

General concepts of epitaxial thin films of functional perovskite-type oxides

This chapter discusses the basic concepts related to thin film heterostructures of transition metal perovskite-type oxides, their interfaces and the defects associated with the relaxation mechanisms of these films. The first part of this chapter discusses the structural and physical properties of transition metal perovskite-type oxides, which are the base for understanding the behaviour of these materials. A basic overview of perovskite crystalline structure and the principal distortions of perovskite structure is given. A general description of the electronic structure and magnetic properties is also provided. Finally, special attention is paid to lanthanum manganese oxides, in particular to the two materials studied in this work: $LaMnO_3$ (LMO) and $La_{0.7}Sr_{0.3}MnO_3$ (LSMO). In the second part of this chapter, the main concepts related to thin film heterostructures are presented, including a brief description of the nucleation process and growth methods together with an overview of the epitaxial strain and main relaxation mechanisms of thin films. The main interfacial effects resulting from dissimilarity in the heterostructures at the interface are also discussed. The chapter ends with a presentation of the main defects in crystals.

2.1. Physical properties of transition metal perovskite-type oxides

2.1.1. Perovskite crystalline structure

The magnetic and electronic properties of the transition metal perovskite-type oxides are strongly correlated with crystal structure. Perovskites have the general formula ABX_3 where A and B are cations, A being usually an alkaline earth or rare earth element and B a transition metal, and X an anion, usually fluorine or oxygen. All compounds studied in this work are oxides, so X corresponds to oxygen (O). Normally, the A cation is relatively large and the B is smaller. The A cation is surrounded by twelve O anions in a cuboctahedral coordination while the B cation is surrounded by six O anions in an octahedral coordination.

The ideal perovskite structure has simple cubic symmetry, belonging to the space group Pm-$3m$. The base unit cell can be seen in Figure 2.1(a), with the A cation at the vertices and the O ions at the centre of the faces forming the octahedral around the B cation in the centre of the cube. However, it

can be also described with *B* cations at the vertices and the *A* ion at the centre of the cube. Thus, the perovskite structure forms a three dimensional framework of corner sharing BO_6 octahedra with the *A* cation in the centre of the cube defined by eight corner sharing octahedral units (Figure 2.1(b)).
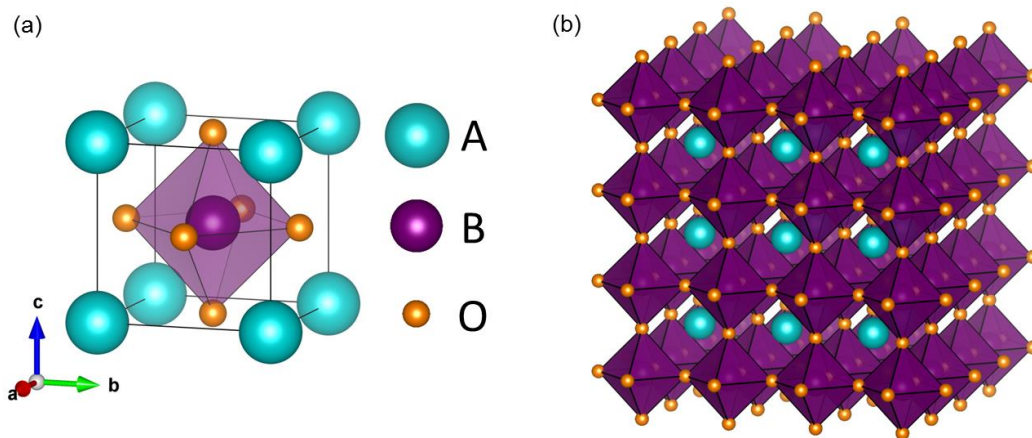
Figure 2.1: (a) A cubic perovskite unit cell, with *A* cations at the corners and *B* cations in the centre of the cube in the octahedra formed by the O ions. (b) The perovskite three dimensional framework.

The ideal cubic perovskite structure presents all the *B*-O-*B* bonds with 180° angle and a regular BO_6 octahedra, but most perovskites are distorted from this ideal cubic structure. Depending on the different elements occupying the *A* and *B* sites, and the partial substitutions at each site, the structure can deviate from the cubic symmetry to accommodate a certain distortion. The distortion from the ideal perovskite can be quantified by the tolerance factor (*t*) proposed by Goldschmidt [8]:

$$t=\frac{r_A+r_O}{\sqrt{2}(r_B+r_O)} \qquad \text{(Eq. 2.1)}$$

where r_A, r_B and r_O are the mean ionic radii of the *A* cation, *B* cation and O anion, respectively. For the stable-cubic structure *t*=1, however, oxide compounds with perovskite structure may form for a range of 0.89 < *t* <1.02 [9]. The perovskite structure accommodates this misfit in the ion sizes, inducing different kind of structural distortions. These distortions are of interest as they can affect the physical properties of materials, particularity electronic and magnetic properties [1].

Distortions of the octahedron

Distortion from the ideal perovskite structure could be divided into three components [10]: (1) the tilting pattern of the BO_6 octahedra, (2) the deformation arrangement of BO_6 octahedron and (3) the displacement of the *B* cation from the centre of the octahedron. These different distortions may occur individually or combined, but usually distortion (2) is associated with distortion (3) as both distortions are derived from electronic instabilities of the transition metal cation. These distortions are now explained in more detail.

(1) *Tilting of the BO_6 octahedra*

This is the most common distortion mechanism and the most important in establishing the space-group symmetry of the perovskite. Octahedral tilting occurs in perovskites with a *t*<1, while for a *t*=1 or

t>1 they often exhibit no octahedral tilting [11]. Usually, this distortion occurs as a result of the fact that the *A* cation is too small for the corner sharing octahedral network [12]. Thus, the *B*-O bonds are under compression while *A*-O bonds are under tension and tilting of the undistorted octahedra shortens the *A*-O bonds relaxing the stress. The BO_6 octahedra tilt as rigid units, about the principal axes of the primitive cubic cell, maintaining the connectivity of the octahedral framework. Furthermore, when an octahedron is tilted in some particular way, it causes tilting of the neighbouring octahedra. As a result, a cooperative tiling of the BO_6 octahedra takes place [13].

The tilting of the octahedra has effects on the unit-cell parameters and interaxial angles, and results in a lowering of the space group symmetry [13]. The various combinations of octahedral tilting and the resulting space-group symmetries have been described previously [11, 13-16]. Glazer [13] identified 23 tilting systems in terms of the rotations around *a*-, *b*- and *c*-axes parallel to the three cubic lattice vectors. These tilting systems and the resulting space-group symmetries were subsequently revised and corrected by Woodward [12, 15] and Howard and Stokes [16], who demonstrated that some tilting systems cannot construct a framework of regular octahedra and that small distortions of the octahedra must occur to preserve their connectivity.

(2) *Distortions of the BO_6 octahedra units*

The oxygen octahedron may be distorted by the Jahn-Teller distortion, which occurs due to electronic instabilities of the metallic *B* ion of the octahedra. The theorems of Jahn-Teller predict that distortions of the ideal octahedral geometry will occur providing an energetic stabilization by removing the electronic degeneracy usually associated with the *d*-electrons on the *B*-site cation [17]. Typically, the first order Jahn-Teller distortion is manifested as an elongation of some *B*-O bonds and a shortening of the remaining *B*-O ones. It has been shown that a larger energetic stabilization take place when the primary distortion mechanism is an elongation of two transversal bonds and contraction of the equatorial remaining four bonds, or an inverse distortion, a contraction of two transversal bonds and elongation of the equatorial remaining four bonds [18]. An example of the Jahn-Teller distortion is observed in ternary perovskites such as $LaMnO_3$, which presents a distortion where two *B*-O bonds shorten and two *B*-O bonds lengthen [11].

The associated arrangement of the elongations is called a cooperative Jahn-Teller distortion and determines the resulting symmetry of the system. These cooperative Jahn-Teller distortions describe the orbital ordering arrangement [19].

(3) *Displacements of the B cations*

The *B* cation may shift from the centre of its octahedron. These cation displacements result in a polar ferroelectric distortion. This distortion results in a further lowering of the crystal symmetry into a polar space group [20], but does not directly affect the lattice parameters, except by a relatively small distortion of the octahedra [13]. These distortions are often referred to as second-order Jahn-Teller effect [21].

2.1.2.Electronic structure

The electronic and magnetic properties of the perovskite-type oxides are not only determined by the crystal structure but also by the nature of d-electron orbitals of the transition metals in the structure. Transition metals have an electronic structure with an incomplete d-shell. This partly filled d-orbital controls the chemical behaviour and electronic properties of these materials [22].

The 3d states of the transition metal in a free ion are five-fold degenerate, as illustrated in Figure 2.2(a). However, if the transition metal ion is in an octahedral structure, the inter-electronic correlations governed by the Hund rules are perturbed by the octahedral crystal field (Coulomb repulsion due to the oxygen anions). Thus, the degeneration of the five d-orbitals is broken by the octahedral crystal field and the orbitals are split in two groups with different energy levels: the e_g doublet ($3z^2$-r^2 and x^2-y^2 orbitals) with high energy and the t_{2g} triplet (zx, yz and xy) orbitals with low energy, as illustrated in Figure 2.2(a). The orientation of these 3d-orbitals in the octahedra structure can be seen in figure Figure 2.2(b). The e_g orbitals are directed towards their oxygen neighbours and a 3d-electron in these orbitals has its energy raised by the Coulomb interaction. The t_{2g} orbitals are oriented between their oxygen neighbours, and an electron in these orbitals has an energy less affected by these Coulomb interactions. The crystal field splitting, Δ_{CF}, (10Dq) between the t_{2g} and e_g orbitals depends on the transition metal, its valence and the distance from the oxygen ions. The value of this splitting is about 2-3 eV in typical oxides with a perovskite structure [22].
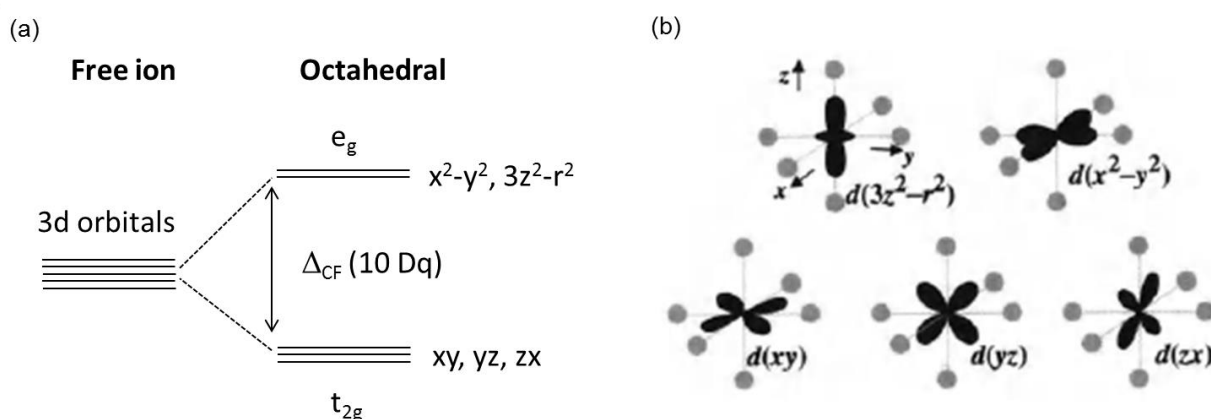
Figure 2.2: (a) Schematic representation of 3d one-electron energy levels of a Mn free ion and in an octahedral coordination where the degeneration of the five d-orbitals is broken by the octahedral crystal field. (b) Schematic illustration 3d-orbitals taken from Maekawa *et al*. [22].

In the case of manganese oxides, Δ_{CF} is in the order of 1.5 eV. However, it changes with Mn valance. For example, typical values for Mn^{4+}, Mn^{3+} and Mn^{2+} in oxides are 2.5 eV, 1.8 eV and 1.0 eV [23] and estimates for manganese perovskites from soft X-ray spectroscopy are 2.4 eV for Mn^{4+} and 1.5 eV for Mn^{3+} [24].

Each of the five d-orbitals can accommodate one electron of each spin orientation (up and down). The parallel electron spins are energetically favourable to fill in first, following the Hund first rule, due to minimization of the Coulomb repulsion energy [25].

2.1.3. Magnetism in transition metal oxides

The magnetism in materials arises from the coupling between magnetic moments leading to magnetically ordered states. This coupling of the magnetic moments is known as exchange interactions. Exchange interaction is described by the constant (J), which gives the separation of the electronic energy levels for parallel and antiparallel spin orientation. The exchange interaction between the neighbouring magnetic ions forces the atomic moments into parallel (ferromagnetism) or antiparallel (antiferromagnetism) alignment with their neighbours. The ferromagnetic coupling of neighbouring atoms is related to positive J>0, whereas antiferromagnetic properties, with antiparallel spin orientation at neighbouring atoms below the critical Néel temperature, T_N, are due to a negative exchange constant J<0. As a function of spin ordering, three types of antiferromagnetism are distinguished: A-type, the intra-plane coupling is ferromagnetic while inter-plane coupling is antiferromagnetic; the C-type, the intra-plane coupling is antiferromagnetic while inter-plane coupling is ferromagnetic; and the G-type, both intra-plane and inter-plane coupling are antiferromagnetic. The phenomenon of ferromagnetism and antiferromagnetism occurs below a critical temperature, T_C; above this temperature atomic moments are randomly aligned, resulting in a paramagnetic phase.

In the case of a transition metal in the perovskite structure, the moments are coupled by an indirect exchange. This indirect exchange couples moments over relatively large distances and it acts through an intermediary, through non-magnetic ions, such as oxygen. The superexchange and the double exchange are two possible mechanisms of indirect exchange which are particularly important in transition-metal oxides. The first one describes how antiferromagnetic ordering occurs, for example in the $LaMnO_3$. On the other hand, the double exchange mechanisms take places in a mixed valence compound, such as the oxide ferromagnet $La_{0.7}Sr_{0.3}MnO_3$, and describe the magneto-conductive properties of these materials. The double exchange predicts that this electron movement from one species to another will be more energetically favourable if the electrons do not have to change spin direction, thereby achieving the ferromagnetic alignment of moments.

The ferromagnetic behaviour is adequately described in the so-called band model, which is based on the one-electron density of states, considered separately for the two possible spin orientations, up ($\uparrow$) and down ($\downarrow$). There is an imbalance between the number of electrons of both electron spin orientations and the spin system can be divided into majority ($\uparrow$) and minority ($\downarrow$) spins. The macroscopic ferromagnetic moment at low temperature, results from the excess of majority spins over the number of minority spins. The ferromagnetic metals conduct in two independent channels of conduction, one for each spin orientation. These two currents are coupled by spin mixing. However, some materials present different density of states for each spin orientation at the Fermi level. For example, in the so-called half-metals such as $La_{0.7}Sr_{0.3}MnO_3$, the density of states at the Fermi level is zero for one spin direction and non-zero for the other. In this case, the material acts as a conductor (metallic) to electrons of one spin orientation, but as an insulator to the opposite spin orientation.

2.1.4. Lanthanum manganites perovskites

Usually, the transition metal perovskite-type oxides take the name according to the transition metal in the *B*-site. The transition metal in the structure of the complex perovskite oxide compounds

studied in this work is the manganese (Mn), and such compounds are denoted as *manganites* ($A_x MnO_3$). The *A*-sites in the manganite compounds studied in this work ($LaMnO_3$ and $La_{0.7}Sr_{0.3}MnO_3$) are totally or partially occupied by La and they can be named *lanthanum manganites*.

The physical properties of *manganites* are mainly determined by the mixed valence state of the manganese in the compounds. It is possible to obtain a mixed valence state of the Mn by various substitutions of the *A*-site (A_x^1 and A_{x-1}'') in the perovskite formula. If La^{3+} is completely occupying the *A*-site, the Mn in the *B*-site is Mn^{3+}, such as in $LaMnO_3$. However, with the partial substitution of La^{3+}, for example by Sr^{2+}, it is possible to obtain a mixed valence manganese compound ($La_{1-x}Sr_xMnO_3$). Thus, the mixed valence oxides can be viewed as a solid solution between end members. For example, the end members $LaMnO_3$ and $SrMnO_3$, with a formal valence state $La^{3+}Mn^{3+}O_3^{2-}$ and $Sr^{2+}Mn^{4+}O_3^{2-}$, lead to mixed valence compounds, such as $(La_{x-1}^{3+}Sr_x^{2+})(Mn_{x-1}^{3+}Mn_x^{4+})O_3^{2-}$.

In the case of manganese, the nominal electronic configurations of Mn^{2+}, Mn^{3+} and Mn^{4+} are $3d^5$, $3d^4$ and $3d^3$, respectively. The Mn^{2+} has a very stable configuration and a half-filled shell $t_{2g}^{3\uparrow}e_g^{2\uparrow}$ with $S=\frac{5}{2}$ (the electron spin angular momentum). The Mn^{3+} and Mn^{4+} have three spin-up electrons that fill the t_{2g} band but in the case of Mn^{3+} there is another spin-up electron in the e_g band, so Mn^{3+} has the partly-filled shell $t_{2g}^{3\uparrow}e_g^{1\uparrow}$ with $S=2$, whereas the Mn^{4+} has a shell $t_{2g}^{3\uparrow}$ with $S=\frac{3}{2}$. This occupancy of one-electron energy levels in octahedral coordination is represented in Figure 2.3. In the case of compounds with Mn^{3+}, the half filling of e_g orbitals is the driving force for the symmetry breaking by the Jahn-Teller distortion of the BO_6 octahedra. This distortion of BO_6 octahedron lowers the symmetry of the cubic crystal field producing a tetragonal distortion of the octahedral with asymmetric *B*-O bonds and a breaking of the degeneracy of $3z^2$-r^2 and x^2-y^2 orbitals in such a way that the centre of gravity of the t_{2g} levels and the centre of gravity of the e_g levels is unchanged, as illustrated in Figure 2.3
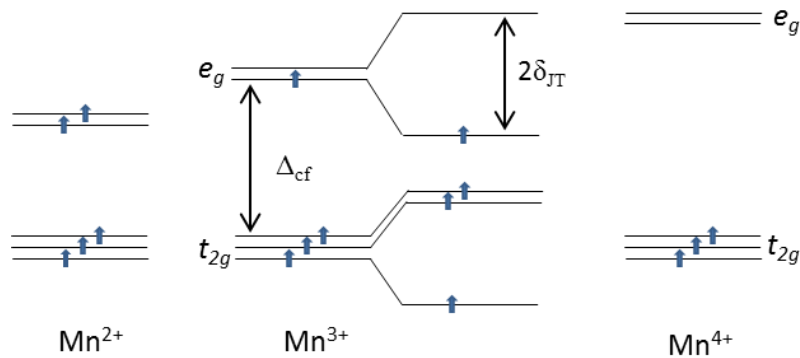
Figure 2.3: The occupancy of one-electron energy levels for Mn^{4+}, Mn^{3+} and Mn^{2+}. The effect of Jahn-Teller distortion is to lower the energy of Mn^{3+} resulting in a tetragonal distortion, but it leaves the others unchanged. Figure adapted from Coey *et al*. [9].

Across the mixed valence states obtained by the substitution in the *A*-site, the properties of transition metal perovskite-type oxides may be completely altered, as shown for the mixed valence manganese compound $La_{1-x}Sr_xMnO_3$ in Figure 2.4. The end members of this compound at low temperatures have an antiferromagnetic and insulator behaviour, which is the case of $LaMnO_3$ that

presents *A*-type antiferromagnetism, while a compound with values of *x* around 0.33 has a ferromagnetic and metallic behaviour. Moreover, at these values of x, the Curie Temperature (T_c) is maximum, T_c=370 K [26], which is above room temperature. This makes very interesting the use of this material for the development of room temperature devices.
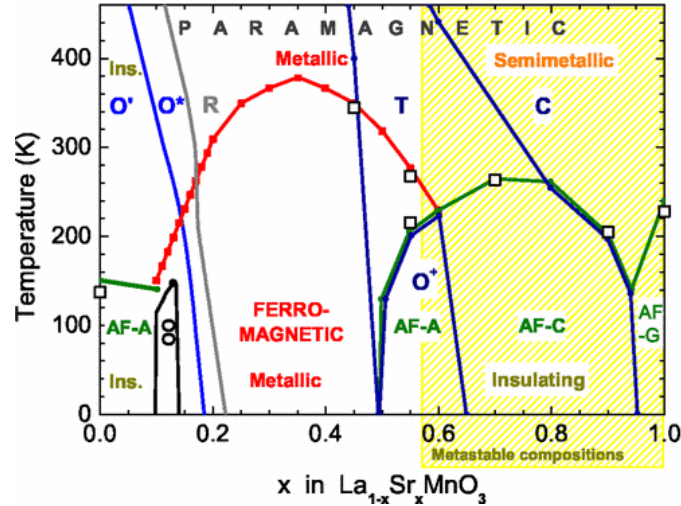
Figure 2.4: Phase diagram of La$_{1-x}$Sr$_x$MnO$_3$ as a function of Sr concentrations (x). Figure taken from Szewczyk *et al.* [27].

2.2. Thin film heterostructures: strain engineering

2.2.1. Nucleation and growth mechanisms

The first processes taking place during the thin film deposition are the nucleation and growth process. They determine the structure and morphology of a particular film and the related interface between film and substrate. Before obtaining a continuous film, a sequence of nucleation events occur during the early stage of deposition, typically accounting for the first few hundred angstroms of film thickness. The nucleation can occur in a number of ways, at step edges, defects, etc., and once the critical nucleus size is reached, the growth of nucleus can occur in many ways. Different growth modes can be described in more detail with simple thermodynamic models for the nucleation and growth of film materials. Thus, the morphology of the film that grows on top of the substrate will depend on the balance between surface and interface energies and the growth modes may be expressed in terms of the interfacial energies, γ, [28, 29].

The mechanical equilibrium among the horizontal components of the interfacial energy between the constitutive phases yields Young's equation

$$\gamma_{sv} = \gamma_{fs} + \gamma_{fv} \cos\theta \qquad\qquad \text{(Eq. 2.2)}$$

where γ_{sv} is the surface free energy of the substrate-vacuum interface, γ_{fv} is the surface free energy of the film-vacuum interface, γ_{fs} is the surface free energy of the substrate-film interface and θ is the contact or wetting angle. This equation provides a way to distinguish and better understand the three

basic modes of film growth illustrated in Figure 2.5 and namely: (a) *island growth* or Volmer-Weber, (b) *layer-by-layer* or Frank-Van der Merwe, and (c) *Stranski-Krastanov* [28, 29].
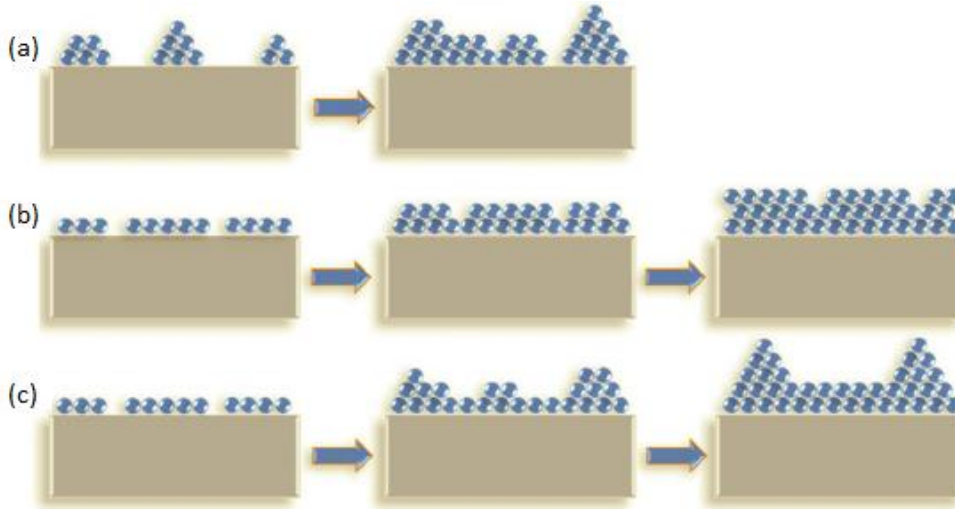
Figure 2.5: Illustrations of the basic growth modes: (a) Island growth, (b) layer-by-layer growth and (c) Stranski–Krastanov growth. Figure taken from Martin *et al.* [30].

(a) *Island growth (Volmer ⁻Weber growth)* occurs when $\gamma_{sv} < \gamma_{fv} + \gamma_{fs}$ which makes $\theta > 0$. If the influence of γ_{fs} is disregarded, this relation suggests that island growth occurs when the surface energy of the film exceeds the surface energy of the substrate. This happens as atoms or molecules in the deposit are more strongly bound to each other than to the substrate. Thus, the smallest stable clusters nucleate on the substrate and grow in three dimensions to form islands. This is often the case when the film and substrate materials are dissimilar. This growth mode is typically observed in the growth of metal and semiconductor films on oxide substrates [28], but there are also a few examples of oxide films on oxide substrates [31, 32].

(b) *Layer-by-layer growth (Frank–Van der Merwe growth)* happens when $\gamma_{sv} \geq \gamma_{fv} + \gamma_{fs}$ which makes $\theta = 0$. In this growth mode, a film with low surface energy wets a substrate with a higher surface energy. This growth mode displays the opposite characteristics of island growth, the atoms or molecules in the deposit are more strongly bound to the substrate than to each other. Here, the extension of the smallest stable nucleus occurs in two dimensions, resulting in the formation of planar films. When the first monolayer is complete, it is covered with a slightly less tightly bound second layer, so each new layer starts to grow only when the last is completed. A classic example of this growth mode is the epitaxial growth of oxide and semiconductors materials. The field of oxide thin film growth has developed around the ability to control materials through this and other similar growth modes [30].

(c) *The layer-by-layer plus island or Stranski-Krastanov (S-K)* growth mechanism is an intermediate combination of the previous two modes. Thus, initially $\gamma_{sv} \geq \gamma_{fv} + \gamma_{fs}$ takes place and one or several complete monolayers are formed. However, elastic energy is stored in the film due to interfacial tensions as a result of the film-substrate lattice mismatch, and after a certain thickness it gives $\gamma_{sv} < \gamma_{fv} +$

γ_{fs} and island growth occurs. This growth is common and has been observed in a number of metal–metal and metal–semiconductor systems.

In the case of octahedral framework systems, as transition metal perovskite-type oxides, the flexibility of the lattice to accommodate large interfacial dissimilarities favours layer by layer grown, wetting of the substrate, hindering of the formation of islands [33]. However, the formation of island growth has been obtained by the combination of different structural families using chemical solution deposition, such as perovskite/rock-salt ($La_{0.7}Sr_{0.3}MnO_3$/MgO) [31], fluorite/perovskite (CeO_2/$LaAlO_3$) [34], and perovskite/fluorite ($La_{0.7}Sr_{0.3}MnO_3$/Y-stabilized ZrO_2) [32]. Moreover, the strong sensitivity of the growth mode to interfacial subtleties has been demonstrated in pulsed laser deposited Y-stabilized ZrO_2/$SrTiO_3$ (fluorite/perovskite) system, in which the fluorite film formed continuous films or islands depending on the atomic termination plane of the $SrTiO_3$ substrate [35].

However, other than thermodynamic considerations, growth is also dependent on the kinetics of the system, including the rate of adatom arrival, temperature and pressure, which are the tools used to control the growth of these materials [30].

2.2.2. Epitaxial strain and relaxation mechanism

Epitaxial growth is the extended single-crystal film formation on top of a crystalline substrate. The epitaxial strain is obtained as a result of epitaxial growth, which submits the film structure to in-plane biaxial strain, either compressive or tensile depending on the cell parameter mismatch with the substrate. Thus, an important characteristic of epitaxy is the lattice mismatch strain or misfit (f) between the grown film and the substrate, which is defined as:

$$f = \frac{a_s - a_f}{a_f}$$

(Eq. 2.3)

where a_f and a_s are the bulk lattice parameters of the film and substrate, respectively. Typically, $|f| <$ 0.1 (in terms of absolute value) is a requirement for epitaxy [30]. Following the definition of the mismatch in the (Eq.2.3), a positive sign of f means that the equilibrium cell structure of film is smaller than the substrate and therefore when growing on a larger substrate the film is submitted to a tensile stress. In contrast, a negative sign of f means the film is submitted to a compressive stress. A specific amount of strain can be imposed on a film by the substrate, according to the choice of mismatch between the lattice constants of the substrate and the film and their relative orientations.

There are two main types of epitaxy: homoepitaxy and heteroepitaxy. Homoepitaxy refers to the growth of a film on a substrate of the same material, thus film and substrate are identical, the lattice parameters are perfectly matched and there is no interfacial-bond straining. In the case of heteroepitaxy, the film and substrate are different materials and the lattice parameters are unmatched, but have similar structures to guide the growth of the film. If the lattice mismatch is very small, then the interfacial structure is essentially like a homoepitaxy (Figure 2.6(a)). However, differences in film and substrate chemistry and thermal expansion coefficient can strongly influence the electronic properties and perfection of the interface. If the lattice parameters are slightly more mismatched, substrate and

film lattices strain to accommodate their crystallographic differences during the early film formation stages and a coherent interface results from a lattice strain, presenting a perfect lattice matching (Figure 2.6(b)). This usually occurs between dissimilar materials which have the same crystal structure.

FILM

SUBSTRATE

MATCHED   STRAINED   RELAXED
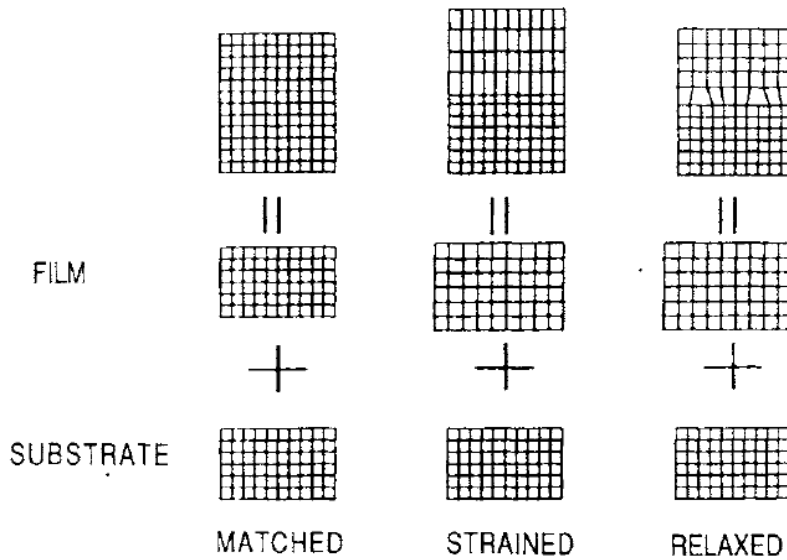
Figure 2.6: Schematic representation of different heteroepitaxial growths and the resulting interfaces. (a) A film and substrate with a very small lattices mismatch, similar to a homoepitaxy, (b) strained epitaxy with a coherent interface and (c) relaxed epitaxy with a partially coherent interface. Figure taken from Ohring [28].

According to the classical model by Frank and van der Merwe [36] and Matthews-Blakeslee [37], very thin films strain elastically to incorporate the same interatomic spacing as the substrate, via an elastic deformation. This type of film growth is usually referred to as *pseudomorphic* and gives rise to a coherent film. Assuming that the film and substrate have the same Young's, Y, modulus and same shear, G, modulus, the elastic strain energy, E_e, is defined as $E_e = Yh\varepsilon^2/(1-v)$, where ε is the biaxial elastic strain, v is Poisson's ratio and h the film thickness. As the film thickness increases, the elastic strain energy also rises. Above a critical thickness, h_c, the elastic strain energy surpasses the energy associated with a relaxation of the film by misfit dislocations, via a plastic deformation. Thus, above the critical thickness, total strain energy E_T (per unit area) is a sum of the elastic and dislocation energies $E_T = E_e + E_d$. The Peierls–Nabarro model holds that a pure edge dislocation only accommodates uniaxial strain [38]. Thus, the biaxial strain in the films is necessarily accommodated by the formation of a square grid array of misfit dislocations, as shown in lattice-mismatched heterostructures of III–V semiconductors, such as GaAsP/GaAs [39]. Assuming that misfit dislocations are arranged in a square grid with a spacing of S, the elastic strain in the film is reduced from its initial misfit value f to $\varepsilon = f - b/S$, where b is the magnitude of the Burgers vector. The quantity b/S is proportional to the number of misfit dislocations. As the film thickness increases, misfit dislocations progressively accommodate interfacial strain in the system, leading to a relaxed epitaxy film. This relaxed epitaxy film is obtained when $b/S = f$, and the film strain disappears [28]. A semi-coherent interface results from a relaxed film by misfit dislocations. This kind of interface presents dislocations and a partial matching (Figure 2.6 (c)).

However, epitaxial perovskites often avoid misfit-dislocation mechanisms, and misfit strain is relieved by a combination of symmetry changes and ferroelastic domains. Some examples are found among a variety of functional films, such as ferroelectric $PbTiO_3$ [40], multiferroic $BiFeO_3$ [41] and $TbMnO_3$ [42], and half-metal $La_{0.7}Sr_{0.3}MnO_3$ [43, 44].

2.2.3. Interfacial effects

The chemical and structural arrangement of an interface may be different depending on the substrate morphology and roughness, chemical interactions, diffusion rates, and nucleation processes. Two main types of interfaces can be distinguished: sharp and rough. The sharp interface is characterized by a sudden change from the film to the substrate within an atomic spacing distance. Such interfaces arise because of low interdiffusion rates and the lack of interaction between film and substrate atoms. The rough interface is a result of either a preexisting substrate morphology roughness, the interdiffusion between the film and substrate atoms (referred to as a diffusion interface) or due to the formation of a new compound at the interface (a compound interface). A diffusion interface is characterized by a gradual change in composition between film and substrate. In contrast, a compound interface is characterized by a layer or multilayer structure which is created by chemical reaction and diffusion between film and substrate atoms. Schematic illustrations of these interface arrangements are show in Figure 2.7.
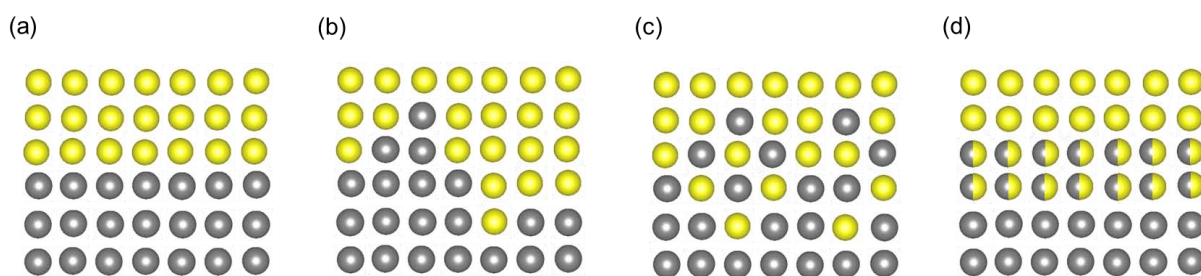
Figure 2.7: Interface arrangements: sharp interface (a) and rough interface (b)-(d). Different kinds of rough interface are presented: (b) preexisting substrate roughness, (c) inter-diffusion interface and (d) new compound interface, respectively.

In furthermore, the interfaces react to accommodate the dissimilarities between the film and the substrate in a cooperative way. Thus, the subtle equilibrium among the different degrees of freedom of the system is perturbed [1, 33]. As a result of the dissimilarities between the film and the substrate, misfit strain, polar discontinuity and modification of the octahedral tilting arrangement may occur at the interface. These are discussed further below.

Misfit strain

As has been previously mentioned, the coherent growth of a film on a substrate produces an elastic strain to accommodate the lattice mismatch between the film and the substrate. The change in the in-plane lattice parameter may be accommodated entirely by two different possibilities: a change in the in-plane metal-oxygen bond lengths or a change in the type and/or magnitude of the tilt patterns and rigid rotations of the oxygen octahedra. The first accommodation mechanism changes the B-O bond length while the B-O-B bond angles remain unchanged. This accommodation mechanism may produce a

tetragonal distortion of the film; the in-plane parameter is adapted to the in-plane parameter of the substrate by a reduction or an elongation of the equatorial B-O bond lengths due to compressive or tensile strain, respectively (Figure 2.8(a) and (b)). In the second accommodation mechanism, the B-O-B bond angles change while the B-O bond length remains unchanged. The rotation of the octahedra may be about the axis perpendicular or/and an axis parallel to the substrate as is shown Figure 2.8(c) and (d).

These two accommodation responses will have drastically different effects on the functionalities of the film. A change in the B-O bond length will affect the magnitude and symmetry of the crystal field splitting, whereas changes in B-O-B bond angles determine the strength and the sign of magnetic superexchange interactions [45, 46]. However, both mechanisms generally occur simultaneously. Based in the calculations of Rondinelli and Spalding [1], it could even happen in counterintuitive ways: a compressive strain may cause an increase in the B-O length if the B-O-B angle change dominates, and viceversa. Most of the calculations have been proven to predict the fully strained situation, however, upon the strain is partially released by the formation of defects a new scenario occurs, which may show changes in the B-O length, B-O-B angle and octahedra arrangements.
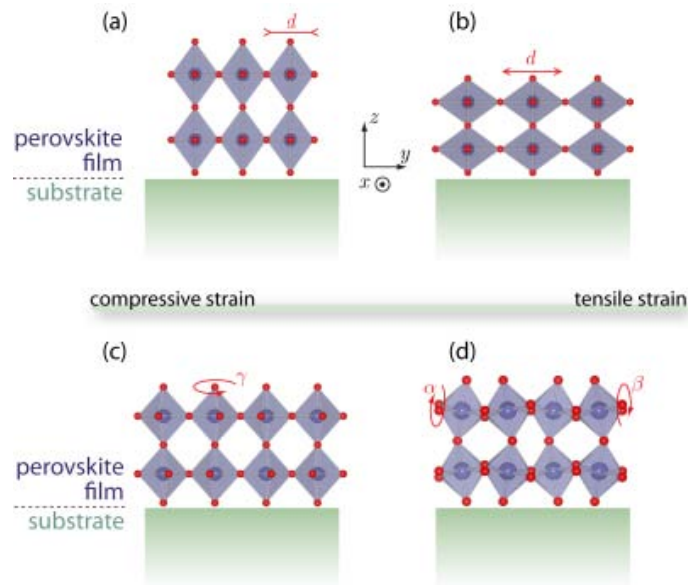
Figure 2.8: Schematic representation of film in-plane lattice parameter accommodation mechanism, through a BO_6 distortion by a contraction (a) or elongation (b) of the equatorial B-O bond lengths or through a rotation perpendicular to the substrate (c), and/or about an axis parallel to the substrate plane (d). Figure adapted from Rondinelli and Spalding [1].

In the case of a cubic structure grown on a cubic structure; the misfit strain is principally defined by the in-plane lattice mismatch. However, in the case, for example of a rhombohedral structure on a cubic structure, the total misfit strain is defined by the in-plane lattice mismatch and shear strain. This is the case of La$_{0.7}$Sr$_{0.3}$MnO$_3$ grown on SrTiO$_3$, in which discrepancies between the predictions of the theoretical models and the experimental results have been observed in the relaxation mechanism of this system [43]. These discrepancies are an example of the ability of materials to propagate interfacial perturbations to the film at a lower energy cost than that associated with the formation of the misfit dislocation network needed to plastically relax the stored strain energy [33].

Misfit strains have important consequences on the electronic structure of the films. They have the ability to break the $(x^2 - y^2)/(3z^2 - r^2)$ orbital degeneracy [47], similar to the Jahn-Teller distortion, thus modifying their electron occupancy and eventually leading to orbital reconstructions. Preferential orbital occupancies in the e_g doublet induced by the interface have been shown by X-ray linear dichroism investigations [48, 49]. The first studies concluded that the out-of-plane $3z^2 - r^2$ orbitals are preferentially occupied independently of the specific nature of the interface, as an intrinsic consequence of the symmetry breaking [48]. However, a later investigation, which revealed that the observed X-ray linear dichroism is rather a consequence of the superposition of interfacial and free surface effects, found that a tensile strain favours the occupancy of the in-plane $x^2 - y^2$ orbitals, while a compressive strain favours the occupancy of the out-of-plane $3z^2 - r^2$ ones, in agreement with simple electrostatic arguments [49].

Polar discontinuities

The polar discontinuities may arise from the fact that individual atomic layers AO and BO_2 in ABO_3 perovskites can be electrically charged. Figure 2.9 depicts a partial view of the possible interfaces: B-site termiated (a) $La_{0.7}Sr_{0.3}MnO_3$ on AlO^{2-} terminated (001)$LaAlO_3$, and (b) $La_{0.7}Sr_{0.3}MnO_3$ on TiO^{2-} terminated (001)$SrTiO_3$. Thus, the net charge per area unit is +2/3e and -2/3e in $La_{0.7}Sr_{0.3}MnO_3$, zero in $SrTiO_3$, and +1e and -1e in $LaAlO_3$ (e is the electron charge).
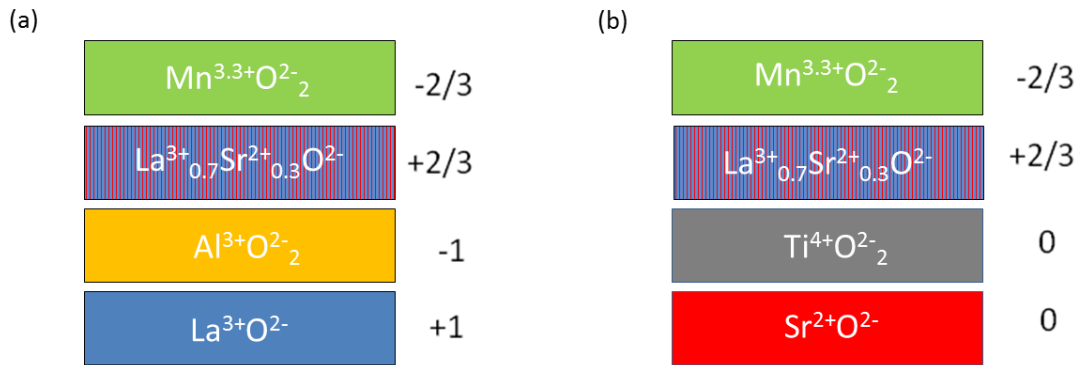
Figure 2.9 : The polar discontinuity illustrated for atomically abrupt (001) interfaces between $La_{0.7}Sr_{0.3}MnO_3$ on (a) AlO^{2-} terminated $LaAlO_3$ and (b) TiO^{2-} terminated $SrTiO_3$.

In the absence of any interface reconstructions, the polar discontinuities lead the electrostatic potential to divergence with thickness, resulting in the so-called polar catastrophe [50], which forces the interfacial reconstruction. Nakagawa *et al.* [50] suggested that in transition metal perovskite-type oxides, chemical roughening is not the only option for a charge rearrangement; mixed valence charge compensation can occur if electrons can be redistributed at lower energy cost than redistributing ions. Their analysis of distribution of charges and ions across the $LaAlO_3$-$SrTiO_3$ interfaces showed an asymmetry between the different plane termination sequences, indicating that in one case the charge rearrangement is compensated by the electrons while in the other is compensated by the ions [50].

The reconstruction due to the polar discontinuities often leads to unanticipated behaviours. These however, in some cases are unwanted as they alter the intrinsic material properties at the interface. An example is the polar discontinuity in $La_{0.7}Sr_{0.3}MnO_3$ on $SrTiO_3$. The $La_{0.7}Sr_{0.3}MnO_3$ exhibits

metallic behaviour and mobile charges can screen the diverging potential [51], resulting in a compensating charge transfer of 1/3e. This would lead to a shift of the Mn valence at the interface towards 3^+, as confirmed by different spectroscopic analyses [43, 52, 53]. This charge enrichment together with a preferential occupation of d-e$_g$ $3z^2$-r^2 orbitals [48, 54] leads to a local C-type antiferromagnetic ordering at the interface, the so-called "dead-layer", which is a few unit cells in width and exhibits a large decrease in conductivity [43]. Thanks to the progress in the atomic control of interfaces in oxide heterostructures, the detrimental effects of the dead-layer can be avoided by precise modifications of the interfacial architecture [55], or polar discontinuities can even be exploited to intentionally induce hole doping avoiding the disorder effects typically associated with chemical doping [51].

Octahedral tilt discontinuities

A more subtle dissimilarity is that between the octahedral tilt systems of the film and the substrate. The substrate tends to transmit its octahedral pattern to the film, or viceversa, which is referred to as interfacial octahedral coupling. Interfacial octahedral coupling has motivated intense research on engineering novel tilt patterns with specific functionalities across the use of this phenomenon [1, 56, 57]. Octahedral coupling across the interfaces is supported by recent advances in electron microscopy, which have provided direct access to oxygen positions [58, 59]. An example is the propagation of the octahedral tilt pattern of a rhombohedral LaAlO$_3$ substrate into an epitaxial cubic SrTiO$_3$ film that has been directly determined using the negative spherical aberration imaging technique [58].

2.2.4. Self-organized defects

A local defect disturbs the regular arrangement of atoms in a perfect crystal structure. Defects can be generated during the relief of the strain, such as misfit dislocations or domain walls between crystal domains with different orientation. These defects influence many film properties, such as chemical reactivity, electrical conduction and mechanical behaviour [28]. The interest in these defects is due to the fact that the core of defect the often shows a different structure and symmetry from the rest of the film material at the nanoscale [60-62], and they may be considered a different phase with a different behaviour. Moreover, some of these defects exhibit a strong tendency towards self-organization with characteristic length scales of around tenths of nanometres.

The defects may be classified as point, line, planar or volume defects.

Point defects:

Point defects occur only at a single lattice point that can be either a lattice site or a non-lattice site. The different possible point defects are: a vacancy, interstitial atoms and substitutional atoms. The vacancy is formed by the removal of an atom (cation or anion) from an atomic site while interstitial atoms are formed by the introduction of an atom into a non-lattice site. The atom introduced at this interstitial site may be an atom of the parent lattice (self-interstitial atom) or an extrinsic atom (impurity interstitial atom). In substitutional atoms, an atom of the parent lattice lying in a lattice site is replaced by the extrinsic atom. It is known that vacancies and interstitials can be produced in materials by plastic

deformation and high-energy particle irradiation. All the point defects mentioned produce a local distortion in the perfect lattice. Moreover, additional effects are important when the removal or addition of atoms (cation and anion) changes the local electric charge in the lattice. To preserve an overall neutral charge, the vacancies must occur either in groups of opposite sign, forming di-vacancies known as Schottky defects, or in association with interstitials of the same ion, Frenkel defects. Another defect, that does not correspond to any of the point defects described previously, is an antisite defect. This type of defect is defined as the exchange between the positions of atoms of differences species. For example, in the case of perovskite structures, the introduction of an *A* cation in a *B* perovskite site together with the introduction of *B* cations at the *A* site.

Linear defects: dislocations

Linear defects are commonly called dislocations. The dislocations can be described as being caused by the termination of a plane of atoms in a crystal or by inserting an extra plane of atoms. Dislocation lines can end at the surface of a crystal and at grain boundaries, but never inside a crystal. Thus, dislocations must either form closed loops or branch into other dislocations [63].

The most useful definition of a dislocation is given in terms of Burgers circuit. The Burgers circuit is any atom-to-atom path taken in a crystal containing dislocations which forms a closed loop. If the same atom-to-atom sequence is made in a crystal and the circuit does not close, then the circuit must enclose one or more dislocations. The vector required to complete the circuit is the Burgers vector, $\mathbf{b}$ [63].

Two main types of dislocations are edge and screw dislocations. A dislocation has two characteristics that allow these two types of dislocations to be distinguished: a line direction ($\mathbf{u}$), which is the direction running along the edge of the extra plane; and the Burgers vector, which describes the magnitude and direction of distortion to the lattice. In an edge dislocation, the Burgers vector is normal to the line of the dislocation ($\mathbf{b} \cdot \mathbf{u} = \mathbf{0}$) while in a screw dislocation the Burgers vector is parallel to it ($\mathbf{b} \cdot \mathbf{u} \neq \mathbf{0}$). In the most general case, the dislocation line lies at an arbitrary angle to its Burgers vector and the dislocation line has a mixed edge and screw character. However, the Burgers vector of a single dislocation has fixed length and direction, and is independent of the position and orientation of the dislocation line [63].

The dislocation can move through the crystal when enough force or stress is applied from one side of the crystal structure, breaking and joining bonds with them until it reaches the grain boundary. The plane containing the dislocations line and the Burgers vector is the glide plane. In order to facilitate the movement through the crystal lattice the dislocations can decompose into partial dislocations. Considering a dislocation with a Burgers vector, $\mathbf{b}$ it can be decomposed into partial dislocations with Burgers vectors $\mathbf{b}_1$ and $\mathbf{b}_2$, if the energy state of the sum of the partials is lower than the energy state of the original dislocation. This is summarized by *Frank's Energy Criterion*: $\mathbf{b} > \mathbf{b}_1 + \mathbf{b}_2$ is favourable to decompose into partial dislocations while $\mathbf{b} < \mathbf{b}_1 + \mathbf{b}_2$ is not favourable [63].

In the case of thin film hetersotructures, as previously mentioned, the formation of misfit dislocations at the interfaces is the common relaxation mechanism for relieving the misfit strain. The

misfit dislocations often arrange themselves into highly ordered periodic patterns, induced by the repulsive forces between misfit dislocations, as well as their mobility along the interfaces, which depends on the elastic properties of the material and the deposition conditions. As was previously mentioned, the relation between the lattice strain and the misfit dislocations is given by $f = b/S$ for a relaxed film. Dislocation spacing within the 10–30 nm range are commonly obtained, which is far below the miniaturization limits achievable in oxides by top-down approaches [64]. As expected, an increase in f results in an increase in misfit dislocation density [65]. Thus, dislocation spacing can be manipulated through an appropriate choice of the substrate and film thickness

Planar defects

Planar defects disrupt the long-range stacking sequence. Examples of planar defects are: grain boundaries, stacking faults and twin walls. The grain boundary occurs where a crystallographic direction in a crystal changes drastically, for example, between two randomly oriented grains. A stacking fault is a change in stacking sequence of atomic planes resulting from the removal or introduction of an extra layer. The twin wall acts as a mirror plane between adjacent orientational domains, or twin domains, generally formed by phase transition from a high symmetry phase to a lower symmetry.

Volume Defects

Volume defects, such as precipitates, voids and bubbles can occur under certain circumstances and have important effects on the properties of crystalline solids [63]. The formation of a random distribution of precipitates or phase segregations in a material may produce a nanocomposite formed by the base material and the phase segregated. A novel concept to develop new functional devices is based on the self-organization of vertical heteroepitaxial nanocomposites (VHN) [66, 67]. Thus, if the segregated phase has a vertical orientation the resulting nanocomposite can be considered as a VHN. $La_{0.7}Ca_{0.3}MnO_3$ [66] or $La_{0.7}Sr_{0.3}MnO_3$ [68, 69] base nanocomposites are examples of self-assembled VHN, which highlight this new physical phenomena.

Chapter 3

Methodologies and Methods

The aim of this chapter is to describe the methodologies and methods used in relation to the structural characterization of the thin films investigated in this study, with special attention paid to transmission electron microscopy (TEM). Techniques to grow films and to characterize their physical properties are also introduced.

3.1. Transmission Electron Microscopy

TEM is a powerful tool for materials science investigation. It has different operation modes and a broad range of characterization techniques which can offer a variety of information. It can reveal structural and chemical information with atomic resolution using electron diffraction, imaging and spectroscopic analysis. The main content of this section is based on the text books given in Ref. [70] and [71].

3.1.1. Techniques and equipment employed

A variety of TEM techniques were used for the characterization of the films presented in this thesis. Conventional TEM, high resolution (HR)TEM measurements, selected area electron diffraction (SAED), diffraction contrast imaging, scanning (S)TEM (high angle annular dark field (HAADF), medium angle annular dark field (MAADF) and low angle annular dark field (LAADF)) imaging, spectroscopic analyses (energy dispersive X-ray spectroscopy (EDS) and electron energy loss spectroscopy (EELS)) were performed with a FEI Tecnai F20 S/TEM equipped with a field emission gun (FEG) and operated at 200 kV. This microscope is located at the Institut Català de Nanociència i Nanotecnologia (ICN$_2$), Bellaterra, Spain. Conventional TEM and diffraction contrast imaging were also performed with a Jeol JEM-2011 operating at 200kV at the Servei de Microscòpia, Universitat Autònoma de Barcelona (UAB), Bellaterra, Spain. A FEI Tecnai F20 SACTEM equipped with Schottky FEG, a spherical aberration corrector (120 pm resolution) and operated at 200 kV was used to obtain HRTEM images with higher spatial resolution. In addition, a Hitachi HF3300 electron microscope working at 300 kV and equipped with a cold FEG and an imaging aberration corrector CEOS aplanator was also used to obtain HRTEM images in planar view orientation. Both microscopes are located at the Centre d'Élaboration de Matériaux et d'Etudes Structurales (CEMES - CNRS), Toulouse, France. Annular dark field (ADF) images and EELS spectrum-images (SI) of cross-section samples were

acquired using a Nion UltraSTEM 200 operating at 100 kV at Laboratoire de Physique des Solides (LPS)-CNRS, Orsay, France. HR-STEM imaging combined with spectroscopic analysis (EDS and EELS) at atomic scale were obtained with a FEI Titan[3]™ G2 60-300 S/TEM and Titan[3]™ 80-300 S/TEM operated at 300 kV. Both microscopes were equipped with a FEG and a monochromator. Titan[3]™ G2 60-300 S/TEM was equipped with a third order-image aberration corrector (130 pm resolution), a Super-X four quadrant detector and a Gatan Quantum dual EELS spectrometer, and Titan[3]™ 80-300 S/TEM was equipped with a third order probe aberration-corrector (70 pm). Both are located at Center for Electron Microscopy and AnalysiS (CEMAS), Materials Science and Engineering department of Ohio State University (OSU), Columbus, USA.

3.1.2. TEM sample preparation

The thin film specimens must be electron transparent to be observed by TEM, so their thickness has to be less than 100 nm. However, it is better for the interpretation of the experimental results, especially for performing HRTEM or electron spectroscopy, if they are as thin as possible i.e., only a few tens of nm. Therefore, the method for preparing the TEM sample is an important first step in obtaining good TEM results.

There are many ways to prepare a TEM specimen. The method varies depending on the kind of samples to prepare. In this study, traditional mechanical polishing was used to prepare the thin film samples for observation by TEM. With this method, preparing a sample normally requires a few days, which is longer compared with other methods of TEM thin foil specimens, for example using a focused-ion beam instrument which only needs a few hours to prepare a sample. However, mechanical polishing is cheaper and allows larger viewing areas, while being less aggressive and avoiding possible ion implementation effects.

TEM samples can be prepared in cross-section or in planar view orientations relative to the surface plane of the thin film sample, depending on the observation of interest. If a cross-section view is required then the plane of polishing must be perpendicular to the film-substrate interface and it is then possible to observe the film and the substrate separately as well as the interface between them. The first step to prepare a cross-section consists of cutting two equal slides of the sample using a diamond wire. The cut is made perpendicular to the zone axis of interest, [100] or [010], as was the case of the samples presented in this work. Then the two slices are glued together face to face with epoxy resin. The result is a sandwich with the substrate on the external parts and the film in the internal part with a thin layer of epoxy in the middle. In this study, the sandwich was then cut in small slices, with a width of 600 μm, and one of these slices was polished until the sample had a thickness of less than 20 μm using a Multipolishing machine and grinding papers of decreasing diamond crystallite radius from 15 μm to 0.1 μm. An alcohol based lubricant was used during the polishing. The reduction of the thickness during the polishing was controlled by a micrometre. In parallel, an inspection of the polishing surface was performed using an optical microscope to check that there were no furrows or scratches. For better manipulation, the sample was glued in a commercial copper TEM ring of copper of 3 mm diameter with a hole in the centre with a diameter of 1 mm or 1.5 mm or 1 mm x 2 mm (ellipsoid hole) depending of cut and the original size of the

sample. Finally, ion (Ar$^+$)-milling with a Precision Ion Polishing System (PIPS), Gatan, Inc., using a low angle (6º - 7º) and low acceleration voltage (3-5 KeV), was performed until a hole was created. Finally, the voltage was decreased to 0.1 KeV to obtain larger and cleaner viewing areas.

In the TEM sample planar view, the film and the substrate are superposed. Normally, this kind of sample is easier to prepare than cross-section. The plane of polishing is parallel to the film-substrate interface, so the film is protected and only the substrate is polished. The rest of the process is the same as in cross-section. In this study, the sample was polished manually to obtain a thickness of less than 20 µm. A copper TEM ring was then glued on top of the sample which was then thinned with an ion milling using the PIPS until a small hole appeared surrounded by an electron transparent area.

3.1.3. Interaction of electrons with matter

The variety of information that can be obtained by TEM is due to the wide range of signals that arise when electrons interact with a specimen. The signals used in this thesis are summarized in Figure 3.1. When the incident electrons interact with the specimen atoms, they can be deflected by passing close to other electrons or the positive nucleus of an atom. These Coulomb (electrostatic) interactions cause electron scattering which can be classified in terms of coherency and elasticity.
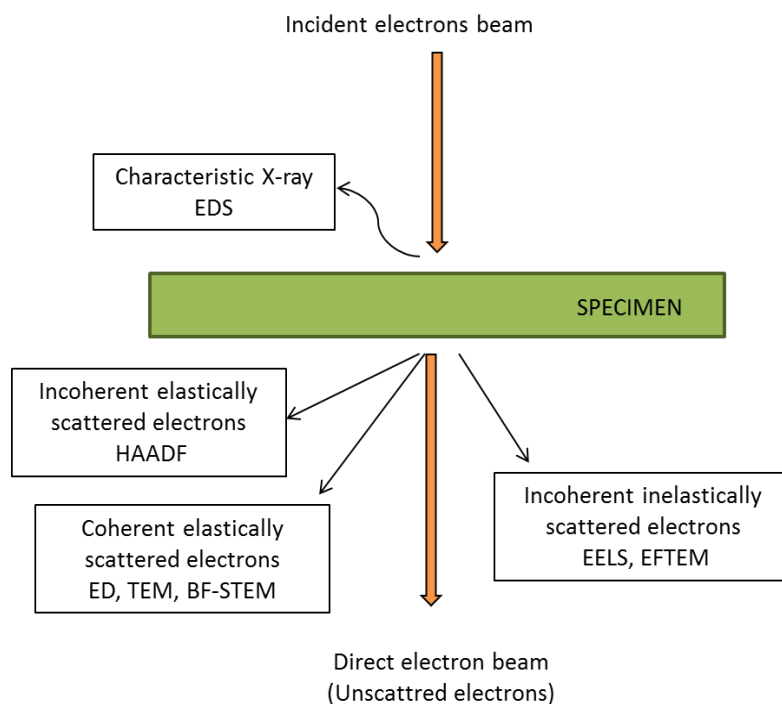
Figure 3.1: Schematic representation of some of the resulting signals that arise when electrons interact with a specimen.

The separation of the electron scattering into coherent and incoherent can be done if the electrons are considered as waves. If the electrons maintain a phase relationship after the scattering event, they are termed coherently scattered electrons while if they end up with no phase relationship between them they are termed incoherently scattered electrons.

Elasticity, on the other hand, is based on the particle nature of the electrons and is related to the degree of electron energy loss after scattering. If there is no energy loss, the result is termed elastic scattering whereas if there is some measurable energy loss, the result is termed inelastic scattering. Elastic scattering involves Coulomb interaction with atomic nuclei (by Coulomb attraction by the nucleus). If an incident electron approaches close enough to the nucleus, it is deflected through a large angle (Rutherford scattering). However, the majority of electrons travel further from the nucleus centre of an atom and incident electrons are therefore scattered through small angles. Elastic scattering is usually coherent, if the specimen is thin and crystalline. Elastic coherently scattered electrons occur at relatively low angles (<10°) in the forward direction and are used in imaging and diffraction modes (TEM, ED and bright field (BF)-STEM). At higher angles (>10°), elastic scattering becomes more incoherent and is used in HAADF imaging modes.

In contrast, inelastic scattering occurs as a result of Coulomb interactions between an incident electron and the electrons that surround each atomic nucleus (by Coulomb repulsion). The incident electron might transfer a part of its energy to an electron localized in any of the atom's electron shells. In the interaction with an inner-shell electron, an incident electron can transfer an amount of energy to an inner-shell electron, leading to the ejection of this electron and a reduction in the incident electron energy. Inelastic electron scattering is predominantly used in analytical electron microscopy, providing chemical and other types of information about the specimen, and are measured with EELS and energy filtered transmission electron microscopy (EFTEM) analysis. As a result of the inner-shell scattering, the atom is highly excited (or ionized) and will rapidly lose its excess energy, leading to the emission of electromagnetic radiation characteristic (X-rays) or Auger electrons. X-rays collected by EDS are also commonly used in analytical electron microscopy.

3.1.4. Basics of TEM

A TEM microscope is similar to an optical device, transferring information from the specimen to an image. The optics consist of a series of lenses and apertures aligned along the optic axis, as illustrated in the scheme of a conventional TEM (in imaging mode), shown in Figure 3.2. The TEM illumination system is formed by an electron gun and condenser lenses, which can provide either a parallel or a convergent beam. In the case of conventional TEM imaging and ED patterns, the specimen is illuminated by a parallel electron beam, whereas the specimen is illuminated by a convergent electron beam in STEM imaging, convergent beam diffraction and EELS and EDS analysis.

The image formation process in a conventional TEM starts with a parallel beam incident onto the sample. Electrons coming from the illumination system are scattered by the sample located in the object plane of the objective lens. Scattered electrons coming from the same point of the sample are focused on the image plane of the objective lens, leading to the first intermediate image. Conversely, electrons scattered in the same direction are focused on the back focal plane, leading to the formation of a diffraction pattern. The change in the strength of the intermediate lens allows selection of either the image plane (real space) or of the diffraction pattern (reciprocal space) for the second intermediate image. Finally, a set of projection lenses magnify and projects the intermediate image towards the viewing screen or computer display.
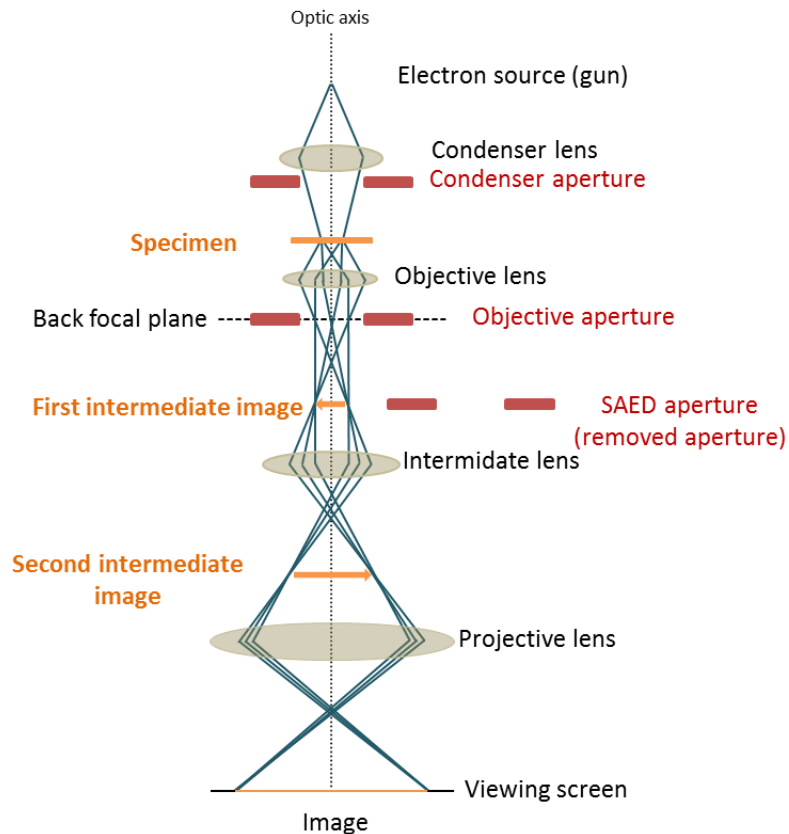
Figure 3.2: Schematic illustration of an ideal electronic microscopy in TEM image mode.

In the case of STEM images, electrons are focused before they reach the specimen to form a small electron probe which is then scanned over the specimen. The generated signal at each point is simultaneously recorded by selected detectors building up an image [72].

However, it is never possible to transfer all the information because of imperfections in the lens system, which can cause loss of some data and distorted images. The main lens aberrations are astigmatism, spherical and chromatic. Astigmatism aberration can be corrected during instrument alignment. The spherical and chromatic aberrations limit the resolution in TEM. However, the implementation of spherical aberration correctors in modern microscopes has pushed the achievable spatial resolution for imaging and spectroscopy into the sub-angstrom region [73-78]. These aberration correctors can be set up in the TEM column to compensate the condenser lens (probe-corrected) in STEM mode, or the objective lens (image-corrected) in TEM mode.

The different images modes and the characteristic information provided by each mode are now examined.

3.1.5. Electron diffraction

Electron diffraction (ED) provides basic information on structure, symmetry and atomic arrangements in crystalline materials. It is a collective scattering phenomenon with electrons being elastically scattered by atoms in a regular array. The incoming plane electron wave interacts with the

atoms and secondary waves are generated, which interfere with each other, in either a constructive or a destructive manner. The result of the propagation electron wave through the crystal is a diffraction pattern comprising a regular array of scattered intensities. The electron diffraction pattern is basically the projection of the reciprocal lattice section in the plane of the crystal normal to the incident beam.

The relation between interplanar distance (d_{hkl}) and diffraction angle (θ), which is the distance between the reflection and the origin of the reciprocal lattice, is given by the Bragg law [79],

$$n\lambda = 2\, d_{hkl} \sin\theta ,$$ (Eq. 3.1)

where λ is the wavelength of the electron incident beam and n is the diffraction peak order. Interplanar distances (d_{hkl}) can be measured because the wavelength λ of the electrons is known. The electron diffraction pattern provides the interplanar distances (d) of the (hkl) planes belonging to a [uvw] zone axis, which is defined as the incident beam direction with respect to the specimen.

If the specimen is crystalline or has a periodic structure, the diffraction pattern consists of sharp Bragg reflections. The measured distances from the centre spot (transmitted beam) to the diffraction spots yield the d_{hkl} for each spot in the electron diffraction pattern. The measurement of d_{hkl} together with the angles between the planes permits phase identification. In addition, a deviation of the pattern periodicity can be easily detected, allowing the identification of different crystalline phases or the presence of defects. Furthermore, by using the selection area aperture it is possible to select a specific region in the crystal (across the TEM image) to obtain a diffraction pattern with the contribution of the diffracted beams coming only from the selected region.

In this work, electron diffraction was used as follows: i) to set the material in a zone axis, which is one of the first steps in a TEM session and is specially required for HRTEM images in thin films; ii) to analyse the structure of specific regions by obtaining a ED pattern or a selection area (SA)ED; and iii) to perform diffraction contrast images and analysis. All these types of images are discussed in the following section.

3.1.6. TEM imaging

TEM images are formed by coherent elastic electron scattering. There are two forms of contrast leading to two main types of TEM images: amplitude contrast images and phase contrast images. The contrast in amplitude contrast images is attributed to the change in amplitude of either the transmitted beam or the diffracted beam. Thus, amplitude contrast results from variations in mass or thickness, or a combination of the two, due to the absorption, dynamic scattering or microstructural features. In the case of the phase image, the contrast arises from differences in the phase of the electron waves scattered thought a thin specimen. The main difference between phase contrast and amplitude contrast images is the number of beams collected by the objective aperture in the back focal plane of the objective lens.

Amplitude contrast images

Amplitude contrast images are formed by the selection of one or more beams in the back focal plane using a small objective aperture. There are two different operation modes: bright field (BF) and dark field (DF). In a BF condition, the diffracted beams are excluded by objective aperture and only the transmitted beam is selected in the back focal plane. In contrast, in DF condition, one or more diffracted beams are selected by the objective aperture and the contrast in the image reveals regions that contribute to the intensity coming from the selected beams.

o *Diffraction contrast analyses*

Diffraction contrast is produced by coherent elastic electron scattering and is a special form of amplitude contrast where the scattering occurs at special Bragg angles. By tilting the sample, it is possible to obtain the two-beam condition, in which only one diffracted beam (**g**) is strong. Two-beam condition can be used to analyse crystal defects due to the fact that scattering near the defect is dependent on its local strain.

Thus, diffraction contrast analyses can be used to analyse dislocations. For effective contrast analysis of dislocations, the $\mathbf{g} \cdot \mathbf{b}$ criterion must be accomplished, where **g** is the diffraction vector and **b** is the Burgers vector. A dislocation is characterized by its dislocation line (**u**) and Burgers vector (**b**). In the case of an edge dislocation, which is described by a **b** normal to **u**, the dislocation line can be observed under a $\mathbf{g} \cdot \mathbf{b} \neq 0$ condition, where **g** is parallel to **b**. In contrast, under a $\mathbf{g} \cdot \mathbf{b} = 0$ condition (invisibility condition), **g** is perpendicular to **b** and the dislocation is not visible in the image. By examining the invisibility criterion for various **g** vectors, the dislocation Burgers vector can be determined.

Edge dislocations in LSMO thin films grown on a LAO substrate can be seen in the two-beam diffraction contrast images show in Figure 3.3. Figure 3.3(a) shows a DF image of a 3.5-nm-thick LSMO film, where the LSMO family of planes **g**(020) are set into Bragg conditions. The changes in the amplitude contrast induced by the presence of the [010] dislocation lines can be observed as they are under a $\mathbf{g} \cdot \mathbf{b} \neq 0$ condition. In Figure 3.3(b) a BF image from a 6-nm-thick LSMO is shown. This image was obtained with **g**(010) and the [100] dislocation lines can be observed. In the DF images, dislocation lines appear as bright lines (Figure 3.3(a)) while in BF images the dislocation lines appear as dark lines (Figure 3.3(b)).
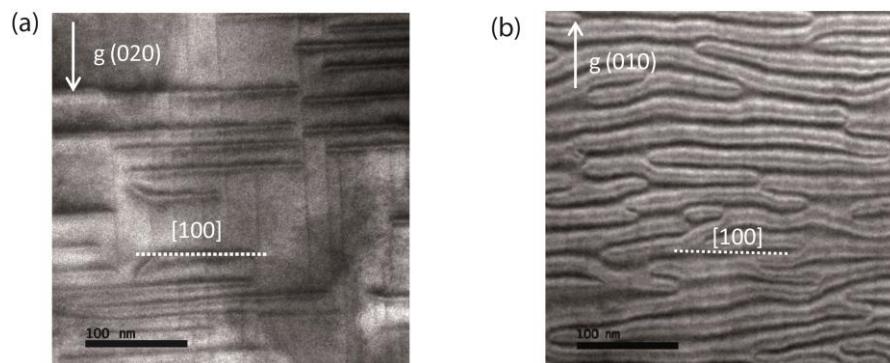

Figure 3.3: Two-beam diffraction contrast images from LSMO films. (a) DF image from a 3.5-nm-thick LSMO film and (b) BF image from a 6-nm-thick LSMO film, obtained with **g**(020) and **g**(100), respectively.

In this work, diffraction contrast analysis was used to analyse dislocations and to determine Burgers vectors.

Phase contrast images

Phase contrast images are formed by interference of more than one beam. To obtain a phase image, a large objective aperture and several beams, including the direct beam, are selected. The phase contrast is very sensitive to different factors: thickness, orientation, or scattering factor of the specimen, and variations in the focus or astigmatism of the objective lens. Due to its sensitivity, the phase contrast can be exploited to image the atomic structure of thin specimens.

Phase contrast images often present fringes (periodic contrast), such as Moiré fringes. Moiré fringes can result from the interference of two sets of lattice planes that have similar periodicities. The lattice fringes that appear as a result of this interference are not direct images of the structure, but they give information about the lattice spacing and orientation of the specimens. There are two different types of interference: the Rotational Moiré and the Translational Moiré, often referred to as misfit. Translation moiré patterns normally appear on films grown on a substrate having different lattice parameters whereas rotation moiré patterns appear for instance twist boundaries. The way to analyse the spacing and orientation of the moiré fringes is to consider the diffraction vectors from the two lattices. As an example, if two parallel misfit planes are superimposed, the **g**-vectors will be parallel resulting in dark and bright parallel fringes as shown in the schematic representation of Figure 3.4.
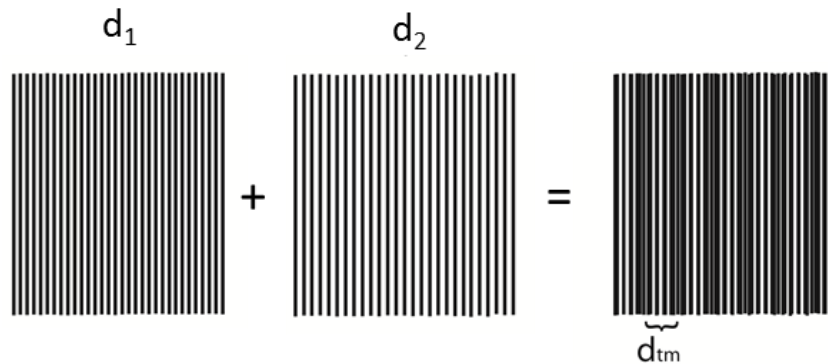
Figure 3.4: Schematic representation of the formation of Translation Moiré fringes. In the left, the set of planes with d_1 spacing; in the middle, the set of planes with d_2 spacing and at the right the resulting fringes of the interference of the two previous set of planes. $d_1 < d_2$.

These fringes correspond to the transitional Moiré fringes and the spacing between these fringes, $\mathbf{g}_{tm}$, is given by the **g** vectors of two sets of planes, thus

$$\mathbf{g}_{tm} = \mathbf{g}_2 - \mathbf{g}_1, \qquad\qquad \text{(Eq. 3.2)}$$

where $\mathbf{g}_1$ and $\mathbf{g}_2$ are assigned **g** vectors to the bigger and smaller lattice spacing parameters, d_1 and d_2, respectively. Thus, the $\mathbf{g}_{tm}$ vector corresponding to a set of translational Moiré fringes with spacing d_{tm}, is described as

$$d_{tm} = \frac{1}{\mathbf{g}_{tm}} = \frac{1}{\mathbf{g}_2 - \mathbf{g}_1} = \frac{\frac{1}{\mathbf{g}_2} \cdot \frac{1}{\mathbf{g}_1}}{\frac{1}{\mathbf{g}_1} - \frac{1}{\mathbf{g}_2}} = \frac{d_2 d_1}{d_1 - d_2} \quad . \qquad \text{(Eq. 3.3)}$$

In the case of thin films, moiré patterns can be used to locate and give information on dislocations which are present in one material but not the other, so moiré fringes may be related to a dislocation in the plane of the interface, since these locally relax the misfit. The images can always be related directly to the projected Burgers vector of the dislocation. But care must be taken with using moiré fringes to analyses interfaces and defects.

o *High resolution transmission electron microscopy images*

In the phase contrast imaging mode, if the point resolution of the microscope is sufficiently high and a suitable crystalline sample is oriented along a zone axis, then High resolution transmission electron microscopy (HRTEM) images are obtained. In these images, individual atoms of a crystal and its defects can be identified, and in many cases, the atomic structure of a specimen can be directly investigated. Contrast in HRTEM images arises from interferences, which make interpretation of HRTEM images far from easy and require careful consideration.

The incident parallel electron beam, ideally a plane wave of coherent electrons, interacts elastically while passing through the specimen. Both the electron wave phase and amplitude leaving the specimen are affected by such interactions. Thus, the exit wave electron function, $\Psi_o(\mathbf{r})$, contains information about the specimen structure. In a first stage, the objective lenses produce the diffraction pattern of the sample. This can be represented, by a Fourier Transform (FT) operation, which generates an image of the corresponding diffraction pattern. The wavefront can be represented by a total diffracted wave, $\Psi_d(\mathbf{g})$. In the second stage, the interference between the beam leads to a real space image, i.e. to a wavefront given by the image wave, $\Psi_i(\mathbf{r})$, obtained as the result of the inverse FT. However, the relationship between the exit wave and the image wave is a highly nonlinear one and is a function of the aberration of the microscope (astigmatism, spherical and chromatic), which reduces the image quality.

In this work, HRTEM images were used as follows: i) to obtain local structural information about the specimen, lattice parameters and the structure of defects; ii) to identify phases; and iii) to analyse the strain fields associated with the defects by strain maps. The two last ones are introduced in more detail.

(1) *Phase identification*

Atomic spacing information can be extracted by taking the Fast Fourier Transform (FFT) of the HRTEM image. Image processing in Fourier space is performed in a similar way to image formation in the TEM [72]. Mathematically, the objective lens performs a FT that creates the diffraction pattern of the object in the back focal plane and an inverse FT that makes the interference of the diffracted beams back to a real space image in the image plane (lattice image). Thus, FFT of an HRTEM image yields a diffractogram of spots (points) in an arrangement similar to an electron diffraction pattern of the same specimen.

As with electron diffraction patterns, FFT of HRTEM images can be used to identify a crystalline phase. Nevertheless, FFT can be obtained from regions of specimen on the order of few nanometres rather than the micrometres typical of conventional SAED. This makes HRTEM a useful tool in the analysis of nanostructures.

In this work, FFT were obtained from HRTEM images by selecting specific regions in the micrograph. The d_{hkl} and angles between a pair or set of planes were measured from these FFT using a diffraction tool plug-in for Digital Micrograph software developed by the University of Cadiz. The phase identification and indexation of the FFT were performed using Eje-Z software [80, 81] and the structural data of known phases. This software allows comparison of a pair of d_{hkl} and the angle between them with a database [82] allowing phase identification. In the phase identifications and indexations performed during this thesis, errors of 0.3 Å and 3° were permitted.

(2) *Strain maps by GPA*

Strain fields can be analysed with HRTEM images using different algorithms, such as the Geometrical Phase Analysis (GPA) [83]. GPA is widely used, for example to analyse dislocations and thin film strain fields [62, 84-87]. The GPA approach is based on combining real-space and Fourier-space information. Displacements are measured by calculating the 'local' Fourier components of the lattice fringes in an image [88]. The intensity of an image, $I(\boldsymbol{r})$, is written as

$$I(\boldsymbol{r}) = \sum_g I_g(\boldsymbol{r})e^{2\pi i \boldsymbol{g} \cdot \boldsymbol{r}},$$

(Eq. 3.4)

where **g** are the reciprocal lattice vectors describing the undistorted lattice. The local Fourier components are obtained by filtering in Fourier space, and have an amplitude and phase:

$$I_g(\boldsymbol{r}) = A_g(\boldsymbol{r})e^{iP_g(\boldsymbol{r})}$$

(Eq. 3.5)

where the amplitude, $A_g(\boldsymbol{r})$, describes the local contrast of the fringes and the phase, $P_g(\boldsymbol{r})$, describes their position. The phase is related to the displacement field, $\boldsymbol{u}(\boldsymbol{r})$, with the following relationship [88] :

$$P_g(\boldsymbol{r}) = -2\pi \boldsymbol{g} \cdot \boldsymbol{u}(\boldsymbol{r}) \, .$$

(Eq. 3.6)

An individual phase image gives only the component of the displacement field in the direction of **g**. By selecting two non-colinear reciprocal lattice vectors in the Fourier transform, it is possible to obtain a two dimensional displacement field of the selected HRTEM image. Thus, the two dimensional displacement fields can be determined two phase images, $P_{g1}(\boldsymbol{r})$ and $P_{g2}(\boldsymbol{r})$ by

$$\boldsymbol{u}(r) = -\frac{1}{2\pi}\left[P_{g1}(\boldsymbol{r})\boldsymbol{a}_1 + P_{g2}(\boldsymbol{r})\boldsymbol{a}_2\right],$$

(Eq. 3.7)

where $\boldsymbol{a}_1$ and $\boldsymbol{a}_2$ are the base vectors for the lattice in real space corresponding to the reciprocal lattice defined by $\boldsymbol{g}_1$ and $\boldsymbol{g}_2$. The two dimensional displacement field is determined from the gradients in the $P_{g1}(\boldsymbol{r})$ and $P_{g2}(\boldsymbol{r})$. Once the displacement field is determined, the components of the strain

tensor ($\mathcal{E}_{xx}$, $\mathcal{E}_{yy}$ and $\mathcal{E}_{xy}$), dilatation (Δ_{ij}) and planar rotation (w_{ij}) can be calculated following classical elasticity theory [89].

The precision and the spatial resolution of the strain maps depend on the size of the mask used to select the particular frequency of interest, **g**, in Fourier space. Precision is described as the accuracy on the measurement while spatial resolution is defined as the minimum resolvable distance in the image [90]. The precision of this method has been tested by measuring a continuous displacement field around a dislocation core with an accuracy of 0.03 Å [85].

The strain maps performed in this thesis were created using the GPA software [83] developed in the Digital Micrograph environment. The selected phase and the size of the mask used to create displacement fields and strain maps are discussed in the experimental part of sections 5.4.3 and 6.4.2.

3.1.7. STEM imaging

There are different methods of STEM imaging depending of the detector used to collect the elastically scattered electrons. As shown schematically in Figure 3.5, there are three main types of detector: a bright field (BF) detector, an annular dark field (ADF) detector, and a high angle annular dark field (HAADF) detector. The BF detector detects the intensity in a small solid angle (<10 mrad) around the direct beam, whereas the ADF detector, which is a disc with a hole in the centre, detects scattered beams between 10-50 mrad. Because the HAADF detector has a much larger diameter than the ADF detector, it can detect electrons scattered at high angles (>50 mrad), which are mostly incoherent. The main difference between ADF and HAADF is the contribution of Bragg diffracted beams to the image: in ADF this contribution is still relevant while in HAADF it is negligible.
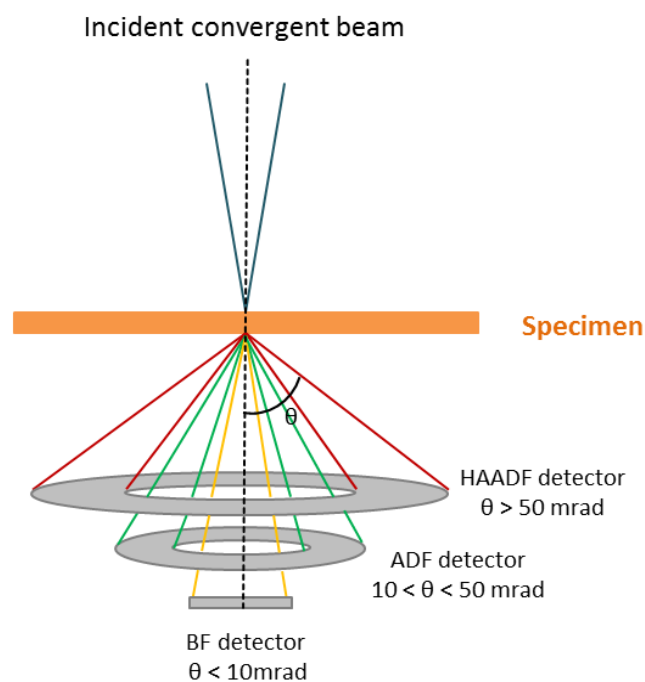

Figure 3.5: Schematic representation of different STEM detectors.

The principal advantage of the HAADF configurations is that image contrast depends on the Z value (called Z-contrast), with an almost Z^2 dependence [91], and it is possible to obtain chemical information. This type of images permits the direct visualization of structures and defects. However, because of the Z dependence of HAADF images, light atoms are difficult to detect, especially in the particular case that they are combined with heavier ones. Additional information can be obtained by changing the camera length of the HAADF detector. As the camera length of the detector increases, the collection angles decrease and as a result, diffraction contrast information appears as the image becomes less incoherent [92]. In HAADF, large inner collection angles (>50mrad) are employed which exclude diffraction contrast. In contrast, in low angle (LA)ADF a more modest inner collection angle is used allowing contrast from defects and deformations of the lattice [93]. Thus, HAADF gives information about the chemical composition while LAADF provides information about the strain and medium angle (MA)ADF is an intermediate situation.

In this study, STEM imaging combined with spectroscopic analysis were used to analyse chemical information of films and nanostructures. HAADF, MAADF and LAADF images were used to analyse strain and chemical information associated with defects. Additionally, HAADF images with atomic resolution, acquired with probe corrected microscopy, were used to analyse the local structure of the defects.

3.1.8.Analytical transmission electron microscopy

As previously mentioned, valuable chemical information is given by inelastically scatted electrons and secondary signals resulting from the interaction of the incident electrons with the specimen. EELS and EDS analyse the inelastic scattering electrons and secondary signals (X-ray), respectively. Both spectroscopies can be used in quantitative way to measure chemical concentrations of the elements in the sample.

Advantages of EDS include the ability to cover more elements of the periodic table and the possibility to use of thicker samples. However, EELS offers substantially more information beyond elemental identification, such as information about the oxidation state and coordination, and is well suited to the detection of light elements, which are difficult to analyse with EDS. EELS also offers better spatial resolution and analytical sensitivity, both at the single-atom column level.

Spectroscopic analysis is usually performed using STEM. In this technique, an angstrom-sized electron probe is scanned across a sample to collect either EELS or EDS. The development of the spherical aberration (C_S) corrected microscope with large convergence angles and small probes compatible with high currents has enabled atomic-scale chemical mapping in both STEM-EELS [73, 74] and STEM-EDS [75-78, 94]. However, in both spectroscopies quantitative analysis is sometimes difficult to perform due to a variety of effects such as electron beam spreading, delocalization, channelling, and dechannelling, which are dependent on chemical composition of the atomic columns [75, 95, 96]. In some studies involving STEM-EELS mapping, image contrast reversals have been observed and attributed to beam channelling between adjacent atomic columns [95, 97]. Although in EDS, the localization of X-ray scattering potentials can lead to a directly interpretable

chemical map [75], equivalently to HAADF imaging [96], recent work has shown that the contribution of thermally scattered electrons can greatly affect the contrast in such chemical maps [98]. In addition, studies of interfaces have revealed that the apparent atomic column size can depend on both channelling and sample thickness [77, 78]. These drawbacks can be avoided by using thin samples (25-30 nm) [94].

In both spectroscopies, one spectrum is recorded at every pixel as the electron probe is scanned over the specimen. Three different experiments can be performed: a punctual analysis, in which only one spectrum is acquired; a line scan profile, in which various spectra are acquired following a line; and mapping or spectrum images (SI), in which various spectra are acquired in a two dimensional area. In the latter case, spectra can be transformed into quantitative images of the distributions of all the elements present in the specimen. From such images quantitative data can be extracted describing elemental changes associated with inhomogeneous nanostructures.

In this study, both EELS and EDS were used according to the needs and aims of the experiments and are now explained in more detail.

Electron Energy Loss Spectroscopy (EELS)

The EELS consists of the analysis of the energy distribution of initially monoenergetic electrons after they have passed through a specimen and interacted with it. This technique provides large amounts of information about the chemistry and the electronic structure of the specimen atoms, which in turn reveals details of their bonding/valence state, the nearest-neighbour atomic structure, their dielectric response, the free electron density, the band gap (if there is one), and the specimen thickness. The spectrometer separates the electrons according to their kinetic energy and produces an electron energy loss spectrum, showing the number of electrons (scattered intensity) as a function of their decrease in kinetic energy.

Typically, an EELS spectrum consists of three parts: a Zero-loss peak (ZLP), a low-loss region and a core-loss region, as is shown in Figure 3.6. The ZLP or "elastic" peak represents electrons that are transmitted without sustaining measurable energy loss, including unscattered electrons, elastically scattered electrons and those that excite phonon modes, for which the energy loss is less than the experimental energy resolution. The low-loss region, <50 eV, involves excitation of the outer-shells of the electrons and contains electronic information from the more weakly bound conduction and valence-band electrons. This region contains the plasmon response either as a single peak, or a series of peaks in thicker specimens. The low-loss region of the spectrum is directly related to the thickness of the specimen in terms of the inelastic mean free path, λ. At the core-loss region, >50 eV, the electron intensity decreases rapidly. Superimposed on this decreasing intensity are features that represent inner-shell excitations. This region contains the ionization edges, which rise sharply at the ionization threshold. The energy-loss coordinate of the edge is approximately the binding energy of the corresponding atomic shell, thus revealing the elements present within the specimen.
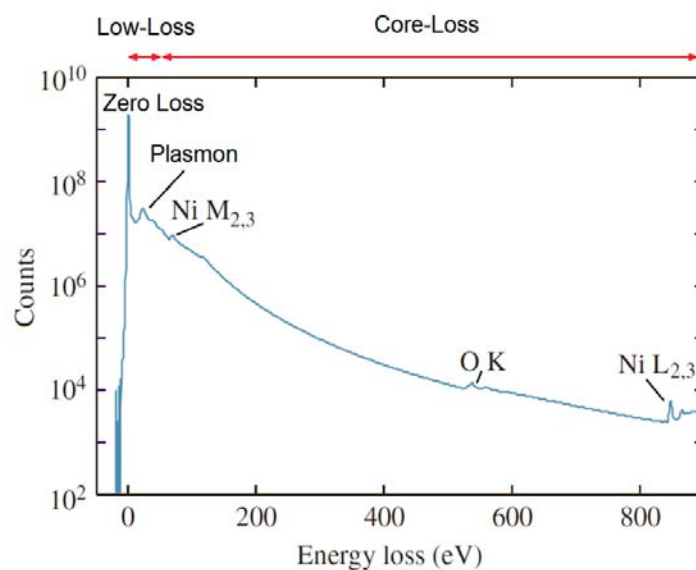
Figure 3.6: An EELS spectrum displayed in logarithmic intensity mode, showing zero-loss and plasmon peaks in the low-loss region and ionization edges arising from each element (in this case O and Ni) in core-loss region. Figure adapted from Williams [70].

○ **_Dual_ EELS**

Dual EELS allows the recording of both the low-loss and core-loss regions of the EELS spectrum at each pixel [99, 100] . Additional processing methods become practical due to the presence of both low-loss and core-loss information. These methods include removal of energy shift to allow accurate chemical shift measurements; assessment of sample thickness; deconvolution of plural scattering; and correlation of low-loss signals with core-loss features.

In this work dual EELS spectrum images where used to analyse the chemical features related with the investigated crystal defects. Processing of the resulting data sets was performed in Digital Micrograph using a combination of EELS plug-in tool and built-in routines. The processing procedure to obtain the intensity elemental maps was as follows:

(1)   _Energy shift correction and thickness measurements_

In the correction of the energy shift, the ZLP acts as a self-calibration for the low-loss region. The low-loss spectra are shifted to leave the ZLP in the same spectrum channel at each spatial pixel. Because, in dual EELS the core-loss spectrum is recorded immediately after the low loss spectrum, it is assumed that the shift required for the core loss spectrum is the same as that required for the low loss at the same pixel, permitting correction of the energy shift in the core loss. In this study, the ZLP was used to correct the energy shift of core-loss and to compute the thickness. The thickness was computed using the ZLP by applying the Log-Ratio function [71].

(2)   _Noise reduction_

The principal component analysis (PCA) is used in the hyperspectral EELS raw data to remove the noise [101, 102]. PCA is a statistical method that separates the information into a number of components. A limited number of components have most of the information, while the rest contain

only noise. Thus, the individual components with significant information (principal components) can be used to reconstruct the data, reducing the noise [103]. In this work, the PCA provided by Lucas *et al*. [104] for Digital Micrograph environment and that provided in the Hyperspy suite [105] were used to remove random noise from the EELS spectra.

(3)   *Background removal*

After PCA, the standard procedure is to fit a power law background function before each energy peak and extrapolate the fit function under the edge to remove the background of the spectrum [71]. In this study, special attention was paid at this step to avoid possible artefacts due to the background substation.

(4)   *Remove plural scattering*

Finally, there is typically a high probability that a transmitted electron will be inelastically scattered more than once, giving a total energy loss equal to the sum of the individual losses. This plural scattering is usually significant and generally unwanted because it distorts the shape of the energy-loss spectrum. Fortunately, it can be removed by various deconvolution procedures. In this work, the plural scattering was removed using the ZLP and the Fourier ratio deconvolution [71].

As an example Figure 3.7 shows the appearance of a spectrum in each processed stage: original (black), after PCA (red), after background subtraction (green) and after deconvolution (blue); for a Mn-$L_{2,3}$ energy edge.
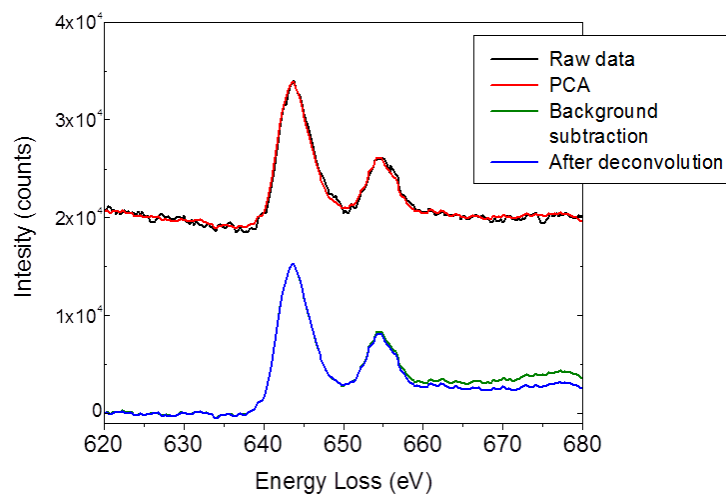
Figure 3.7. Example of a spectrum in each processed stage: original (black), after PCA (red) after background subtraction (green) and after deconvolution (blue); for Mn-$L_{2,3}$ energy edge.

o   ***Structural information from EELS: White-line ratios and chemical shifts***

As has been previously mentioned, besides elemental identifications EELS may provide information on the electronic structure and bonding. Both the valence electron peaks and the ionization edges possess a fine structure that reflects the crystallographic or electronic structure of the specimen. Even with an energy resolution of ~ 2 eV, it is possible to distinguish between different forms of an element.

The *L* ionization edges of transition metals and the rare-earth elements usually display sharp peaks occurring near the edge, which are known as white lines. These white-lines contain rich information about the density of unoccupied states near the Fermi level and the chemical bonding of the metal. The *L* edge of transition metals consists of two white lines, L_3 and L_2, as a result of transitions from the spin orbit split $2p_{2/3}$ and $2p_{1/2}$ levels to the available states in the $3d$ unoccupied band [106], which hybridize with oxygen $2p$ orbitals in the case of oxides. Variations in the $L_{2,3}$ intensity ratio or chemical shifts are typical fingerprints of changes in the oxidation state [106-110].

(1) $L_{2,3}$ *ratio*

From the degeneracy of the initial states, i.e. four $2p_{2/3}$ electrons and two $2p_{1/2}$ electrons, a white line intensity ratio of 2 is typically expected [106]. However, different values ratios have been found for some $3d$ transition metals [111]. The $L_{2,3}$ ratio increases with the number of electrons in the $3d$ bands, from the $3d^0$ toward $3d^5$ configuration, and then decreases toward the $3d^{10}$ configuration [112-114]. In addition, with a $3d$ metal such as Mn, the $L_{2,3}$ ratio decreases when the Mn oxidation state increases [73, 106, 107, 110, 112, 114]. Consequently, the white line ratio can be used to measure the transition metal valency.

There are different methods for quantifying the $L_{2,3}$ white line intensity ratio [106, 108, 112, 114, 115]. Here, the Mn-$L_{2,3}$ ratio was measured following the procedure described by Varela *et al*. [73]. As the continuum needs to be removed before extracting the $L_{2,3}$ intensity ratio, a Hartree-Slater cross-section function, available in Digital Micrograph, was used to subtract it. A 10 eV wide window placed right after the L_2 line was used for scaling purposes of the cross-section function. After subtracting the continuum, the remaining signal under the L_3 and L_2 lines was integrated within two 10 eV wide windows, the first one placed at the onset of the L_3 line, and the second one next to the first. The resulting integrated intensity values were used to calculate the $L_{2,3}$ intensity ratio. The error bars were determined by changing the position and the width of the integration windows.

(2) *Energy shift of the L_3 and L_2 peaks*

Other changes to take into consideration may be an energy shift of the L_3 and L_2 peaks. As the average manganese oxidation state decreases, the L_3 and the L_2 peaks tend to shift to slightly lower energies [107, 110]. For example, from Mn^{3+} to Mn^{+4} a shift of 1.5 eV in energy of both peaks is characteristic [116].

In this work the absolute value of L_3 and L_2 peak positions was defined fitting the peak centre of mass position by fitting AmpGaussian function ((y=y0+A*exp(-0.5*((x-xc)/w)^2)) by Origin.

o **Simulation of EEL spectra**

In order to assess the possible influence of subtle structural distortions of the octahedral coordination of the Mn cation on the estimation of the Mn oxidation state, Mn-$L_{2,3}$ edge spectral simulations were carried out using CTM4XAS [117].

In this study, the effect of a distortion in the coordination environment of Mn^{3+} and Mn^{4+} cations was simulated by reducing the cubic (O_h) symmetry (characterized by a cubic crystal field

splitting, 10*Dq*) to tetragonal (*D*₄ₕ). The degree of tetragonal distortion was tuned through parameters *Ds* and *Dt*, which define the splitting of the e_g and t_{2g} levels according to Δe_g = *4Ds + 5Dt* and Δt_{2g} = *3Ds − 5Dt*. For parameters 10*Dq*, *Ds* and *Dt*, values describing a distorted environment reported in the literature [54] were used.

Energy dispersive X-ray spectroscopy (EDS)

The interaction of the electrons with the atoms of the specimen produces X-ray characteristics of the atom which emitted them. These X-rays are detected by a solid state detector, resulting in energy spectra which give information about the composition of the specimen.

The conversion of X-ray count in atomic% may be performed by the Cliff-Lorimer method [118], assuming the thin foil criterion. This criterion assumes that the specimen is thin enough and absorption or fluorescence can be ignored. Under this criterions the concentration ratio between A and B elements is proportional to the measured intensity ratio. The principle is expressed in the equation:

$$\frac{C_A}{C_B} = k_{AB} * \frac{I_A}{I_B}$$

(Eq. 3.8)

which relates the number of X-ray counts, I_A and I_B, from elements A and B to their concentration C_A and C_B with the Cliff-Lorimer k-factor, k_{AB}. The k-factor is a proportionality constant which depends on the elements being analysed, the energy of the incident electrons, and the relative sensitivity of the X-ray detector for the different X-rays. It can be estimated from theoretical considerations or it can be measured by analysing a specimen of known composition.

In this study, TIA software was used to process and quantify punctual, line profiles and spectrum maps analysis. Selected energy windows were used for each element with previous background subtraction. However, in the case of high resolution EDS-SI, Bruker software was used to collect and process the data. The element profiles were extracted from EDS-SI by integrating net counts areas in the map. In the case of atomic resolution EDS-SI the elemental intensities were extracted from the maps by fitting Gaussian peaks to the atomic columns and then were converted in atomic%. The k-factors were measured at a reference zone in which the film and substrate was considered stoichiometric.

3.2. Other structural characterization techniques

3.2.1. X-ray diffraction

The X-ray diffraction (XRD) is a technique used for determining crystal structure and lattice parameters due to the X-ray wavelength having the same order of magnitude as the interatomic distances of crystals and molecules. If a crystal structure is irradiated with a monochromatic X-ray beam, the crystalline material disperses the X-ray elastically in a certain direction due to constructive interferences, creating a diffraction pattern. A constructive interference is produced when conditions

satisfy Bragg's Law (Eq.3.1). The diffraction will occur if the normal to the atom planes is dividing the angle between the incident and the scattered beam.

The XRD measurements of the films presented in this thesis were mainly performed with X'Pert Pro MRD-Panalytical diffractometer at ICN_2. The lattice parameters of the films were determined from HR-XRD using a four-angle goniometer and primary optics consisting of a parabolic mirror and a 4xGe(220) asymmetric monochromator. The in-plane lattice parameters were determined in the same equipment with a parabolic mirror in the incidence beam optics, fixed grazing angle of 0.5° on the sample, and parallel plate collimator in the diffracted optics. The 2D X-ray reciprocal space mapping experiments were performed using also the X'Pert Pro MRD-Panalytical diffractometer at ICN2. The X-ray measurements were performed by Dr. J. Santiso, J. Roqueta and Dr. F. Sandiumenge.

3.2.2. Scanning Electron Microscopy

Scanning electron microscopy (SEM) allows obtaining topography and composition information. The sample surface is scanned with a high energy electron beam (20-30k V) and the electrons can be scattered elastically or inelastically resulting in different secondary signals as was introduced in section 3.1.3. In SEM, all the information of interest is obtained from scattered electrons and secondary signals scattered backwards from the sample. This is in contrast to TEM, in which almost all the electrons are scattered forward. The main information derived from SEM is as follows:

- **Secondary electrons (SE):** electrons from the direct beam scatter inelastically with electrons from the sample surface. Their signal provides information about topography.

- **Backscattered electrons (BSE):** beam electrons are reflected from the sample by elastic scattering. The intensity of the BSE signal is strongly related to the atomic number (Z) of the specimen. Thus, the signal provides information about the distribution of different elements in the sample (atomic contrast), in addition to topography. In addition, the signal collected may provide information about microstructure, for example twinning in the film [44], through a process called channelling. It is also referred to as orientation contrast (OC). Details on the principles governing OC in BSE images can be found in Ref. [119].

In this work, SEM was used to analyse the surface morphology of the thin films using QUANTA FEI 200 FEG-ESEM at ICMAB and FEI Magellan 400L SEM at ICN_2. In addition, OC-SEM images were obtained in order to determine dislocation densities over large area. An advantage of this technique is that it does not require a particular sample preparation for the materials analysed. SEM measurements were performed by Dr. Ll. Balcells and Dra. Z. Konstantinovic.

3.2.3. Atomic Force Microscopy

Atomic force microscopy (AFM) is a type of scanning probe microscopy (SPMs). AMFs measure the electrostatic forces between the cantilever tip and the sample. The main force is the interatomic

"Van der Waals force", dependent on the distance between the atoms. If the tip is sufficiently far from the sample, it has a certain free oscillation amplitude and resonance frequency. However, when the tip engages with the sample, the oscillation amplitude, phase and resonance frequency are modified due to the interactions between the sample and the tip. Depending on the distance between the tip and the sample, AFM can be used in three different modes: a contact mode, a non-contact mode and an intermittent or tapping contact mode, each of which offers different advantages and drawbacks.

In this work, the surface morphology of the thin films was examined using AFM. The AFM measurements presented in this work were taken using PicoSPM, Molecular Imaging, in tapping mode, at the ICMAB by Dr. Ll. Balcells.

3.3. Thin film growth techniques

Growth techniques are usually classified according to whether the deposition process method is mainly physical or chemical. In physical methods, the film material is moved by evaporation or ejection of the material from a source (target) to the substrate, whereas chemical methods involve chemical reactions and the precursor undergoes a chemical change at the substrate surface or in the vicinity of the substrate. Physical methods typically employ vacuum evaporation and sputtering whereas chemical methods typically use a gas phase or a solution phase.

The thin films studied in this thesis were grown by physical deposition methods using radio frequency (RF) magnetron sputtering and pulsed laser deposition (PLD). For both deposition techniques, a good calibration of the conditions is important because the different parameters can result in different growth modes and film quality. There now follows a brief description of these two depositions techniques.

3.3.1. Radio frequency magnetron sputtering

The sputtering technique consists of bombarding a target material typically a dense ceramic pellet of the same composition as the thin film. The aim is to eject neutral atoms from the target and to deposit them onto the substrate. Firstly, a glow discharge plasma of a certain gas (usually Ar or O) is created around the target. Ions from the plasma are then accelerated towards the target by applying an electrical potential. These ions collide with the target causing neutral atoms from the target to be ejected and to be deposited on the substrate. A wide range of oxide materials (semiconductor, dielectric, insulating, magnetic, and superconducting) has been grown via the sputter deposition processes [30, 120].

A magnetron consists of two concentric magnets which create a magnetic field. The magnetron confines the electrons from the plasma close to the target. The electrons are forced to make a helicoidal trajectory around the magnetic field lines by the Lorentz force which results in more ionization of the gas atoms and more collisions with the target. Thus, the sputtering deposition process is enhanced and higher sputter rates are achieved. Another advantage of the magnetron is

that relatively fewer electrons reach the substrate (less heating and less substrate damage). Furthermore, a net flow of ions towards the target and atomic ablation occurs when the applied voltage difference between the target (cathode) and the rest of the chamber is constant (DC). A RF AC signal can then be added to the DC voltage to overcome the positive charge accumulations which prevents the growth of insulating material. Thus, RF-sputtering enables the use of insulating targets [121-123].

In this study, the $La_{0.7}Sr_{0.3}MnO_3$ films were grown using a RF-magnetron sputtering, following the procedure described by Z. Konstantinović *et al.* [124]. The films were growth using RF-magnetron sputtering at the ICMAB laboratory by Dra. Z. Konstantinović and Dr. Ll. Balcells.

3.3.2. Pulsed Laser Deposition

The pulsed laser deposition (PLD) technique uses the interactions of a laser beam with a material surface [125]. The PLD system consists of a vacuum chamber equipped with pumps, a target holder, substrate heater and various instruments to control the deposition environment of the system [30]. A high-power laser situated outside a vacuum deposition chamber is focused by means of external lenses onto a dense ceramic target surface with the desired cation composition. Regardless of the laser used, the absorbed beam energy is transformed into thermal, chemical, and mechanical energy, causing electronic excitation of target atoms, ablation and the formation of glowing plasma. The plasma forms a plume of several centimetres long, normal to the surface of the target, consisting of an assorted group of energetic neutral atoms, molecules, ions, electrons, atom clusters, microionized particulates, and molten droplets. The high-energy species in the plasma are collected and condense onto a substrate and form a film [28].

In this study, the $LaMnO_3$ films were grown using a PLD with a KrF excimer laser operating in ultraviolet at 248 nm [126, 127]. The films were growth using a PLD at the ICN_2 laboratory by J. Roqueta and Dr. J. Santiso.

3.4. Functional properties characterization techniques

In order to correlate the physical properties of the films with the defects analysed in this work, the following characterization techniques were used in collaboration with members Oxide Nanophysics group from ICN_2 and Physical Chemistry of Surfaces and Interfaces group from ICMAB.

3.4.1. Scanning Probe Microscopy (C-AFM, MFM, FMM)

Scanning probe microscopes (SPMs) are used to obtain images of nanoscale surfaces and structures. SPMs use a physical probe (tip) to scan back and forth over the surface of a sample while monitoring some interaction between the probe and the surface. The probe is mounted on a flexible cantilever, allowing the probe to follow the surface profile while the cantilever is deflected by a force. SPMs can measure deflections caused by many kinds of forces, including mechanical contact, electrostatic forces, magnetic forces, chemical bonding, van der Waals forces, and capillary forces.

Many scanning probe microscopes can image several interactions simultaneously depending on the probe mechanics.

In this work, three different modes of SPM were used to characterize the local fusional properties of the films: conducting-atomic force microscopy (C-AFM), magnetic force microscopy (MFM) and force modulation microscopy (FMM).

Conducting - atomic force microscopy (C-AFM)

Conducting atomic force microscopy (C-AFM) is a combination of atomic force microscopy (AFM) and scanning tunnelling microscopy, which uses electrical current to construct the surface profile of the sample. The current flows through the metal-coated tip of the microscope and the conducting sample. Usual AFM topography, obtained by vibrating the tip, is acquired simultaneously with the current, which is usually recorded in contact mode. This permits correlation of the spatial topography feature on the sample with its conductivity, and distinguishes C-AFM from scanning tunnelling microscopy which only records current.

In this study, C-AFM was used to obtain local electrical conductivity. The C-AFM images presented in this thesis where acquired under a N_2 gas environment to diminish any possible humidity effect, using commercial conductive CrPt coated Si tips mounted on cantilevers with $k=40$ Nm^{-1} (Budgetsensors). A detailed explanation can be found in Ref. [128]. These measurements were performed with SPM from Nanotec Electronica, at ICMAB by Dra. C. Ocal and Dr. M. Paradinas.

Magnetic force microscope (MFM)

The spatially resolved magnetic behaviour can be investigated by magnetic force microscopy (MFM). In MFM, a sharp magnetized tip is used to scan a magnetic sample and the tip-sample magnetic interactions are detected. Different kinds of magnetic interactions can be measured by MFM, including magnetic dipole–dipole interaction. MFM scanning typically uses non-contact AFM mode.

The MFM images presented in this thesis were taken with Nanosensors MFM tips. Phase contrast images were obtained at different tip distances from the film surface (h), while adjusting the amplitude ratio (AMFM$/A$sp) of MFM imaging (AMFM) vs topography imaging set point (Asp). A detailed explanation can be found in Ref [128]. These measurements were performed with MFP3D Asylum at ICN_2 by Dra. N. Domingo.

Force Modulation Microscopy (FMM)

Force modulation microscopy (FMM) is a variety of AFM-based mode where the tip in direct contact with the surface is forced to vibrate at a high frequency (typically of several 100's of KHz) in order to evaluate the mechanical response of the material. Any variation in the contact resonance frequency is related to the local sample stiffness, i.e., a positive shift in frequency corresponds to stiffer mechanical properties.

In this work, the spatially resolved mechanical response of the surface of the films was analysed by FMM. The topography was collected in contact mode and an AC voltage was applied to the piezoelectric actuator at the cantilever in order to induce this vibrational motion. The contact resonance frequency was tracked by a dual AC resonance tracking system. The topography of the films did not change during the measurement, meaning that they were performed in the elastic regime. These measurements were performed with MFP3D Asylum at ICN_2 by Roberto Moreno.

Chapter 4

Self-organized Mn₃O₄
nanoinclusions in LaMnO₃ films

4.1.Introduction

Renewed attention has been paid to undoped LaMnO$_3$ (LMO) perovskite due to the interfacial phenomena that show heterostructures composed of LMO, such as the appearance of ferromagnetism in LaMnO$_3$/SrTiO$_3$ [129] and LaMnO$_3$/SrMnO$_3$ [130] and the observation of exchange bias in LaMnO$_3$/LaNiO$_3$ superlattices [131]. Despite the fact that LMO is an antiferromagnetic insulator in its stoichiometric bulk state with T_N ~ 140 K [132, 133], in the works mentioned previously, the LMO films present a strong ferromagnetic behaviour. The origin of this unexpected ferromagnetism is unclear. Strain or deviations from the LaMnO$_3$ stoichiometry (typically either La or Mn cation vacancies, which may easily change the Mn oxidation state), have been suggested as the source of this anomalous magnetic behaviour [127, 134-140].

Usually, heteroepitaxial multilayers are used to increase the concentration of interfacial effects. New strategies have been developed in this direction, such as vertically heteroepitaxial nanocomposites (VHN), which provide a novel concept to develop new functional devices [66, 67]. The advantages of this VHN, in contrast to the convectional multilayers structures, are for example, a vertical contact area between two immiscible compounds much larger than the interfaces between substrate and film, strain tunability to large thicknesses and the possibility to self-assemble [141]. La$_{0.7}$Ca$_{0.3}$MnO$_3$[66] or La$_{0.7}$Sr$_{0.3}$MnO$_3$ (LSMO) [68, 69] based nanocomposites are examples of self-assembled VHN, which highlight these new physical phenomena. A detailed example is the system LSMO:Mn$_3$O$_4$ that has often been proposed as a potential nanocomposite due to the chemical compatibility of Mn$_3$O$_4$ with the whole manganite perovskite family [142]. In this case, the spontaneous formation of LSMO:Mn$_3$O$_4$ VHNs is driven by a spinodal decomposition mechanism, if the composition ratio [La+Sr]/[Mn] < 1 [143]. The generation of a vertical lattice strain is found to be related to the different domains and grain boundary structures and directly impacts on the ferromagnetic properties of the material [69]. In the case of undoped LaMnO$_3$, manganese segregation is expected to occur when La deficiency leads to a non-stoichiometric ratio of La/Mn < 0.9 [144]. Thus, the formation of a random distribution of Mn$_3$O$_4$ or MnO phases has been reported

in LMO bulk samples [145, 146] and thin films [147]. The comprehension of the formation of manganese oxide segregates is fundamentally important as they are a characteristic secondary phase in several complex manganese oxides thin films and heterostructures, and they may also modify the structural quality and functional properties of heterostructures [148-150]. Furthermore, manganese oxides are extremely attractive for potential applications due to their electrochemical, optical and catalytic properties [151-154].

In this chapter, the spontaneous formation of regular vertically aligned nanoinclusions of a manganese oxide (MnO_x) embedded in an antiferromagnetic LMO matrix is analysed via a microstructural characterization of a LMO:MnO_x thin film nanocomposite. The different orientation domains and twins of the LMO matrix with respect to the substrate are determined and the manganese oxide phase is identified. Moreover, the crystallographic orientation relationship between the matrix and the nanoinclusions is stablished. A preliminary inspection performed at the interfaces between the MnO_x-LMO and LMO-substrate permits identification of a secondary phase La-rich close to LMO-substrate interface. Finally, the formation mechanisms of the LMO:MnO_x nanocomposite are discussed.

4.2. Experimental methods

Thin films of LMO with self-assembled manganese oxide nanoinclusions were prepared from stoichiometric LMO ceramic targets by PLD with a KrF excimer laser. The conditions for obtaining the nanocomposite were optimized at 850ºC deposition temperature under vacuum conditions (background pressure of $<5 \times 10^{-4}$ mTorr) [126, 127]. The laser fluency was kept below <1 J/cm^2 with 10Hz pulse repetition rate. The films were grown on top of (100)SrTiO$_3$ (STO) and (100)LaAlO$_3$ (LAO) substrates and their thickness was maintained between 30 and 100 nm as determined by X-ray reflectometry. The surface morphology was studied by SEM and AFM. The structural characterization was carried out by XRD using a four-angle diffractometer with a Cu-Kα radiation source (X'Pert Pro MRD-Panalytical).

The detailed microstructure and the chemical composition were investigated by TEM of cross-section specimens of LMO/STO. Cross-section specimens were prepared by conventional cutting, gluing and grinding procedures, followed by an Ar-ion milling step down to electron transparency by PIPS. HAADF images, EDS profiles and EELS-spectrum images (SIs) were obtained to identify the composition of the nanoinclusions using a FEI Tecnai F20 S/TEM operated at 200 kV. EELS-SIs of cross-section samples were also carried out in dual EELS mode with a FEI Titan^3™ G2 60-300 S/TEM operating at 300 kV, equipped with a dual EELS spectrometer. The PCA provided by Lucas *et al.* [104] for Digital Micrograph was used to remove the random noise in the EELS-SI. The La/Mn ratio was obtained from EDS of areas in the matrix tilting the sample out-of-zone axis in order to minimize the electron channelling. SAED and HRTEM images were obtained to identify the oxide manganese phase and the relationship between the nanoinclusions and the matrix using a FEI Tecnai F20 S/TEM operated at 200 kV. FFT were obtained from HRTEM images by selecting specific regions in the micrograph (the matrix, the nanoinclusion, and the interface between them) using the diffraction

tool plug-in for Digital Micrograph software, which allows the measurement of the distances and angles between the planes. The phase identification of manganese nanoinclusions and indexation of the FFT were performed using the Eje-Z software[80, 81] and the structural data of different manganese oxide phases [155-164] reported in the American Mineralogist Crystal Structure Database (AMCSD) [82]

All the structural drawings and schemes were produced by using VESTA software [165].

4.3. The LaMnO$_3$:MnOx nanocomposite

Both systems, LMO films grown on STO and LAO substrates, present a nanocomposite surface as can be observed in SEM images presented in top of Figure 4.1(a)-(b). The nanocomposite is formed by nanoinclusions, which are the bright rectangular shapes with a dark area in the centre shown in the SEM images. These nanoinclusions are uniformly distributed in flat matrix and have typical base dimensions of 40 nm x 150 nm, on STO substrate, and 40 nm x 90 nm, on LAO substrate. They are mainly oriented with the rectangular sides following the main axes of the substrate ([100] and [010]). Moreover, the nanoinclusions exceed by several nanometres the surface height of the matrix, which is flat with low roughness <0.5nm, as can be observed in the AFM images presented in the lower part of Figure 4.1(a)-(b). The statistical analysis of the inclusions showed that the size is enhanced in the case of films grown on STO substrate compared to those on LAO. This suggests that the different mismatch with substrate plays a role in the statistical size distribution of the segregates since the average La/Mn ratio in the films is essentially the same.
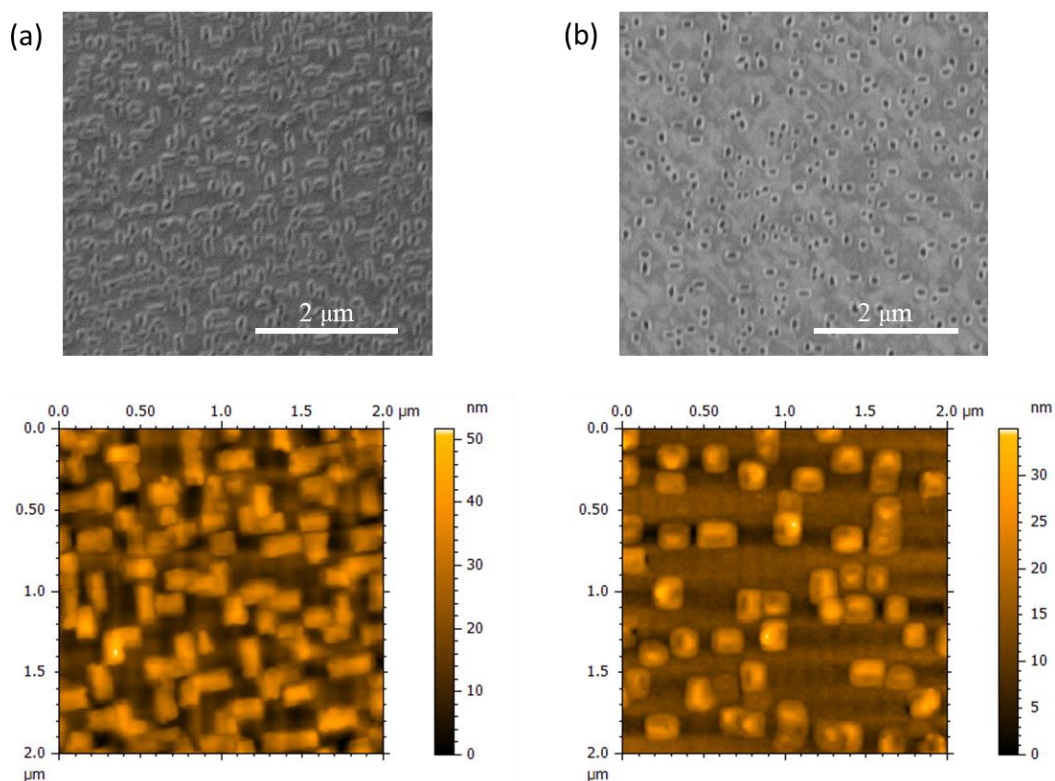

Figure 4.1: Surface morphology of 40-nm-thick LMO nanocomposite films. SEM (top) and AFM (down) images of LMO films grown on top of (a) STO and (b) LAO substrate. Figure modified from Pomar *et al.* [126].

Preliminary microstructural analysis performed in a sample of ~ 60-nm-thick LMO film on STO reveals that the nanoinclusions have a wedge-like shape and do not reach the interface with the substrate. This can be observed in Figure 4.2, which shows a HAADF image of a cross-section viewed along the [010] STO direction. This image presents a different contrast between the matrix (bright contrast) and the nanoinclusions (dark contrast) indicating a different cation composition between them. The nanoinclusions reach a depth of ~ 64 nm, ~ 10 nm above the interface with the substrate, leaving a thin matrix layer between the bottom of the nanoinclusions and the substrate interface. Furthermore, the image shows the coexistence of nanoinclusions cut along either the short or long axis. From those cuts along the short axis, also one can see a slight tilt of one of their borders with respect to the vertical direction, which will be discussed in more detail later on.
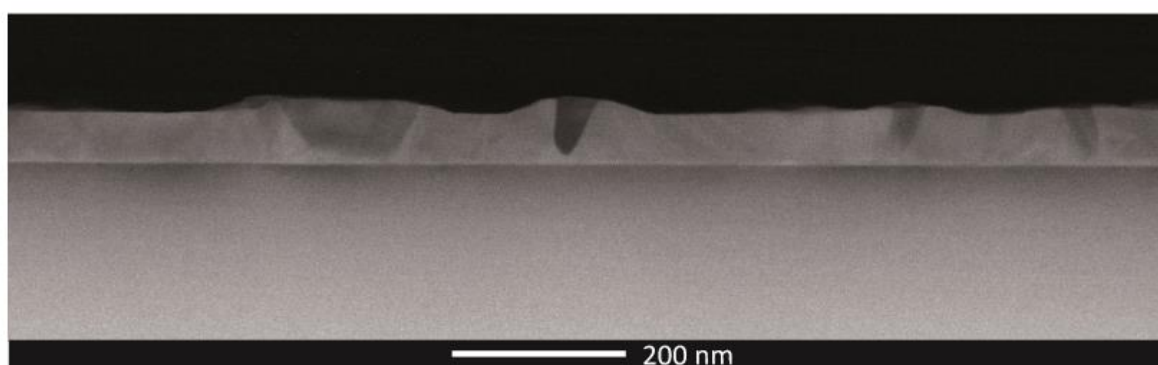

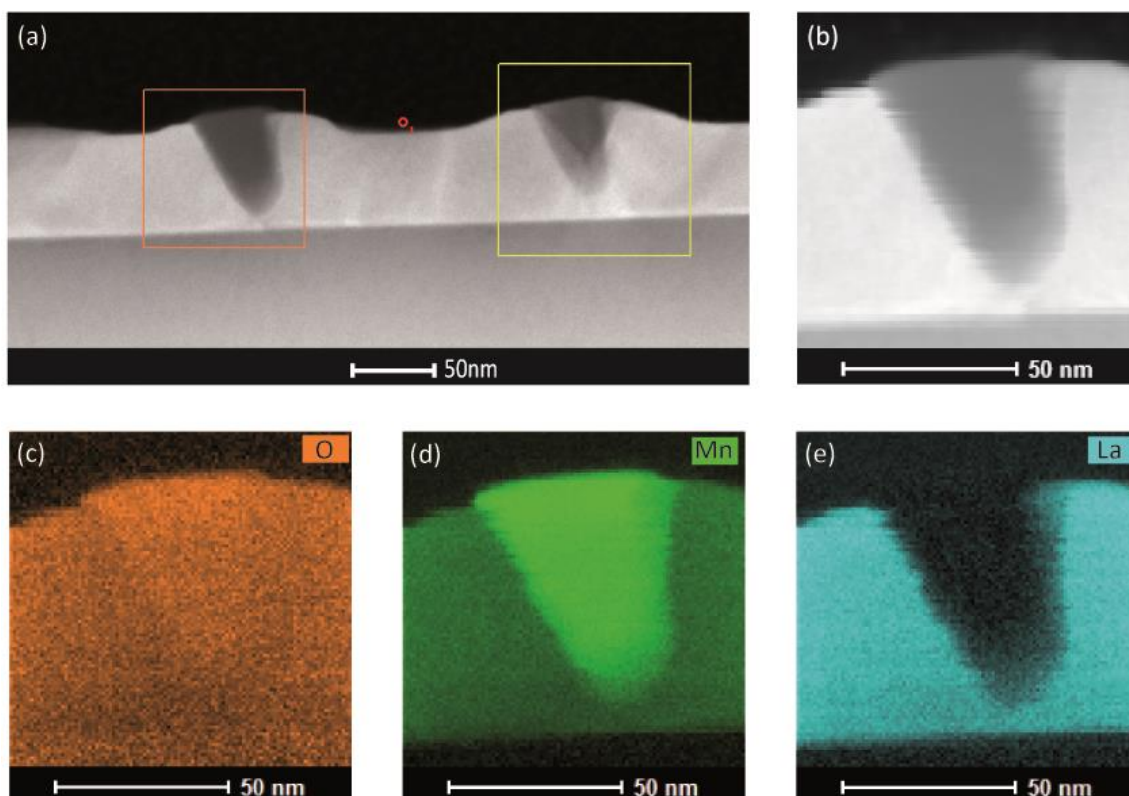Figure 4.2: HAADF image of a ~ 60-nm-thick film grown on STO.

Figure 4.3: EELS-SI of a LMO film grown on STO. (a) HAADF image where an orange square indicates the region of the EELS-SI was performed. (b) HAADF image acquired simultaneously with EELS-SI. (c), (d) and (e) elemental maps obtained from O-K, Mn-$L_{2,3}$ and La-$M_{4,5}$ intensities, respectively.

The presence of the nanoinclusions implies changes in the thickness and surface topography of the surrounding LMO matrix. The HAADF images reveal that the matrix surrounding the nanoinclusions is thicker than the matrix away from the nanoinclusions. Thus, the matrix away from the nanoinclusions has a thickness of ~ 57 nm while the matrix closer to the nanoinclusions reaches the height of the upcoming nanoinclusion and has a thickness of around ~ 70 nm.

Chemical analysis, performed by EDS profiles and EELS-SIs, of the specimen grown on STO, corroborate differences in the compositions between the matrix and the nanoinclusions. The spectroscopic analysis reveals that the matrix has a composition corresponding to the LMO, while the nanoinclusions are formed by a manganese oxide phase (MnO$_x$) as can be seen in the EELS-SI elemental maps of a nanoinclusion presented in Figure 4.3. These elemental maps show an increase of Mn intensity while La is absent inside the nanoinclusion. In addition, a ratio La/Mn ~ 1 is obtained from the LMO matrix by EDS.

4.3.1. LaMnO$_3$ matrix: Domain orientations in the LaMnO$_3$ matrix

The crystal structure of the bulk LMO is described by an orthorhombic *Pbnm* space group with unit cell parameters *a* = 5.533 Å, *b* = 5.727 Å and *c* = 7.668 Å at room temperature [133]. At growth temperatures (T=850ºC), although LMO is still exhibiting *Pbnm* crystallographic structure, all Mn-Mn matching distances are nearly equal (*a*/√2 ~ *b*/√2 ~ *c* /2 = 3.932 Å) [166]. Thus, it can be considered as a cubic structure with a cube-on-cube epitaxial relationship with the substrate. However, during cooling, at a temperature of 477ºC, the cooperative Jahn-Teller transition takes place in LMO. Due to JT transition, the MnO$_6$ octahedral of LMO are highly distorted and unit cell parameters change to acquire the values described previously for room temperature. To accommodate these structural distortions to the substrate lattice, films may grow in either (110) or (001) orientations, which implies that the orthorhombic *c* parameter is oriented in-plane or out-of-plane, respectively, as is illustrated in Figure 4.4.
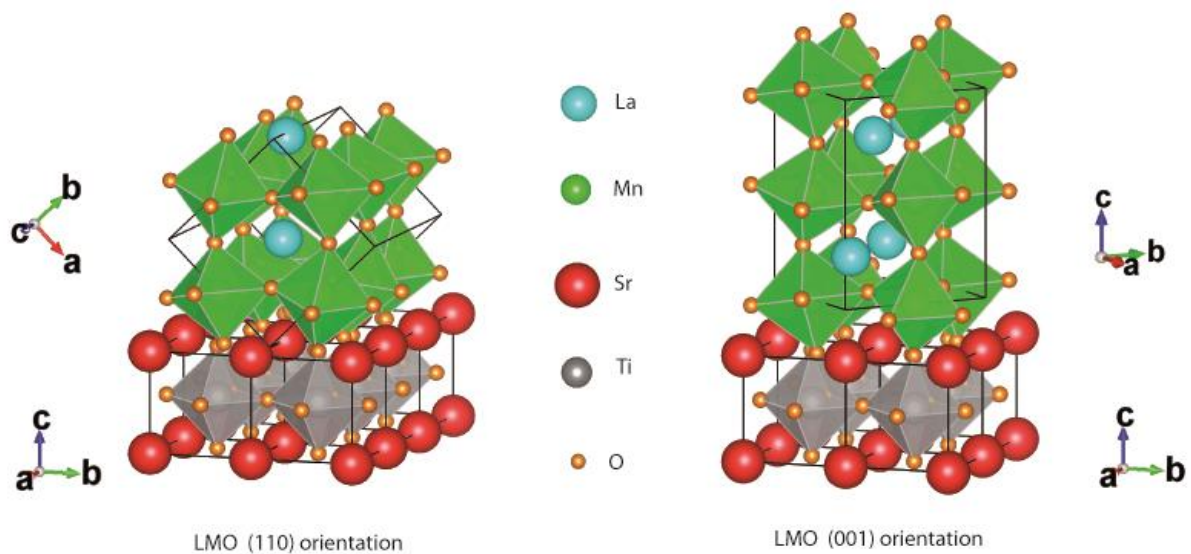

Figure 4.4: Schematic representation of the epitaxial growth directions of orthorhombic LMO thin films on cubic substrate. On the left, LMO (110) orientation (*c* parameter in-plane) and on the right, LMO (001) orientation (*c* parameter out of plane). Figure modified from Roqueta *et al*. [127].

In the case of the samples studied here, the *c* unit cell parameter is contained in the plane, which is favoured due to lower mismatches with the substrate. In the case of the *c* unit cell parameter contained in the plane, there are the two different possible matching Mn-Mn distances $d_{[110]LMO}$ = 3.982 Å and $d_{[001]LMO}$ = c_{LMO}/2 = 3.834 Å, as is schematically represented Figure 4.5. Thus, there are two possible in-plane lattice parameter values, which are confirmed by the reciprocal $2\theta - \Phi$ area scans at grazing incidence around 220 and 004 orthorhombic in-plane reflections (not shown). These scans showed the presence of two peaks occurring at different 2θ angles, which is the signature of twinned domains with two in-plane lattice parameters. Similar results were obtained previously for films grown on STO at lower oxygen pressures (5 x 10^{-3} mTorr) [127]. This means that the *c*-axis essentially follows both the [100] and [010] directions of the substrate.
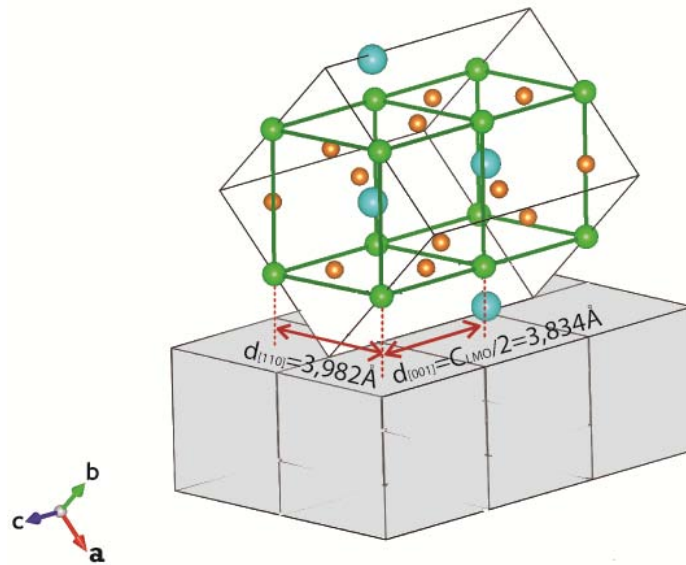

Figure 4.5: Schematic representation of the (110) epitaxial growth of orthorhombic LMO thin films on cubic perovskite substrates. Figure modified from Pomar *et al.* [126].

The obtained values of $d_{[110]LMO}$ and $d_{[001]LMO}$ from the XRD are 3.952 Å and 3.875 Å (on STO), and 3.947 Å and 3.857Å (on LAO), respectively. The approximate resulting residual strains (ε_{res}) from theses experimental values are presented in Table 4.1, jointly with the mismatch values (ε_{cal}) calculated with the expected distances ($d_{[110]LMO}$ = 3.982 Å and $d_{[001]LMO}$ = c_{LMO}/2 = 3.834 Å). A compressive strain is expected for both matching distances ($d_{[110]LMO}$ and $d_{[110]LMO}$) on LAO, while on STO, $d_{[110]LMO}$ results in a compressive strain, but $d_{[001]LMO}$ in a tensile strain.

Table 4.1 shows that the residual strains are closer to the mismatch values, which jointly with in-plane lattice parameters, indicate that the LMO thin films are almost in a relaxed state. Moreover, from standard $2\theta - \theta$ XRD measurements, the pseudocubic LMO out-of-plane unit cell parameter was also determined, obtaining 3.985 Å for LMO on STO and a larger value of 4.006 Å for LMO on LAO. In both cases, the estimation of pseudocubic unit cell volume leads to $\sim$ 61 Å^3, close to the expected bulk value for orthorhombic stoichiometric LMO [133].

	ε_{cal}		ε_{res}	
	STO	LAO	STO	LAO
d$_{[110]LMO}$	-2%	-5%	-1%	-4%
d$_{[001]LMO}$	2%	-1%	1%	−2%

Table 4.1: Misfit values obtained from d$_{[110]LMO}$ and d$_{[001]LMO}$ expected (ε_{cal}) and measured by XRD (ε_{res}).

The relative orientations of film and substrate were also observed by XRD reciprocal space maps, as depicted in Figure 4.6. The map shows the area around the main symmetrical 002 reflection of the LAO substrate. The position of the main film peak close to the substrate peak is compatible with 220 LMO, which corresponds to *c* in-plane oriented domains. The observation of the 221 LMO reflections indicates the formation of orthorhombic *Pbnm* LMO. The fact that the 221 reflection lies along *Q*x direction supports the *c* in-plane orientation of the LMO. The two separate reflections at lower Qz values are consistent with reflections from MnO$_x$ with their *c*-axis tilted 9° at both sides of the vertical direction.
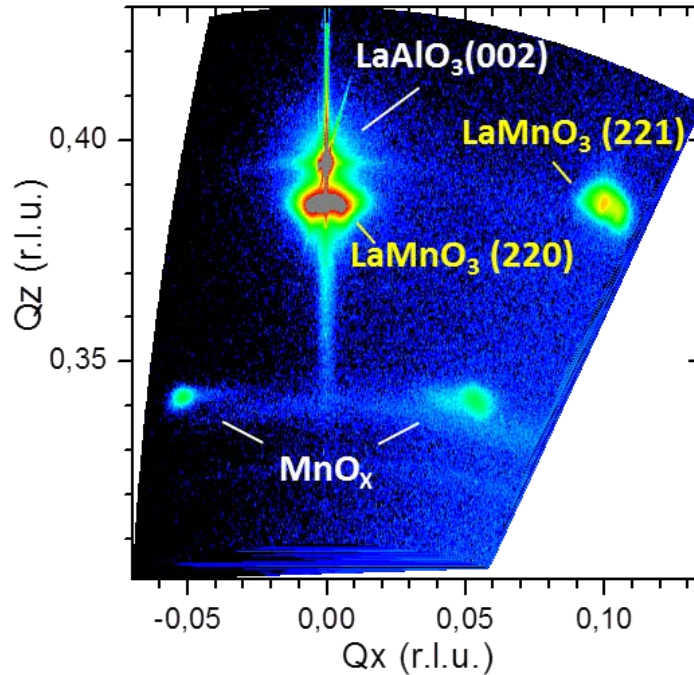

Figure 4.6: XRD reciprocal space map around the 220 LaMnO$_3$ and 002 LaAlO$_3$ main reflections showing the presence of 221 half order reflection of *c* in-plane LaMnO$_3$, and the presence of 9∘-tilted *c* out-of-plane MnO$_x$ domains. Figure modified from Pomar *et al*. [126].

The presence of twin domains in the LMO matrix is confirmed by cross-section analyses of the LMO film grown on STO. Two different orientations of LMO are identified by the change in the contrast pattern of HRTEM images, as can be observed in Figure 4.7(a). If the *c*-axis is perpendicular to the zone axis of the HRTEM image and parallel to the plane of the image, a rectangular pattern is formed in HRTEM image. This rectangular pattern has the shorter side perpendicular to the interface

and the longer side parallel to the interface as can be observed on the right of the HRTEM image presented in Figure 4.7(b). The corresponding FFT is presented in Figure 4.7(b) (inset right) also shows a rectangular pattern, even though rotated 90°. The in-plane and out-of-plane lattice parameters measured from the FFT of the HRTEM image are 7.827 Å and 4.103 Å, respectively. In this case, the in-plane lattice parameter corresponds to the c-parameter, thus the c-axis is parallel to the [100] directions of the substrate, and the zone axis of the LMO in the image is [110]. This orientation of LMO will be noted as LMO_A.
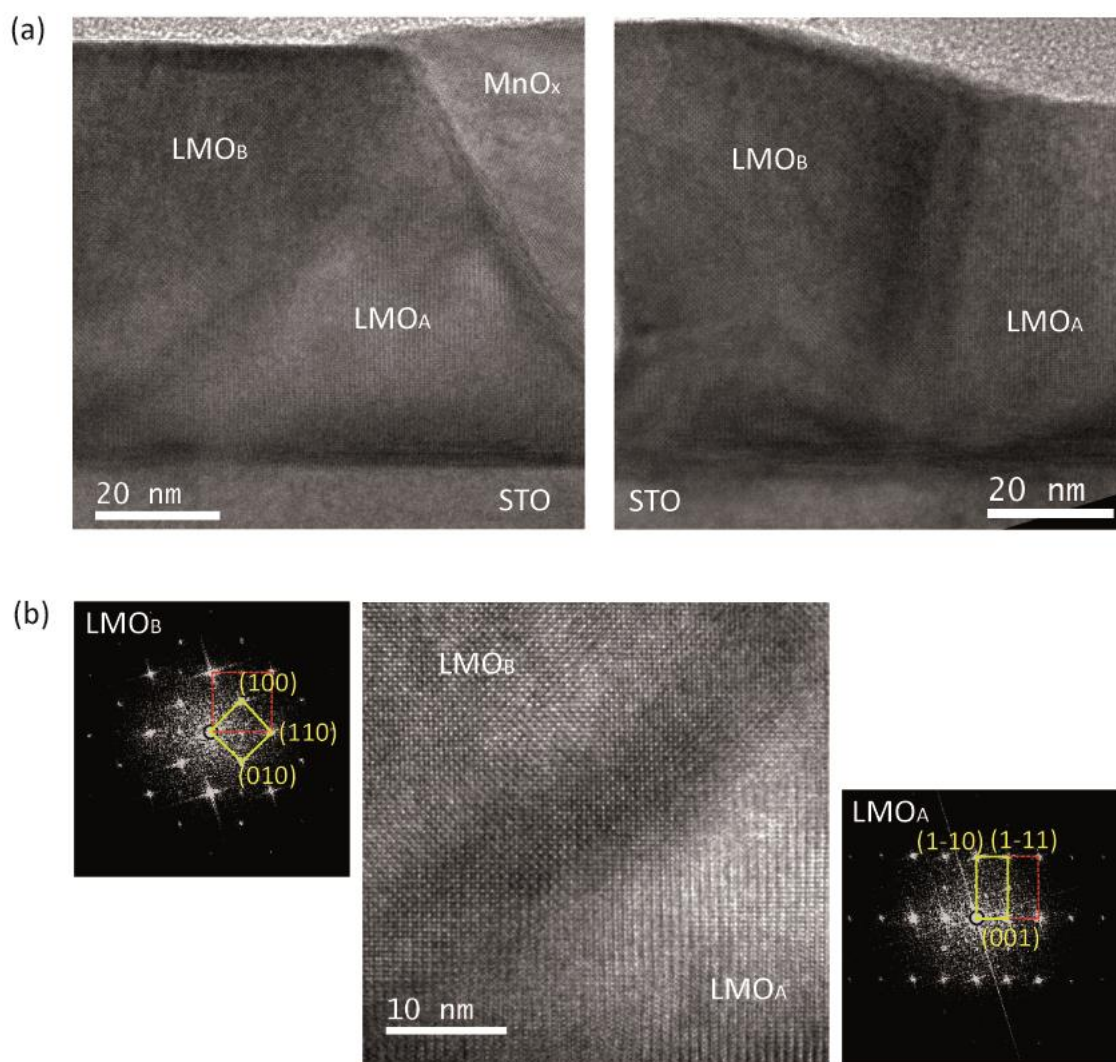

Figure 4.7: (a) Low-magnification bright field TEM images of the different LMO domains. (b) A HRTEM image of the different orthogonal domains shown in (a) left. At the right of the image, a LMO domain with the c-axis parallel to the zone axis [001] of the image and corresponding FFT. At the left of the image, a LMO domain with the c-axis perpendicular to the zone axis of the image, [110], and the corresponding FFT. In the FFTs, the yellow square marks the unit cell of corresponding orientation while the red discontinued line corresponds to the substrate unit cell as a reference.

Conversely, if the c-axis is parallel to the zone axis of the HRTEM image, i.e. perpendicular to the plane of the image, a cubic pattern rotated 45° with respect to the interface with the substrate appears in the HRTEM images. This contrast pattern can be observed in the left part of the HRTEM image and in corresponding FFT presented in Figure 4.7(b) (inset left). In this case, the zone axis of

LMO in the image is [001] and this orientation of LMO will be referred to as LMO$_B$, corresponding to the LMO domain rotated 90º. The in-plane and out-of-plane lattice parameters measured from the FFT of the HRTEM image are 4.044 Å and 4.073 Å, respectively. However, the orthorhombic axes are rotated 45º clockwise and counter-clockwise with respect to the in-plane lattice parameter. Comparing the interplanar distance between the 45º clockwise spots and the 45º counter-clockwise spots of the FFT, it is possible to distinguish two interplanar distances, 5.868 Å and 5.649 Å, respectively.

Here, all the values obtained by the FFT are larger than those expected for the LMO bulk [133] and those measured by XRD measurements [126]. It is not possible to determine the absolute value from the FFT, but it serves as a qualitative observation of the tendencies and the differences expected between the different parameters. Thus, considering the reported *a* and *b* orthorhombic unit cell parameters, 5.53 Å and 5.72 Å [133], respectively, it is possible to assign the smaller distance obtained experimentally, 5.649 Å, to the *a*-axis and the longer distance, 5.868 Å, to the *b*-axis. In this way, a detailed inspection of the HRTEM images, and the corresponding FFT, of this LMO orientation, reveals the presence of this orientation domain rotated 180º in the out-of-plane direction. This indicates the presence of two *c*-axis directions, one pointing inside the plane of the image (001) and the other pointing outside the plane of the image (00-1). However, while the LMO$_{B'}$[001] with respect to the LMO$_{B''}$[00-1] is identified by the HRTEM images and corresponding FFT, the two different LMO$_A$ orientations (LMO$_{A'}$[110] and LMO$_{A''}$[-1-10]) are not distinguished. A schematic representation of the LMO domains is presented in Figure 4.8
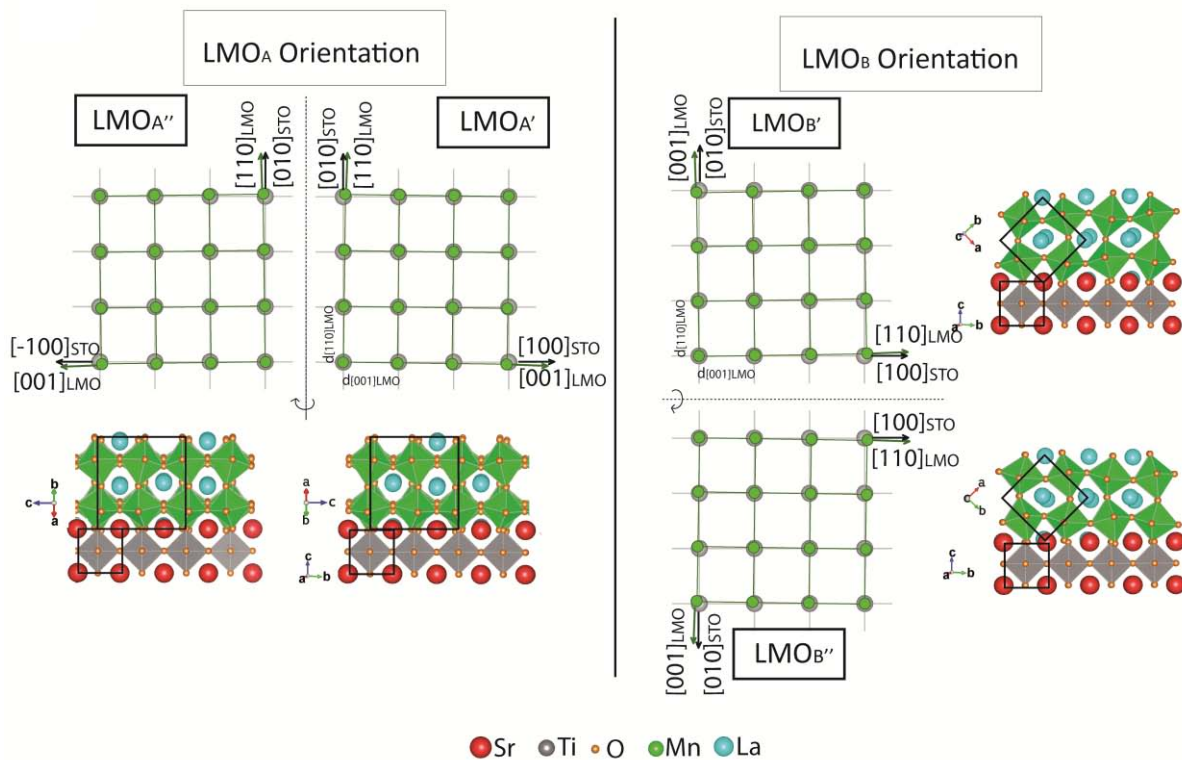

Figure 4.8: Schematic representation of the LMO domain orientations with respect to the substrate. The Mn/Ti lattice represents a planar view of the domains while octahedra framework represents a cross-section view of the domains. Modified from Pomar *et al.* [126].

4.4.Self-organized nanoinclusions of MnO$_x$

The manganese oxide that forms the nanoinclusions could present a simple or a mixed Mn oxidation state (Mn^{2+}, Mn^{3+} or Mn^{+4}). The different phases of MnO$_x$ depending on the oxidation state are MnO(II), Mn$_2$O$_3$(III), Mn$_3$O$_4$(II-III) and MnO$_2$(IV). The structural data of different manganese oxides reported in the literature are presented in Table 4.2.

In general, manganese may easily alter its valence forming different oxide stoichiometries in response to the environmental conditions. Thus, in the vacuum conditions used in the present work, MnO, Mn$_3$O$_4$ or Mn$_2$O$_3$ may be formed depending on the residual oxygen partial pressure in the chamber [147]. MnO is a cubic rock-salt with a = 4.45 Å[167] while Mn$_3$O$_4$ and γ-Mn$_2$O$_3$ exhibit spinel-like structures. Mn$_3$O$_4$ is a hausmannite mineral with a distorted spinel structure with manganese ions placed on two non-equivalent sites, tetrahedral (Mn^{2+}) and octahedral (Mn^{3+}). The structure is described by the tetragonal *I4$_1$/amd* space group with unit cell parameters of a = 5.76 Å and c = 9.47 Å [160, 161]. A very similar structure is reported for γ-Mn$_2$O$_3$ with a = 5.79 Å and c = 9.40 Å[168].

Composition	Mineralogical name	Space Group	Lattice Parameters (Å)	Reference
MnO	Manganosite	*Fm3m*	a=4.4449 Å	[155]
	Manganite	*Pnnm*	a=4.4200Å, b=5.2300Å, c=2.8700Å	[156]
Mn$_2$O$_3$	Bixbyite	*I2$_1$3*	a=9.4100Å	[158]
	α-Mn$_2$O$_3$	*Pcab*	a=9.4157Å, b=9.4233Å, c=9.4047Å	[157]
	γ-Mn$_2$O$_3$	*I4$_1$/amd*	a=5.79Å, c=9.40Å	[168]
Mn$_3$O$_4$	Hausmannite	*I4$_1$/amd*	a=5.7620Å, c=9.4390Å, a=5.7691Å, c=9.4605Å	[160], [161]
	high-pressure polymorph	*Pmab*	a=9.5564Å, b=9.7996Å, c=3.0240Å	[159]
MnO$_2$	Todorokite	*P2/m*	a=9.7890Å, b=2.8340Å, c=9.5510Å, β=93.700º	[162]
	Ramsdellite	*Pnma*	a=9.2734Å, b=2.8638Å, c=4.5219Å	[163]
	Pyrolusite	*P4$_2$/mnm*	a=4.3880Å, c=2.8650Å, γ=120º	[164]

Table 4.2: Structural data of the manganese oxides [155-164] reported in AMCSD [82].

The HRTEM images of different nanoinclusions were analysed to identify the MnO$_x$ phase. These images reveal that the nanoinclusions are crystalline but highly distorted. The analyses of HRTEM images indicate that manganese oxide has a spinel crystal structure with interplanar distances of 5.2 Å in-plane and 9.2 Å out-of-plane.

Figure 4.9(a) shows a TEM image of two nanoinclusions. A HRTEM image of the nanoinclusion and the corresponding FFT obtained from the red square region marked in (a) are shown in Figure

4.9(b). The structural data of different manganese oxides [155-164] reported in AMCSD [82] were used to index the FFTs. The resulting interplanar distances of the different spots measured from the FFT of nanoinclusions and marked in the FFT presented in Figure 4.9(b) right panel, are shown in Table 4.3. Assuming an error of 3° and 0.3Å, the FFT pattern of nanoinclusions can be indexed as a Mn_3O_4, with a disorientation of 9° of the out-of-plane parameter with respect to the LMO-substrate perpendicular plane. Despite the fact that the MnO phase, the Bixbyite[158], and the α-Mn_2O_3 phase[157] are discarded, the γ-Mn_2O_3 phase, which is not reported in AMCSD, has a similar structure to a Mn_3O_4 phase and its appearance can not be ruled out.
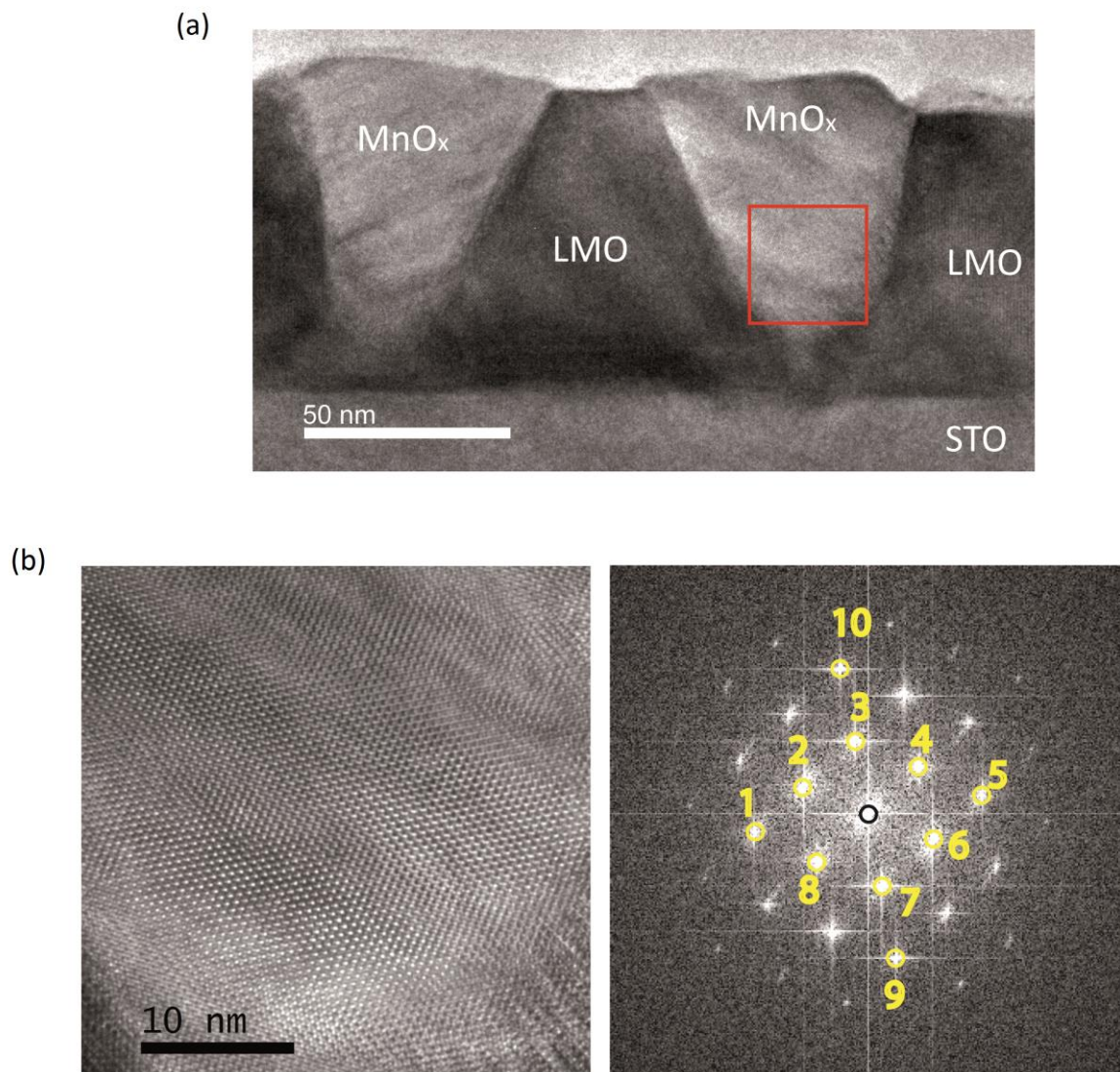
(a)

(b)

Figure 4.9: (a) TEM image of two nanoinclusions in the LMO matrix. (b) HRTEM image of a nanoinclusion (left), and the corresponding FFT (right), obtained from the red square region marked in (a). The interplanar distances obtained from the spots marked in FFT are presented in Table 4.3

Spot	d-Spacing (A)	Angle to previous spot (º)
1	3.06	0.00
2	5.04	31.38
3	4.72	57.37
4	5.21	58.47
5	3.06	32.77
6	5.04	31.38
7	4.72	57.37
8	5.21	58.47
9	2.39	58.38
10	2.39	180

Table 4.3: Interplanar distances obtained from the FFT of the HRTEM image presented in Figure 4.9 The spots correspond to those marked in the FFT.

SAED patterns are also used to identify the MnO_x. However, the size of the aperture is not small enough to select only a nanoinclusion, as shown in the inset of Figure 4.10(a). A complex ED pattern is observed due to the contribution of the MnO_x and two principal orientations of LMO (LMO_A and LMO_B), as can be seen in the Figure 4.10(b). The indexing of the SAED permits distinguishing the spots that correspond to the LMO orientations with respect to the ones of MnO_x. Some indexed reflections are marked in the SAED, jointly with the unit cell for both orientations of LMO and the Mn_3O_4 phase. However, the diffraction pattern shows kinematically forbidden reflections, such as the (002) and (00-2) of Mn_3O_4, or the (-100) and (1-10) of LMO_A and (100), (110) and (010) of LMO_B. Taking into account that the substrate is also contributing to the SAED, some reflections at the position corresponding to the forbidden LMO reflections may correspond to STO reflections. Moreover, these forbidden reflections may also appear due to dynamic scattering events, especially for thick specimens.
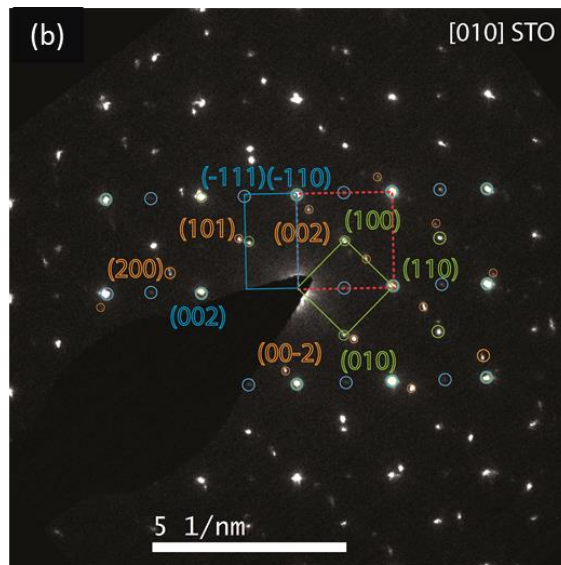
(a)
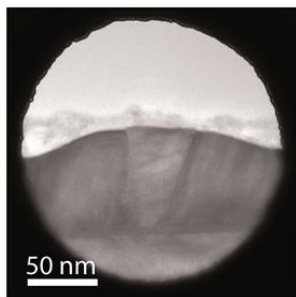
Figure 4.10: (a) TEM image which shows the size of the area selection, larger than one nanoinclusion. (b) SAED of a nanoinclusion. Corresponding reflections of LMO_A, LMO_B and Mn_3O_4 marked in blue, green and orange, respectively.

The Mn$_3$O$_4$ phase in the nanoinclusions is confirmed by comparing the energy loss O-*K* edge shape with those reported in the literature [106, 110]. Dual EELS-SIs were acquired from a MnO$_x$ nanoinclusion and LMO matrix. The energy loss O-*K* edge and Mn-*L*$_{2,3}$ edge from a nanoinclusion are presented Figure 4.11.
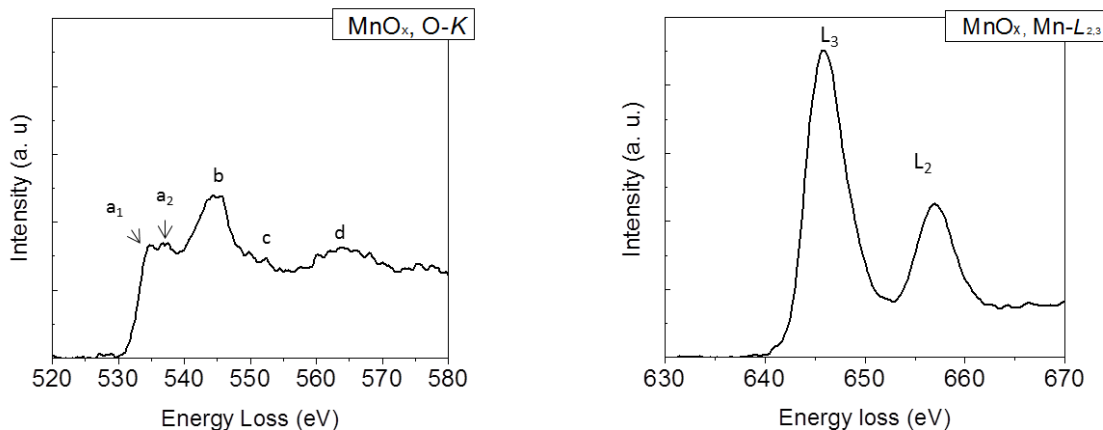

Figure 4.11: Energy loss O-*K* edge and Mn-*L*$_{2,3}$ edge spectra of a nanoinclusion.

The variation of the O-*K* edge fine structure of the different manganese oxides has been analysed in previous studies [106, 110, 169]. The O-*K* edge provides information on excitations of O 1*s* electrons to the 2*p* bands [73]. Four peaks may be distinguished in O-*K* edge fine structure of manganese oxides, although not all of them are always present in every manganese oxide. The first peak **a**, called pre-peak, is found around 530eV and is attributed to the transition from 1*s* core levels to oxygen 2*p* states hybridized with manganese 3*d* orbitals [106, 170, 171]. The second peak **b**, is related to the projected unoccupied oxygen *p* states mixed with the manganese 4*sp* band at higher energy above the Fermi level [106]. The two last peaks, **c** and **d**, can be interpreted in terms of the multiple scattering of the excited electrons with low kinetic energy. These features are sensitive to the local structure around the oxygen site, which means that the features are similar if crystal structures are identical [172].

The pre-peak may consist of one or several peaks which can be interpreted in terms of the ligand field and exchange splitting [170]. Splitting is observed in the pre-peak of Mn$_3$O$_4$, Mn$_2$O$_3$ and MnO$_2$, while in the MnO spectrum, there is only one peak [106]. Kurata *et al.* [106] observed that the pre-peak in Mn$_3$O$_4$ and MnO$_2$ splits in two peaks (**a$_1$** and **a$_2$**) and in Mn$_2$O$_3$ in three peaks (**a$_1$, a$_2$** and **a$_3$**). This pre-peak splitting in Mn$_3$O$_4$ has been also observed by Tan *et al.*[110]. In the spectrum obtained from the MnO$_x$ nanoinclusions in the present work (Figure 4.11) the pre-peak appears split in two peaks, **a$_1$** (534.5 eV) and **a$_2$** (537 eV), and the shape of O-*K* edge is similar to that corresponding to Mn$_3$O$_4$ reported un the literature [106, 110]. In addition, in the same reports the Mn-*L*$_3$ edge for Mn$_3$O$_4$ appears to be split [106, 110]. In the Mn-*L*$_{2,3}$ spectrum presented in Figure 4.11, the *L*$_3$, does not show any splitting, probably due to the insufficient energy resolution of the spectrum presented here. From this analysis it can be concluded that the inclusions consist of Mn$_3$O$_4$ phase.

4.5. MnO$_x$ nanoinclusions – LaMnO$_3$ matrix interface

The analysis of 14 different nanoinclusions shows a tendency to form a boundary with the LMO matrix tilted 35º and 10º away from the vertical axis at each side of the nanoinclusions. HRTEM images reveal that this boundary has an incoherent interface. Figure 4.12 and 4.13 shows the HRTEM images of two different nanoinclusions included in the LMO matrix. The FFTs of the nanoinclusions and the surrounding LMO matrix were acquired and used to identify the relative crystallographic orientation of the Mn$_3$O$_4$ inclusions long axis with respect to the LMO matrix. In this case, only LMO$_A$ and LMO$_B$ orientations are considered, without distinguishing between the twin domains corresponding to each LMO orientation. The corresponding FFT of each region are shown below the corresponding HRTEM image with the mean spots indexed. The indices are coloured to differentiate the spots corresponding to the LMO orientation (LMO$_A$ in blue and LMO$_B$ in green) from those corresponding to the Mn$_3$O$_4$ (in orange). The nanoinclusions are found in two different relationships with the matrix: embedded in a single LMO domain and at the interface between two orthogonal LMO domains.

In the case of the Mn$_3$O$_4$ nanoinclusion presented in Figure 4.12, it is found at the boundary between LMO$_A$ and LMO$_B$ orientation domains. Thus, one of the long sides of the Mn$_3$O$_4$ nanoinclusion is aligned with the [001] LMO direction while the other is aligned with [110] LMO direction. In contrast, in the nanoinclusion presented in Figure 4.13 that is embedded in a single LMO$_B$ orientation domain, both long sides of the nanoinclusion are aligned with [001] LMO direction. Surprisingly, only these two situations are observed as the long sides of the Mn$_3$O$_4$ nanoinclusion fully embedded in LMO$_A$ domains were not observed.
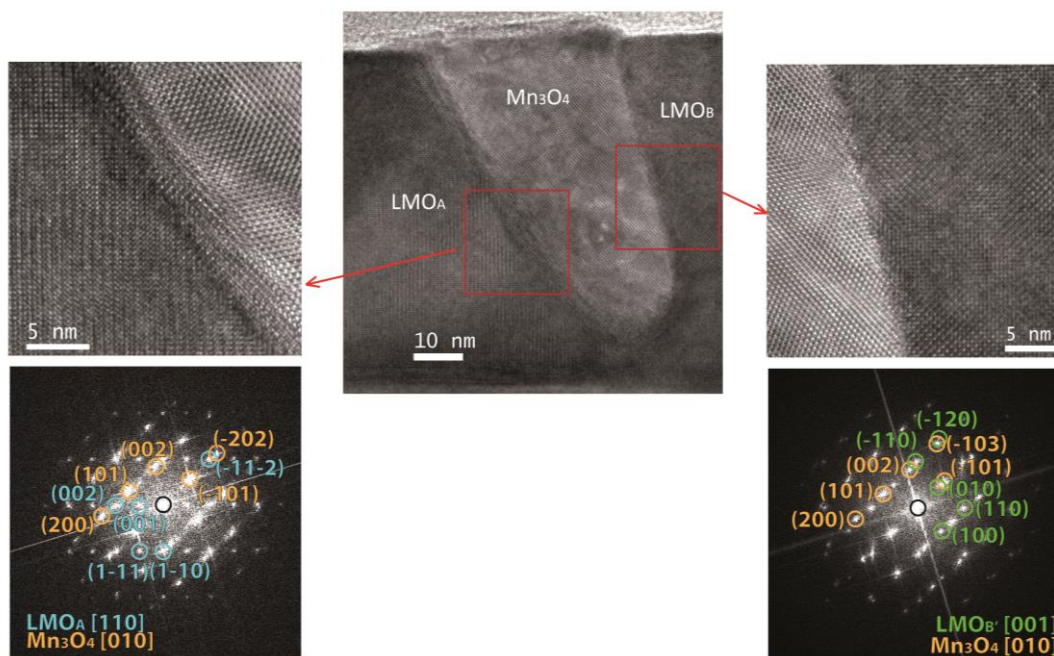

Figure 4.12: HRTEM images of a nanoinclusion embedded at the interface between two different LMO domains. The inset shows the corresponding FFT obtained from the interface of LMO$_A$/Mn$_3$O$_4$ on the left and from the interface of LMO$_B$/Mn$_3$O$_4$ on the right with the main spots indexed (LMO$_A$ in blue, LMO$_B$ in green and Mn$_3$O$_4$ in orange).
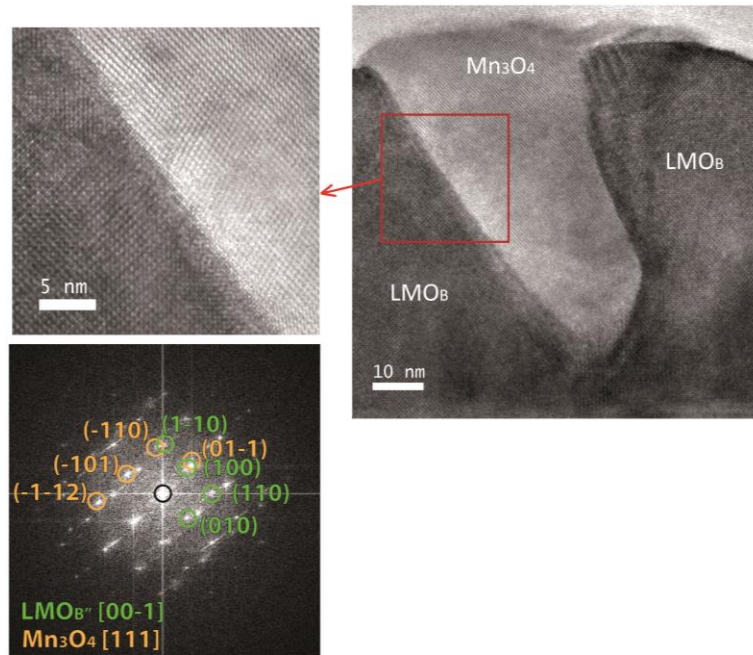
Figure 4.13: HRTEM image of a nanoinclusion embedded in a single LMO domain. Inset shows the corresponding FFT image obtained from the interface of LMO_B/Mn_3O_4 with the main spots indexed (colours as in Figure 4.12).

The crystallographic relative orientation of the nanoinclusion and the LMO was determined by analysing FFTs obtained from HRTEM images. As it is shown in the FFTs not strictly parallel planes are identified between the nanoinclusion and the matrix. The planes that are almost parallel are used as the most accurate description for the corresponding crystallographic orientation. Thus, for the nanoinclusion embedded between the two different LMO domains (LMO_A-LMO_B), the crystallographic orientation relationships are: (i) $<110>_{LMO}$ || $<010>_{Mn3O4}$ / $(-11-2)_{LMO}$ || $(-202)_{Mn3O4}$ and (ii) $<010>_{Mn3O4}$ || $<001>_{LMO}$ /$(-103)_{Mn3O4}$ || $(-120)_{LMO,}$ with disorientation angles of 2º and 1.5º respectively, while for the nanoinclusions in the middle of a LMO_B domain is $<00-1>_{LMO}$ || $<111>_{Mn3O4}$ / $(100)_{LMO}$ || $(01-1)_{Mn3O4,}$ with a disorientation angle of 1.5º. Thus, the two zone axes of Mn_3O_4 nanoinclusions ([010] and [111]) are parallel to the [010] direction of the STO. Both orientations have a similar crystallographic orientation with respect to the perovskite substrate, which may be defined as (001)-oriented cube on diagonal (in-pane rotations of 45º) but with a slight c-axis tilting of 9º.

4.6. Interface Layer

The other relevant feature identified by HRTEM imaging and spectroscopic analysis (EDS and EELS vertical profiles) is the presence of an epitaxial (001)-oriented layer of a La-rich secondary phase in the interface region between the film and the substrate. On the one hand, spectroscopic analyses reveals a decrease of Mn and O intensities while the La intensity is maintained when approaching the interface from the film side, as it is shown in EELS elemental edge intensity profiles presented in Figure 4.14(a). Thus, an increment of La/Mn ratio takes place at the region closer to the interface between the LMO and the substrate, as is shown in Figure 4.14(a). On the other hand, HRTEM images reveal a change in the contrast pattern at the region closer to the interface of the LMO with the

substrate. This secondary phase, of around ~ 2 nm thickness, has interplanar distances of 3.94 Å in-plane and 13.5 Å out-of-plane. The atomic column arrangement in the TEM image may correspond to the insertion of supplementary LaO planes along the film growth direction resulting in the formation of the La_2MnO_4 Ruddlesden-Popper structure.
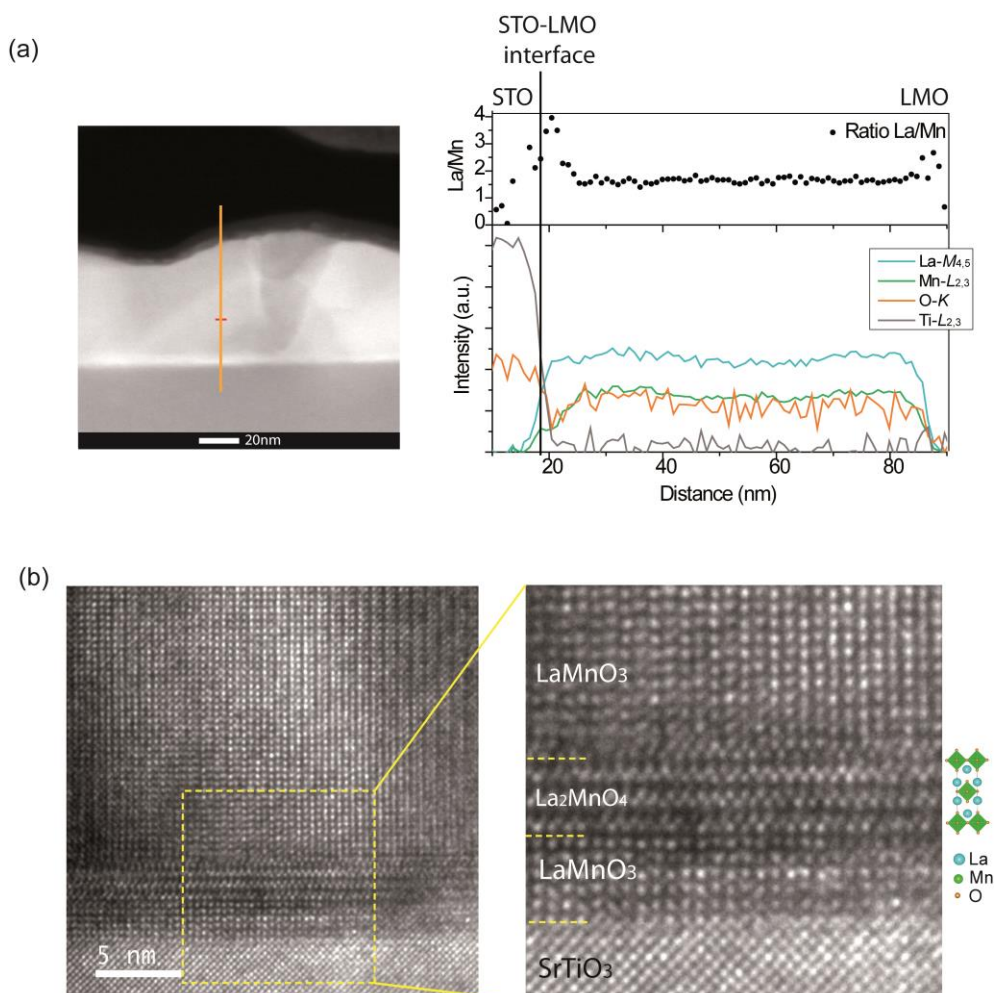

Figure 4.14: (a) EELS O-K, Mn-$L_{2,3}$ and La-$M_{4,5}$ edge intensity profiles taken along the orange line marked in the HAADF image. (b) HRTEM images close to the interface between nanocomposite and substrate showing the presence of a epitaxial Ruddlesden-Popper La_2MnO_4 phase.

In addition, this layer is not directly in contact with the substrate but a few unit cells above it, laying on a LMO interlayer as shown in Figure 4.14(b). Furthermore, this secondary phase is not observed continuously along the entire interface.

The formation of La-based oxides such as La_2O_3 has been reported in LMO stoichiometric films [144]. However, the measured parameters of the La-rich phase observed in the sample studied here, plus the fact that the spectroscopic analysis indicates the presence of Mn clearly points to a Ruddlesden-Popper La_2MnO_4 phase.

4.7. Phase segregation mechanism

Chemical phase segregation occurs typically due to the gain in free energy by nucleating a stable secondary phase which exceeds the energy cost associated with the creation of new interface. In the case of epitaxial thin films, the strain associated with the mismatch between the lattice parameter of film (and possible secondary phases) and the substrate may promote a segregation of selected composition. Previous investigations show the occurrence of a three phase oxide manganese nanocomposite as a relaxation mechanism of a similar material (La$_{1-x}$Sr$_x$MnO$_3$)[173-175] to that studied here. In these works, the formation of La-Sr-O islands during the growth of La$_{1-x}$Sr$_x$MnO$_3$ films has been observed. The misfit relaxation mechanism governs the outcropping of these islands at the surface. The appearance of these La-Sr-O islands result in unbalance of the stoichiometry of the film which is compensated by the formation of a Sr$_3$Mn$_2$O$_7$ Ruddlesden-Popper phase. Despite the formation of La-Sr-O islands, the LSMO film was fully strained [174], while in our case the LMO films are almost relaxed.

As was previously mentioned in section 4.4, in the vacuum conditions used in the growth of the LMO films presented in this work, the manganese might adopt an oxidation state of Mn^{+2}. In the case of La-deficient thin films, Mn^{2+} occupying the La^{3+} sides has been reported [176, 177]. In fact, considering the cations radius of 0.97 Å for Mn^{2+} (in a octahedral coordination) and 1.172Å for La^{3+}, and the Goldschmidt tolerance factor for perovskites, these substitutions could be feasible in the LMO perovskite up to the solubility ratio [144]. However, in the case studied in the work presented here, the matrix preserves the La/Mn ~ 1, and the main mechanism to accommodate Mn^{2+} ions is by the formation of Mn$_3$O$_4$ segregates. Thus, the Mn$_3$O$_4$ particles should be formed on LMO films during the growth process and it is possible that the Mn$_3$O$_4$ spinel nucleates cube-on-cube on the cubic LMO. During cooling, the LMO Jahn-Teller transition takes place and Mn$_3$O$_4$ nanoinclusions have to accommodate their shape to the surrounding LMO orientation domains. Moreover, the resulting stoichiometry unbalance due to the formation of Mn$_3$O$_4$ nanoinclusions is compensated by the creation of a La-rich phase (La$_2$MnO$_4$), in contrast to La$_2$O$_3$ reported in LMO stoichiometric films [144].

4.8. Conclusions

In this chapter, the formation of self-organized Mn$_3$O$_4$ nanoinclusions in films of LaMnO$_3$ grown by PLD is reported. Different orientation domains are present in the orthorhombic LMO matrix. The values of residual strain and in-plane lattice parameters indicate that the LMO thin films are almost in a relaxed state.

Spectroscopic analyses and HRTEM imaging suggest that the nanoinclusions are formed by Mn$_3$O$_4$. The Mn$_3$O$_4$ nanoinclusions formation results in the accommodation of the Mn^{2+} cations produced because of the vacuum growth conditions. The Mn$_3$O$_4$ nanoinclusions present a wedge shape and are uniformly distributed in the matrix, aligned with the main axis of the substrate. The presence of the nanoinclusions affects LMO matrix thickness and the surface topography. In

particular it produces an increment of thickness and surface facets close to the nanoinclusions. The crystallographic orientation relationship of the Mn_3O_4 nanoinclusions with the LMO matrix results from the accommodation of the cubic Mn_3O_4 spinel, which nucleate in a nearly-cubic LMO matrix during the growth at high temperature. Moreover, the resulting stoichiometry unbalance is partially accommodated by the creation of an epitaxial La-rich Ruddlesden-Popper La_2MnO_4 phase close to the interface with the substrate.

Chapter 5

Twin walls in La$_{0.7}$Sr$_{0.3}$MnO$_3$ grown under tensile stress

5.1.Introduction

Chapters 5 and 6 analyse self-organized misfit relieving defects in La$_{0.7}$Sr$_{0.3}$MnO$_3$ (LSMO) formed as a result of the relaxation mechanisms of these films. Two different stress scenarios are studied: self-organized defects as a result of the relaxation mechanisms of LSMO under tensile stress, grown on (001)SrTiO$_3$ (STO) (this chapter), and under compressive stress, grown on (001)LaAlO$_3$ (LAO) (in chapter 6).

LSMO is a half-metal room temperature ferromagnet (T_c ~ 370 K). In bulk form, it is a rhombohedral perovskite, which belongs to the *R-3c* space group [26]. It is characterized by equal octahedral tilts about the three cartesian axes of the pseudocubic unit cell, belonging to the $a^-a^-a^-$ Glazer tilt system [14], and has a unit cell parameter, *a*, of 3.881 Å and a rhombohedral or pseudocubic interaxial angle, α_{pc}, of 90.37° [178]. Thus, the rhombohedral structure may be described as a compression along [111] direction of a cubic structure.

If a rhombohedral structure is grown on a cubic substrate, the misfit between these structures can be divided into two strain contributions: (i) a shear strain $\chi = \tan \emptyset$, relative to the underlying (001) plane of a cubic substrate, where $\emptyset = \alpha_{pc} - 90°$ is the shear angle, and (ii) the conventional lattice parameter linear strain given by $\mathcal{E} = (a_s - a_f) / a_f$, where a_s and a_f are the in-plane lattice parameters of the substrate and the film, respectively. In the case of the LSMO grown on STO, the values of these two strain contributions are $\chi = 6.4 \times 10^{-3}$ and a tensile misfit of $\mathcal{E} = 6.2 \times 10^{-3}$, where $a_s = a_{STO} = 3.905$ Å and $a_f = a_{LSMO} = 3.881$ Å.

Thus, two elastic energies contribute to the total strain energy (E_T) of the rhombohedral film grown on a cubic substrate [179]: the shear, $E(\chi) = (1/2)G\chi^2 h$, and normal, $E(\mathcal{E}) = 2[(1+v)/(1-v)]G\mathcal{E}^2 h$, elastic energies, where v is the Poisson's ratio, G is the shear modulus and h is the film thickness. Consequently, the total strain energy can be described as $E_T = E(\chi) + E(\mathcal{E})$. In the case of LSMO grown under tensile stress on STO, with $v \sim 0.33$ [43] and G = 68.2 GPa [180], the elastic energies per unit film thickness are $E(\chi)/h$ = 1.4 MPa and $E(\mathcal{E})/h$ = 10 MPa [44]. Classic models predict a plastic relaxation of $E(\mathcal{E})$ at a critical thickness of ~10 nm by dislocations [181]

while it is expected that $E(\chi)$ would be relieved from the initial growth stages by twinning on the (100) and (010) planes perpendicular to the interface [182, 183]. Despite the energetic contribution of the normal elastic energy is significantly larger, by almost one order of magnitude, the formation of dislocations does not occur [43, 182]. However, it was found that $E(\chi)$ is relieved by twinning after a shear transition at a critical thickness of 2.5 nm [43, 44]. These discrepancies show the ability of these complex oxides formed by octahedral frameworks to develop other efficient strain relaxation mechanisms at a lower energy cost than those associated with the formation of the misfit dislocations.

In previous studies of misfit accommodation mechanisms and the structural characterization of $La_{1-x}Sr_xMnO_3$ doped manganese perovskites, such as $La_{0.9}Sr_{0.1}MnO_3$ or $La_{0.7}Sr_{0.3}MnO_3$ grown under tensile stress on STO single crystals, twin domains (TDs) have been found [43, 44, 182, 184-186]. In Refs. [43] and.[44], the thickness dependence of lattice distortions and the evolution of the shear strain from the early stages (1.9 nm) of stain relaxation of up to 475 nm are investigated. Those authors found that the in-plane lattice parameter remains fully strained up to h = 475nm while the out-of-plane lattice parameter changes continuously as a function of thickness. According to the evolution of the lattice parameters they identified four different deformation regimes as a function of thickness (h): (I) for h <2.5 nm, (II) for 2.5 nm< h <10 nm, (III) for 10 nm> h >25 nm, and (IV) for h >25 nm up to 475 nm, as is illustrated in Figure 5.1(a). The deformation regimes were defined through lattice distortion mechanisms driven by the polar discontinuity and octahedral tilt effects [43]. The lattice distortion mechanisms correlated with the deformation regimes are presented in Figure 5.1(b).
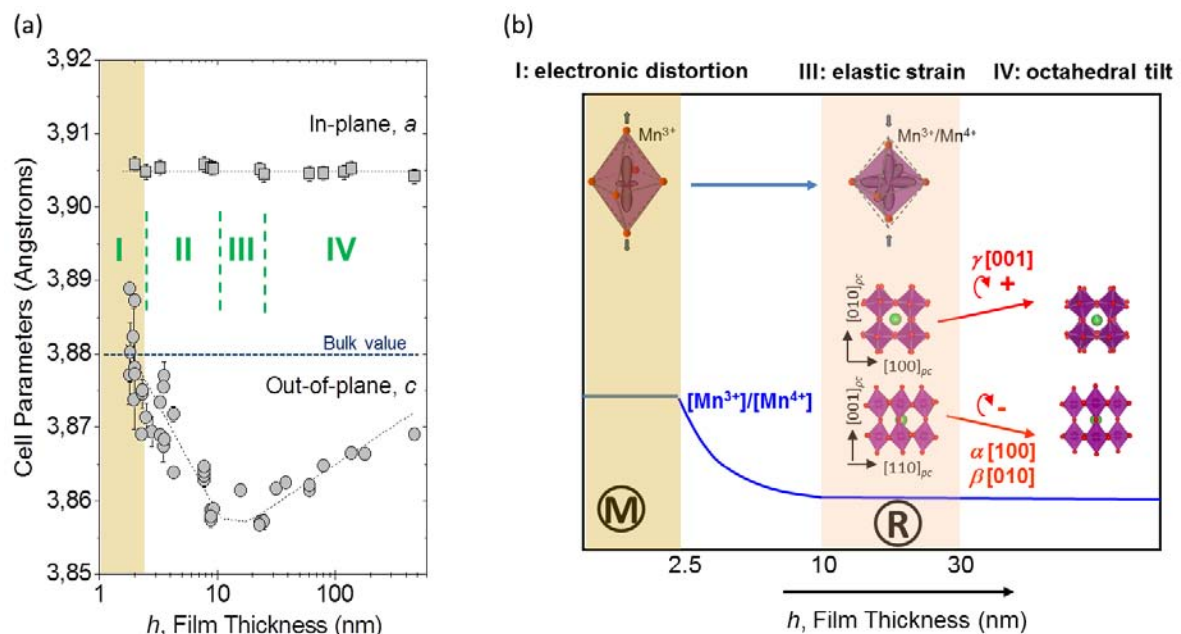

Figure 5.1: (a) Thickness dependence of the in-plane and out-of-plane lattice parameters measured by XRD. The shadowed area indicates the non-twinned thickness range. I, II, III and IV correspond to the deformation regimes. (b) Mechanisms of lattice distortions correlated with the deformation regimes. M and R indicate monoclinic and rhombohedral states, respectively. Figures adapted from Sandiumenge, *et al.* [43].

According to these regimes, TDs appear above a critical thickness of 2.5 nm, after the occurrence of a monoclinic distortion. This distortion results from the charge enrichment towards the interface due to the polar discontinuity between LSMO and STO, and simultaneously cancels the shear component of the misfit strain [43]. The formation of TDs is associated with the formation of the rhombohedral structure, which condenses at 10 nm. At thicknesses of between 25 and 475 nm the in-plane and out-of-plane shear components were found to follow divergent trajectories indicating a progressive perturbation of the octahedral framework by a combination of octahedral tiltings [43]. This allows the in-plane lattice parameters to remain fully strained within the explored thickness [43, 44]. Despite these structural perturbations, the TD size follows a $h^{1/2}$ dependence as is showed in Figure 5.2, which is the dependence predicted for homogeneous films by equilibrium models [44].
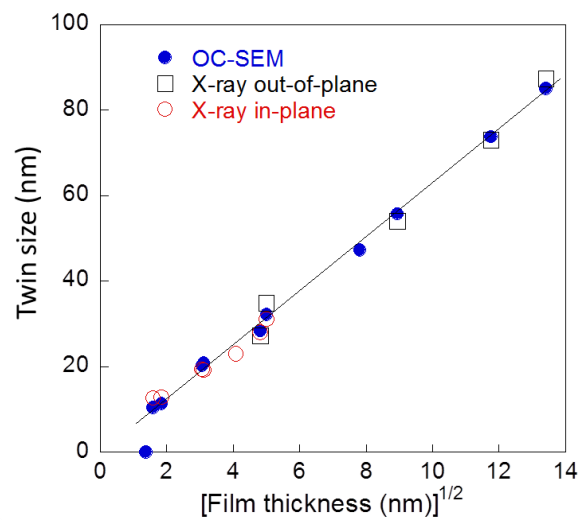

Figure 5.2: Twin domain size dependence on $h^{1/2}$ as derived from direct inspection of OC-SEM images and in-plane and out-of-plane XRD measurements. Figure from Santiso, *et al*. [44]

TDs are bounded by ferroelastic twin walls (TWs), which are defined to satisfy the compatibility between two orientations of the spontaneous strain on the contact plane [187]. However, TWs have associated large strain gradients perpendicular to the TW plane [188] and within the TW region the crystal structure becomes highly distorted with respect to the TD regions. The presence of such distortions in strongly correlated electron oxides may affect their electrical and magnetic functionalities.

Domain walls in ferroic complex oxides have attracted considerable interest in recent years due to their distinctive functional behaviour relative to that exhibited by bulk material [60, 189]. Some examples of this distinctive behaviour are ferroelectric polarization in SrTiO$_3$ [190], superconductivity in insulating WO$_{3-x}$ [191], ferrielectricity in ferroelastic CaTiO$_3$ [192], enhanced conductivity in BiFeO$_3$ [193, 194], insulating behaviour in YMnO$_3$ [195], ferromagnetism in TbMnO$_3$ [61] and a ~10^9 times increase in conductivity in 90° head-to-head walls in canonical ferroelectric BaTiO$_3$ [196]. The distinctive functional behaviour is especially interesting in the doped manganese perovskites, which exhibit a variety of phenomena, such as ferromagnetic coupling, large

magnetoresistance, metal-insulator transition, half-metallic character, and cooperative orbital ordering [26]. However, despite their fascinating hetero-interfacial behaviour [197], TWs in these materials remain unexplored.

In this chapter, a detailed study of TWs and their implications on the functional properties of the surface of the LSMO films is presented.

5.2. Experimental methods

$La_{0.7}Sr_{0.3}MnO_3$ films, with thicknesses of between 40-100 nm, were deposited on (001)-oriented, TiO_2 terminated $SrTiO_3$ (STO) substrates by RF magnetron sputtering, following the procedure reported by Konstantinovic *et al.* [124].

Planar view and cross-section TEM samples of 40 and 50-nm-thick films were prepared by conventional cutting, gluing and grinding procedures, followed by an Ar milling step down to electron transparency and perforation by PIPS at a small incidence angle. Convectional TEM images and ED patterns in planar view of specimens were performed with FEI Tecnai F20 S/TEM microscope working at 200kV. HRTEM images in planar view were obtained using a Hitachi HF3300 electron microscope working at 300 kV. These HRTEM images were used to obtain strain component maps by the GPA software [83, 85]. HRTEM and STEM (HAADF, MAADF and LAADF) images of cross-section samples were obtained by a FEI Tecnai F20 S/TEM microscope working at 200 kV with a probe convergence semi-angle of 11,7 mrad. The camera lengths used were 70 mm, 200 mm and 490 mm, corresponding to inner and outer collection angles of 107-200 mrad, 38-200 mrad and 15-94 mrad, respectively. HAADF and MAADF images and EELS-SIs of cross-section samples were acquired using a Nion UltraSTEM 200 operating at 100 kV with a probe convergence angle of 35 mrad. These images were acquired with inner and outer detector angles of 50–75 mrad and 80-210 mrad, respectively. The data shown here used a 50 mrad EELS collection angle and the spectra were denoised using PCA as provided in the Hyperspy suite [105]. To avoid the possibility of any small shift or signal shape change being lost through an excessive noise removal, the first three components appearing to contain only noise were left in the PCA reconstruction.

In addition to the microstructural study, conducting atomic force microscopy (C-AFM), force modulation microscopy (FMM) and magnetic force microscopy (MFM) investigations were carried out in collaboration with C. Ocal, R. Moreno and N. Domingo, respectively, in order to establish a correlation between the structure and the physical properties of the TWs. These results are included here for completeness. Local electrical conductivity was investigated by C-AFM measurements using a commercial head and software from Nanotec under an N_2 gas environment (RH ≈ 2%). Simultaneous topographic images $z(x,y)$ and current maps $I(x,y)$ and characteristic I -V curves of the TWs and TDs were acquired. The spatially resolved mechanical response of the surface of the films was analysed by analysing contact resonance frequency images obtained by FMM (MFP-3D, Asylum Research). Finally, the spatially resolved magnetic behaviour of the films was investigated by MFM. Phase contrast images were obtained at different tip distances from the film surface, while adjusting

the amplitude ratio of MFM imaging *vs* topography imaging set point. All the procedures followed to obtain these measurements are reported in Ref. [128].

5.3. Twin microstructure in La$_{0.7}$Sr$_{0.3}$MnO$_3$

The LSMO films on STO analysed here have a film thickness of around 50 nm with a twin domain size of around ~40 nm in accordance with a TD size/thickness dependence of $h^{1/2}$ (Figure 5.2). The different TDs and TWs of a LSMO film on STO can be observed in the planar view multi-beam bright-field low-magnification image viewed along [001] presented in Figure 5.3(a). Despite the fact that (100) and (110) TW orientations are allowed in a rhombohedral LSMO (-*3m*) derived from cubic phase (*m3m*) [187], in the LSMO epitaxial films studied in this work, only (100) and (010) TW orientations, perpendicular to the interface between the film and the substrate were found [43, 44]. This selection of only (100) and (010) TW orientations perpendicular to the interface is promoted by the epitaxial growth of a rhombohedral film on a cubic substrate [183].
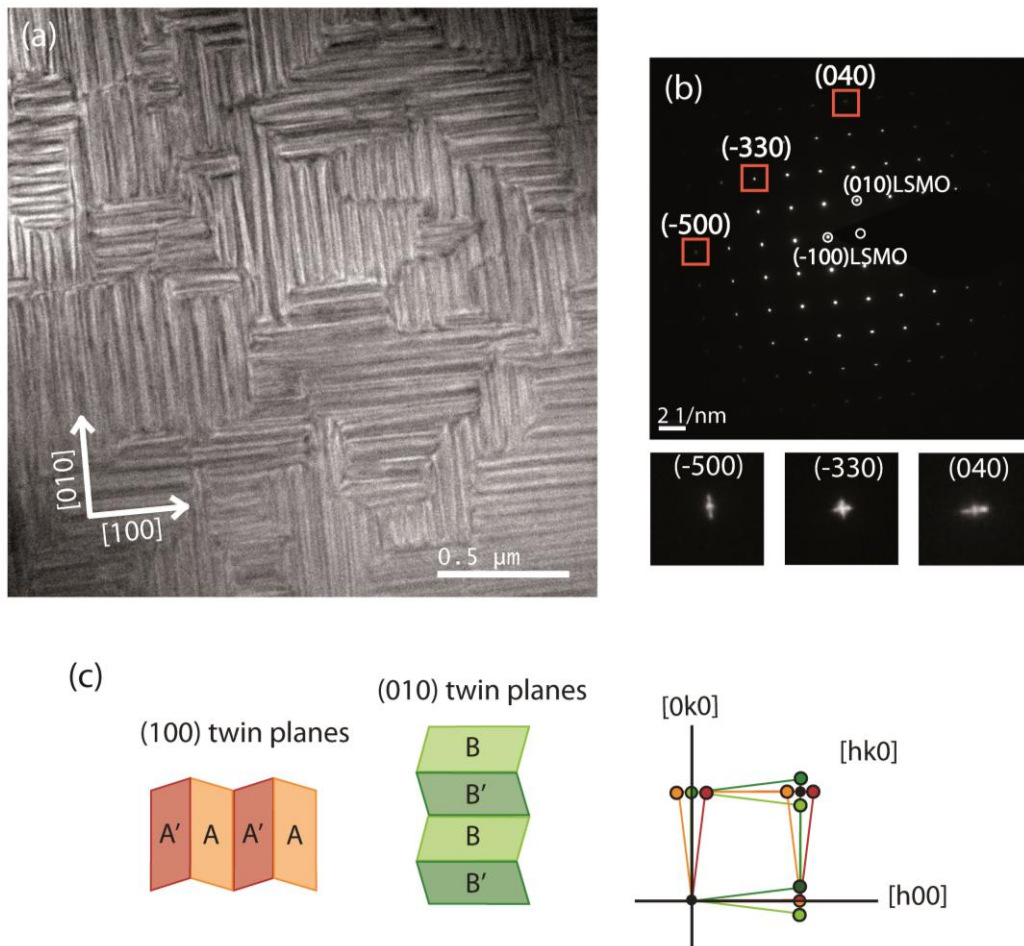

Figure 5.3: (a) Planar view low-magnification multi-beam TEM image of TDs and TWs in a 50-nm-thick LSMO film. (b) Corresponding ED pattern. The red squares mark the (040), (-330) and (-500) reflections, which are enlarged below the diffraction pattern to observe the contribution of the twin domains. (c) Schematic representation of the contribution of the twin domains in the in-plane diffraction pattern. Modified from Santiso *et al.* [44].

The presence of TDs produces a splitting of the (h00) and (0k0) reflections in the ED pattern, along the [010] and [100] directions perpendicular to the TWs, respectively. In some cases, the splitting is not clearly discerned and only an elongation can be observed, as it is shown in Figure 5.3(b). This elongation is due to the different contributing spots, and they may be distinguished at high order reflections. For example, in the (-500) reflection, it is possible to distinguish a central spot surrounded by two spots along the [010] direction. The central spot comes from the TDs separated by the (100)TW, which present a common $a*$ reciprocal direction, while the two surrounding spots come from the TDs separated by the (010)TW, where their $b*$ reciprocal axis are split along [100]. In the case of (hh0) reflections, for example the (-330) one, five spots are observed. The central spot corresponds to the substrate contribution and the four outer spots correspond to the different TDs. A schematic representation of the expected diffraction from a twinned structure along (100) and (010) is represented in Figure 5.3(c), which shows the contribution of the different TDs to the diffraction pattern.

The LSMO film in multi-beam TEM cross-section view images with different magnifications exhibit contrast bands perpendicular to the film-substrate interface as can be observed in Figure 5.4(a) and (b), indicated by orange arrows. In the case of the images presented in Figure 5.4(a) and (b) the contrast comes only from the (010) TWs between the TDs. Figure 5.4(c) shows the diffraction pattern of the film and the substrate obtained from the same cross-section sample. The high index spots in the diffraction pattern are split perpendicularly to the TWs due to the different orientations of $c*$ in adjacent domains. This effect can be observed in (003), (-203) and (203), which have been magnified to facilitate the observation, and where the splitting is marked by yellow lines.

The in-plane lattice parameter of the film (measured on a HRTEM image following the procedure described in Annex A) is fully strained, $\sim 3.910 \pm 0.009$ Å, while the out-of-plane lattice parameter, $\sim 3.88 \pm 0.02$ Å, tends to the LSMO bulk equilibrium lattice parameter. The film thicknesses studied in this work are above the pure elastically strained state of the rhombohedral structure that takes places at ~ 10 nm, where the out-of-plane lattice parameter presents a minimum of ~ 3.85 Å [43]. As the thickness increases, the out-of-plane lattice parameter of these films increases as a result of the rigid octahedral tilts. The values measured by XRD for a similar film thickness (~ 50 nm) are 3.905 Å for the in-plane lattice parameter and 3.862 Å for the out-of-plane lattice parameter [43], which agree within experimental error with those derived from HRTEM images.

In the interface region, the in-plane lattice parameter is fully strained, 3.896 ± 0.009 Å and closer to that measured in the film. In contrast, the out-of-plane lattice parameter, 3.851 ± 0.008 Å, is shortened compared with the film lattice parameter. This region at the interface with a compressed out-of-plane lattice parameter can be distinguished in HRTEM images by changes in the contrast as can be seen in Figure 5.5(a). In this image, it is possible to distinguish a bright contrast at the interface. Moreover, it is possible to observe three domains due to their change in contrast. Thus, there is a brighter central narrow domain (D_A), which ends in a wedge shape near the substrate, embedded in a larger dark domain (D_B). These domains do not reach the interface with the substrate

as can be seen in laterally compressed images presented in Figure 5.5(b). These laterally compressed images were obtained from the upper part of the film and the interface regions of the image presented in (a). The laterally compressed image corresponding to the film region (Figure 5.5(b)) magnifies the change in the tilt through the (001) planes and facilitates the localization of the TWs. In this compressed image it is possible to observe that the twin angle increases in the TWs. The twin angle is reduced as the TW gets closer to the LSMO-substrate interface, until the (100) planes of two adjacent domains have the same tilt, as can be observed in the laterally compressed image from the interface region (Figure 5.5(b)). This indicates that the TW does not reach the interface, ending ~ 2 nm above. This suggests the presence of an interface layer (IL) between the domains and the substrate as is schematically represented in Figure 5.5(c).
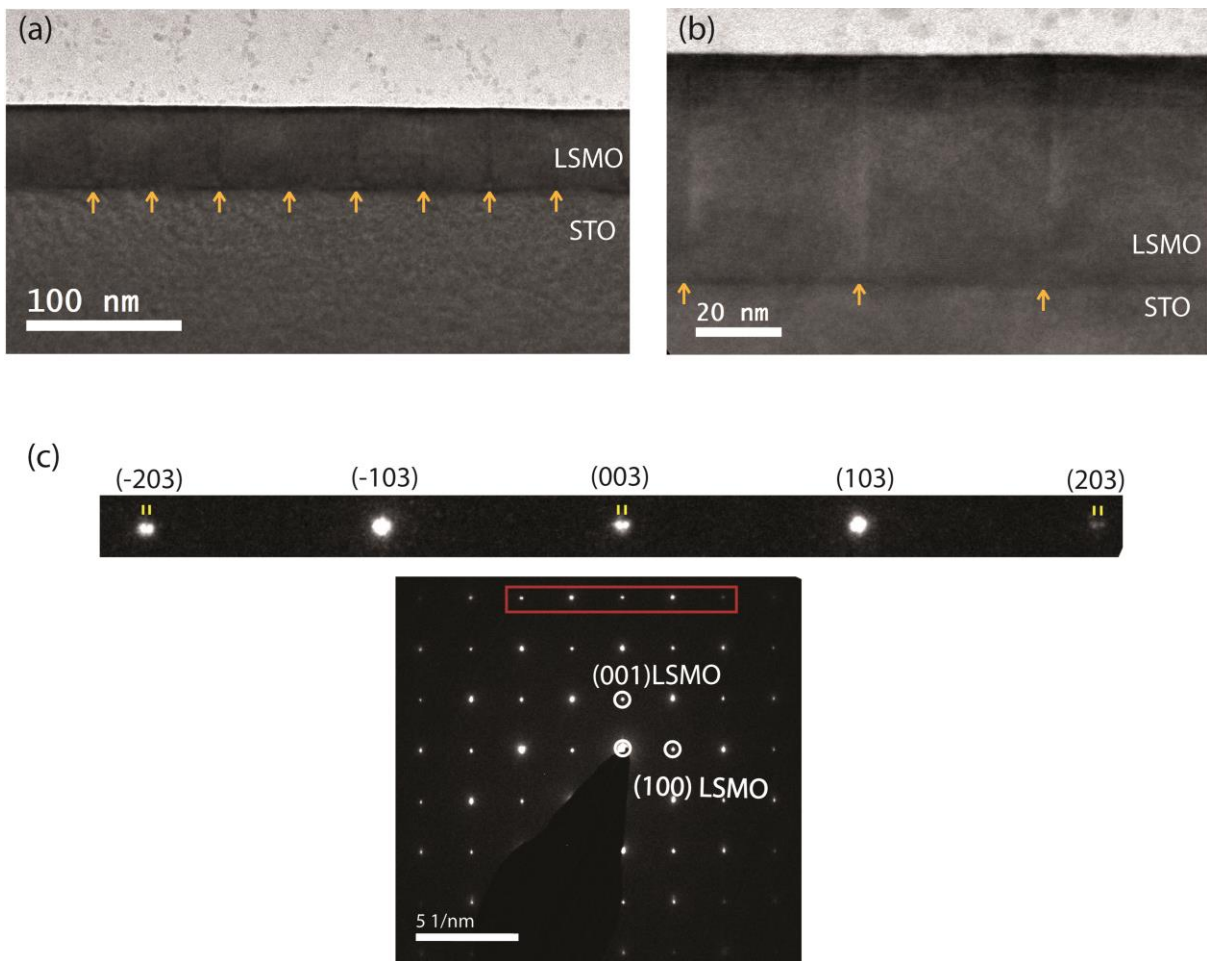

Figure 5.4: (a) and (b) low-magnification TEM cross-section images of a 50-nm-thick LSMO film. Orange arrows mark the TW. (c) ED pattern obtained from the same sample. A red rectangle marks the magnified row. The yellow lines in the magnified image show the splitting.

This short out-of-plane lattice parameter is in strong contrast with previous observations in the ultra-thin films, which exhibit an anomalously large out-of-plane lattice parameter attributed to the reduction of Mn cations to screen the polar discontinuity [43]. Although the origin of this discrepancy is unknown, it suggests a structural and/or electronic reconstruction of this layer as the film grows and it becomes buried at the interface.
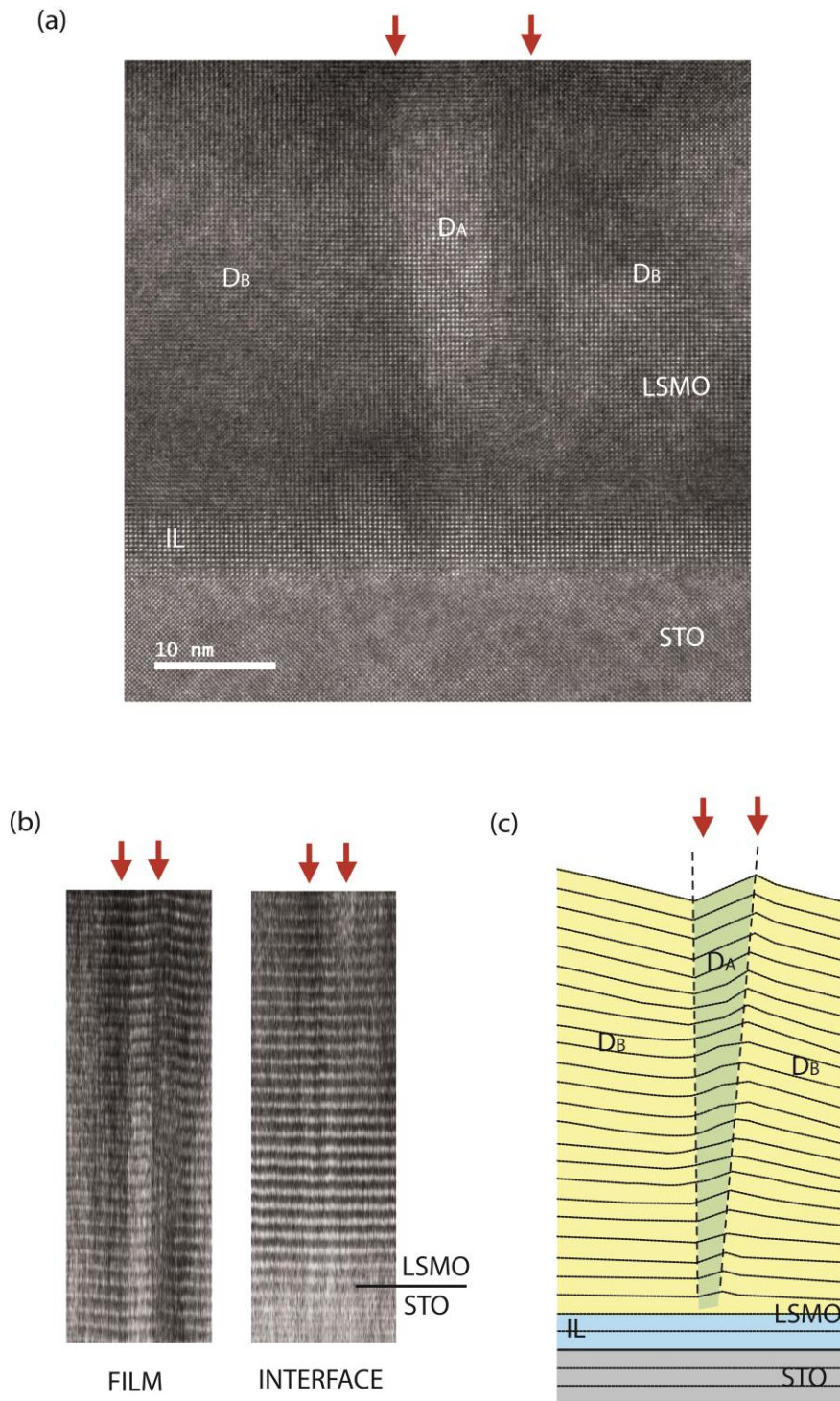
Figure 5.5: HRTEM image viewed along [010] of (a) a narrow domain (D_A) embedded in a larger domain (D_B). The TWs are marked with red arrows. (b) Laterally compressed images of the central and the interface regions of the image presented in (a). (c) Schematic representation of (a). Dark dashed lines correspond to the (100) plane. The narrow domain (D_A) is represented in green colour embedded in a larger domain (D_B) represented in yellow, separated by dark dashed vertical lines, which correspond to the TWs. The interface layer (IF) and the STO substrate are shown in blue and grey colours, respectively.

The MAADF and HAADF images obtained by aberration-corrected microscopy clearly demonstrate the presence of a different region at the interface (Figure 5.6). In the MAADF image

shown in Figure 5.6(a), it is possible to distinguish two different brighter regions. The first one, marked with red arrows, is a continuous layer through the interface, with a thickness of ~ 1.5-2 nm. The thickness of this layer agrees with the thickness of the interfacial layer observed in HRTEM images shown in Figure 5.5. The second one, marked with blue arrows, is a thicker discontinuous region, which seems to appear at the base of alternating TDs and seems therefore associated with strain or different orientations of the TDs. In the HAADF image shown in Figure 5.6(b) the contrast almost disappears, indicating that the contrast observed under MAADF conditions is mainly due to strain. However, an enhanced contrast is still observed which can be attributed to a higher average atomic number. According to the atomic numbers of La (Z = 57) and Sr (Z = 38), this enhanced contrast suggests an interface layer with a higher La/Sr ratio. Such a depletion of Sr at the interface would be in agreement with reports signalling a tendency of Sr cations to diffuse towards the film surface [198-201], although further work is required to elucidate the origin of the contrast associated to this interface.
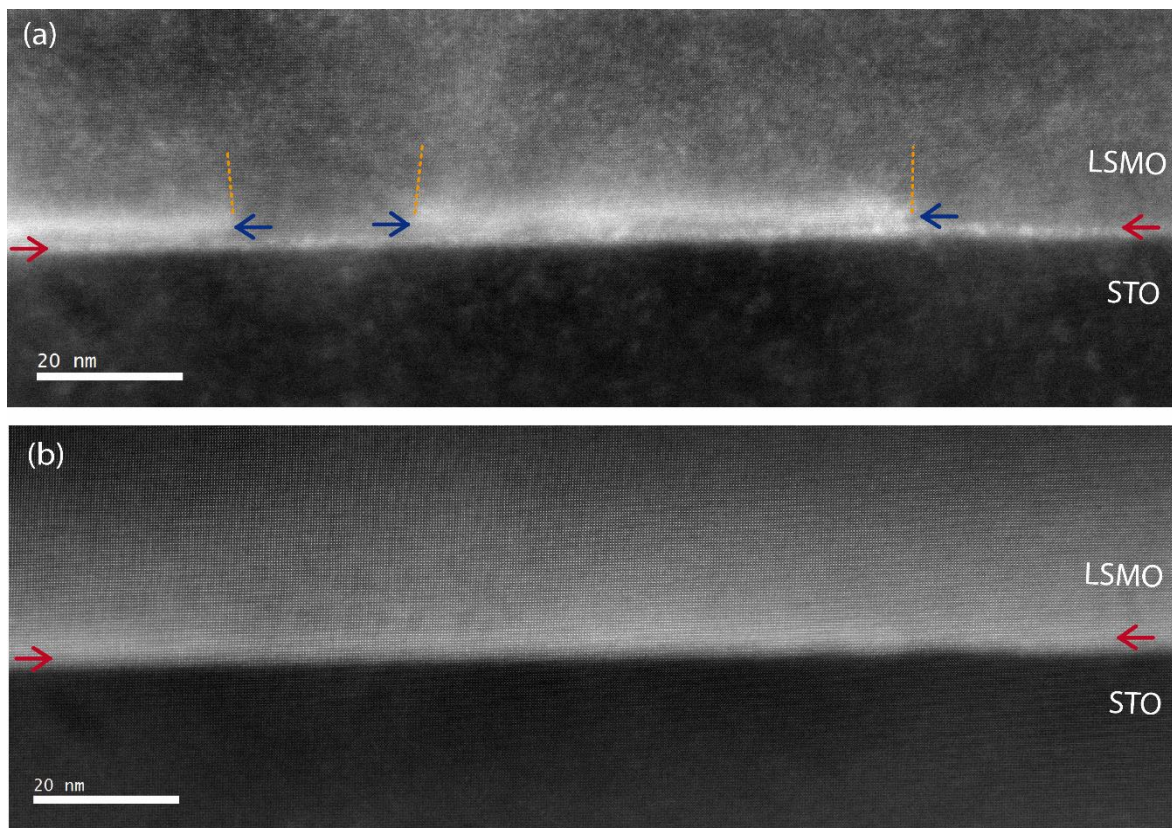

Figure 5.6: Cross-section (a) MAADF and (b) HAADF images from the same region obtained by aberration-corrected microscopy. Orange lines mark the approximate position of the TWs. Red arrows indicate a continuous interface layer and the blue arrows indicate the strain region at the base of alternating TDs.

5.4. Twin walls between LSMO twin domains

A HRTEM cross-section image of a (010) TW in a 40 nm LSMO film is presented in Figure 5.7(a). The approximate position of the vertical TW is indicated by red arrows. The TW can be distinguished in the HRTEM image due to the tilting of (001) planes. A weak change in the contrast of HRTEM image may be observed between both domains. Despite the clear contrast bands that permit to

distinguish the twin domains in low magnification TEM images, in HRTEM images, the TWs are not easy to observe.
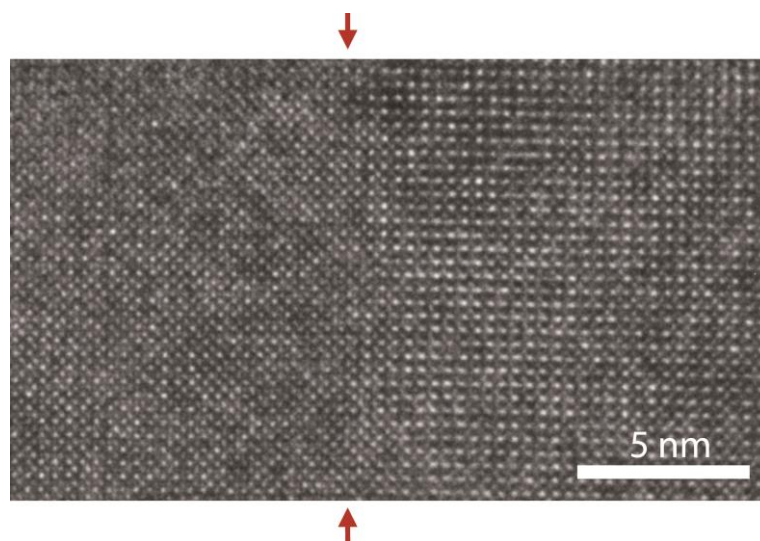

Figure 5.7: HRTEM image viewed along [010] of a TW marked with red arrows.

5.4.1.Chemical inspection of twin walls

Different chemical effects may be expected at the TW, for example a variation of La/Sr composition in the *A*-site or even the formation of a different phase, as was observed in domain walls of TbMnO$_3$ [61]. In order to inspect possible chemical changes in the TWs, firstly low magnification HAADF images were acquired (see Figure 5.8). These images do not show any contrast that permits the identification of the TWs and suggest that there are not significant chemical changes associated with it. However, a TW may be formed by only a few unit cells, and a local variation of La/Sr composition in the *A*-site or electronic changes cannot be discarded from low magnification HAADF images. A HR-HAADF analysis is necessary. However, the lack of contrast in the HAADF images makes it very difficult to find the location of the TWs in high resolution images. To facilitate the location of the TWs different camera lengths were tested to find the optimal conditions for distinguishing the TDs.

As the detector camera lengths increases, the collection angles decrease and diffraction contrast information appears in the image, becoming less incoherent [92]. Thus, HAADF gives information about the chemical composition while LAADF provides information about the strain and MAADF is an intermediate situation. Figure 5.8 shows low-magnification cross-section images from the same region of the film in HAADF, MAADF and LAADF conditions. In the HAADF images, no contrast is observed as has been previously mentioned. In the MAADF image, it is also still difficult to distinguish the twin domains. However, the LAADF image contains brighter and darker bands which may be attributed to the orientation contrast from the presence of different TD orientations. Moreover, it can be clearly seen that the contrast is further enhanced along the TWs, pointing to a localized enhancement of the strain level. Thus, the use of LAADF conditions makes possible to identify the domains and to approximately localize the position of the TWs.
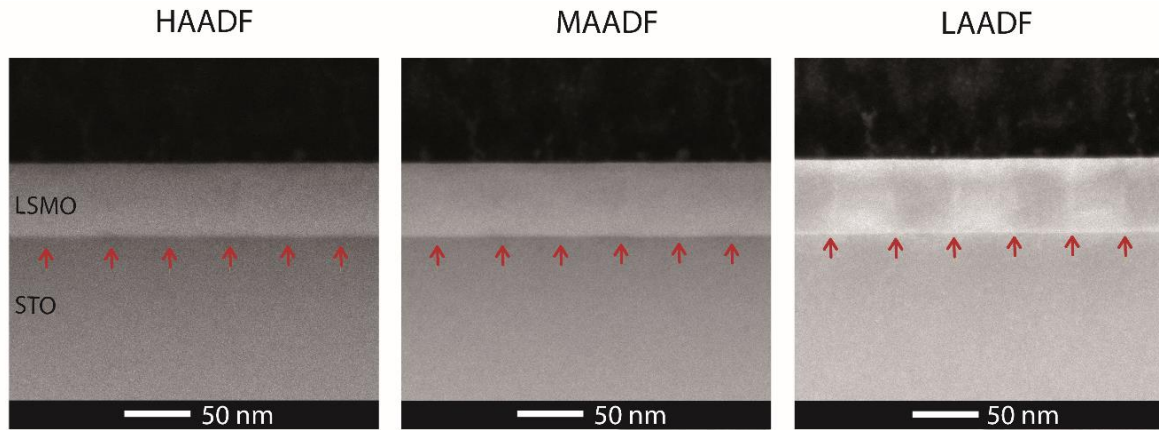
Figure 5.8: Low-magnification cross-section images from the same region of the film in HAADF, MAADF and LAADF conditions. Red arrows mark the position of the TWs.

In order to inspect in detail possible chemical changes in the TWs, a preliminary analysis with a spherical aberration-corrected microscope was performed. A HR-HAADF image of a (010)TW is shown in Figure 5.9. In this image, the influence of strain is negligible and the brightness of each atomic column is proportional to the atomic number (Z). Thus, brighter and bigger dots correspond to the La/Sr sublattice while columns of alternating Mn and O atoms are hardly visible. Even though the TW is marked by arrows in Figure 5.9(a), it is not easy to distinguish it unless the image is inspected in detail. Thus, in a magnified image from the region of the TW in Figure 5.9(b), at each side of the red arrows it is possible to observe that the planes are tilted, specifically if the image is compressed, as in Figure 5.9(c). The image does not reveal any distinctive feature associated to the position of the TW separating the two adjacent domains. This suggests that cationic antisite order is not produced at the TW and that a variation of the La/Sr ratio in the A-site, if present is not significant. Another possible effect at the TW could be a variation in the oxidation state of the Mn cation.
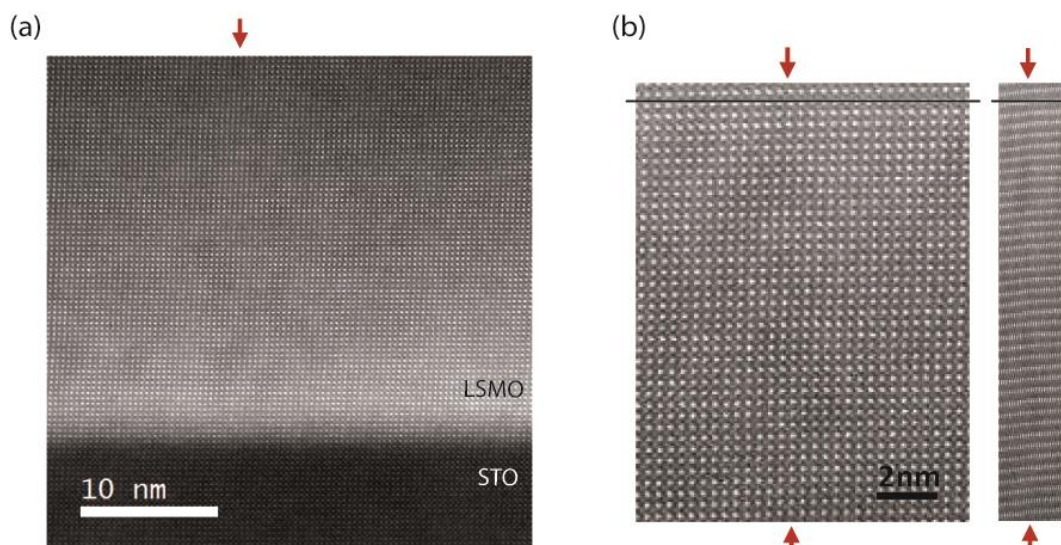

Figure 5.9: (a) Cross-section HR-HAADF image viewed along [010]. (b) Magnified view of the 010 TW. (c) Laterally compressed image. The black line is parallel to the (100) planes at the right of the TW. Red arrows mark the position of TW.

EELS-SIs were acquired to detect possible variations in the oxidation state of the Mn cation. The method applied examines the variation in the $L_{2,3}$ intensity ratio in the Mn-$L_{2,3}$ edge, which is known to range from roughly 4 in Mn^{2+} to values below 2 in Mn^{4+} [110]. Figure 5.10 shows the summed spectra obtained from regions including the TW area (red) and the two domains at each side of the TW (blue and green). No difference in the spectrum structure can be observed, neither is there any shift in the L_3 peak onset, which can also be used as a measure of oxidation state [110].
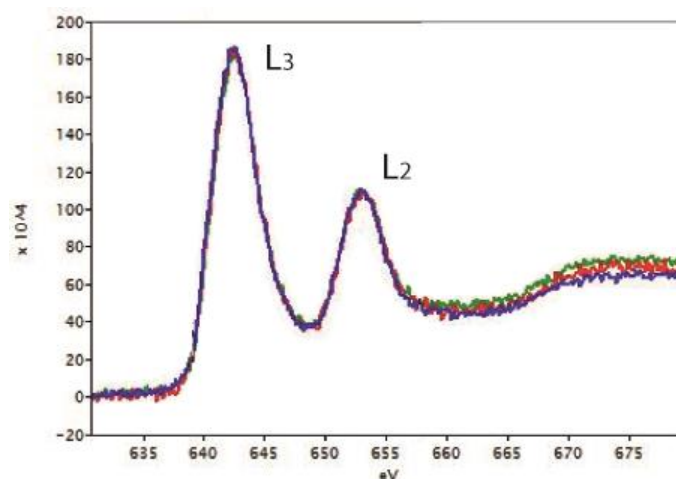

Figure 5.10: Mn-$L_{2,3}$ edges obtained from the TW in red and the TDs in blue and green.

This analysis does not reveal any variations in the oxidation state of Mn, which together with the HAADF images, suggest that there are no measurable chemical changes associated with the TW.

5.4.2. Local functional properties of twin wall regions [128]

Surface enhanced conduction at the twin walls

Figure 5.11(b) shows the current map acquired simultaneously with topography (Figure 5.11(a)) of a 40-nm-thick film. This current map reveals dark lines parallel to the [100] and [010] directions, which are superimposed on a uniform current background. Since the maps were acquired at a negative bias, darker contrast lines indicates enhanced conductivity. The separation between these conducting lines agrees with the lateral size of the twin domains expected for a 40-nm-thick film, as can be seen in the averaged current profile presented in Figure 5.11(c), suggesting that the position of the conducting lines corresponds to the TWs.

The characteristic I-V curves obtained from one TW (black line) and an adjacent TD (grey line) are shown in Figure 5.11(d). The voltage range was limited to ±1V to minimize undesired structural or chemical perturbations derived from the resistive switching effect observed in LSMO films [202]. The I-V response is linear at low voltages (see inset in Figure 5.11(d)) as expected for tunneling conducting systems.

The local mechanical response of the films was probed by FMM to check possible effects on the C-AFM measurements due to the local variations of the elastic response of the film surface leading to variations in tip-surface contact area. Topography and corresponding contact resonance

frequency images are shown in Figure 5.12 (a) and (b), respectively. The brighter lines in the contact resonance frequency images match with the underlying twin pattern and they indicate a clear positive shift of the frequency response along the TWs, indicating that the TWs are harder than the TDs. If the surface were softer in a particular position the tip would have a larger contact area reducing the contact resistance, resulting in an increased of the current. The fact that the TWs are harder would go in the opposite direction, and therefore the observed increase in the current is related to the material conductance rather than variations in the tip-surface contact area. The topography did not change during the measurement, indicating that they were performed in the elastic regime. This observation rules out any contribution of surface elasticity to the observed enhancement in conductivity.
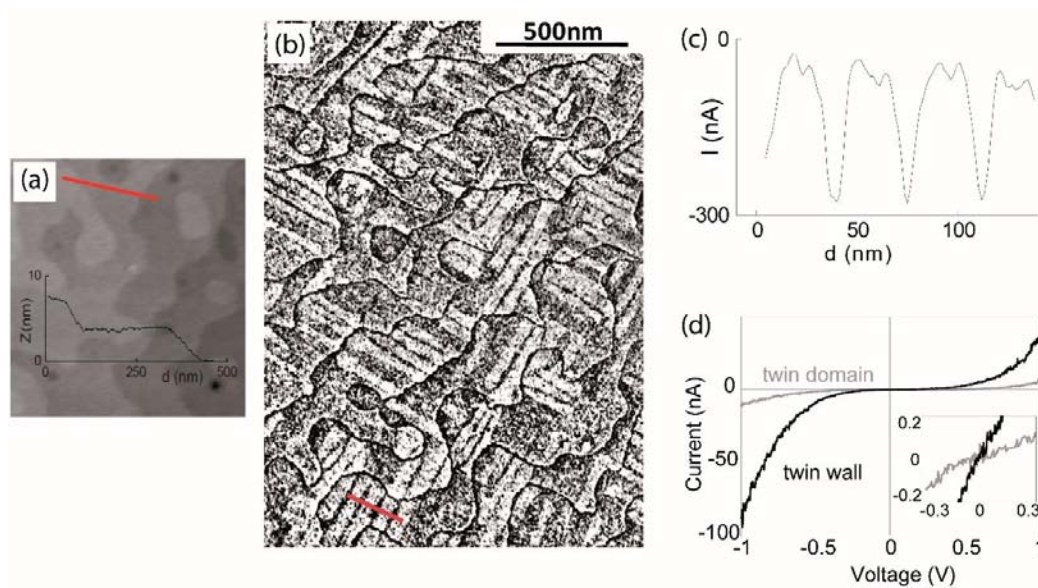

Figure 5.11: Local electrical conductivity measurements of a 40-nm-thick LSMO film. (a) AFM topographic image (profile along the red line shown as inset). (b) Current map acquired at V = −1.4V. Note that negative (dark) current values are measured for Vtip < 0. (a) and (b) are presented with the same scale. (c) Averaged current profile along the red line in (b). (d) *I-V* characteristics obtained at the TWs (black) and on the TD (gray). Each *I -V* corresponds to the average of five different measurements on the same position. In spite of the low current detected at low voltages both *I -V* curves present a linear behaviour around *V* = 0. Inset is a zoom at the linear regime. Figure modified from Balcells *et al.* [128].
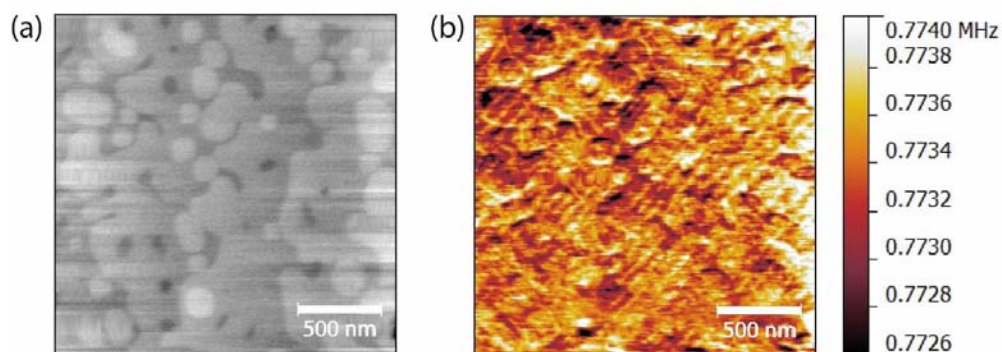

Figure 5.12: (a) Topography and (b) corresponding contact resonance frequency image. Brighter stripes in (b) are directed along the [100] and [010] directions and are attributed to the TWs. Figure from Balcells *et al.* [128].

Enhanced ferromagnetic moment at twin walls

In order to investigate the magnetic properties at the TW, magnetic force microscopy (MFM) was used. MFM images as a function of the tip-surface distance are shown in Figure 5.13. These images also show the presence of an ordered linear pattern, which matches with the underlying arrangement of TWs, superimposed on a homogeneous darker background. Figure 5.13(a) is a topographic image of the area analysed in Figure 5.13(b) through (d). As the tip-surface distance is reduced from Figure 5.13(b) to (d), the concomitant reduction in oscillation amplitude (to avoid the short range topography interactions) noticeably improves the lateral resolution of the images but deteriorates the signal to noise ratio. For higher distances the tip magnetic moment mainly interacts with the stray fields of long-range ferromagnetically ordered magnetic moments present in the bulk of the sample, resulting in a low magnetic phase contrast over blurry areas as observed in Figure 5.13(b). Superimposed on this interaction background, a series of lines running parallel to the [100] and [010] directions can be observed, that can be attributed to the signal coming from the TWs. At the working tip-sample distances shown in Figure 5.13(b) and (c), the tip stray magnetic field is too weak to disturb the intrinsic magnetic order at the TWs. When the tip-surface distance is further reduced, the TWs appear brighter than the twin domains owing to a stronger attractive tip-sample interaction. At these distances, the tip stray magnetic fields are strong enough to overcome the coercive magnetic field of the TW and align the magnetic moments during the scan. From this analysis, the magnetic configuration of the films can be described as composed of two ferromagnetic materials, one corresponding to the TDs and a second one with a larger ferromagnetic moment, corresponding to the TWs.
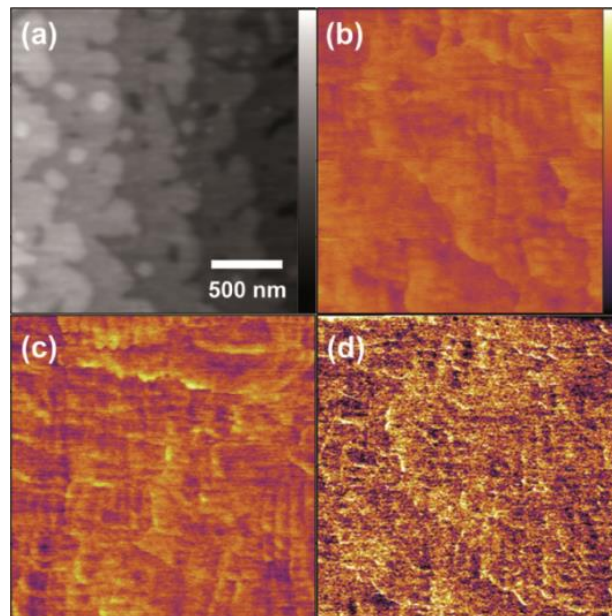
Figure 5.13: (a) Topography image of a LSMO thin film surface. The colour scale bar corresponds to a full range of 3 nm. (b) to (d) MFM phase contrast over the same area as in (a) under different conditions: (d) $h = 15$ nm and $A_{MFM}/A_{sp} = 0.9$, (c) $h = -11$ nm and $A_{MFM}/A_{sp} = 0.5$, and (d) $h = -22$ nm and $A_{MFM}/A_{sp} = 0.12$. The colour scale bar for all MFM images is shown in (d) and corresponds to a full range scale of 2.5°. In (b) and (c) the tip coercive field is smaller than the coercive field of the TWs, which accordingly appear darker than the TDs. In (d) the tip coercive field becomes larger than the coercive of the TWs, causing a contrast reversal (TWs appear brighter than the twin domains). Figure from Balcells *et al.* [128].

5.4.3.Strain state of twin walls [128]

In order to understand the origin of these magnetic and electrical conductivity modifications, the strain state of the TWs was investigated by aberration corrected HRTEM images in planar view. Figure 5.14(a) shows a filtered HRTEM image of a (100)TW. The TW is recognized through the tilt of the (010) planes, which correspond to the twin angle, $\Omega = 2(\alpha_{pc} - 90°) \sim 0.8°$, where α_{pc} is the pseudocubic interaxial angle. However, the laterally compressed image shown in Figure 5.14(b) reveals an increase of this angle in the middle of the TW as is shown in the schematic representation of Figure 5.14(c).
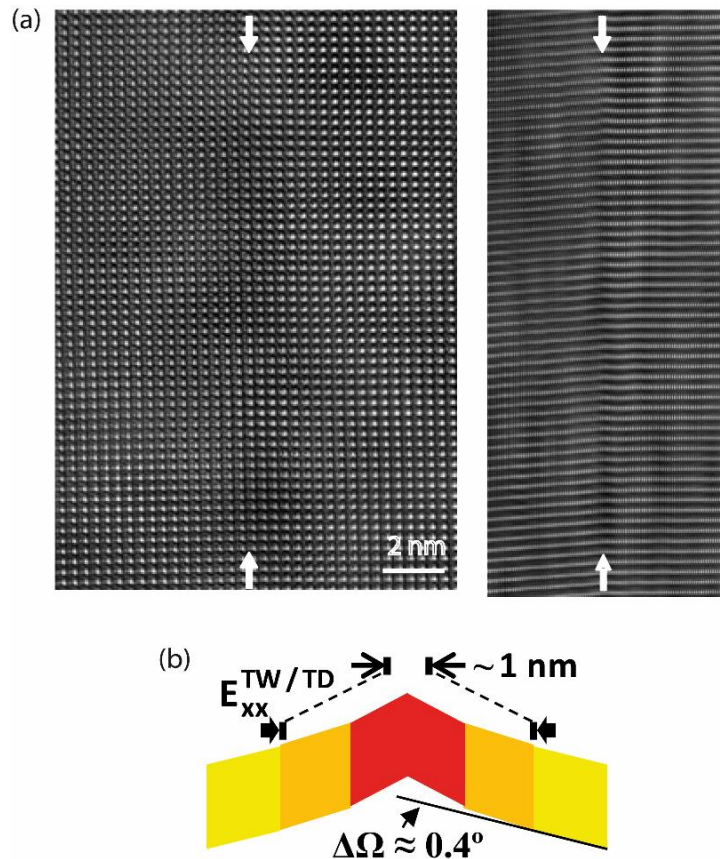

Figure 5.14: (a) Planar view HRTEM image of a (100) TW (indicated with vertical arrows) viewed along the [001] axis, of a 40-nm-thick film. Right panel: Compressed image to emphasize the increase of twin angle in the TW. (c) Schematic drawing illustrating the distortion of the structure in the TW.

This increment of the twin angle may be quantified in the rotation map, as shown in Figure 5.15(a). This map was computed from GPA [83, 85], taking the (010) and (100) phases. The right domain was used as a reference to perform the strain maps. The rotation map clearly shows a discontinuous ridge corresponding to an increase in the twin angle up to $\sim 1.5°$ within a ~ 1-nm-thick region centred at the TW. Moreover, the corresponding map of the $\mathcal{E}_{xx}$ linear strain component perpendicular to the TW, Figure 5.15 (b), also reveals a ~ 1-nm-thick region centred at the TWs which is submitted to a severe compressive strain of $\mathcal{E}_{xx}^{TW/TD} = -3.5\%$, relative to the TD. The compression at the TW is consistent with the increased hardness observed by FMM.
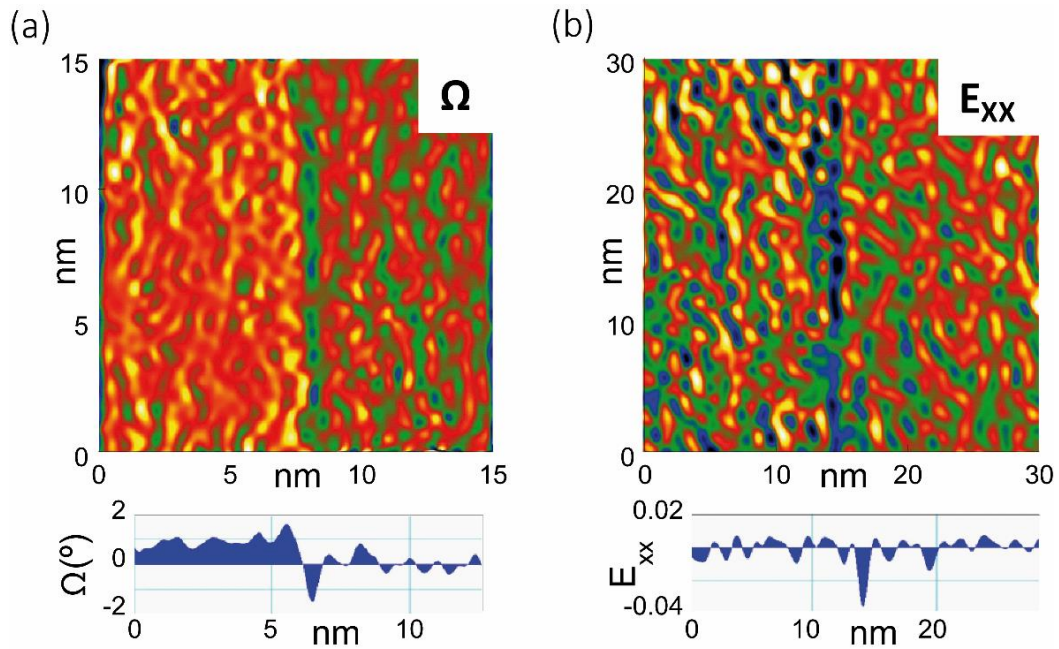
(a)

(b)

Figure 5.15: (a) and (b) show the corresponding twin angle and $\varepsilon_{xx}^{TW/TD}$ maps, along with their averaged profiles, as obtained by GPA analysis. $\varepsilon_{xx}^{TW/TD}$ is the strain component perpendicular to the TW, relative to the TD.

Considering the TW with respect to the fully in-plane strained TDs, with a misfit $\varepsilon_{xx} \sim + 0.6\%$ with respect to the substrate [43], the effective compression relative to the bulk LSMO phase is $\sim - 2.9\%$. Thus, the twined film can be viewed as a self-organized nanostructure consisting of 1-nm-thick sheets of strongly compressed LSMO (−2.9%) embedded in a matrix of tensile strained LSMO, as illustrated schematically in Figure 5.16. As previously mentioned, the TD size of these films depends of the thickness of the film, S(h), following the dependence $h^{1/2}$. Thus, through an appropriate selection of the thickness film it is possible to obtain a self-organized nanostructure with control over the width of TDs between thin sheets of strongly compressed LSMO at the TWs.
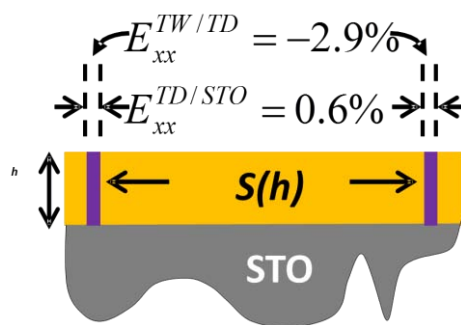
Figure 5.16: Schematic drawing of the twinned film viewed as a self-organized composite material.

This compressed region at the TW is a result of the distortion of the octahedral framework. The TW region may be described as a combination of rigid BO_6 octahedral rotations about the *pseudo*cubic unit cell axes, α (or equivalently <Mn-O-Mn> bond angle distortions, $\delta\Theta$) and an elastic stretching/compression of the B-O bonds, $\delta d.$ These distortion mechanisms are illustrated in the Figure 5.17.
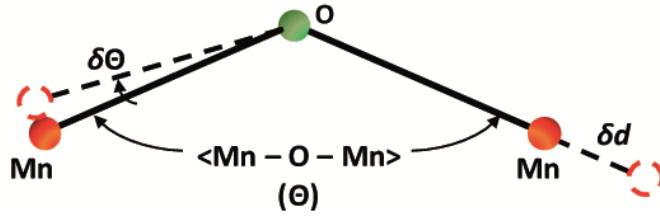
Figure 5.17: Illustration of the distortion mechanisms of the octahedral framework: octahedral tilting distortion of the <Mn-O-Mn> bond angle by $\delta\Theta$ and distortion of the MnO$_6$ octahedra results in the elastic stretching or compression (δd) of the Mn-O bond.

In order to understand the strain state of the TW, the connection between the overall shear distorion, $\emptyset$, and the rigid octahedral tilts about the *pseudo*cubic unit cell axes, α, following geometrical formalisms derived for rhombohedral perovskites, can be expressed as [203]:

$$\alpha = \sin^{-1} \sqrt{(3\cos\alpha_{pc}/1\text{-}2\cos\alpha_{pc})\,/\sqrt[3]{3}} \qquad \text{(Eq. 5.1)}$$

where $\alpha_{pc} = (\Omega + \pi)/2$. Ω is the twin angle and is described by two times the shear angle, $\Omega = 2\emptyset$. The octahedral tilt inside the TW derived from this approximation is thus $\alpha_{TW} = 7.55°$, larger than the bulk value, $\alpha = 5.2°$ (as calculated from <Mn-O-Mn> = 165.24° [204]). The amount of strain accommodated by rigid octahedral tilts is only $\Delta a/a_{TD} = \cos^2\Delta\alpha - 1 = -0.0014$. Therefore, most of the compression is driven by a severe shortening of the Mn - O bonds of ~ - 2.7%.

The influence of strain in the band width (W) of ABO_3 perovskite compounds is mediated through the relative modifications induced in the <Mn-O-Mn> bond angle and the Mn-O bond length, which control the overlap integrals between the Mn *3d* and the O *2p* orbitals. This double dependence is described by the empirical formula [205]:

$$W \propto \frac{\cos\varphi}{d_{Mn-O}^{3.5}} \qquad \text{(Eq. 5.2)}$$

where φ is the "tilt" angle given by

$$\varphi = \frac{1}{2}\ (\pi\text{-<Mn-O-Mn>}) = \frac{2\alpha}{\sqrt{2}} \qquad \text{(Eq. 5.3)}$$

In the bulk LSMO structure: <Mn-O-Mn> = 165.24° (φ = 7.38°, α = 5.2°) and d_{Mn-O}= 1.964 Å [204]. Thus, combining (Eq. 5.2) and (Eq. 5.3) gives $\frac{\cos\varphi}{d_{Mn-O}^{3.5}}$ = 0.0934. In the TW, the calculated value α_{TW} = 7.5° corresponds to φ_{TW} = 10.68° (the <Mn-O-Mn> bond angle decreases to 158.64°). The distortion of the octahedral framework in the TW is thus described by $\delta\Theta/\Theta$ = - 0.040 and $\delta d/d$ = - 0.027, yielding $\frac{\cos\varphi}{d_{Mn-O}^{3.5}}$ = 0.1019.

Therefore, despite the stronger angular distortion, the balance between $\delta\Theta/\Theta$ and $\delta d/d$ results in a broadening of the bandwidth inside the TW, thus explaining the observed enhancement in conductivity. It is worth mentioning that even smaller variations of the $\frac{\cos\varphi}{d_{Mn-O}^{3.5}}$ ratio, induced in bulk

manganite by cationic substitutions at the *A*-site, cause huge variations in T_C of about 200 K [178]. This behaviour is also consistent with theoretical work showing that compressive strains in half-doped manganite epitaxial films promote an increase of T_C [206]. A similar competition between Mn-O shortening and <Mn-O-Mn> bond angle variations has been used to explain a *Tc* increase in LSMO under hydrostatic pressure [207].

5.5.Conclusions

TWs between the twin domains in LSMO films grown under tensile stress have been characterized by different transmission electron microscopy techniques. The twin domains can be distinguished in low-magnification TEM and STEM (MAADF-LAADF), due to the contrast changes in the images induced by the different orientation domains. The TWs are identified by the tilt change through the (100) or (010) planes in high resolution TEM and STEM. However, the small twin tilt angle and the weak (in HRTEM) or non-existent (in HRSTEM) contrast changes in these high resolution images make the identification of the TW difficult.

An increase of the twin angle was found at the TW. In cases where a twin domain was observed to disappear towards the substrate, the tilt angle is observed to decrease gradually. The TW does not reach the interface, but ends at an interfacial layer which very likely exhibits a different crystal structure. The contrast in the HAADF suggests a possible depletion of Sr and LAADF indicates a strain state.

The strain analysis of the TWs reveals that the TW is a compressed region in a biaxially tensile strained LSMO matrix. An enhancement of the electrical conductivity and the strengthening of the magnetic interactions at the TW region of the film is correlated with the compressive strain state. Thus, a film formed by twin domains can be viewed as a self-organized nanostructure consisting of 1-nm- thick sheets of strongly compressed material embedded in a matrix of tensile strained LSMO.

Chapter 6

Misfit relaxation mechanism in $La_{0.7}Sr_{0.3}MnO_3$ films grown under compressive stress:

Atomic and chemical structure of dislocation cores and surface patterning by associated strain fields

6.1. Introduction

The most common strain relaxation mechanism in lattice mismatched heterostructures is the formation of misfit dislocation (MD) arrays at the interface. This relaxation mechanism is described in the classical model by Frank and van der Merwe [36] and Matthews-Blakeslee [37], who report that the films grow pseudomorphically with a substrate (via elastic deformation) below a certain critical thickness. Above this critical thickness, the film usually releases the accumulated strain energy by the generation of MDs (via plastic deformation), which progressively accommodate the strain toward the equilibrium bulk structure [208]. MD arrays in perovskite oxide heterostructures have been reported recently, for example in $SrRuO_3/SrTiO_3(100)$ [209], $(Ca_{1-x}Sr_x)(Zr_{1-x}Ru_x)O_3/SrRuO_3/SrTiO_3(100)$ [210], $La_{0.5}Ca_{0.5}MnO_3/SrTiO_3(100)$ [211], $BaTiO_3/SrTiO_3(100)$ [212], $PrScO3/SrTiO3$ [213] and $La_{0.7}Sr_{0.3}MnO_3/LaAlO_3(001)$ [214].

A semi-coherent interface results from the presence of MDs exhibiting two well differentiated regions separated by a transition zone. The first region corresponds to the dislocation core, which may be considered as a different phase due to the reconstruction of bonds and atomic coordination's [215, 216]. Recent examples of this are the 5-fold coordinated Fe^{2+} in dislocation cores in $BiFeO_3$ on $SrRuO_3$ due to the removal of one O column [216], which is also reported in oxygen deficient dislocation cores in $SrTiO_3$ [217, 218], or the formation of fcc TiO_2 phase, consisting of edge-sharing TiO_6 octahedra, at the tension region of the dislocation core of $SrTiO_3$ [219]. Furthermore, a segregation of a particular element around the dislocation core may be produced due to the strain, which is the case of the Pb segregation, together with an oxygen deficiency, ~ 1 nm around dislocation cores at the interface between $PbZr_{0.52}Ti_{0.48}O_3$ and $SrRuO_3$ [62]. The second region corresponds to the region between the dislocations where the film is strained with respect to the original bulk structure. This region is described by the long-range strain field of the dislocations,

which are key for the realization of periodic functional bulk and surface patterns due to the strong sensitivity of the electronic structure to strain.

MDs play an interesting role in oxides because they can form self-organized patterns at the nanometre scale, in which the dislocation core and the surrounding area can behave differently from bulk material [217, 218, 220, 221]. Commonly, misfit dislocations arrange in a regular square network. A homogenous dislocation nucleation process, high dislocation mobility within the interface, and effective repulsive forces generated between misfit dislocations induce their self-arrangement [222]. Moreover, the overlapping of strain fields from individual dislocations causes lateral modulations of lattice distortions, which may extend up to the free surface and modulate the physical properties of thin films. In addition, the strain field from misfit dislocations forms a strain pattern which may promote the growth of ordered nanostructures on the film surface and may be used as a nanotemplate. In this direction, MDs have been used to produce strain guided patterned surfaces in semiconductor [223, 224] and metal[23] systems. However, the extension of this concept to oxide epitaxy remains unexplored.

In this chapter, microstructure, interface and defects present in $La_{0.7}Sr_{0.3}MnO_3$ (LSMO) ultrathin films grown on (100)$LaAlO_3$ (LAO) substrates are studied. A detailed study of structural, chemical and electronic changes associated with the core of edge dislocation at the interfaces between LSMO film and the LAO substrate is also performed. The progressive self-organization of the MD network occurring during the epitaxial growth of these films and the evolutions of parameters is also investigated. Special attention is paid to ultrathin films of only a few (3.5 and 6) nanometres thick where the strain field of the dislocations affects surface topography and current distribution.

6.2. Experimental methods

The LSMO thin films, with thicknesses of 2, 3.5, 6 and 14 nm, were epitaxially grown on (001)-oriented LAO substrates (from Crystec. GmbH) by magnetron sputtering, as described in Konstantinovic *et al.* [124]

OC-SEM images were obtained in order to determine dislocation densities over large areas. The overall film structure and the ordering of the MD network were analysed by XRD.

The effects of the formation of MDs on the surface morphology were examined by AFM in tapping mode. Local electrical conductivity maps were measured by C-AFM. The lateral resolution of the technique is, in principle, limited by the tip radius of ~ 10 - 20 nm. In the employed set-up, the sample was grounded and the voltage was applied to the tip. An external *I-V* converter (Stanford Research Systems) was used to provide access to a wide range of compliance currents (1pA to 1mA).

Planar view and cross-section TEM samples were prepared by conventional cutting, gluing and grinding procedures, followed by an Ar milling step down to electron transparency and perforation, using a PIPS at a small incidence angle. Low-magnification TEM images, HRTEM images, diffraction contrast images, ED and STEM (HAADF and LAADF) images of samples in planar view were obtained

by using a 200 kV FEI Tecnai F20 S/TEM electron microscope. The HAADF and LAADF images were obtained using camera lengths of 70 mm and 490 mm, respectively. HRTEM images of cross-section samples were obtained using a 200 kV FEI Tecnai F20 S/TEM electron microscope and a 200 kV Cs-corrected FEI Tecnai F20 SACTEM electron microscope. HRTEM images were used to obtain strain component maps by GPA [83]. For HRTEM images obtained with Cs-corrected microscope, camera distortions were corrected for the GPA analysis. STEM combined with EDS was performed using a 200 kV FEI Tecnai F20 S/TEM electron microscope with a convergence semi-angle of 17.1 mrad.

HAADF combined with spectroscopic analyses of cross-section samples were performed in the image-corrected FEI Titan^{3}™ G2 60-300 operating at 300 kV, equipped with a Super-X four quadrant detector and a Gatan Quantum dual EELS spectrometer. HAADF images and dual EELS-SI of cross-section samples were acquired with a probe convergence angle of 10.12 mrad. The EELS data were acquired using a 15.64 mrad collection angle. The EELS spectrometer was vertically binned by 130x to improve the readout speed. Dual EELS-SI (spectra-per-pixel) were acquired by scanning the beam over areas which contained a single dislocation and areas in the interface between the dislocations. The zero-loss and core-loss, from 500 eV to 900 eV, were acquired for every pixel compensating for the intensity difference between them. The core-loss acquisition time per pixel was 0.5 s and for the low-loss spectrum it was 0.001 s. A dispersion of 0.25 eV per channel was used. Spatial drift correction was applied in order to minimize drift effects. The energy resolution measured as the full width at half-maximum of the zero-loss peak through the sample was ~ 1.75 eV. HAADF images and EDS mapping of cross-section samples were acquired with a probe convergence angle of 10.12 mrad and an annular detector inner radius of 138 mrad. EDS spectral mapping data were acquired by scanning the beam over areas which contained a single dislocation and areas in the interface between the dislocations.

Moreover, HAADF imaging was performed by using the probe-corrected FEI Titan^{3}™ 80-300 operating at 300 kV. The images of cross-section samples were acquired with a probe convergence angle of 10.98 mrad and an annular detector inner radius of 69.08 mrad.

6.3. Misfit dislocations in La$_{0.7}$Sr$_{0.3}$MnO$_3$

LSMO presents a unit cell parameter of 3.881 Å, a_f, [178] and it grows under a compressive stress on a LAO substrate, which has a parameter of 3.79 Å, a_s. Thus, the misfit strain is given by:

$$\varepsilon = \frac{a_s - a_f}{a_f} = \frac{3.790\ \text{Å} - 3.881\ \text{Å}}{3.881\ \text{Å}} = -0.023 \qquad \text{(Eq. 6.1)}$$

The OC-SEM image in Figure 6.1(a) shows a clear contrast forming a crossed pattern of parallel lines following the [100] and [010] directions. Due to the low film roughness, as can be observed in the AFM image presented in Figure 6.1(b), and to the use of backscattered electron detector, the contrast in the OC-SEM image is related to crystallographic defects or the strain field [119]. Thus, these lines are related to the presence of MDs at the interface, suggesting that the misfit strain

between the LSMO and LAO is partially relieved by the formation of the MDs. However, the MDs are not present in all the film thicknesses.
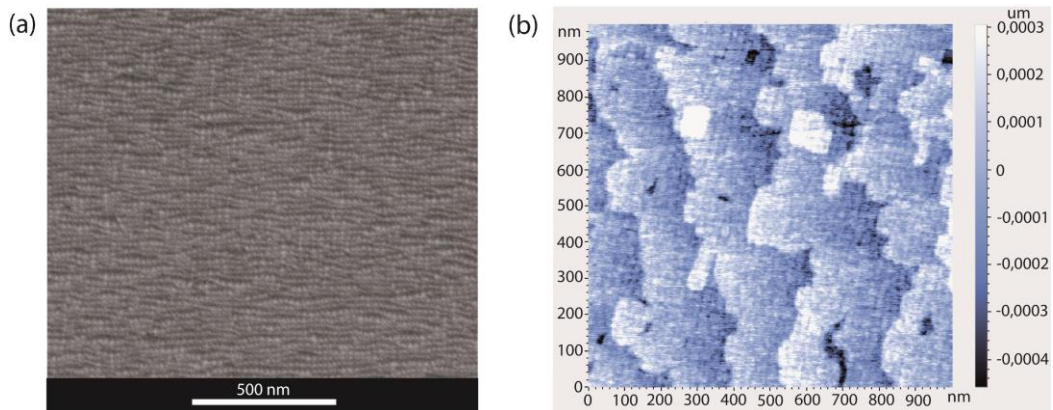

Figure 6.1: (a) SEM and (b) AFM images of a 6-nm-thick film defining a crossed pattern contrast following the directions [100] and [010]. Figure modified from Santiso *et al.* [225].

The presence of dislocations was corroborated by HRTEM images. In the HRTEM images of a cross-section view of a 2-nm-thick film shown in Figure 6.2 (a), it is possible to observe that the film is dislocation free and coherent with the substrate. On the other hand, HRTEM images of cross-section views of 3.5, 6 and 14-nm-thick films exhibit a dislocated interface, as can be observed in the HRTEM image of the thicker film shown in in Figure 6.2(a). The position of the dislocations is marked by orange arrow.
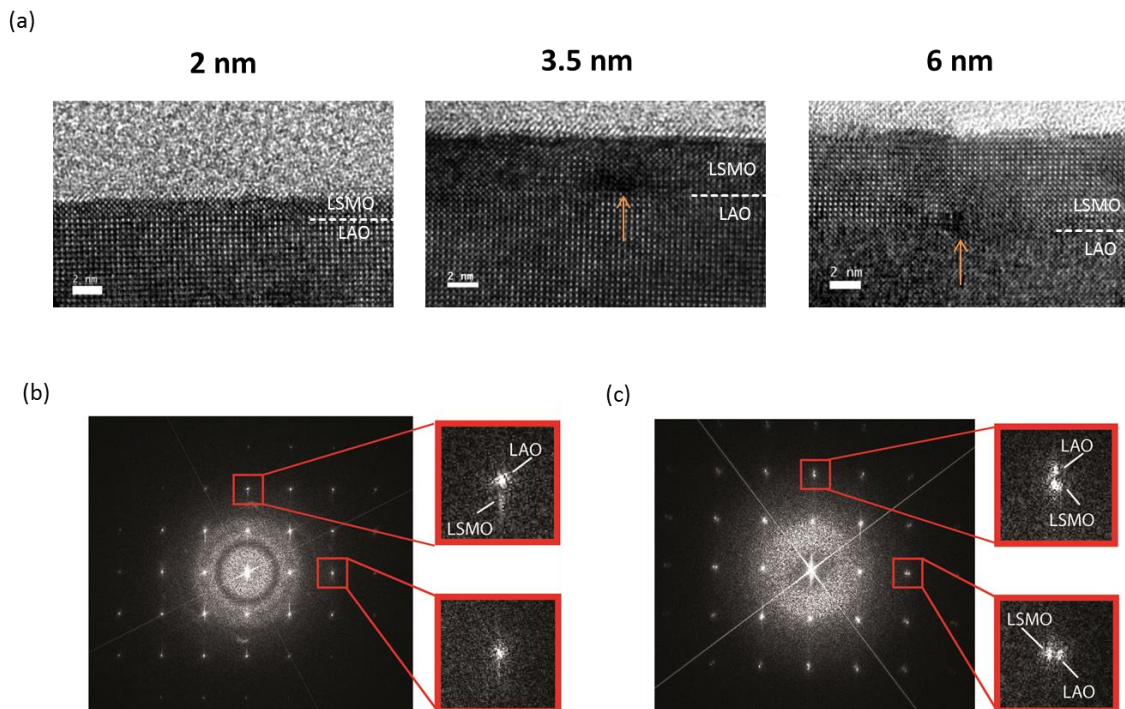

Figure 6.2: (a) HRTEM images in cross-section view along [010] direction of 2, 3.5 and 6-nm-thick films. (b) FFT obtained from a HRTEM image of 2-nm-thick film and (c) FFT obtained from a HRTEM image of 14-nm-thick film. The red squares in the FFT mark the enlarged spots shown in the inset.

Figure 6.2 (b) shows a FFT of a HRTEM image of the 2-nm-thick film. The FFT only shows single spots in [100]* direction, corresponding to the in-plane lattice parameters. Nevertheless, it shows an elongation of the spots in the [001]* direction suggesting the presence of a different out-of-plane lattice parameter. In contrast, the corresponding FFT of a 14-nm-thick film image shows a radial splitting of the spots as expected for a relaxed film (Figure 6.2 (c)). In the case of intermediate films (3.5 nm and 6 nm) the radial splitting is not so evident and the FFT suggest that the films are partially relaxed. The relaxations state of the different films is confirmed by the in-plane and out-of-plane unit cell parameters analysed by XRD. Figure 6.3 shows the evolution of in-plane and out-of-plane lattice parameters as a function of the film thickness. In the thinnest films (2 nm thick), the in-plane lattice parameters are coherent with those of the substrate, while the out-of-plane lattice parameter is expanded, as is expected for an elastic response of the film to an in-plane compression. Above this thickness, in the 3-nm-thick film, dislocations are formed and the parameters start to relax towards the bulk LSMO parameters, as shown in Figure 6.3.
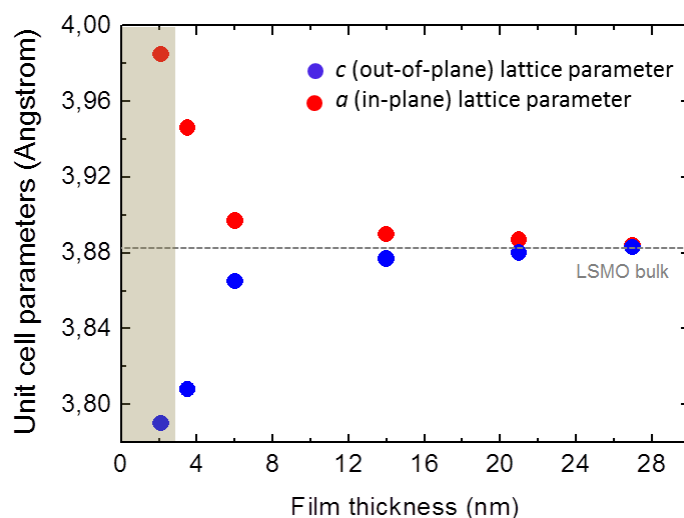

Figure 6.3: Evolution of in-plane and out-of-plane lattice-parameters in function of thickness measured by XRD. Courtesy of Dr. J. Santiso.

The presence of MDs produce a complex contrast pattern in multi-beam low-magnification TEM images, as can be observed in Figure 6.4(a). In this image it is possible to distinguish dark fringes forming a crossed pattern. In the centre of this grid formed by the dark fringes there are four bright areas, which are still observed in the HRTEM image presented in Figure 6.4 (b), related to the strain field produced by MDs. Despite the strong strains associated with the dislocations, the HRTEM image shows high crystal quality in a perfect atomic column arrangement.

This complex contrast is observed particularly in 6 and 14-nm-thick films. Despite the complexity in analysing and explaining the origin of this contrast, due to the contribution of more than one beam in the image, one possible explanation could be that the complex contrast pattern corresponds to Moiré fringes. If the (100) lattice planes of the LSMO and LAO are considered, taking into account their lattice parameters, 3.881 Å and 3.79 Å, respectively, the spacing of the translational Moiré fringes would be ~ 16 nm. However, in the case of the 6-nm-thick film the

spacing measured by the dark fringes in the image in Figure 6.4(a) is ~ 20 nm. This suggests that the in-plane lattice parameter of the LSMO is not fully relaxed. If the experimental LSMO lattice parameter, 3.865 Å, measured by XRD for the 6-nm-thick film is considered, the resulting translational Morié fringe spacing is ~ 19,5 nm, which is closer to the experimental measured value.
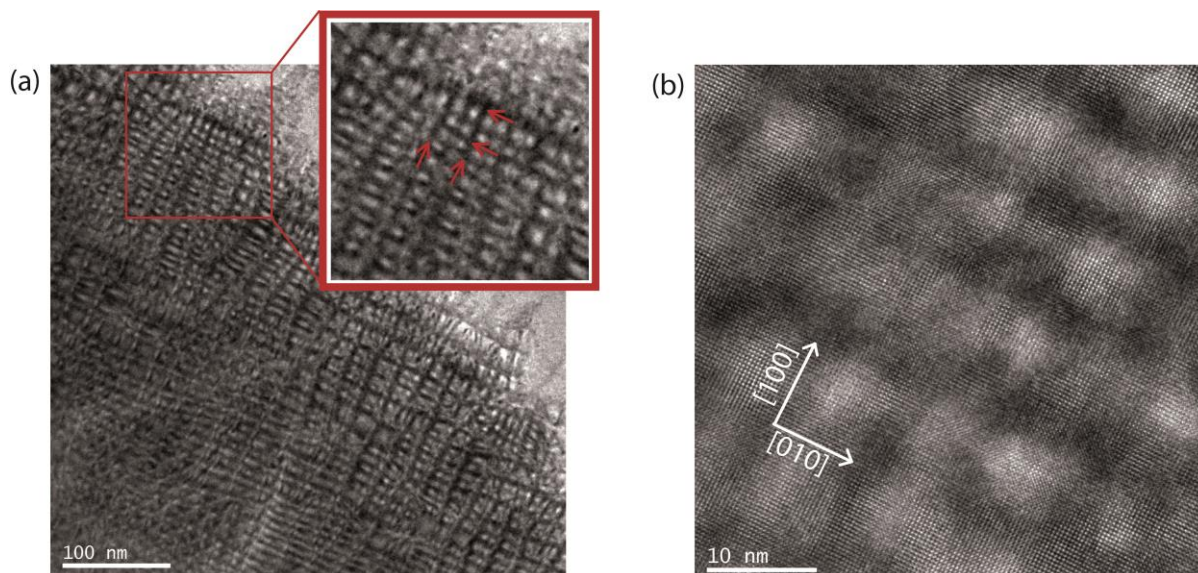
Figure 6.4: Planar view (a) multi-beam bright-field low-magnification TEM image, and (b) HRTEM image from a 6-nm-thick LSMO film, viewed along [001] direction. In (a), red arrows mark the dark lines forming a crossed pattern, corresponding to the MDs.

If the fringes obtained from the perpendicular set of (010) planes are superimposed on the fringes obtained by set of (100) planes, as represented in Figure 6.5, this results in the network contrast pattern as that is observed in the TEM image shown in Figure 6.4. However, the four bright areas still remain unexplained suggesting a more complex situation.
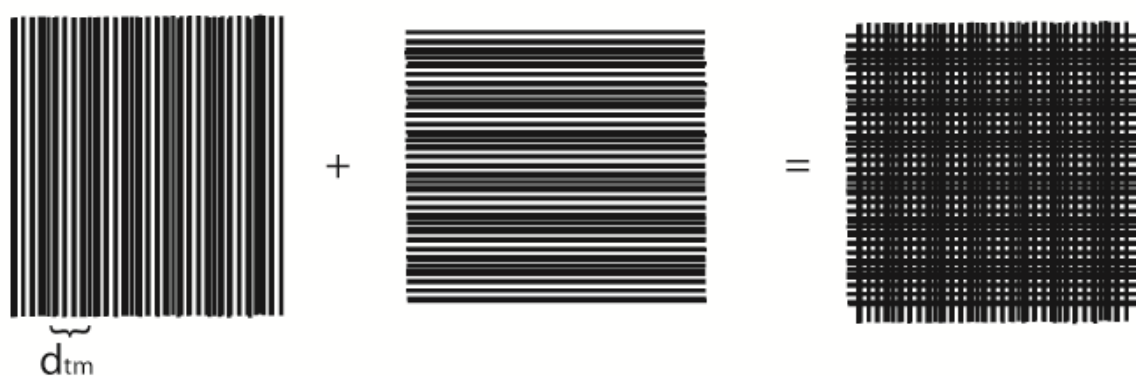
Figure 6.5: Schematic representation of the Moiré pattern obtained by superimposition of two orientations of translation Moiré fringes.

The planar view HAADF images show bright lines, probably related to the presence of dislocation lines, as shown in Figure 6.6. The spacing of the lines agrees with those measured by SEM images, thus these lines probably correspond to the position of the dislocations lines. These bright lines may indicate that these areas are thicker or have a different composition with respect to the

darker areas, or that there are some contributions from the dislocation strain fields. As these films present a low roughness surface, possible changes in thickness could be a result of inhomogeneous milling during TEM sample preparation, which was discarded by SEM analysis (Annex B). In order to determine whether this contrast is related to a chemical modification or to the dislocations strain field, EDS and EELS chemical microanalysis were performed on planar view and cross-section specimens of 6-nm-thick films. The pixel size of the EDS maps and line profiles was ~ 1 nm, while the acquisition time was ~ 1s per pixel for the maps and between 10s and 30s for the profile. The La-*L*, Sr-*K*, Mn-*K*, O-*K* and Al-*K* line energies were used to perform the elemental count maps and the line profiles. These maps did not show variations of the element concentrations above the noise of the spectrum. Therefore, this suggests that if there are some variations related to the presence of dislocations, they are smaller and/or located in very small regions closer to the dislocation core. Thus, the contrast variations are attributed to strain associated with dislocations.
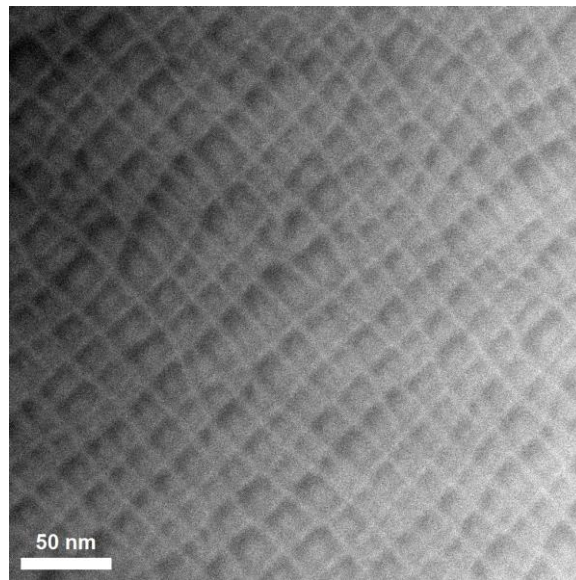
Figure 6.6: A HADDF image of 6-nm-thick film.

6.4. Dislocation core structure and its vicinity

A dislocation is characterized by its dislocation line ($\boldsymbol{u}$) and Burgers vector ($\boldsymbol{b}$). The relation between the line and the Burgers vector describes the geometry of the dislocation. Thus, an edge dislocation is described by a $\boldsymbol{b}$ normal to $\boldsymbol{u}$, while a screw dislocation by a $\boldsymbol{b}$ parallel to $\boldsymbol{u}$.

The Burgers vector can be determined by drawing a Burgers circuit around the dislocation core. Figure 6.7 shows an image of a dislocation core in a 6-nm-thick film viewed along the [010] direction. The dislocation line runs along the observation axis. The Burgers circuit, marked with yellow circles, yields a Burgers vector $\boldsymbol{b}_x = a$[100] parallel to the interface, as indicated in Figure 6.7. Thus, misfit dislocations have an edge character with the glide plane (GP) parallel to the interface.
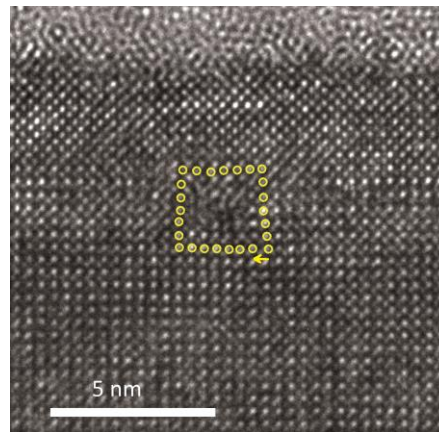
Figure 6.7: HRTEM cross-section image of a 6-nm-thick film, viewed along the [010] direction. Yellow circles mark the Burgers circuit.

Another way to determine the Burgers vector and the direction of the line is by diffraction contrast analysis, using the $\boldsymbol{g} \cdot \boldsymbol{b}$ criterion, where $\boldsymbol{g}$ is the diffraction vector. Figure 6.8 shows planar view diffraction contrast images of 3.5 nm ((a)-(c)) and 6 nm ((d)-(f)) film thickness acquired near the [001] zone axis to determine the Burgers vector. Thus, in the image shown in Figure 6.8(a), with the family of planes $\boldsymbol{g}(100)$ set into Bragg conditions, the changes in the amplitude contrast induced by the presence of the [010] dislocation line can be observed as they are under a $\boldsymbol{g} \cdot \boldsymbol{b} \neq 0$ condition.
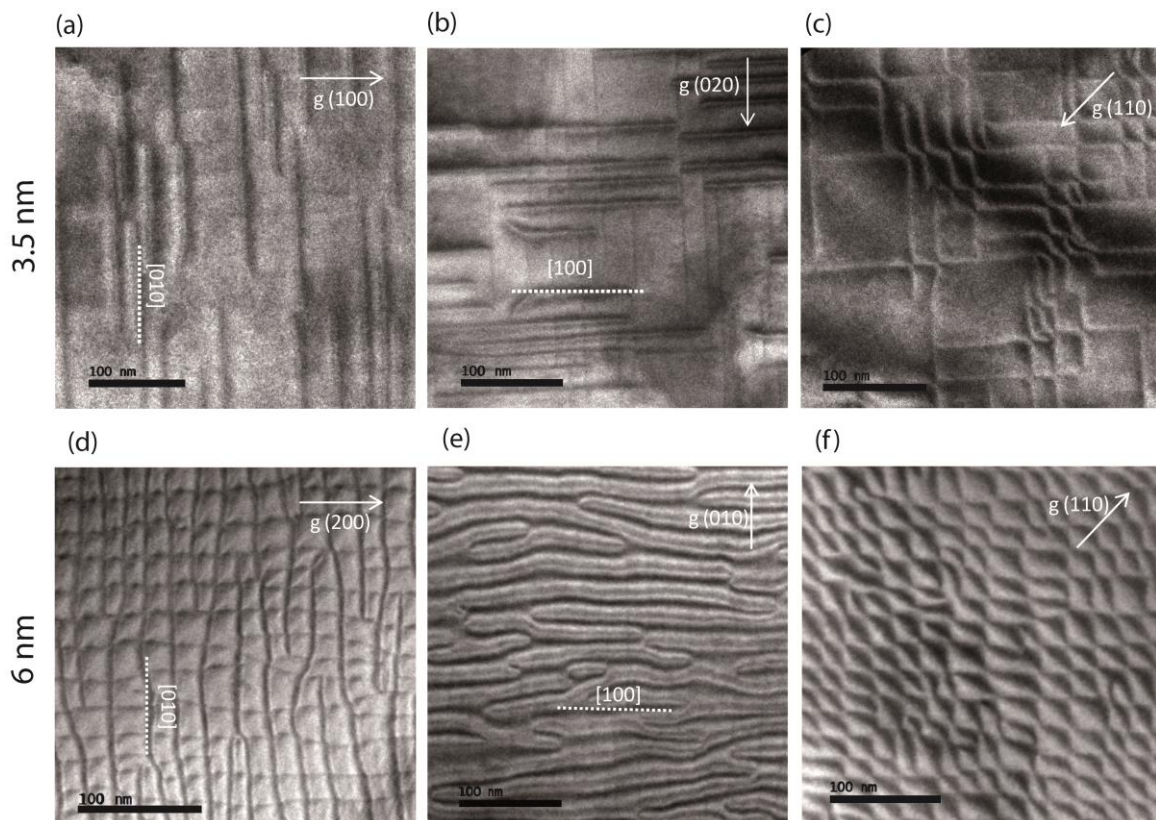
Figure 6.8: Planar view diffraction contrast images of 3.5 and 6-nm-thick films acquired near the [001] zone axis. (a), (b) and (c) correspond to the 3.5-nm-thick film imaged with $\boldsymbol{g}(100)$, $\boldsymbol{g}(020)$ and $\boldsymbol{g}(110)$, respectively. They are acquired in dark field conditions. (d), (e) and (f) correspond to the 6-nm-thick film imaged with $\boldsymbol{g}(200)$, $\boldsymbol{g}(010)$ and $\boldsymbol{g}(110)$, respectively. They are acquired in bright field conditions.

However, the other family of dislocations fulfils the invisibility condition $\boldsymbol{g} \cdot \boldsymbol{b} = 0$ and as a result, the dislocations cannot be observed. In the case of the image in Figure 6.8(e), obtained with $\boldsymbol{g}$(010), the situation is inverted and the [100] family of dislocations is observed. In the case of the images shown in Figure 6.8(c) and (f), obtained with $\boldsymbol{g}$(110), both families of dislocations are under $\boldsymbol{g} \cdot \boldsymbol{b} \neq 0$ condition and both contribute to the contrast in the image, though in the case of the 6-nm-thick film, the contrast pattern is more complex. $\boldsymbol{g}$(020) and $\boldsymbol{g}$(200) diffraction vectors were also used and the corresponding images are shown in Figure 6.8(b) and (d). Thus, two families of dislocation lines may be distinguished: one following the [100] direction and the other following the [010] direction, with [010] and [100] Burgers vectors parallel to the interface, respectively.

6.4.1. Atomic structure of the dislocation core

Figure 6.9 shows an atomic resolution HAADF image of a dislocation core in a 3.5-nm-thick film obtained by a probe corrected STEM. In this image the brightness of atomic columns is proportional to the atomic number, Z, therefore brighter dots correspond to the La/Sr or La atom columns occupying the *A*-site sublattice of the *AB*O$_3$ perovskite structure while Mn/O and Al/O columns being hardly visible.
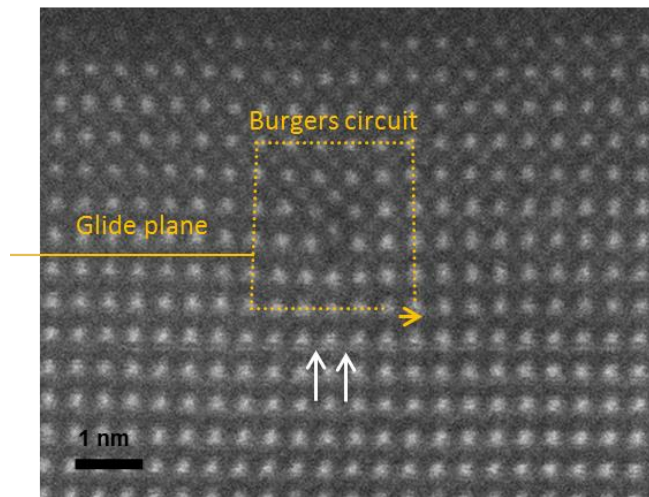
Figure 6.9: Atomic resolution HAADF image of a dislocation core of 3.5-nm-thick film. The Burgers circuit is marked by dashed yellow lines yielding a[100] Burgers vector (yellow arrow), parallel to the interface between the film and the substrate. Two white arrows mark the two extra half planes. The yellow line marks the GP.

The dislocation presents a a[100] Burgers vector parallel to the interface between the film and the substrate. In the perfect **b** = a[100] dislocation, the extra half plane is composed by an *A*-site plane plus a *B*-site/O plane. Since *B*-site/O columns are hardly visible owing to their lower atomic number, at first sight the image suggests a perfect dislocation with a single extra half-plane of *A*-site columns in the substrate side. However, careful analysis of the image reveals that the core is dissociated in two partials corresponding to the two (hardly visible) half extra planes of *B*-site/O columns running along the two vertical arrows shown in the image. Thus, the dislocation core is dissociated, [100] →1/2[100] + 1/2[100] (**b** = **b**$_1$ + **b**$_2$), and presents two extra half planes separated by one unit cell. This dissociation of a dislocation core has been proposed in a [100] edge-dislocation core in SrTiO$_3$ [217] and polymorphism in dislocation cores in MgO [226].

The dislocation dissociation draws a complex scenario with different possible dislocation core structure configurations depending on the GP and the chemical composition of the two extra half planes. For example, four atomistic models of dissociated dislocation cores have been proposed for SrTiO$_3$ [217] and eight atomistic models of misfit dislocation in SrZrO$_3$ on SrTiO$_3$ which result from considering two different termination states: (i) the cation sites of the film coincide with the equivalent sites in the substrate and (ii) the perovskite sequence is broken, implying the coincidence of non-equivalent cation sites between the film and the substrate [227]. Moreover, a more complex scenario occurs if the two extra half planes have a different GP, which may result in other dislocation core structure configurations, such as is observed in MgO [226], and also in some cases found in the present films, though not discussed here.

In the samples studied here, the perovskite sequence ($AO/BO_2/AO/BO_2$…) is continuous across the interface between the film and the substrate. Thus, the possible atomistic models of dislocation core structures presented by Zhang *et al.* [217] are adapted to the present case, from a bi-crystal to a heterostructure, and are used as a reference in the present study. Four different dislocation core configurations may be distinguished, as illustrated in Figure 6.10. In this simplified model, the following considerations are taken into account: (i) the two extra half planes have the same composition; (ii) the GP is the same for the two extra half plans and (iii) the dislocation core has a zero net charge. Thus, the four possible dissociated cores are defined by the GP of the dislocations and the composition of two extra half planes. Considering a simple dislocation, there are two options for GP of the dislocation: either a AO_{GP} or a $BO_{2,GP}$, where A and B refer to the cation positions in the ABO_3 perovskite. When it is combined with the two possible composition of the extra half planes (HPs) (a AO_{HP} or a $BO_{2,HP}$), it results in four possible combinations for a dissociated dislocation core: (a) AO_{GP} - AO_{HP}, (b) $AO_{GP} - BO_{2,HP}$, (c) $BO_{2,GP}$ - AO_{HP} and (d)$BO_{2,GP} - BO_{2,HP}$.

The analysis of the image in Figure 6.9 reveals a dissociated core formed by two half extra planes of BO_2. Thus, if the extra half planes end in an O column, the GP would be an AO plane, as illustrated in Figure 6.10(b), while if the extra half planes end in a Mn/Al/O column, the GP would be a BO_2 plane, as illustrated in Figure 6.10(d). In the image presented in Figure 6.9, both extra half planes probably end at Mn/Al/O columns, so both extra half planes have the same BO_2 GP. This configuration leaves a central plane contained between the two extra half planes (referred to as the axial plane), which is formed by an AO plane under the dislocation and continues as a BO_2 plane above the dislocation, forming an antisite contact on the GP. An atomic model corresponding to this configuration is shown in Figure 6.10(d). Compared to an undissociated core, this one is more compact and is symmetric with respect to a mirror plane perpendicular to the interface. This dislocation core configuration is the most commonly observed in the different dislocation core images analysed in the 3.5 and 6-nm-thick films. However, the analysis of different dislocation images suggests that other dislocation core configurations are possible, such as that built by AO extra half planes. The differences between the different dislocation core configurations are very subtle, and here, only the most common dislocation core structure will be considered.
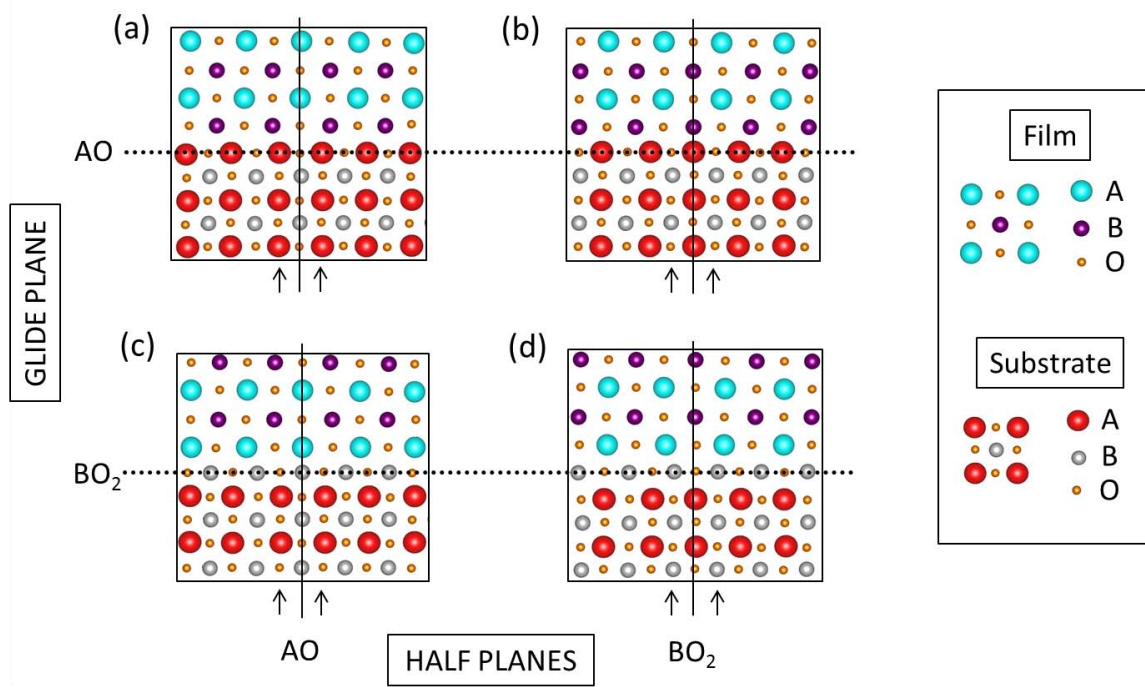
Figure 6.10: Atomic models of dislocation core configurations as a function of the GP and extra half planes composition. (a) and (b) correspond to AO_{GP} with AO and BO_2 extra half planes, respectively. (c) and (d) correspond to $BO_{2,GP}$ with AO and BO_2 extra half planes, respectively.

An inspection of the HAADF images reveals changes in the intensity of the spots in the axial plane. Figure 6.11 shows intensity profiles obtained from the HAADF image along the AO_2 vertical plane (blue) and the BO_2 plane (green) away from the dislocation core. The axial plane (black) is added at the top. In the AO plane intensity profile, the intensity maxima correspond to La-Sr/La atomic columns. Only La is occupying the atomic columns from the substrate to two atomic columns under the GP. Over these two atomic columns under the GP, a decrease in the maxim intensity can be seen in the profile, indicating that La and Sr occupy these positions. The intensity in the BO_2 plane profile is very low and no differences can be observed. Moreover, the position of intensity maxima under the GP agrees with the position of La-Sr/La atomic columns in the substrate due to the influence of AO plane intensity in the profile. In the axial plane, the total intensity and the positions of the maxima under the GP agree with those obtained in the AO plane, while the total intensity and the maxima obtained above the GP agree with those obtained in the BO_2 plane. However, there are two spots more intense than the Mn/Al atomic columns, pointing to the partial occupancy of these B-site columns by heavier and larger cations, such as La^{3+} or Sr^{2+} cations. This leads to the formation of La$_{Mn}^x$ or Sr$_{Mn}'$ antisite defects (expressed using the Kröger-Vink notation [228]) above the GP. Comparing the ionic radii [229] of La^{3+} and Sr^{2+} in octahedral coordination, 1.032 Å and 1.18 Å, respectively, with that of Mn^{3+}and Mn^{4+}, 0.645 Å and 0.530 Å, respectively, the driving force for formation of such defects is considered to be the accommodation of the tensile strain above the GP, which is discussed in the next section. Similar defects have been observed in an analogous misfit dislocation core in BiFeO$_3$ [216].
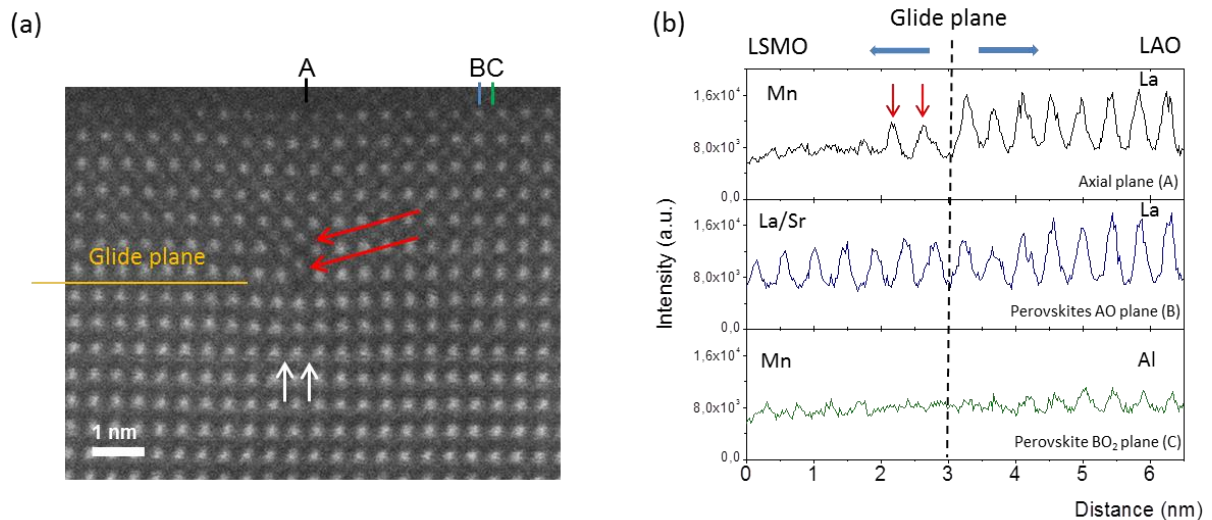
Figure 6.11: (a) The same HAADF image presented in Figure 6.9, in which the respective colour lines mark the planes corresponding to the intensity profiles presented in (b). The two red arrows mark the two more intense spots. (b) Contrast profiles taken along the axial plane (in black) (A); an *AO* vertical plane (in blue) (B); and a *BO*$_2$ plane (in green) (C).

Until now, the dislocation core has been considered not charged. However, according to electron microscopy and computer simulations in previous studies of edge dislocations in STO, the dissociated dislocation core results from a structural relaxation induced by removal of an entire oxygen column at the MD core [217, 218]. Also in heterostructures, such as in PbZr$_{0.52}$Ti$_{0.48}$O/SrRuO$_3$ [62] and BiFeO$_3$/SrRuO$_3$ [216], oxygen deficient dislocation cores are suggested. Moreover, the formation of antisite defects between *A* and *B* sites, or a particular cation segregation as a result of the strain, has been described [62, 216, 219].

6.4.2. Strain field from an individual dislocation

Figure 6.12(a) shows a HRTEM image of a 3.5-nm-thick film and the corresponding strain maps of the in-plane, $\varepsilon_{xx}(x,z)$ (b), and out-of-plane, $\varepsilon_{zz}(x,z)$ (c), strain components around the MD. In the 3.5-nm-thick films, the dislocations are larger spaced compared to thicker films and it is easier to analyse their individual strain field. In this GPA analysis, a medium Gaussian mask was used to select the (110) and (1-10) lattice fringe, which yields a spatial resolution of ~ 1.1 nm. The x-direction is defined as the direction parallel to the interface while z-direction is defined as the direction perpendicular to the interface. In these maps the blue and purple colours indicate a higher level of relaxation with respect to the substrate, as the reference of the lattice was taken in the substrate. Thus, positive strain values indicate an expansion of the lattice with respect to the reference, while negative values indicate a compression.
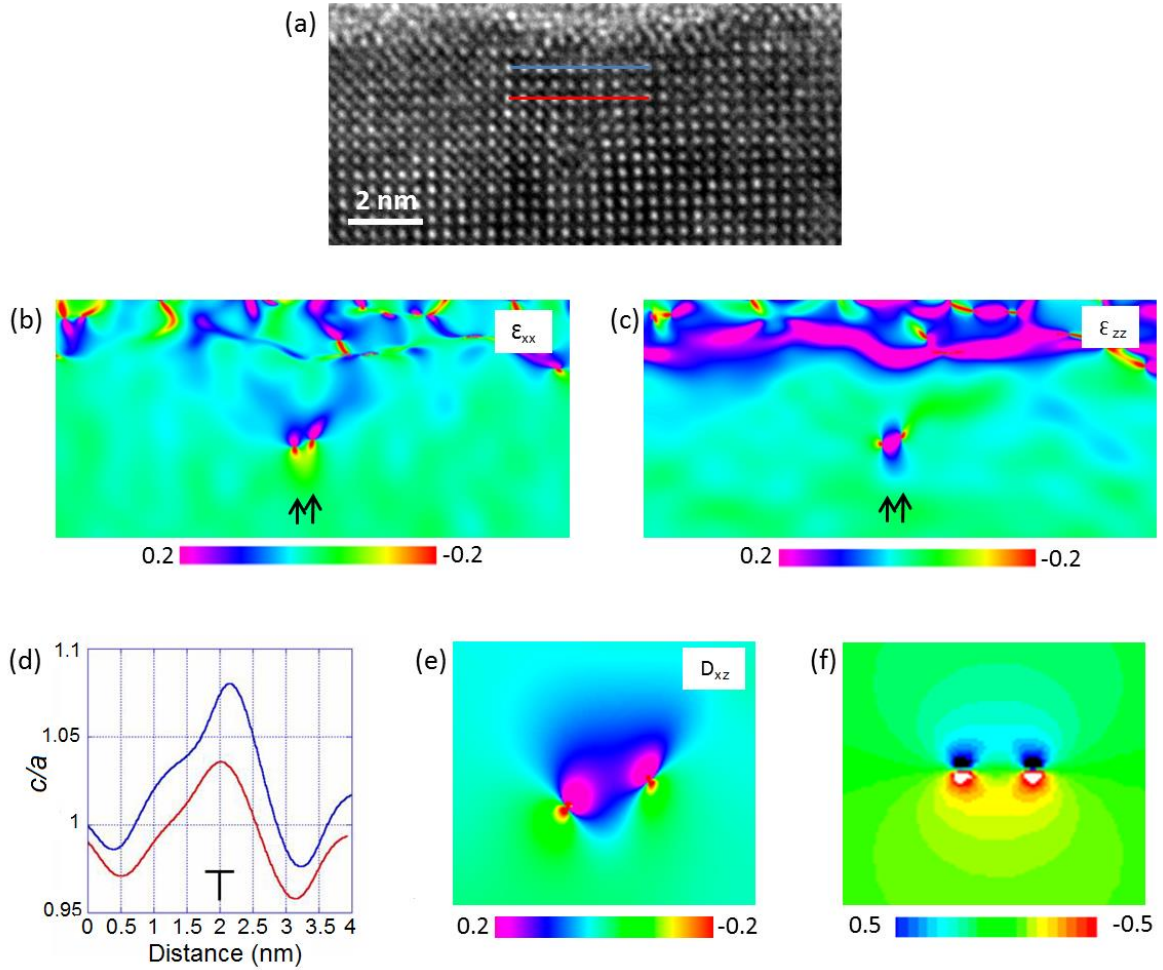
Figure 6.12: (a) HRTEM cross-section image of a 3.5-nm-thick film. (b) In-plane ($\mathcal{E}_{xx}(x,z)$) and (c) out-of-plane ($\mathcal{E}_{zz}(x,z)$) component strain maps obtained from the image shown in (a). (d) Variation of the *c/a* ratio across the position of a buried MD as determined from the experimental $\mathcal{E}_{xx}$ and $\mathcal{E}_{zz}$ strain components maps. The position of the profiles is marked in (a) by red and blue lines corresponding to the red and blue curves, respectively. (e) Dilatation (D_{xz}) map obtained also from the image shown in (a). (f) Theoretical dilatation map of an identical configuration**.**

The position of the two partial dislocations can be clearly distinguished, along with the compressive (red, yellow) and tensile regions (magenta, blue) extending into the substrate and the film, respectively. It can be observed that the $\mathcal{E}_{xx}(x,z)$ map show two arms propagating up to the film surface, while in the $\mathcal{E}_{zz}(x,z)$ map they rapidly vanish as a result of the elastic boundary condition imposed by a free (001) surface. The strain field produces a local increase of the *c/a* ratio above the dislocations. This can be observed in Figure 6.12(d), where the *c/a(x)* dependence at two different z-levels above the dislocation is measured from GPA analysis, following the expression

$$\frac{c_f}{a_f} = \frac{c_{ref}}{a_{ref}} \times \frac{(\mathcal{E}_{zz} + 1)}{(\mathcal{E}_{xx} + 1)} \, , \qquad\qquad \text{(Eq. 6.2)}$$

where $\frac{c_{ref}}{a_{ref}} = 1$. The blue and red curves are taken close to the film surface and at half way from the buried dislocation core, as indicated in Figure 6.12(a). It can be clearly observed that the *c/a* ratio

locally increases in the position just above the dislocation lines and the average *c/a* level increases towards the film surface, which can be attributed to an elastic relaxation perpendicular to the film surface.

The corresponding dilatation map, defined as $D_{xz} = \Delta V/V = \mathcal{E}_{xx} + \mathcal{E}_{zz}$ where *V* is the volume, is depicted in Figure 6.12(d). D_{xz} thus represents the fractional change in volume that can be correlated with the size of cations redistributed around the MD core to accommodate the dislocation strain field. A calculation using linear elasticity is shown in Figure 6.12(f) [230]. Comparison between the experimental and theoretical maps reveals that while the latter exhibits a sharp boundary between the tensile and compressive regions at the GP, in the experimental map a positive dilatation region in blue colour extends between the two partials towards the substrate.

Moreover the displacement field above the dislocation core is clearly manifested as a downward bending of the atomic rows above the dislocation core as may be observed in Figure 6.12(a). This bending is observed in all the dislocated films independently of the thickness. It is quantified in Figure 6.13(a), which shows the measurement of the vertical displacement of the atomic rows. The vertical displacement is measured at 12 unit cell (black) and 17 unit cell (red) above the GP using the HRTEM image presented in Figure 6.13(b). The bending presents a maximum amplitude of ≈1.25 Å at the horizontal locus of the buried dislocation independent of distance of the dislocation core, in agreement with elastic theory [230].
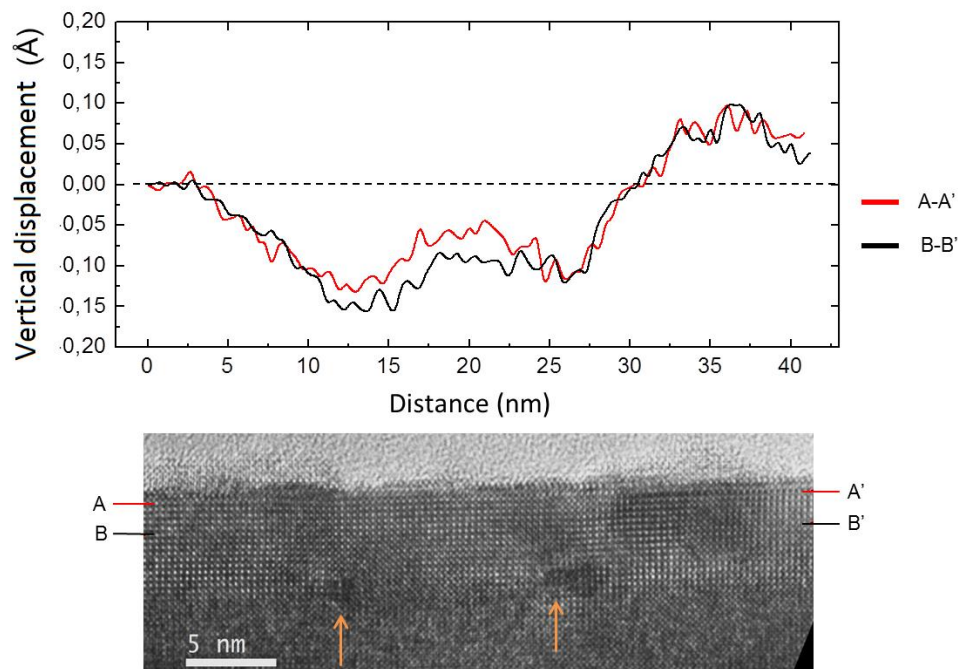

Figure 6.13: (a) Vertical displacements of atomic rows measured at the surface (in red) and closer to the dislocation core (in black) (b) The HRTEM image of a 6-nm-thick film used to measure the vertical displacements. The orange arrows mark the dislocation positions.

6.4.3. Chemical analysis of dislocation cores

Local spectroscopic analyses (EDS and EELS) were performed to identify the chemical changes associated with the strain field of the dislocations.

Dual EELS-Spectrum Images

Figure 6.14 shows the dual EELS-Spectrum image (SI) obtained from a dislocation core. The region used to perform the EELS-SI is shown in Figure 6.14(a), marked by a green box. Figure 6.14(b) shows the HAADF image acquired simultaneously with EELS-SI. This region is relatively thin and the thickness is practically constant. The relative thickness (h/λ, where λ is the mean free path) is shown in Figure 6.14(c), with a mean value of 0.344 and a standard deviation of 0.011 (minimum of 0.306 and maximum of 0.374). An energy window of 35 eV was used to obtain elemental maps of the O-K (528-563 eV), Mn-$L_{2,3}$ (638-873 eV) and La-$M_{4,5}$ (828-863 eV) edges. The resulting elemental maps, together with their overlay, can be observed in Figure 6.14(d),(e), (f) and (g), respectively, where a "T" marks the dislocation core.
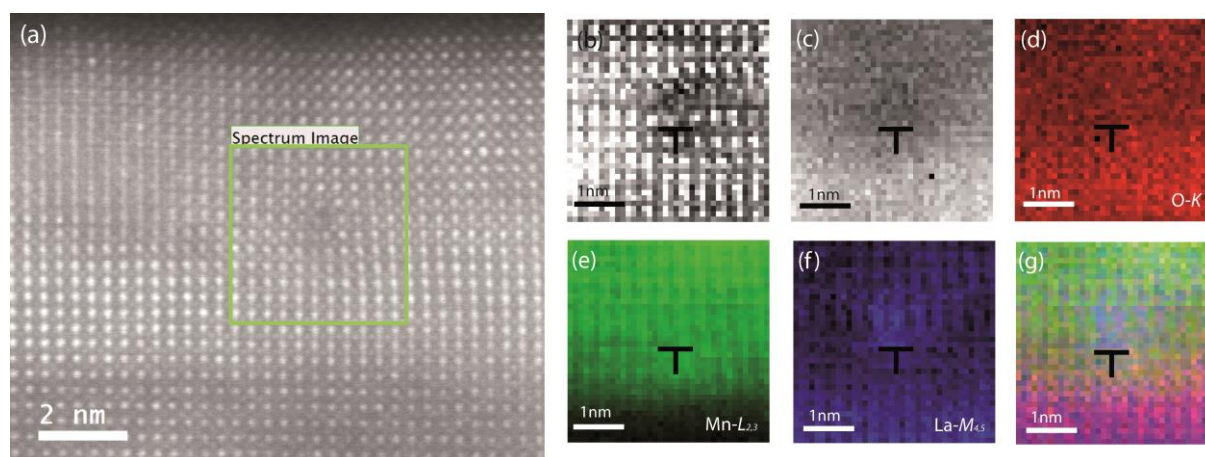
Figure 6.14: EELS-SI from a dislocation core. (a) HAADF image; the green box marks the region where EELS mapping was performed. (b) HAADF image acquired simultaneously with the EELS-SI. (c) Relative thickness image (h/λ). (d)-(f) elemental maps obtained from O-K, Mn-$L_{2,3}$ and La-$M_{4,5}$ intensities, respectively; f) O-Mn-La maps overlay. "T" marks the dislocation core, without considering the dissociation for the sake of simplicity.

In addition to the intensity change between the substrate and the film observed in all the elemental maps, particular intensity variations are observed at the dislocations position in the Mn-$L_{2,3}$ map (Figure 6.14(e)) and the La-$M_{4,5}$ map (Figure 6.14(f)). Despite O-K map (Figure 6.14(d)) does not show any intensity changes associated with the dislocation core, the EDS results show a reduction of the intensity. The La-$M_{4,5}$ map shows an increment in lanthanum signal (Figure 6.14(f)) at the tensile region of the dislocation. Since the La$_{Mn}^x$ antisite defects have been only observed at two specific positions on the axial plane, the increment of La intensity may be attributed to an increase of the La/Sr ratio in this region. Meanwhile, the Mn-$L_{2,3}$ map (Figure 6.14(e)) does not show a clear decrease in the tensile region. Instead, it shows an increase of the intensity under the GP, which will be referred later in the EDS results.

The O-*K* and Mn-*L*$_{2,3}$ edges were analysed in order to obtain information about the electronic structure of the dislocation core and its vicinity. Figure 6.15(a) and (b) show the evolution of the corresponding EEL spectra, across the dislocation core. The dashed spectrum, F, corresponds to a location in the film far away from the dislocations and is included here for reference. Spectrum S corresponds to a position below the GP beyond which the Mn signal vanishes and is used as a reference for the LAO substrate. The zero loss peak taken in a dislocation core was aligned with the zero loss peak of the reference spectra and the spectral intensity was normalized. Six spectra are represented, three above the GP (DF1,DF2 and DF3) and three under GP (DS1, DS2 and DS3). The first spectrum is taken in LSMO film (DF3), ~ 1.8 nm away from the GP, and the last one in the LAO substrate (DS4), ~ 2 nm away from the GP. The GP of the dislocation is situated between spectra DF1 and DS1.
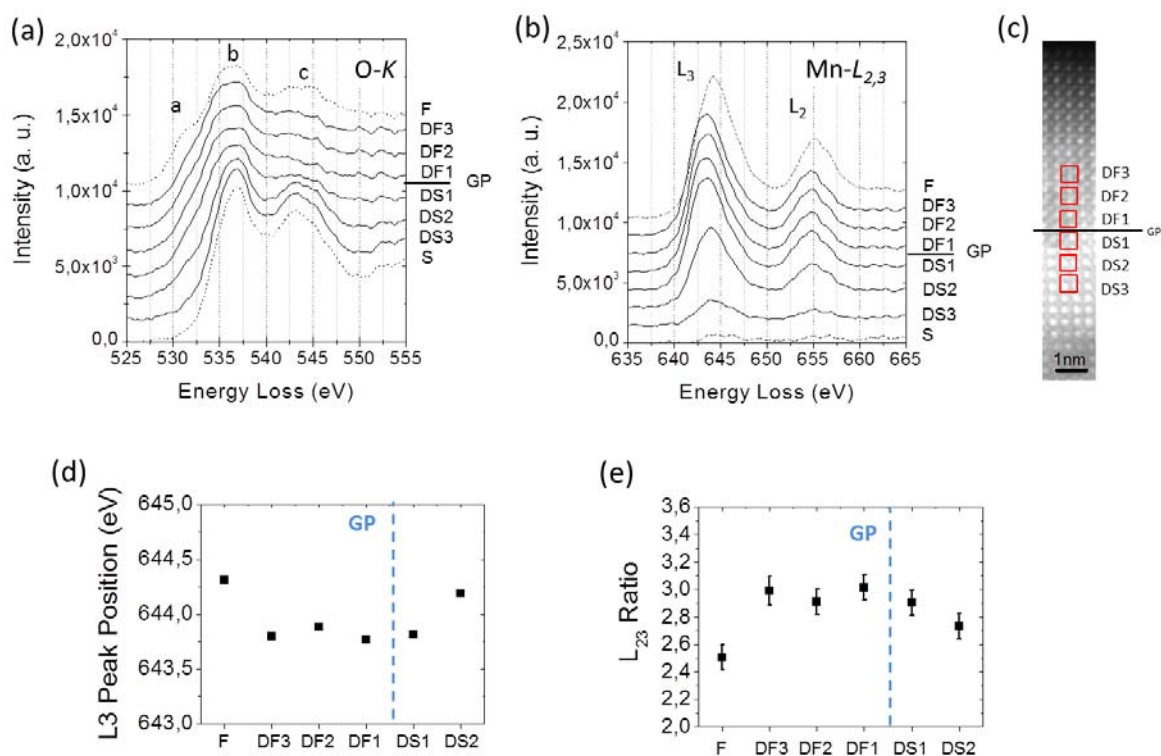
Figure 6.15: Evolution of the energy loss O-*K* edge spectra (a) and Mn-*L*$_{2,3}$ edge spectra (b) across the dislocation. (c) HAADF image where the squares indicate the integrated areas from which each spectrum were obtained. Variation of the *L*$_3$ peak position (d) and the *L*$_{2,3}$ intensity ratio (e). The GP is marked by a vertical blue dashed line.

Figure 6.15(a) covers the energy loss range between 525 and 555 eV, where the O-*K* edge is found (around 530eV). The O-*K* edge is interpreted in terms of the transition from O 1*s* core levels to O 2*p* states hybridized with transition metal states [106, 171]. In the LSMO reference spectrum (F), it is possible to distinguish three different peaks, **a**, **b** and **c**. Peak **a**, also known as pre-peak, appears around 531 eV and is attributed to the manganese 3*d* states [73, 106]. This peak is sensitive to the Mn 3*d* band occupancy; thus, typically, it is weak for Mn^{3+} with fully occupied 3*d* t_{2g} spin up levels and one electron in the e_g level, and becomes stronger as the concentration of Mn^{4+} increases. Consequently, the analysis of this peak gives information on the cation oxidation state [73]. Here, in

the dislocations region this peak is considerably weaker compared with the spectrum of the film (F), and reduces as the Mn concentration vanishes towards the substrate, where the peak disappears. The reduction of this peak may suggest an increment of the Mn oxidation state. The first main peak, **b**, found around 536 eV, is attributed to hybridization with La 5d and/or Sr 3d bands [73]. Thus, under the GP, the intensity of peak **b** increases and its shape becomes sharper and thinner as the spectra get closer to the S spectrum, occupied only by La. Above the GP, a noticeable broadening of the peak is observed due to the A-site becoming progressively shared with Sr cations. The third peak, **c**, found around 543eV is related to the projected unoccupied oxygen p states mixed with the B-site 4sp band [106, 171]. Here, as the GP is approached from the film side, the intensity of peak **c** vanishes and recovers again below the GP, which can be tentatively attributed to the severe distortion of the BO$_6$ octahedra near the MD core.

Figure 6.15(b) covers the 635-655 eV energy loss range, in which the Mn-$L_{2,3}$ edge is found. LSMO is a mixed-valence system, which consists of a mixture of Mn^{3+} and Mn^{4+}, with a nominal oxidation state of Mn$^{3.33+}$. Variations in the Mn-$L_{2,3}$ intensity ratio or chemical shifts are typical fingerprints of changes in the oxidation state [73, 106-109]. In particular, Figure 6.15 (d) and (e) shows an energy shift of the L_3 peak and an increase of the Mn-$L_{2,3}$ intensity ratio relative to the F spectrum in all the spectra taken above the GP and one unit cell below it. The variation of L_3 peak energy with the vertical position across the dislocation core is shown in Figure 6.15 (d). An energy shift value of -0.45eV is kept almost constant from DF3 to DS1, which assuming the nominal oxidation state +3.33 for the unperturbed LSMO film, indicates an oxidation state of +3.03 ($\pm$ 0.03) in the dislocation core. Two unit cells below the GP the Mn oxidation state increases until its concentration vanishes. The increase of the Mn-$L_{2,3}$ intensity ratio observed in Figure 6.15 (e) supports a similar trend [106, 112, 114]. The value obtained from the reference point (F), which is 2.5 ($\pm$ 0.1), according to Ref. [73], yields +3.57 ($\pm$0.14). Now, if this value is considered as a reference for the nominal +3.33, an average oxidation state of +2.7 ($\pm$ 0.2) is obtained for unit cell areas DF3 down to DS1, slightly smaller than that obtained by the chemical shift method. Therefore an oxidation state of 3+ is assumed for Mn cations located in the neighbourhood of the MD core.

Figure 6.16 shows the lateral variation of the energy loss O-K (a) and Mn-$L_{2,3}$ (b) spectra along the GP, as well as an HAADF image (c) indicating the positions from which the spectra were obtained. The GP0 corresponds to the dislocation position while the positive and negative numbers (labelled GP1, GP2, GP3,GP-1, GP-2 and GP-3) correspond to the spectra taken at the left and right positions from GP0, respectively. The reduction of the **c** peak in the O-K edge spectra and the shift of Mn-$L_{2,3}$ edge spectra can be clearly seen, but only in the dislocation core position (GP0).

Thus, both the evolution of the pre-peak intensity and variations in the Mn-$L_{2,3}$ spectral features (chemical shift and $L_{2,3}$ intensity ratio) converged in a charge enrichment in the vicinity of the dislocation core, preferentially in the tensile region above the GP.
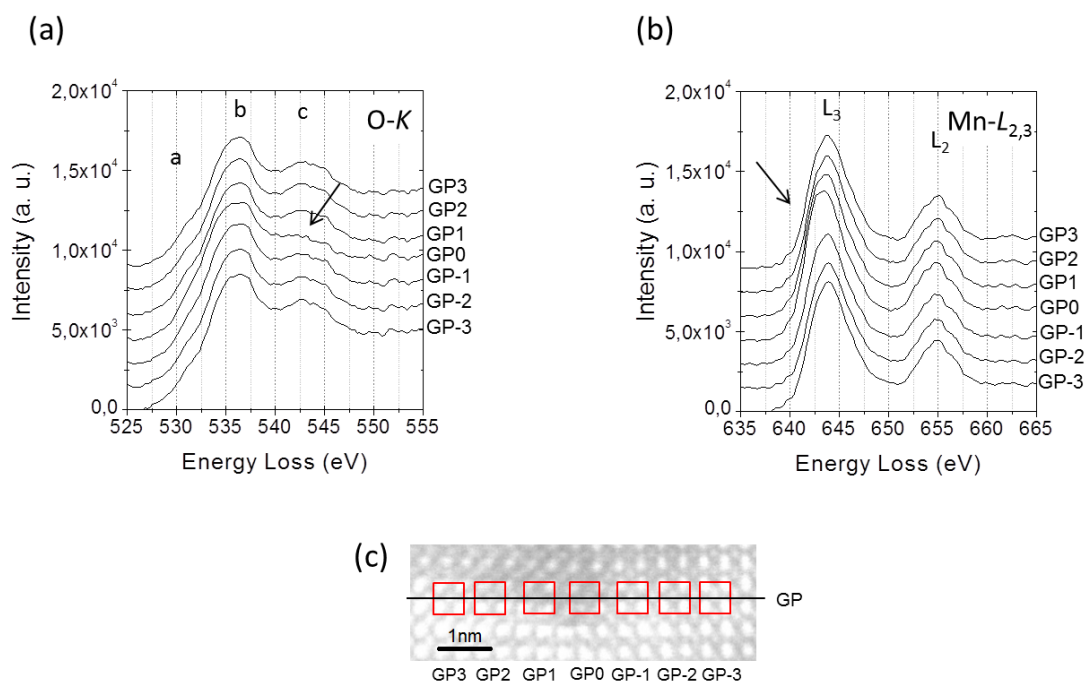
Figure 6.16: Evolution of the energy loss O-K edge (a) and Mn-$L_{2,3}$ edge spectra (b) across the GP. GP0 corresponds to the position of the dislocation core. (c) HAADF image where the squares indicate the integrated areas from which each spectra were obtained.

In order to assess the possible influence of octahedral distortions on the estimation of the Mn oxidation state, Mn-$L_{2,3}$ edge spectral simulations were carried out using CTM4XAS [117]. Computer simulations of the Mn^{3+}-$L_{2,3}$ edge and Mn^{4+}-$L_{2,3}$ under compressive and tensile strain are presented in Figure 6.17(a) and (b). They were performed by reducing the cubic O_h symmetry (characterized by a cubic crystal field splitting 10Dq) to tetragonal D_{4h} and the degree of tetragonal distortion was tuned through parameters Ds and Dt. Parameters 10Dq, Ds and Dt, for relaxed and distorted octahedra were obtained Ref. [54], which are presented in the following table:

Distortion	Symmetry	10Dq (eV)	Dt (eV)	Ds (eV)
c > a (in-plane compressive strain)	D4h	1.1	+0.03	+0.186
c = a cubic (Undistorted)	Oh	1.1	0	0
c < a (in-plane tensile strain)	D4h	1.1	-0.03	-0.186

Table 6.1 Values reported in the Ref. [54] used to perform the EELS simulations presented in Figure 6.17.

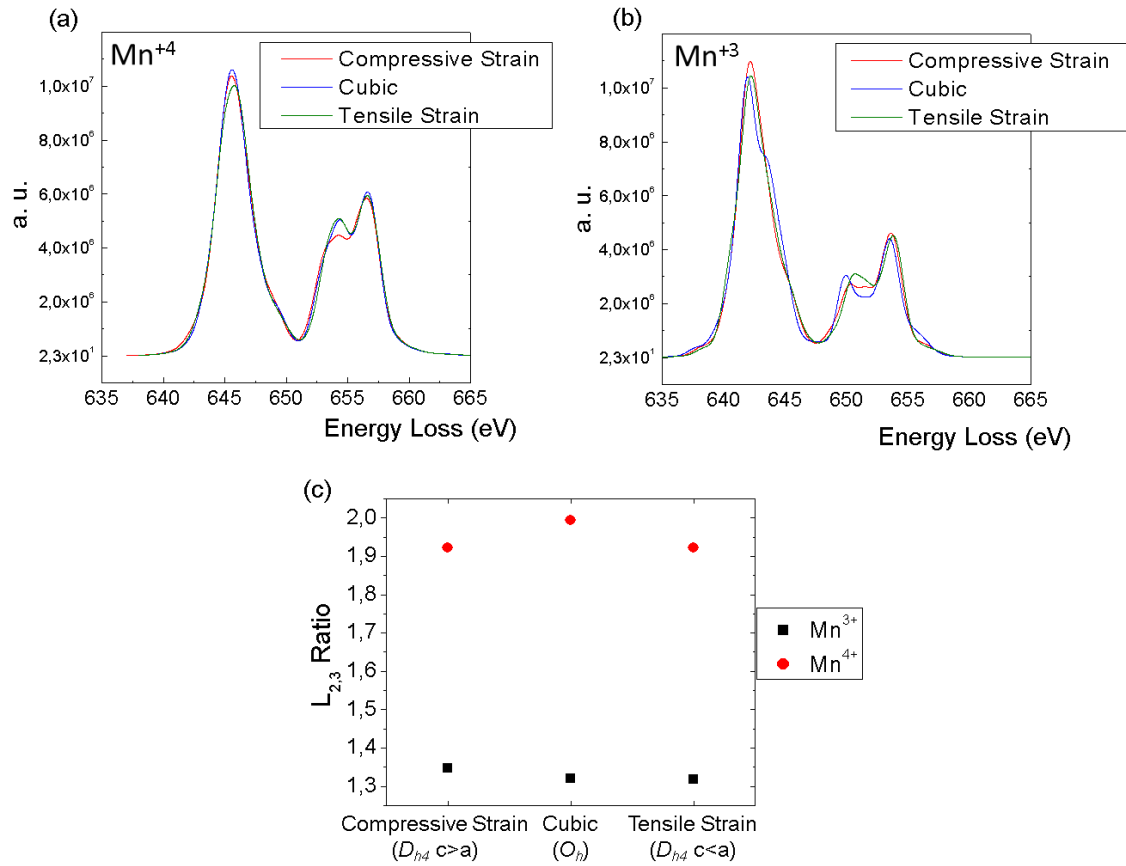Figure 6.17: Calculated Mn-$L_{2,3}$ edges for a cubic crystal field (10Dq=1.1eV) (in blue) and large tetragonal distortions (compressive strain and tensile strain, in red and green, respectively) for Mn^{4+}(a) and Mn^{3+}(b). (c) $L_{2,3}$ intensity ratio obtained from the spectra presented in (a) and (b).

In Figure 6.17(a)-(b), the L_3 energy shift between the Mn^{3+} and Mn^{4+} can be clearly observed. The $L_{2,3}$ intensity ratio obtained from these simulated spectra are shown in Figure 6.17 (c). In the case of Mn^{3+}, the distortion of the MnO$_6$ octahedron slightly reduces the $L_{2,3}$ intensity ratio. In the case of Mn^{4+}, the tensile distortion keep the $L_{2,3}$ intensity ratio constant whereas a compressive distortion induces a slight increase of the $L_{2,3}$ ratio. However, these variations are smaller than those observed in our experimental data.

Atomic resolution EDS

The chemical composition around the dislocation core was accurately investigated by atomic-column resolution EDS. In addition, EDS provide information about Sr and Al, which were not acquired with EELS. Their absorption edges are far higher in energy than the O-K, Mn-$L_{2,3}$, La-$M_{4,5}$ edges, which makes it difficult to acquire all of them together and may reduce the energy resolution of the spectra. Moreover, the concentration expected for Sr is low compared with other elements and Sr-L edge typically shows a high signal noise ratio for mapping.

EDS-SIs were performed in a cross-section view along [010] direction. They were acquired as a series of frames, where the same region was scanned multiple times. Spatial drift correction was applied. For the EDS-SIs presented in this study, the time of collection was typically between 15-30

minutes. Elemental maps were extracted from EDS-SIs with selected energy windows for each element with previous background subtraction. To prevent possible energy overlaps, the energy La-$L\alpha$, Sr-$K\alpha$, Mn-$K\alpha$, O-$K\alpha$ and Al-$K\alpha$ lines were used to perform the elemental maps.
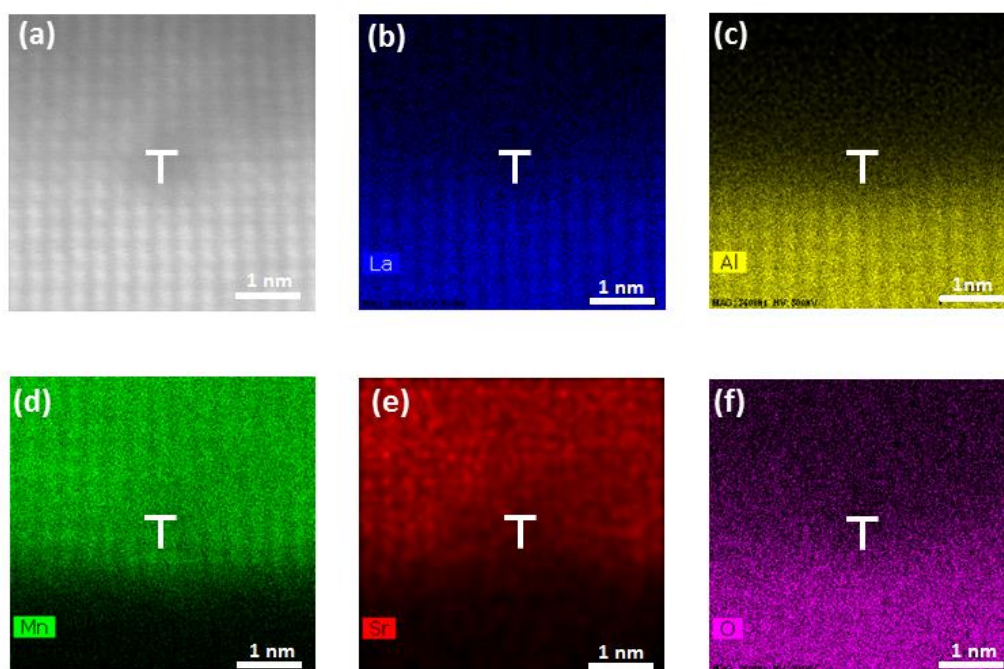

Figure 6.18: HAADF image (a) with the dislocation in the centre and the corresponding EDS elemental counts maps: La-$L\alpha$(b), AL-$K\alpha$(c), Mn-$K\alpha$(d), Sr-$K\alpha$ (e) and O-$K\alpha$ (f). "T" marks the dislocation core.

Figure 6.18 shows a HAADF image (a) with a dislocation in the centre and the corresponding EDS counts maps, La (blue) (b), Al (yellow) (c), Mn (green) (d), Sr (red) (e) and O (pink) (f). These maps present atomic column resolution, except for the Sr and O maps. The low concentration of Sr, 6at% in the total of elemental concertation, is probably the origin of poorer spatial resolution. In the case of O, it is well known that light elements are not well quantified and detected by EDS. The elemental maps corresponding to the film (La, Sr, Mn and O) show a decrease of the counts at the position of the dislocation core. In the case of Sr, a decrease is observed in all the vicinity of the dislocation, in both tensile and compression regions.

These elemental intensity variations can be seen more clearly in the element profiles obtained by integrating areas in the EDS-SI. Figure 6.19 shows the HAADF image of the dislocation core presented in Figure 6.18 along with the rectangular areas that were used to obtain the elemental profiles for comparison. The horizontal EDS profiles (yellow rectangles) were extracted from 2 unit cell height areas just below and above the dislocation GP. A vertical profile in a region separated from the dislocation core was used as a reference for the quantification calculation. It was extracted from a 3 unit cell wide rectangle (in green) on the right of the image going from the LSMO film (top part of the image) to the LAO substrate (bottom part). Given the large number of parameters involved in the intensity of the EDS maps it is important that the reference corresponds to the same image conditions.
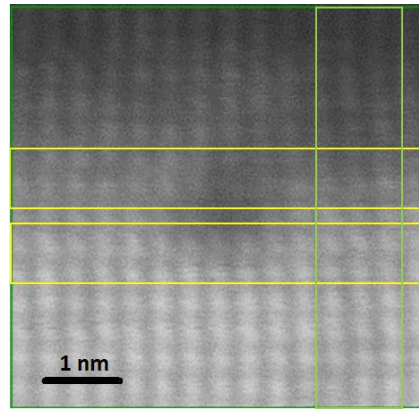
Figure 6.19: HAADF image of the same region where EDS-SI was collected. The rectangular boxes mark the areas used to obtain the horizontal (in yellow) and vertical (in green) element profiles.

Figure 6.20 depicts the raw intensity data obtained from horizontal profiles above and below the dislocation GP, as it is indicate in HAADF image shown in Figure 6.20. These profiles were obtained by summing the x-ray counts in the perpendicular direction of the interface and integrating an area of around 2 unit cells in a different rectangular box of 255 x 38 pixels (corresponding 5.52 nm x 0.82 nm). This includes two *A*-site and two *B*-site rows, along with the corresponding O columns. The zero x-position is placed in the axial plane, which is located at 2.75nm from the left side of the box. The periodic fluctuations of the profiles indicate the atomic resolution of these profiles. The horizontal profiles below the GP clearly display 15 full *A*-site (in the La signal) atomic columns, whereas above they show 14 *A*-site La columns, one column less. Similarly, for the *B*-site, the Mn profiles show one additional column of atoms below the dislocation GP.

Figure 6.20: Elemental count horizontal profiles below (left) and above (right) the dislocation GP.

However, in some parts of the EDS maps there is not a clear atomic resolution for the lighter elements like, Al and O, as well as for Sr, because of its low concentration. In the tensile region, it can be observed 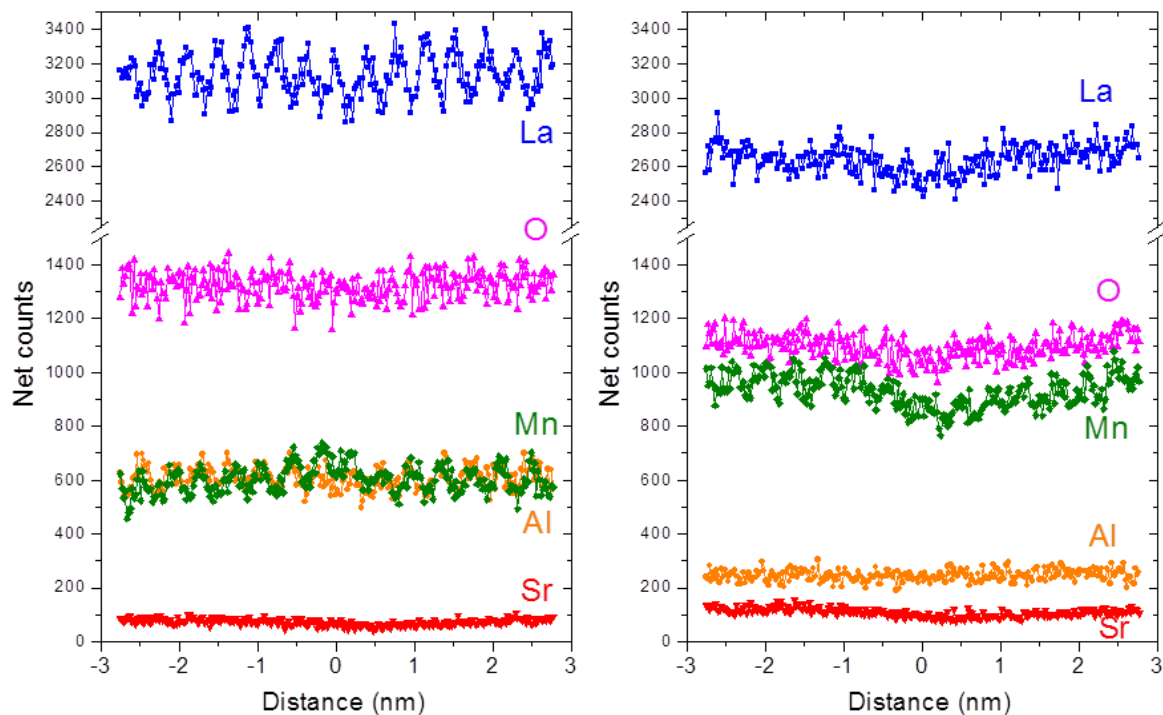that all the elemental counts subtly decrease at the position of the dislocations, except the Al counts, which are constant. On the other hand, in the compression region, an increment of Mn is observed, which agrees with EELS measurements. However, a reduction of Al at this position to compensate for the access of Mn at *B* cation positions is not clearly observed.

It is very likely that the boxes used for integration do not contain exactly the same proportion of each atomic column. A similar effect is probably induced by the fact that there could be some slight strain in the z-direction. Therefore, the intensities below and above the dislocation are not directly comparable and a renormalization process is required.

o **_Profile Fitting_**

In order to apply this renormalization, the profiles were fit to Gaussian curves for each atomic-column position. For La and Mn, with a defined atomic resolution, the positions and intensities of each individual Gaussian peak were set as variable and their full width half maximum (FWHM) was fit as a common variable for all the Gaussians for each different element. For the Sr and Al profiles, which did not show atomic resolution, the peak positions were fixed after those obtained for La and Mn. To adjust the O profile, the peak positions were evenly fixed after the *A*-site and *B*-site columns. Additional Gaussian peaks at both the left and right end of the profiles were also fit to avoid edge effects, although they were not taken into consideration for the normalization. The fitted curves for each element profile are shown in Figure 6.21.
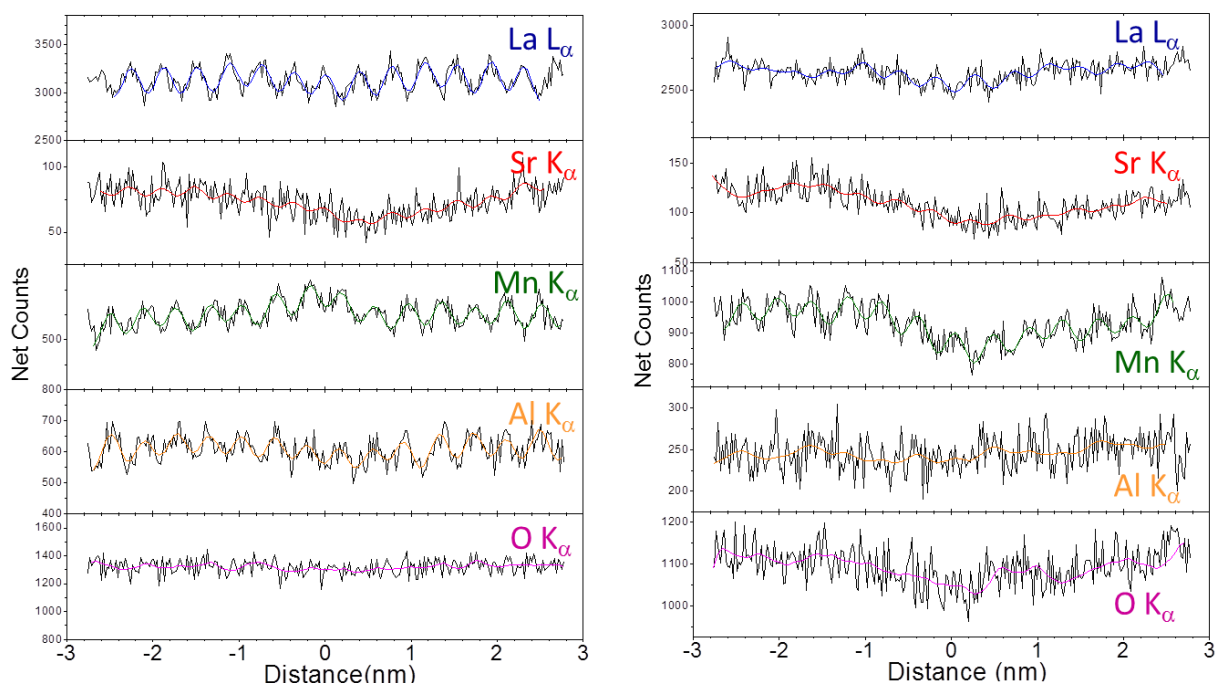
Figure 6.21: Fitted curves for each element profile in the regions below (left) and above (right) the dislocation GP. The vertical axes are scaled to show the fit to the experimental values and the atomic column resolution.

The best fit for the FWHM of the Gaussians was obtained for the values in the Table 6.2:

signal	FWHM (nm) Below GP	FWHM (nm) Above GP
La Lα	0.39	0.49
Sr Kα	0.40	0.45
Mn Kα	0.38	0.43
Al Kα	0.39	0.50
O Kα	0.27	0.29

Table 6.2: FWHM values for each element below and above the GP.

The FWHM values are consistent with those expected [94] for EDS which depend on the energy of the chosen spectral line. The systematic increase in the FWHM values for the map above the dislocation GP is likely to be due to a larger distortion of the unit cell affecting the channelling conditions of the measurement. This blurs the atomic-column resolution due to the larger overlap between the corresponding Gaussian peaks.

Figure 6.22 shows the corresponding integrated intensities below each Gaussian curve in the position of the centre of each atomic column either in the *A*-site or *B*-site position. The O signal was fit to independent Gaussian peaks both in the same positions as for *A*-site and *B*-site cations. The profiles already reveal some trends. The most significant one is the increase of the Mn signal and a concomitant reduction of the Al signal for the profile below the dislocation GP, in the position of the dislocation core, approximately between x = -1 and 1 nm. In this position La and Sr signal seem to reduce slightly. For the profiles above the dislocation GP subtle Sr and Mn reductions were also observed at the dislocation region. Note that the O-K_α intensity seems to show a higher value at the x-positions of the *B*-site cations than the ones at *A*-site cations. This is what is expected for a fully occupied *A*BO$_3$ perovskite alternating *A*O planes and *B*O$_2$ planes. Then, along a vertical plane the oxygen concentration in *B*-positions is twice that in *A*-positions.

For the normalization process, it is necessary to use intensities for each of the elements per unit cell. Therefore, there are two different options: i) either combine the measurements for each *A*-site column position with an average value of the two adjacent *B*-site positions, or the opposite, ii) combine each *B*-site intensity with an average of the two adjacent *A*-site positions. Both methods rendered similar values so here, only the first case is considered. The O-K_α intensity was taken as the sum of the intensities in the position of the *A*-site cation and the average of the adjacent *B*-site positions. The averaged intensities are presented in Figure 6.23. There was no substantial difference between the averaged-per-unit-cell profiles and the profiles at *A*- and *B*-site positions, except for the logical smoothening of Mn-$K\alpha$, Al-$K\alpha$ and O-$K\alpha$ features which have been averaged for each unit cell. These values were then taken as experimental values for the normalization.
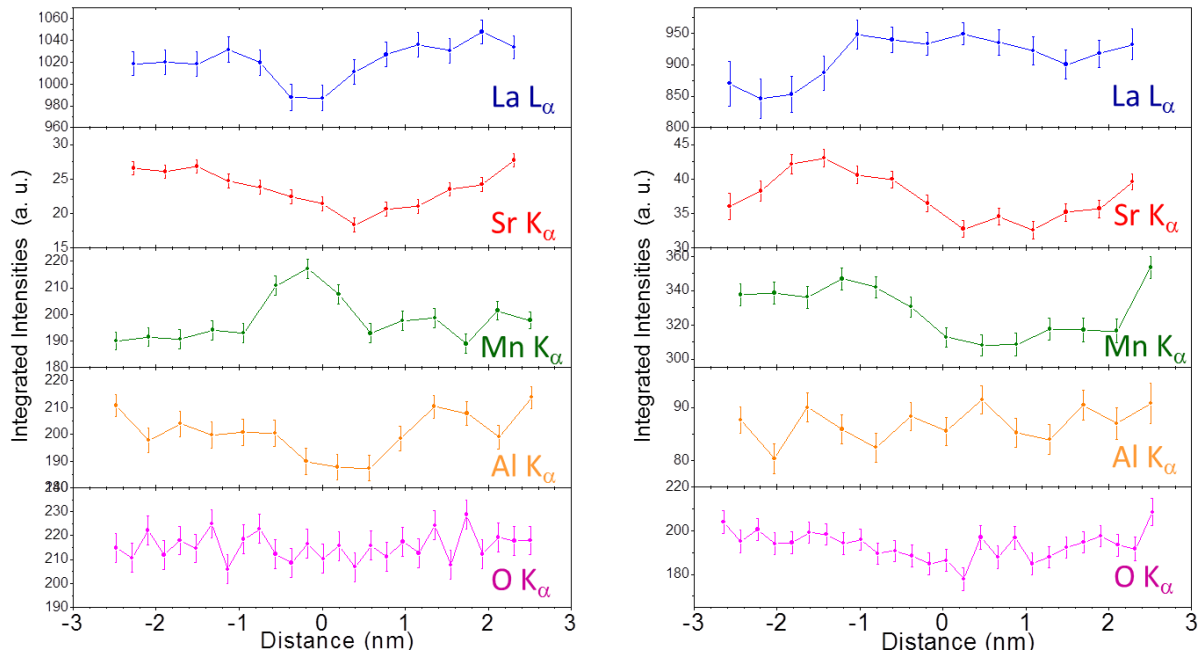
Figure 6.22: Integrated intensities of the fitted Gaussian peaks for the horizontal EDS profiles below (left) and above (right) the dislocation GP. La-*L*α and Sr-*K*α were located in *A*-site positions, while Mn-*K*α and Al-*K*α were in B-site positions. O-*K*α Gaussians were fitted both in *A*- and *B*-site horizontal x-positions.

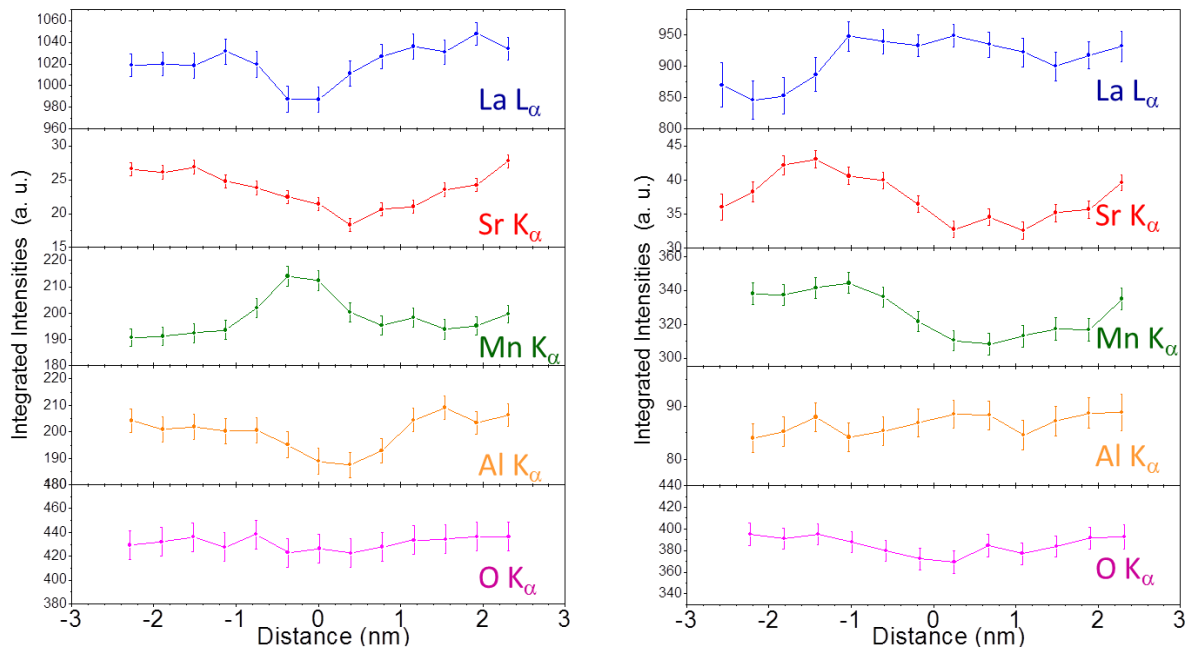Figure 6.23: Integrated intensities averaged for each unit cell (centred in the A-site cation) along the horizontal profile below (left) and above (right) the GP. The averaged values for the *B*-site and O are placed in the position of the corresponding *A*-site for each unit cell.

o ***Quantification of atomic% concentration profiles***

(1) *Determination of k-factors*

The elemental intensity profiles were converted into atomic% to quantify the subtle observed variations. The conversion of X-ray counts into atomic% was performed by the Cliff-Lorimer method [118], assuming the thin foil criterion. The principle is expressed in the following equation introduced in the section 3.1.8:

$$\frac{C_A}{C_B} = k_{AB} * \frac{I_A}{I_B}$$

(Eq. 6.3)

which relates the number of X-ray counts detected (I_A an I_B) from the elements (A and B) to the concentration (C_A and C_B) of the elements in the specimen with Cliff-Lorimer k-factor (k_{AB}), The k-factor is a proportionality constant depending on the elements being analysed, the energy of the incident electrons, and the relative sensitivity of the X-ray detector for the different X-rays. It can be estimated from theoretical considerations or it can be measured by analysing a specimen of known composition. Here, the k-factors were obtained from a reference zone in the analysed sample.

Since the absolute intensities in the EDS maps depend on many factors it is advisable to use a reference value within the same map acquired under the same conditions. Ideally a region of reference for the $La_{0.7}Sr_{0.3}MnO_3$ film could be taken in the top right corner of the image where one can assume that the possible perturbations caused by the presence of the substrate and the misfit dislocations are minimal. The same could be argued for the $LaAlO_3$ substrate. A region on the bottom-right corner could be used as reference. However, under these conditions it would not be possible to extract any information of Al-substitution into Mn position in the film (see example presented in Annex C). To avoid this uncertainty, and with the aim of assessing the total composition for *A*-site, *B*-site and O ions a supercell combining a number of film and substrate positions along a vertical profile is taken as reference.

The vertical profile taken at the right of the map presented in Figure 6.19 overlapping with some parts of the horizontal profiles is shown in Figure 6.24. It was obtained from the sum of the intensities of the different columns in a rectangular box of 54 x 248 pixels (corresponding 1.1694nm x 5.37nm) being approximately three unit cell wide in the horizontal direction of the maps. This vertical profile is taken as reference assuming that the top region (distance = 0 nm) corresponds to stoichiometric $La_{0.7}Sr_{0.3}MnO_3$, while the bottom extreme (distance = 5.5 nm) corresponds to the $LaAlO_3$ substrate. Despite the atomic-column resolution of the map, the Al-$K\alpha$ signal profile is not abrupt, which is an indication of interdiffusion between Al/Mn positions along the interface.

The k-factors were obtained from this reference profile in which the sample was considered stoichiometric, assuming that the integrated area is formed by a $(La_{0.7}Sr_{0.3}MnO_3)_X(LaAlO_3)_Y$ composed structure. A similar procedure was performed using a bi-layer of $La_{0.7}Sr_{0.3}MnO_3$ /$BiFeO_3$ [77]. The total number of unit cells in the reference profile is 14 unit cells, formed by *x* $La_{0.7}Sr_{0.3}MnO_3$ unit cells and *y* $LaAlO_3$ unit cells (*x* + *y* =14 unit cells). Neither HAADF images nor the EDS maps did show a defined

contrast that allowed the identification of the interface plane between $La_{0.7}Sr_{0.3}MnO_3$ film and $LaAlO_3$ substrate. Therefore, the exact number of unit cells for each component was not determined. Given this uncertainty different contacted planes were tested, varying the number of $La_{0.7}Sr_{0.3}MnO_3$ and $LaAlO_3$ unit cells, either (x, y) = (6,8), (7,7) or (8,6). Thus, the k-factors were determined using the Eq.6.3 and the experimental intensities of the reference profile, and the theoretical concentrations were established, $(La_{0.7}Sr_{0.3}MnO_3)_x(LaAlO)_y$.
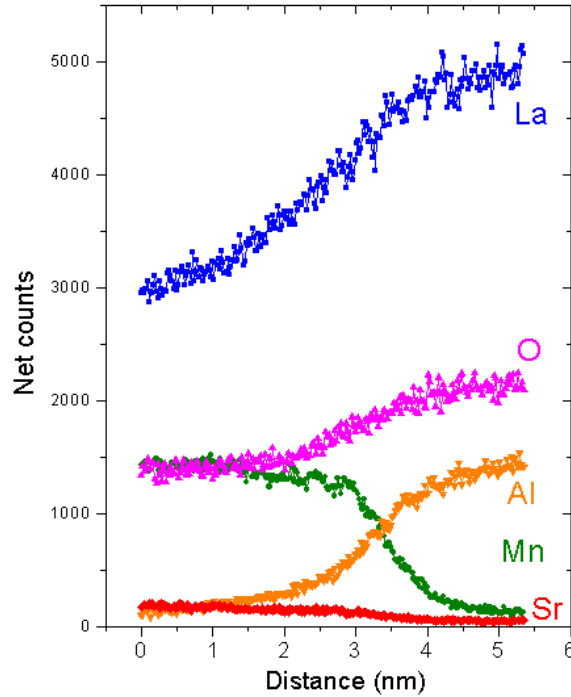
Figure 6.24: EDS elemental counts along a vertical profile in the EDS-SI shown in Figure 6.19.

For example, for the case of a supercell of $(La_{0.7}Sr_{0.3}MnO_3)_7(LaAlO_3)_7$ the total concentrations are

$$C_{(LSMO)7(LAO)7} = C_{La} + C_{Sr} + C_{Mn} + C_{Al} + C_O \ . \qquad \text{(Eq. 6.4)}$$

The atom proportion of $(La_{0.7}Sr_{0.3}MnO_3)_7(LaAlO_3)_7$ supercell are 11.9 atoms of La, 2.1 atoms of Sr, 7 atoms of Mn, 7 atoms of Al and 42 atoms of O. Thus, the relationships between these concentrations are

$$\frac{C_{La}}{C_{Sr}} = \frac{11.9}{2.1} = 5.67 \ , \qquad \text{(Eq. 6.5)}$$

$$\frac{C_{La}}{C_{Mn}} = \frac{11.9}{7} = 1.70 \ , \qquad \text{(Eq. 6.6)}$$

$$\frac{C_{La}}{C_{Al}} = \frac{11.9}{7} = 1.70 \ , \qquad \text{(Eq. 6.7)}$$

$$\frac{C_{La}}{C_O} = \frac{11.9}{42} = 0.28 \,.$$ (Eq. 6.8)

The k-factor that relates the concentrations can be defined using the experimental intensities obtained from the reference profile and extracting it from equation (Eq. 6.3). Thus, the k-factors that relate the different elements concentrations can be obtained by

$$k_{LaSr} = \frac{C_{La}}{C_{Sr}} * \frac{I_{Sr}}{I_{La}} = 5.67 * \frac{I_{Sr}}{I_{La}}$$ (Eq. 6.9)

$$k_{LaMn} = \frac{C_{La}}{C_{Mn}} * \frac{I_{Mn}}{I_{La}} = 1.70 * \frac{I_{Mn}}{I_{La}}$$ (Eq. 6.10)

$$k_{LaAl} = \frac{C_{La}}{C_{Al}} * \frac{I_{Al}}{I_{La}} = 1.70 * \frac{I_{Al}}{I_{La}}$$ (Eq. 6.11)

$$k_{LaO} = \frac{C_{La}}{C_O} * \frac{I_O}{I_{La}} = 0.28 * \frac{I_O}{I_{La}}$$ (Eq. 6.12)

If the total concentration of the supercell (La$_{0.7}$Sr$_{0.3}$MnO$_3$)$_7$(LaAlO$_3$)$_7$ is defined in atomic%, $C_{(LSMO)7(LAO)7} = 100\%$, the concentration of each element can be measured from a combination of (Eq. 6.3) and (Eq. 6.4). Here, the element concentrations were measured from the following expressions:

$$C_{La} = \frac{100}{1 + \left(\frac{I_{Sr}}{k_{LaSr} * I_{La}}\right) + \left(\frac{I_{Mn}}{k_{LaMn} * I_{La}}\right) + \left(\frac{I_{Al}}{k_{LaAl} * I_{La}}\right) + \left(\frac{I_O}{k_{LaO} * I_{La}}\right)}$$ (Eq. 6.13)

$$C_{Sr} = (C_{La}/k_{LaSr}) * (I_{Sr}/I_{La})$$ (Eq. 6.14)

$$C_{Mn} = (C_{La}/k_{LaMn}) * (I_{Mn}/I_{La})$$ (Eq. 6.15)

$$C_{Al} = (C_{La}/k_{LaAl}) * (I_{Al}/I_{La})$$ (Eq. 6.16)

$$C_O = (C_{La}/k_{LaO}) * (I_O/I_{La}) \,.$$ (Eq. 6.17)

In order to obtain the element concentrations at one position it is necessary that all the elements are present. This is a difficult calculation away from the interface, as well as in the substrate, where there aren't counts of Sr and Mn, resulting in a lack of data points.

Figure 6.25 shows an example of the three different element composition profiles obtained from the k-factors measured considering following cases of supercell: (La$_{0.7}$Sr$_{0.3}$MnO$_3$)$_8$(LaAlO$_3$)$_6$, (La$_{0.7}$Sr$_{0.3}$MnO$_3$)$_7$(LaAlO$_3$)$_7$, (La$_{0.7}$Sr$_{0.3}$MnO$_3$)$_6$(LaAlO$_3$)$_8$. The total concentration of cations was

considered by including oxygen in the calculation as well as without oxygen. In an ABO_3 stoichiometric sample, the normalized total concentrations of A and B cations are 1. If the oxygen is considered, the A and B cation concentrations deviate from 1 in all three cases. On the other hand, if the oxygen is not considered, the A and B cation concentrations are best adjusted at 1.
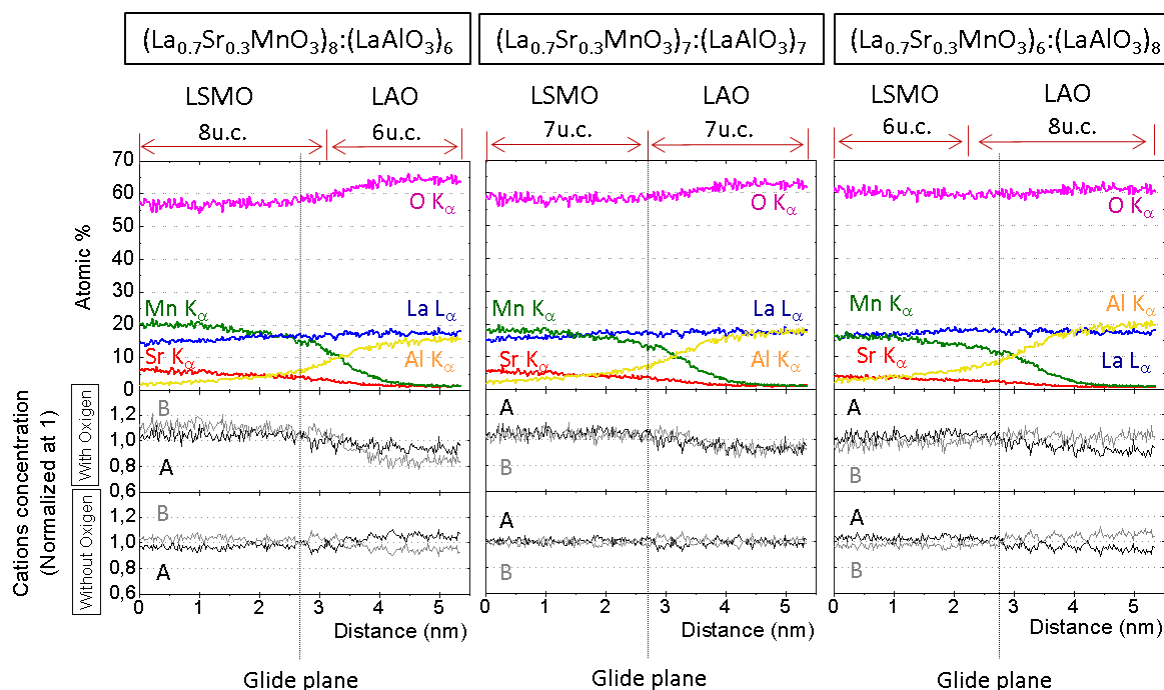
Figure 6.25: Elemental concentration profiles obtained by using the k-factors considering different supercells: $(La_{0.7}Sr_{0.3}MnO_3)_8(LaAlO)_6$, $(La_{0.7}Sr_{0.3}MnO_3)_7(LaAlO)_7$ and $(La_{0.7}Sr_{0.3}MnO_3)_6(LaAlO)_8$.

The best fit to the concentration profiles was found when the composed structure is formed by a total of 7 unit cells of $La_{0.7}Sr_{0.3}MnO_3$ and 7 unit cells of $LaAlO_3$ $((La_{0.7}Sr_{0.3}MnO_3)_7(LaAlO_3)_7)$. This corresponds to the case where the interface plane coincides exactly with GP (at distance=2.65nm). The following Table 6.3 presents the K-factors obtained for this case:

k-factor	Values
k_{La-Sr}	0.173
k_{La-Mn}	0.403
k_{La-Al}	0.287
k_{La-O}	0.128

Table 6.3: k-factors obtained from considering a $La_{0.7}Sr_{0.3}MnO_3)_7(LaAlO_3)_7$ supercell.

These k-factors were used to determine the horizontal concentration profiles. The error of concentrations profiles was defined from the differences between the calculations assuming different $(La_{0.7}Sr_{0.3}MnO_3)_x(LaAlO_3)_y$ combinations in the reference supercell.

(2) *Normalization of the intensity profiles*

The integrated intensities of the reference profile are depicted in Figure 6.26. The integrated intensities of the reference vertical and horizontal profiles in the overlapping regions are different for each element because of differences in the integrating rectangles: 3 unit cells wide and 2 unit cells high for reference and horizontal profiles, respectively (indicated with light grey rectangles in the Figure 6.27(a)). In order to normalize the intensities a correction factor was applied for each element to match the averaged intensities of vertical and horizontals individual profiles within the overlapping boxes. Thus, as in the case of the horizontal profiles the reference one has been fitted to Gaussian peaks. The resulting normalized intensities of the horizontal profiles are shown in Figure 6.27 (b) and (c).

Figure 6.26: Fitted vertical profile (left) and integrated intensities (right) for each element at the position of the corresponding ions.
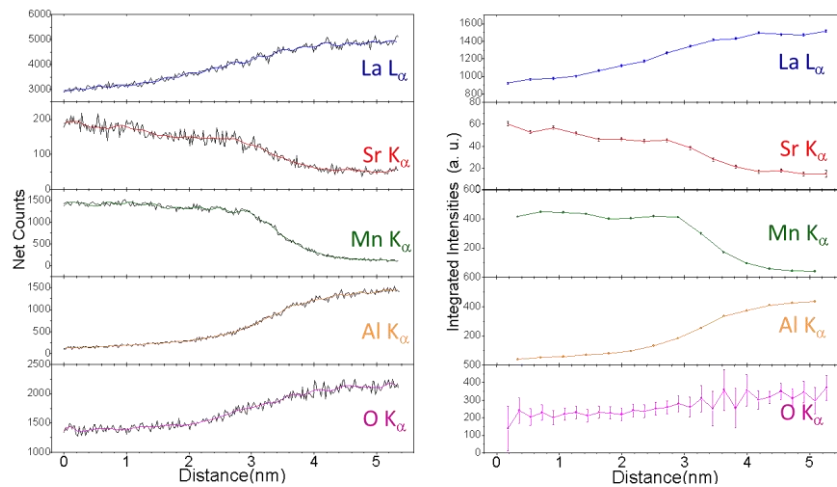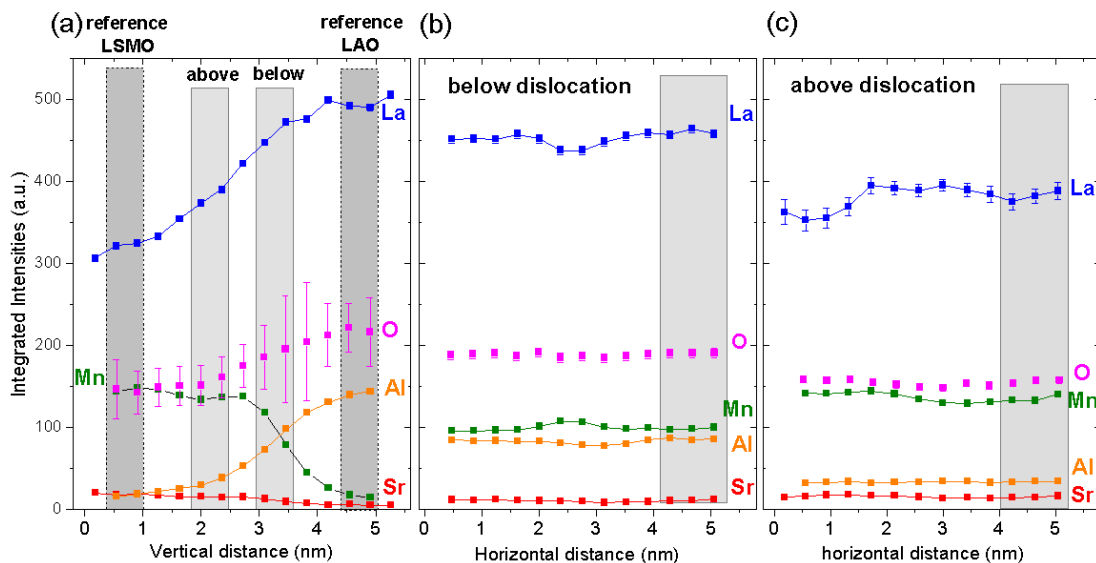

Figure 6.27: (a) Integrated intensities for the vertical [001] reference profile averaged at the *A*-site positions. Normalized intensities of the horizontal [001] profiles below (b) and above (c) the dislocation GP.

(3) *Quantification*

These normalized profiles are taken as the base for the quantification, combining the k-factors and the formulas presented previously. The resulting element concentration horizontal profiles are shown in Figure 6.28. The position of the axial plane is indicated by arrows. The elemental concentration profiles are not strictly symmetric with respect to the axial plane, probably due to inhomogeneities in the strain field and some inaccuracies in the integration reflected by the error bars. It can be clearly seen that the distribution of ionic species above and below the GP, that is in the tensile and compressive regions of the MD core, differ markedly between them.

In the compressive region, below the GP (compressive region), see Figure 6.28(a), the La profile is raised up to ~ 18at% and remains unperturbed by the presence of the MD, while the Sr concentration still shows a slight depression below the core. On the other hand, in the tensile region Figure 6.28(b), there is a clear enrichment in La accompanied by a symmetrical depletion of Sr, although the maximum ~ 2.5at% enrichment is not compensated by the decrease in Sr. This observation rules out Sr'_{Mn} antisite defects as the origin of the increased brightness observed at *B*-site positions sitting on the tensile region in the HAADF image shown in Figure 6.9 The unbalance between La enrichment and Sr depletion extents laterally across the MD and therefore cannot be explained by the formation of La^x_{Mn} antisite defects since they were always observed sitting on the axial plane. Taking into account the ionic radii of La^{3+} in cuboctahedral coordination, 1.36Å and Sr^{2+}, 1.44Å [229], the depletion of larger Sr atoms goes against the accommodation of the tensile strain above the GP.

Figure 6.28: Element concentration profiles of the regions below (left) and above (right) the dislocation GP.

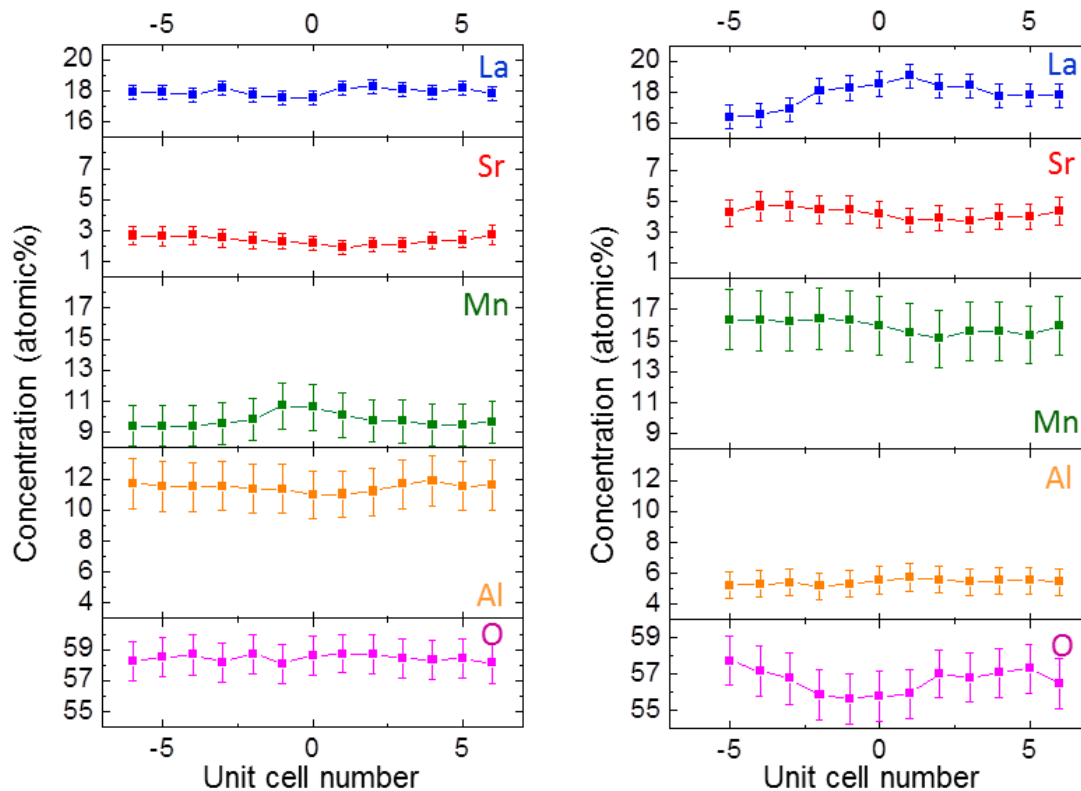The behaviour of *B*-site cations shows different trends. Comparing Figure 6.28 (a) and (b), one observes that above the GP they do not exhibit significant variations, while below it the Mn concentration shows an increase localized below the position of the MD core. The preferential substitution of Al^{3+} (ionic radius, 0.535Å) by larger Mn^{3+} (0.645Å) [229] in the compressive region is again counterintuitive from an elastic energy minimization point of view. However, this localized segregation of Mn nicely correlates with the anomalous dilatation observed in a similar dislocation, as shown in Figure 6.12, suggesting that it might be favoured by the specific core structure.

Comparing the oxygen concentration profiles obtained from the tensile and compressive regions of the MD, it becomes apparent that the GP marks the boundary between two well differentiated ionic landscapes. As commented above, vertical elemental indicate that there is background $V_O^{\cdot\cdot}$ concentration of about 3at% at the film and around the GP. Comparing Figure 6.28 (a) and (b), this background $V_O^{\cdot\cdot}$ concentration of about 3at% is preserved in the first two unit cells above and below the GP, but is selectively increased in the tensile region around the MD core. This behaviour strongly suggests that the vacancy formation energy is further reduced under tensile strain, in agreement with atomistic simulations in ceria [[231], STO [232]] and CaMnO$_3$[233, 234].

Chemical analysis of the interface between dislocations

In order to explore the chemical effects that produce the dislocations in the interface, the region between the dislocations was also analysed. EDS-SI were performed at the region between the dislocations in a cross-section view along [010] direction, following the same procedure described in the previous section.

Figure 6.29(a) shows a HAADF image of 6-nm-thick film where two dislocations may be distinguished marked with black arrows. The green rectangle marks the area used to obtain an EDS map between dislocations. The element concentration profile, obtained by summing the x-ray counts in the parallel direction of the interface of the whole EDS mapped area shown in Figure 6.29(b). The black continuous line in profile marks the dislocation GP as a reference. The profile shows that the interface is blurred by the diffusion between film and substrate. The width of diffusion region of the interface between the dislocations is defined here as the distance between the drop in concentration from 90% to 10%, which is marked with a discontinuous lines in the profiles. The extent of cation diffusion depends on the chemical species and an asymmetric interface is observed with respect to the *A* (Lanthanum and Strontium) and *B* (Manganese and Aluminium) cations. A-site cations interface is sharper (width ~2.3nm), while B-site cations interface seems chemically rougher (width ~ 3.5nm). A similar asymmetry between the extend of *A*- and *B*-site intermixing has been reported for other perovskite epitaxial films [235]. Taking the GP as a reference, it can be clearly seen that dislocations are located in the middle of the *B* cations diffusion interface; one or two unit cells above the interface the LAO. Moreover, as a general trend, the Al concentration (~ 2at%) is present in the whole thickness above the GP. In addition, the oxygen concentration profile shows a slight constant depression, ~ 3at%, on the film side, indicating a background level of oxygen vacancies,$V_O^{\cdot\cdot}$, throughout the film volume. According to the dislocation spacing, this film exhibits a compressive

residual strain of -0.8%, which might be enough to induce a noticeable decrease in oxygen vacancy formation energy [236].
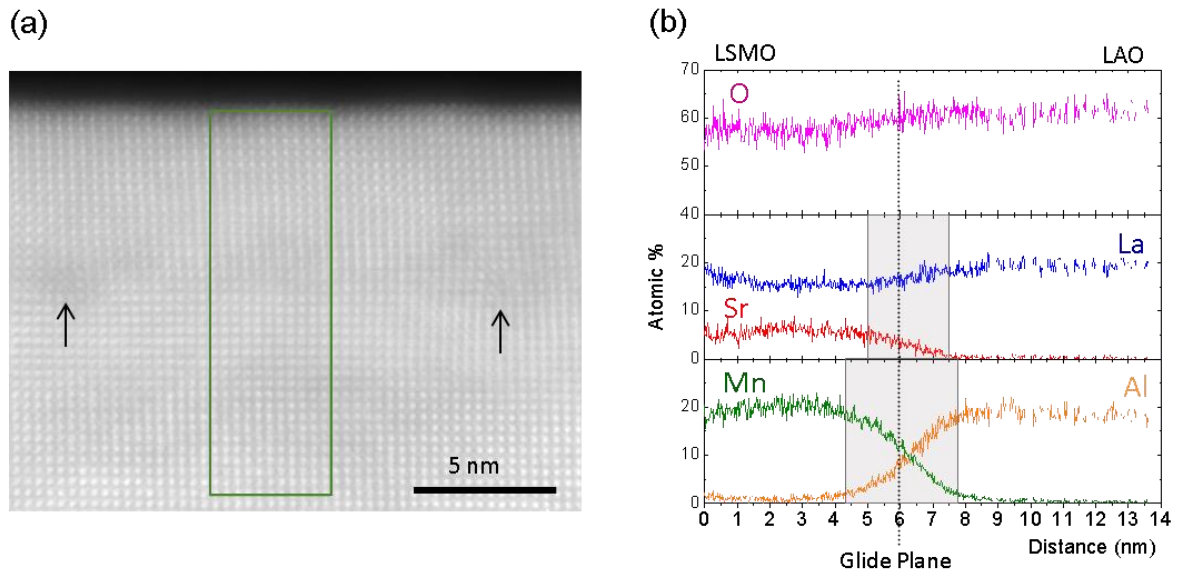

Figure 6.29: Chemical analyses of the interface region from LAO (right) to the LSMO surface (left). (a) A HAADF image with a green square marking the region used to obtain the EDS map between the dislocations. Black arrows mark the dislocations. (b) Elemental concentration profile obtained by integrating the EDS map area. Black continued line marks the position of GP. The respective diffusion regions are marked by grey windows.

The dual EELS-SIs obtained from the region between the dislocations also showed a diffusion zone at the interface. These EELS-SI are used to inspect the evolution of energy loss spectra O-k edge and Mn-L edge, respectively, across the interface between the dislocations. Figure 6.30(a) shows the HAADF image of 6 nm thickness film, where the squares indicate the integrated areas (approx. 1 unit cell) from which each spectrum were obtained by EELS-SI. The F spectrum in the LSMO, ~ 2.7nm above the GP, and the last one in the LAO substrate (S), ~ 2.8nm below the GP are considered the reference spectra from the LSMO and the LAO, respectively (presented previously in Figure 6.15) The region between these spectra includes the diffusion region observed by EDS. Six spectra are contained between these two spectra: three from above the GP to F spectra (IF1,IF2 and IF3) and three from under GP to S spectra (IS1, IS2 and IS3). The GP of the dislocation is situated between spectrum IF1 and IS1.

The O-*K* edge spectra presented in Figure 6.30(b) show that pre-peak intensity reduces as the spectra approaches the substrate where the pre-peak disappears, as in spectra IS2, IS3 and S. The intensity of the peak **b** under the GP increases and the shape becomes sharper and thinner as the spectra get closer to the S spectrum. The intensity of the peak **c** decreases slightly from the F spectra to the IF1 spectra, above the GP, and recovers again below the GP, where the intensity increases and the shape becomes sharper as the spectra get closer to the substrate (b) show that pre-peak intensity reduces as the spectra approaches the substrate where the pre-peak disappears, as in spectra IS2, IS3 and S. The intensity of the peak **b** under the GP increases and the shape becomes sharper and thinner as the spectra get closer to the S spectrum. The intensity of the peak **c** decreases

slightly from the F spectra to the IF1 spectra, above the GP, and recovers again below the GP, where the intensity increases and the shape becomes sharper as the spectra get closer to the substrate.
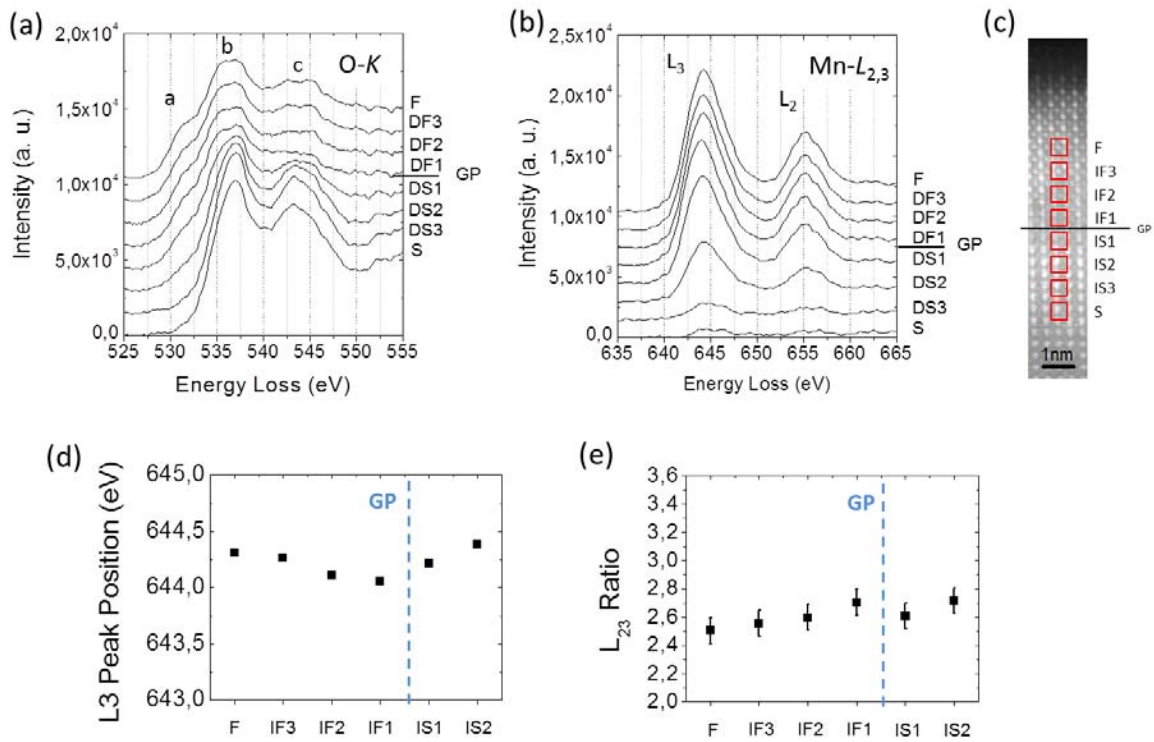
Figure 6.30: Evolution of energy loss O-K edge (a) and Mn-$L_{2,3}$ edge spectra (b) across the interface between dislocations. (c) HAADF image where the squares indicate the integrated areas from which each spectrum were obtained by an EELS-SI. Variation of the L_3 peak position (d) and the $L_{2,3}$ intensity ratio (e). The GP is marked by a vertical blue dashed line.

In the Mn-$L_{2,3}$ spectra presented in Figure 6.30(b) the intensity of the L_3 and L_2 peaks declines from the F spectra to the IF1 spectra and under the GP, both L_3 and L_2 peak intensities are slightly reduced as the spectra gets closer to the substrate and it disappears in IS3 and S spectra. This means that the transition from the film to the substrate is not sharp, it is gradual and starts in the position between IF2 and IF3 spectra, ~ 1.5 nm above the GP, and ends at the position of IS3, ~ 2 nm under the GP. This transition zone covers a region of ~ 3.6 nm, which agrees with the width of the diffusion region observed by EDS.

In addition, a subtle shift of peak L_3 towards less energy is observed in Figure 6.30(d), where the absolute value of the peak at each vertical position is presented. Considering that F is the bulk position of the L_3 peak, and assuming the average +3.33 at this position, an oxidation state decreases to +3.2 ± 0.03 at IF1, on the GP. Moreover, the Mn-$L_{2,3}$ ratio of these spectra are measured and presented in Figure 6.30(e). The evolution of the Mn-$L_{2,3}$ ratio follows a similar trend to the L_3 peak shift. Mn-$L_{2,3}$ ratio follows a gradual increase until reaching the GP.

6.4.4. Electrical charge per unit cell at the MD core

According to these results, the electrical charge per unit cell at the MD core was estimated assuming a Mn oxidation state of +3 and the cation stoichiometry derived from EDS analyses. Results obtained below and above the GP are shown in Figure 6.31 (a) and (b), respectively. It can be observed that the behaviour is drastically different under compressive (a) and tensile (b) scenarios. In the tensile case, a positive charge of $q \sim +0.32$ (± 0.09) decorates the MD core within a lateral range of 4 unit cells and decays with distance from the dislocation although the total extent of the fluctuation is larger than the size of the employed analytical window. Comparison between Figure 6.28 (a) and (b) reveals that the charge enrichment is spatially correlated with the $V_O^{\cdot\cdot}$ concentration. Interestingly, these chemical features are associated with an increased tetragonal distortion, $c/a > 1$. This observation clearly illustrates the coupling between strain and chemical properties in complex oxides at a local level, particularly through the strong sensitivity of $V_O^{\cdot\cdot}$ formation energies [236],[233, 234]. On the other hand, in contrast with the behaviour exhibited under a tensile strain, Figure 6.31 **(b)** shows that below the glide plane, where no preferential formation of $V_O^{\cdot\cdot}$s is observed (see Figure 6.28 **(a)**), charge neutrality is kept through the position of the MD. These results support previous theoretical studies suggesting a dependence of $V_O^{\cdot\cdot}$ formation energies on the sign of the strain [234]. This can be understood taking into account the chemical expansion induced by the reduction of Mn ions surrounding an electron donor $V_O^{\cdot\cdot}$. Moreover, the glide plane appears as a selective membrane for $V_O^{\cdot\cdot}$s, which in turn defines a sharp boundary between charged and neutral regions in the MD core. The observation of positively charged MDs draws a scenario opposed to that reported for MDs in a similar manganite based heteroepitaxial system, $Nd_{0.35}Sr_{0.65}MnO_3$/STO [116]. In that case, though not experimentally determined, it was assumed that no oxygen vacancies are formed in the core region. The mechanism proposed by those authors considers the reorganization of 2D pristine interfacial charges present prior to the formations of MDs into 1D chains along the dislocation strain fields when MDs are introduced in the interface. The present experimental results, however, are consistent with recent theoretical and experimental studies signalling the determining role of dislocation strains in promoting the generation of $V_O^{\cdot\cdot}$s [236] ,[233, 234]. These studies indicate that $V_O^{\cdot\cdot}$s are thermodynamically favored under strain, and thus exert a decisive control on the distribution of cationic species in the strain field, particularly by increasing the ionic volume of Mn as a consequence of the transfer of electrons from the vacancies into unoccupied $d\,e_g$ levels.

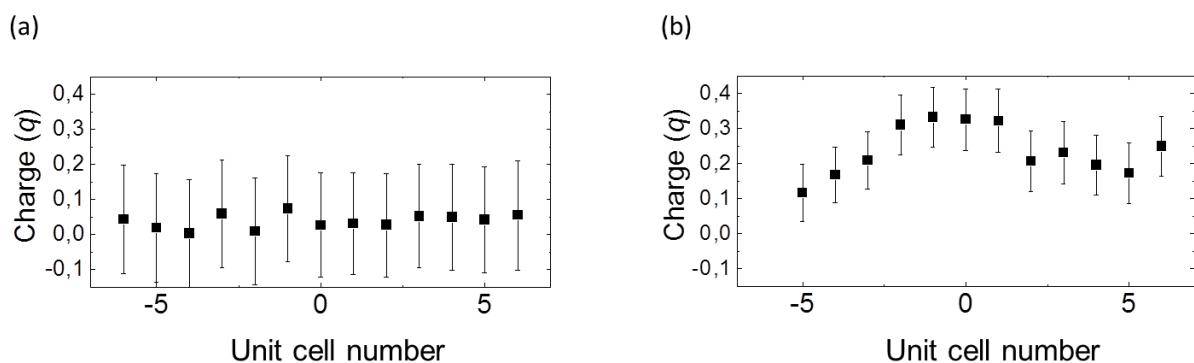(a)   (b)

Figure 6.31: Unit cell charge characteristics computed from the ionic distribution below (a) and above (b) the GP presented in Figure 6.18. Arrows mark the position of the axial plane of the misfit dislocation.

6.4.5.Spatial distribution mechanisms of ionic species around the misfit dislocation core

The basic mechanisms involved in the spatial distribution of ionic species around the MD core are schematically illustrated in Figure 6.32. As indicated, contrary to what would be expected from an elastic energy minimization perspective, Sr cations, larger than La, diffuse away from the tensile zone. This can be understood by the counterbalancing volume effect of the formation of La_{Mn}^x antisite defects, which according to the Shannon ionic radius of La^{3+} and Mn^{3+} in octahedral coordination, 1.032Å and 0.645Å, respectively [229], yield a huge localized positive dilatational strain of 60%. However, the strain field associated by a point strain source is known to induce a shear without dilatation in the neighbouring matrix as well as to decay as $1/r^3$ with distance, r, from the source [237]. Therefore, the strain accommodating effect of point defects is very local and requires an homogeneous distribution of point strain sources to be effective. On the other hand, $V_O^{\cdot\cdot}$s also accumulate in the tensile zone. The radius of an oxygen vacancy in the perovskite structure can be considered similar or slightly smaller than the radius of an oxide ion [231] and therefore their distribution will have only small or negligible effects on the accommodation of the MD strain field. The formation of $V_O^{\cdot\cdot}$s, on the other hand, has important consequences on the electronic structure of Mn ions; in principle each oxygen vacancy leaves two free carriers [238] (though at high vacancy concentrations this number can be lowered [239]) that are transferred to the Mn d band, thus reducing its oxidation state according to the redox reaction:

$$O_O^x + 2Mn_{Mn}^{\cdot} \leftrightarrow V_O^{\cdot\cdot} + 2Mn_{Mn}^x + \tfrac{1}{2}O_2 \uparrow \qquad \text{(Eq. 6.14)}$$
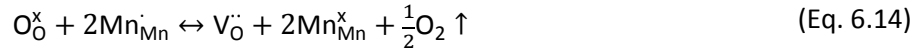
where Mn^{3+} is used as the reference state for the host B-site. According to Eq. 6.15, each oxygen vacancy releases two electrons which reduce two neighbouring Mn^{4+} cations. The average Mn$^{3+}_{0.7}$Mn$^{4+}_{0.3}$ cation has a radius of 0.610Å smaller than the ionic radius of Mn^{3+}. Considering a substitution rate of Mn^{3+} by Al^{3+} (octahedral radius, 0.535Å [229]) of 1/4, the radius of the average B-site cation becomes 0.617Å, close to the bulk value 0.610Å. Thus, within experimental errors, there are no significant differences between the ionic radii of the average B-site cations located in the tensile region and those located in the bulk film far from the influence of the MDs, suggesting that despite the observed cation intermixing most of the MD strain is accommodated by elastic distortion of interatomic bonds. Strikingly, the slight depletion of Sr, leading to a decrease in size of the average A-site cations in the tensile zone, is not compensated by any significant dilatation of the B-sites. In this scenario, the unique significant chemical expansion effect contributing to the relaxation of the tensile strain above the GP of the MD, comes from the formation of La_{Mn}^x antisite defects on the axial plane, which as commented above, have a very local compensation effect.

Interestingly, the results of the present study are in contrast to atomistic simulations of the distribution of trivalent dopants around an edge dislocation in ceria [231]. In that case, the driving force governing the distribution of dopants is the minimization of the elastic energy, i.e., larger dopants accommodate in the tensile zone whilst smaller ones replace Ce^{4+} in the compressive zone. Those authors also conclude that the spatial distribution of $V_O^{\cdot\cdot}$s is dictated by electrostatic interactions: positively charged oxygen vacancies are attracted by negatively charged trivalent dopants regardless they are located in the tensile o compressive regions of the dislocation. Taking

into account the LSMO stoichiometry, $La^{3+}_{1-x}Sr^{2+}_xMn^{3+}_{1-y}Mn^{4+}_yO_{3-\delta}$, charge neutrality imposes $\delta = (x - y)/2$. Since, on the basis of the present EELS analysis, Mn cations located in the neighbourhood of the MD core are in an oxidation state of +3, the charge neutrality condition becomes $\delta = x/2$, which in Kröger-Vink notation reads as $[Sr'_{La}] = 2[V_O^{\cdot\cdot}]$. This relation suggests that the observed depletion of Sr can be attributed to a tendency to minimize uncompensated charges, and importantly, that Sr depletes as a consequence of the preferential formation of $V_O^{\cdot\cdot}$s in the tensile zone. Hence, the positively charged region very likely results from the competition between elastic and electrostatic energies associated with the formation of $V_O^{\cdot\cdot}$s and the diffusion of Sr cations, i.e., the thermodynamic equilibrium value of $[V_O^{\cdot\cdot}]$ in the tensile zone is too high to be compensated by Sr depletion due to the larger ionic radius of Sr compared to the La one.
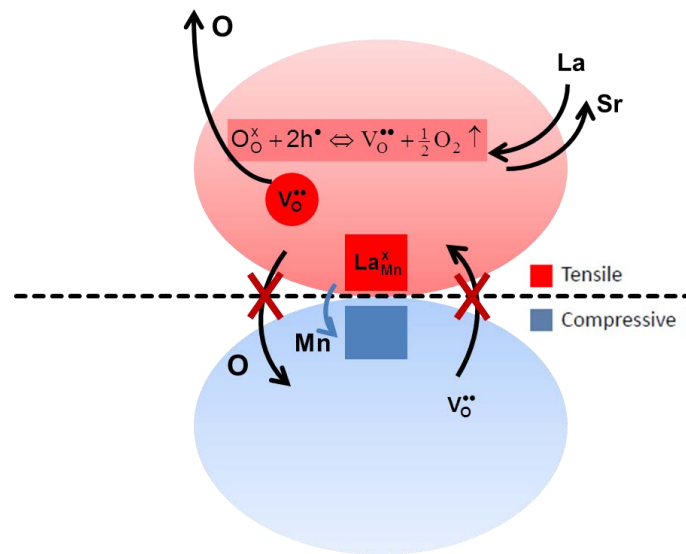
Figure 6.32: Schematic illustration of the basic mechanisms operating in the MD core. Red and blue represent tensile and compressive regions, respectively. The redox reaction indicated in the tensile region is displaced to the right, favouring the formation of electron donor oxygen vacancies, $V_O^{\cdot\cdot}$. Each vacancy nominally releases two electrons which can reduce two neighboring Mn^{4+} cations according to Eq. 6.16. The imbalance between the rate of Sr diffusion out of the core region and the concentration of $V_O^{\cdot\cdot}$ results in a positive charge at the tensile region. The GP acts as a barrier for the redistribution of vacancies as indicated by arrows. La^x_{Mn} antisite defects form at the axial plane, on the tensile region, to accommodate the tensile strain.

6.5. Evolution of misfit dislocations as a function of film thickness [225]

The evolution of MD density as a function of the thickness was analysed by OC-SEM. These images show lines as a projection of the MD network on the interface plane. Thus, OC-SEM images offer a direct method to reveal the presence of MD patterns much simpler than TEM. Figure 6.33 shows OC-SEM images of 2, 3.5, 6 and 14-nm-thick films. The thinnest film (2 nm thick) does not show any evidence of misfit dislocation formation, while 3.5 nm, 6 nm and 14 nm films present a pattern of lines. In the case of 6 nm and 14 nm films, a regular network is formed by a narrow distribution of MDs. Therefore, a critical thickness between 2.0 nm and 3.5 nm can be inferred for the formation of MDs.

2 nm

3.5 nm

6 nm
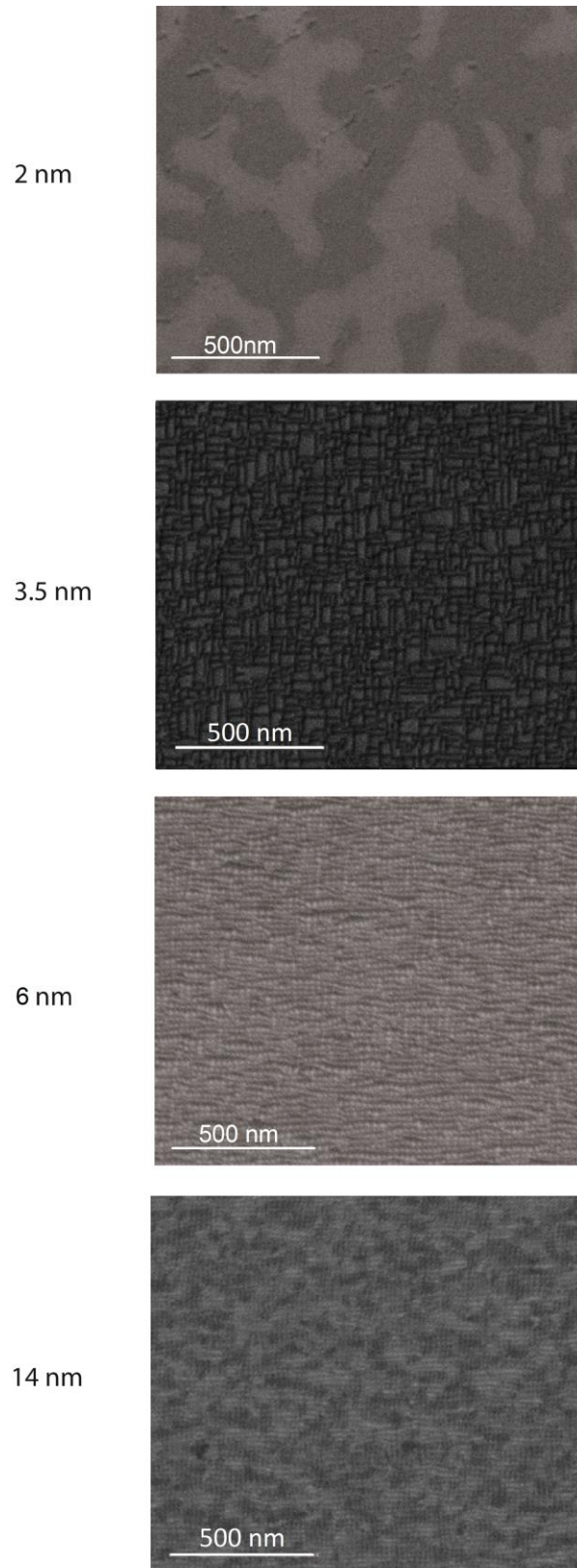
14 nm

Figure 6.33: OC-SEM images of 2, 3.5, 6 and 14-nm-thick films. Courtesy of Dr. Balcells.

6.5.1.Spacing and length evolution of MDs

A progressive increase of MD density as a function of thickness can be observed in Figure 6.33. OC-SEM images were used to quantify MD distribution as a function of film thickness. Figure 6.34 (a) shows the histograms obtained from 190 measurements (95 in each direction) of dislocations spacing for each SEM image. The histograms consist of a single mode Poisson distribution with different mean and standard deviation values. This type of distribution is different from bimodal distributions often observed in semiconductors (in the diluted MD dislocation regime) which are related to the interaction between 60° dislocations with opposite in-plane component to form pure edge dislocations [240]. The film with a 3.5 nm thickness shows a mean dislocation separation of around 38nm, which corresponds to a dislocation linear density of 2.6×10^5 cm^{-1}, while for the 7nm and 14 nm thick samples, the mean separations were 25 nm and 16 nm, respectively, with linear dislocation densities of around 4.0×10^5 cm^{-1} and 6.2×10^5 cm^{-1}.
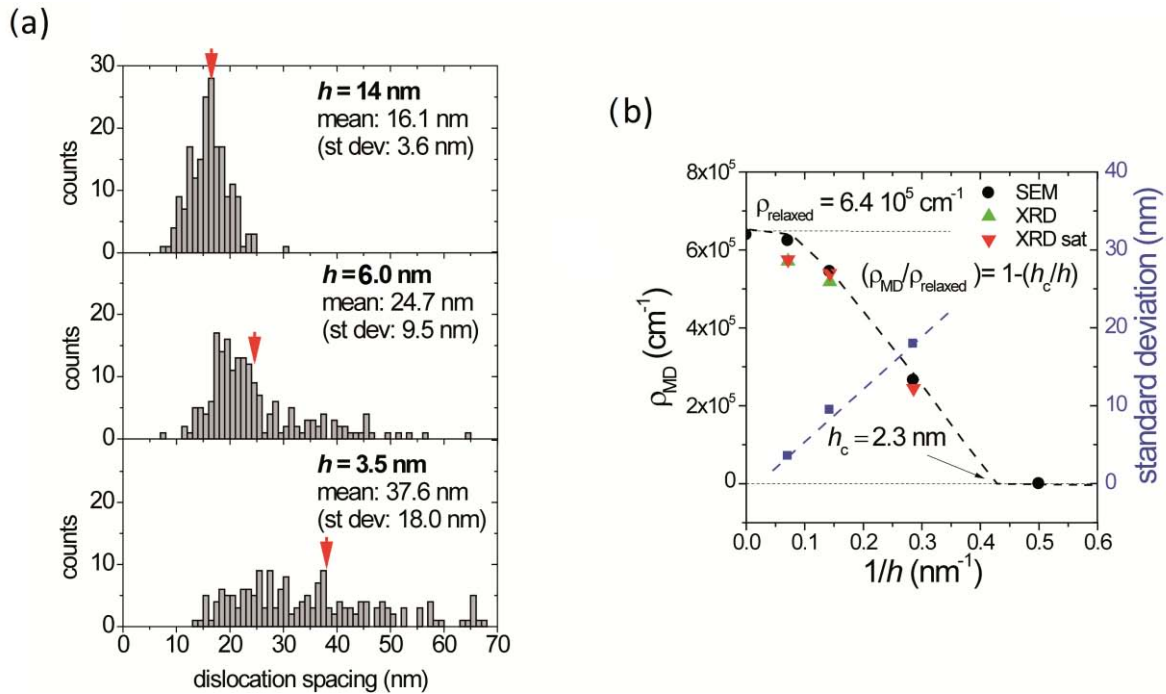
Figure 6.34: (a) Histograms of the separation between consecutive MDs measured from the SEM images of the films of different thicknesses (3.5 nm, 6 nm and 14 nm); (b) dependence of the linear dislocation density versus the reciprocal film thickness, as measured by SEM (black symbols) and XRD as estimated from the LSMO cell parameter values (green symbols), along with the standard deviation of the distribution by SEM (blue symbols) Figure from Santiso *et al.* [225].

Considering a fully relaxed LSMO film, with cell parameter a_{LSMO}= 3.881Å, the theoretical dislocation spacing can be calculated by

$$S= \frac{|b|}{\varepsilon}$$

(Eq. 6.19)

Assuming a burgers vector of one unit cell of the substrate, for example in the direction of [100], **b** = aLAO[100] (|**b**|= 3.79 Å), and a misfit Ɛ = -2.3%, the dislocation spacing for a full relaxation is S=16,5 nm, which corresponds to an MD density of 6.0×10^5 cm^{-1} and means one MD every ~ 43 unit cell of the LAO structure. This spacing is similar to the mean value for 14-nm-thick films measured by SEM images.

The MD spacing can be also estimated by using the in plane parameter values obtained by high-resolution XRD for each film thickness using (Eq. 6.19). For example, for 6 nm and 14nm, with 3.865 Å and 3.877 Å in-plane lattice parameters and Ɛ = -1.9 % and Ɛ = -2.2%, respectively, the spacings are 19.5 nm and 17 nm which corresponds to dislocation linear densities of 5.1×10^5 cm^{-1} and 5.8×10^5 cm^{-1}. All of these calculated values are in agreement with the spacing values measured by SEM.

Thus, the spacing between the MDs reduces with thickness, which translates into a progressive increase of the mean values of the experimental linear dislocation density, reaching almost full relaxation for the 14-nm-thick sample. Figure 6.34(b) shows the dislocations density (ρ), measured by the SEM images (in black) and by (Eq. 6.19) using the X-ray determined parameter (in red), as a function of the reciprocal film thickness (1/ h).

The relationship between MD density and reciprocal film thickness is roughly linear following the expression

$$\rho_{MD} = \rho_{relaxed}(1 - h_c/h) ,$$

(Eq. 6.20)

where h_c is a critical thickness. The MD density follows this expression above h_c and before it reaches saturation at the maximum dislocation density for the fully relaxed films, consistent with Matthews and Blakeslee's model [37]. Thus, the critical thickness value can be extrapolated from the thickness where ρ_{MD} = 0, which is approximately 2.5 nm.

The critical thickness may be derived from thermodynamic equilibrium considerations. Matthews and Blakeslee derived a self-contained expression for the critical thickness, h_c [241]

$$h_c = \frac{b}{4\pi Ɛ} \frac{(1 - v\,cos^2\theta)}{(1 + v)\,sin\,\theta\,cos\,\emptyset} \, ln(\frac{\alpha h_c}{b}) ,$$

(Eq. 6.21)

where b is the modulus of the Burgers vector, Ɛ is the magnitude of the misfit strain, v is the Poisson ratio, and θ and φ are the angles between the Burgers vector and the dislocation line and the interface plane, respectively. The value of the dislocation core parameter, α, may vary between α = 1 and α = 4, and in practical cases, it is obtained from experimental data. As an estimate, in this case, the value of α = 2.72 is assumed, first derived in the Matthews and Blakeslee theory [37]. The values of θ = 90°, φ = 0°, were used in this study. The Poisson ratio, v = 0.32, was calculated from the experimental LSMO cell parameters of the fully strained 2.0 nm film measured by high-resolution XRD, out-of-plane c = 3.985 Å and in-plane a = 3.790 Å. A h_c = ~ 2 nm is obtained, which is slightly

below the experimental. The good agreement between the theoretical and the observed h_c indicates that plastic relaxation is not retarded by kinetic barriers.

The standard deviation of the distribution of MD separation and the distribution of the lengths of the dislocation half-loops also changes with the MD density. The standard deviation is also shown in the graph in Figure 6.34(b) represented by blue dots. It also varies with film thickness, starting with a very wide dispersion for the 3.5-nm-thick sample, of around of ~ 18 nm, and reducing gradually to about 9.5 and 3.6 nm for the 6 and 14-nm thick films, respectively. This distribution follows an almost linear dependence with thickness, approaching a zero value for the thicker films, which indicates the trend towards an ordered arrangement of the MD network. Thus, at the start of MD formation, the standard deviation presents very large values indicating that the separation between the dislocations is random. However, as the MD density increases, the dislocation strain fields interact and progressively narrow their distribution.

On the other hand, the distribution in length of the dislocation half-loops is wide in the 3.5 nm-thick films, with a low density of MDs. In this film thickness, the length goes from tenths to several hundreds of nanometres as is observed Figure 6.33. While some MDs end within the film, most of the MDs end when they meet another perpendicular MD line. This observation is consistent with the ends of MDs turning into threading dislocation half loops emerging at the film surface, previously reported in SiGe and III–V semiconductors [242]. In the 6 nm film, the majority of lengths are hundreds of nanometres long, as observed in the SEM (Figure 6.33).

According to equilibrium theory, the energy barrier needed for a half-loop of critical radius to survive increases with decreasing misfit strain [243]. Therefore, as the misfit is relieved by expansion of existing half-loops, the nucleation of new ones becomes kinetically suppressed. As a consequence, the average dislocation length increases whilst their lateral spacing narrows as the films thicken, in excellent agreement with experimental observation. According to this evolution, the density of threading arms of MDs rapidly decreases as the films thicken, while the strain state of the films becomes determined by the increasingly ordered interfacial MD network.

6.6. Strain distribution within the volume of the dislocated film

6.6.1. In-plane distribution of the strain field:

To visualize the bulk strain state of the dislocated films, a planar view strain sensitive LAADF image was obtained from films with different thicknesses (3.5 nm, 6 nm and 14 nm), as can be observed in Figure 6.35. The change in the contrast in these types of images reveals the strain fields in the film caused by the presence of the buried misfit dislocations. Thus, in a 3.5-nm-thick film, bright lines corresponding to the dislocations can be observed, while the 6 and 14-nm-thick films show a more complex contrast pattern. They show a cross pattern formed by dark lines, where the dark contrast is more intense at the intersections, and with a dark contrast in the centres of the squares. To understand the information that comes from to these contrast patterns, they were compared with the spatial distribution of the residual in-plane strain $\varepsilon_{xx}(x,y)+\varepsilon_0$, arising from a square

network of **b**$_X$ =[100] and **b**$_Y$ =[010] dislocations, using continuum isotropic elasticity. ε_0 is background misfit strain, which in the case studied here is $\varepsilon_{0=}$ -2,3%.
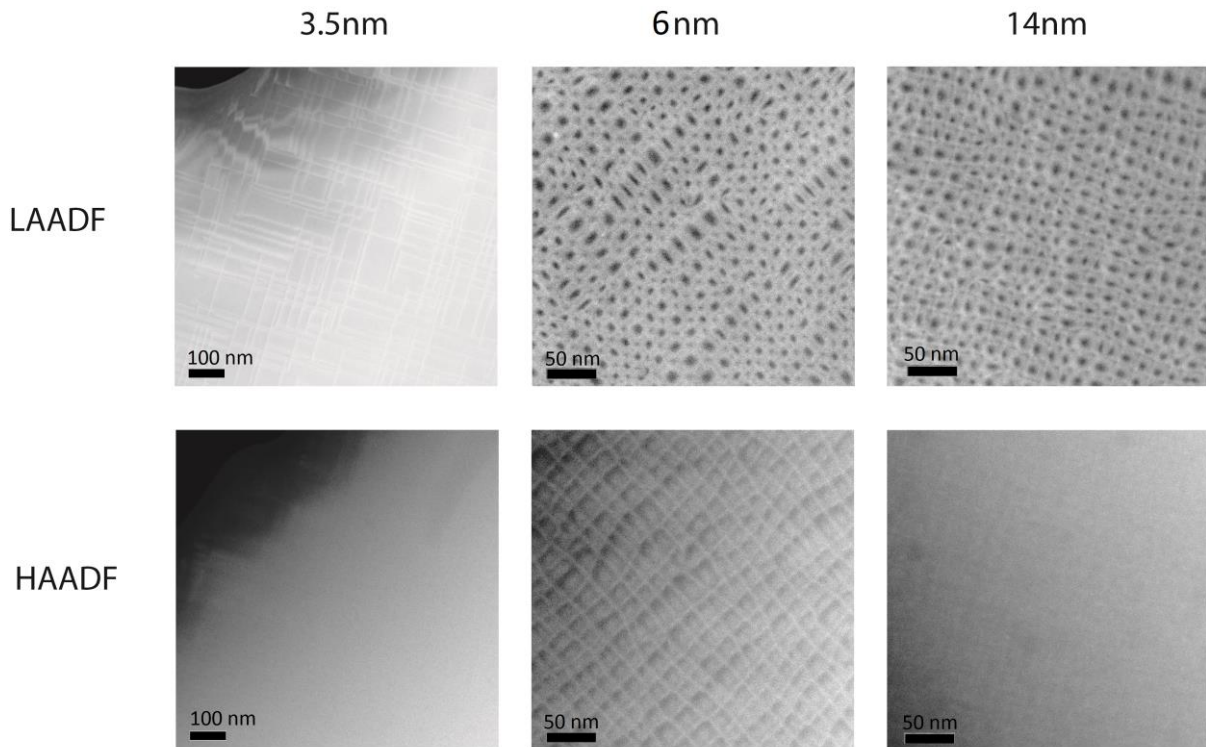
Figure 6.35: LAADF images of 3.5, 6 and 14-nm-thick films at the top from right to left and the corresponding HAADF images at bottom.

The calculated strain map for the 6-nm-thick film is shown in Figure 6.36(b), which presents a good correspondence with the LAADF experimental image (Figure 6.36(c)), in which darker areas correspond to a lower degree of misfit relaxation. Thus, minimum relaxation levels are found in the regions between the dislocations and along the locus of dislocation lines, with a lower minimum at the crossing points, as also observed in the experimental image.
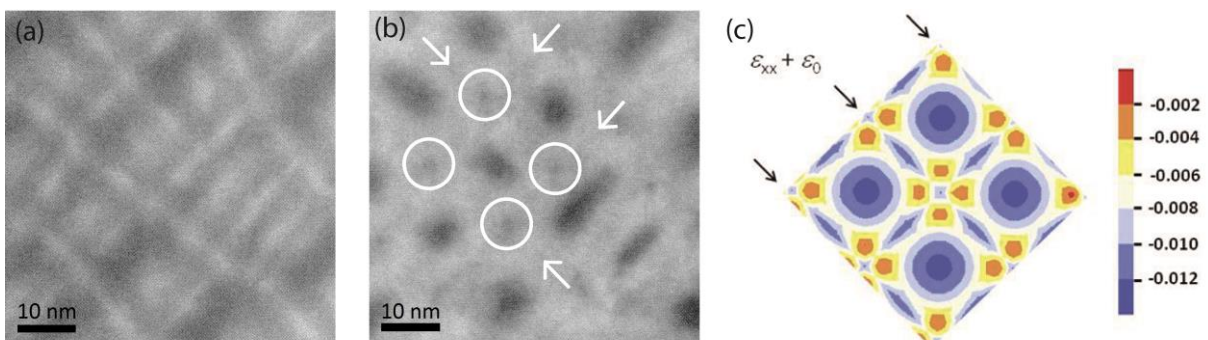
Figure 6.36: (a) and (b) Planar view HAADF image and the corresponding strain sensitive LAADF image of a 6-nm-thick film. Arrows indicate dislocation lines running along the [100] and [010] directions and circles mark their intersections. (c) Calculated distribution of residual strains ($\varepsilon_{xx}+\varepsilon_0$)(x,y) in a similar film; arrows indicate dislocation lines, and colours correspond to different strain levels, as indicated in the colour scale bar. Modified from F. Sandiumenge *et al.* [230]

6.7.Surface strain and functional properties [230]

The strain state of the free film surfaces is estimated using the displacement fields derived from the image dislocation approach [89]. The vertical and horizontal atomic displacements, u_z and u_x, at the free surface of a film with thickness d, induced by an interfacial dislocation with Burgers vector bx, are given by [244]

$$u_z(x) = \frac{b_x}{\pi}\left(\frac{d^2}{x^2+d^2}\right)$$

(Eq. 6.22)

$$u_x(x) = \frac{b_x}{\pi}\left[\frac{-dx}{x^2+d^2} + \tan^{-1}\left(\frac{x}{d}\right)\right] \ .$$

(Eq. 6.23)

Considering that $b_x = a$LAO = 3.79 Å, from (Eq. 6.22), the amplitude of the downward atomic displacement at the dislocation coordinate $x = 0$ is $b_x/\pi \approx \sim 1.20$ Å, in agreement with the displacement field determined from Figure 6.13. The modulation of the surface strain is then obtained by differentiation of (Eq. 6.23) $\mathcal{E}_{xx}(x) = \partial u_x(x)/\partial x$ giving

$$\mathcal{E}_{xx}(x) = \frac{b_x d}{\pi(x^2+d^2)}\left(\frac{x^2-d^2}{x^2+d^2}+1\right).$$

(Eq. 6.24)

The tensile strain given by (Eq. 6.24) is superimposed over the background compressive misfit strain produced by the substrate, $\mathcal{E}_0$, yielding a residual surface strain, $\mathcal{E}_{xx}(x) + \mathcal{E}_0$, which is represented in Figure 6.37 for the 3.5 and 6 nm thick films, respectively. This figure shows three dislocations, the central one at $x = 0$. The assumed dislocation spacings are 25 nm and 19 nm for 3.5 nm and 6 nm thickness films, respectively. For the 3.5-nm-thick film, almost total relaxation ($\mathcal{E}_{xx}(x) + \mathcal{E}_0$)) $\sim \mathcal{E}_0$ occurs at each side of the dislocation line at a distance of about ~ 4 nm. For the 6-nm-thick film, the overlapping of strain fields deletes the fluctuation between adjacent MDs. In this case, complete relaxation is achieved within a region of size similar to the thickness of the film located between the adjacent dislocations.
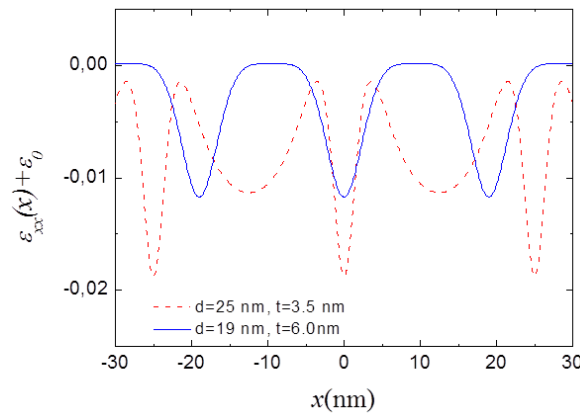
Figure 6.37 Calculated modulation of in-plane strain at the surface of 3.5 and 6-nm-thick films, originated from buried MDs; the spacing between MDs is the average spacing determined experimentally for each thickness. Modified from Sandiumenge *et al.* [230]

6.7.1. Modulation of film topography

A morphological transition occurs from a flat surface observed in the 2-nm-thick film to an undulated surface in thicker films occurs. Figure 6.38(a) shows HRTEM images in cross-section view along the [010] direction of the films of 2 nm, 3.5 nm and 6 nm thickness. The 2-nm-thick film presents a flat surface with unit-cell high steps, while the 3.5-nm-thick film presents an undulation of the surface. This surface undulation is due to outgrowths and a downward bending of the horizontal atomic rows above the dislocation core due to the vertical displacement field of the dislocation, $u_z = b/\pi \sim$ 1.2Å [230]. The outgrowths tend to be formed on the surface at each side of the projected line of the buried MDs (indicted by red arrows in Figure 6.38(a)). Figure 6.38(c) shows AFM images in planar view of the 3.5 and 6-nm-thick films. In agreement with the cross-section HRTEM image of the 3.5-nm-thick film, it is clearly seen that the surface topography consists of a network of ridges and terraces mimicking the underlying dislocation network. Hence, the outgrowths correspond to a section of the ridges observed in the AFM image. However, in thicker films, the outgrowths are no longer present while the bending of atomic planes prevails independently of film thickness, as can be seen in the HRTEM image of the 6-nm-thick film (Figure 6.38(a)). The bending caused by the displacement field of the dislocations, u_z, is clearly seen as a crossed pattern of parallel lines following the [100] and [010] directions in the AFM images, as can be observed in the 6-nm-thick film (Figure 6.38(b)).

Figure 6.38: (a) HRTEM images in cross-section view of films of 2 nm, 3.5 nm, 6 nm thickness (from top to bottom). Orange arrows indicate the dislocation position while the red arrows indicate the outgrowths. AFM images of 3.5 and 6-nm-thick films. Figure adapted F. Sandiumenge *et al.* [230]

The link between the morphological evolution of a free surface and the surface strain state is given by the surface chemical potential [245] $\mu(x) = \mu_0 + \gamma\Omega\kappa(x) + \Omega w(x)$ where µ0 is the c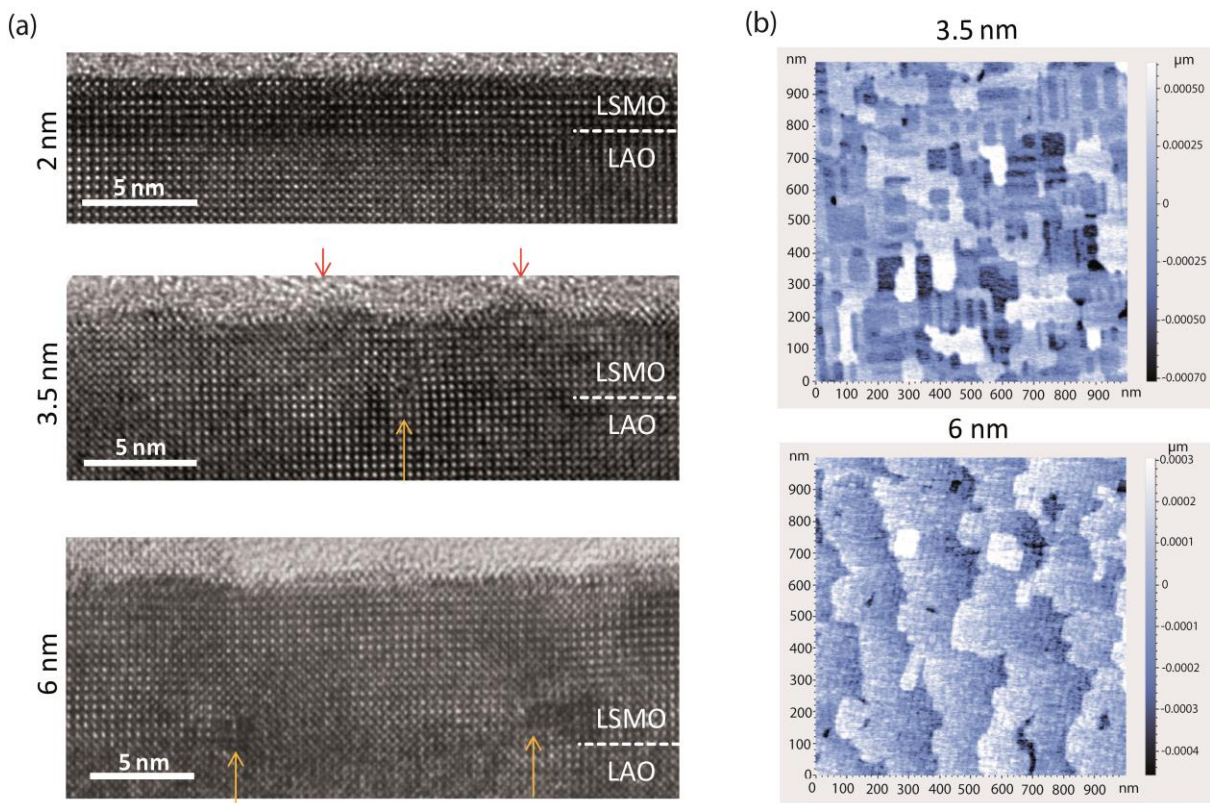hemical potential of the unstressed flat surface, γ is the surface free energy per unit area, Ω is the volume of a growth unit, κ(x) is the surface curvature and w(x) is the local surface strain energy density [246]. Assuming a reasonably flat surface, κ ~ 0, the modulation of the driving force for strain induced surface mass transport due to an underlying pure edge MD located at x=0, Δµ0(x) = µ(x) - µ0 = Ωw(x), can be expressed as

$$\Delta\mu_0(x) = \Omega M\left(\varepsilon_0^2 + \varepsilon_0\varepsilon_{xx}(x) + \frac{\varepsilon_{xx}^2(x)}{2+2v}\right),\tag{Eq. 6.25}$$

where $M = 2G(1+v)/(1-v)$. According to Eq. (6.25), growth units will migrate from highly strained regions to find stable positions at locations exhibiting minimum $\Delta\mu_0(x)$ values at each side of the dislocation. To illustrate this, Figure 6.39 depicts the chemical potential reduction relative to the position of the MD, as a function of distance, x: $\Delta\mu_d(x) = \mu(x) - \mu_d$ (μ_d is the surface chemical potential at the position of the MD) for the 3.5 and 6-nm-thick films. For the 3.5nm film, the fluctuation draws two minima at each side, ~ 4nm away from the MDs. This abrupt gradient in $\Delta\mu_d(x)$ should induce the preferential nucleation of LSMO at each side of the MDs, leading to the formation of the observed topographic pattern in the 3.5-nm-thick film. However, MDs can easily move to rearrange their positions due to the GP being parallel to the interface plane, thus those surface features do not necessarily appear to be associated with them.
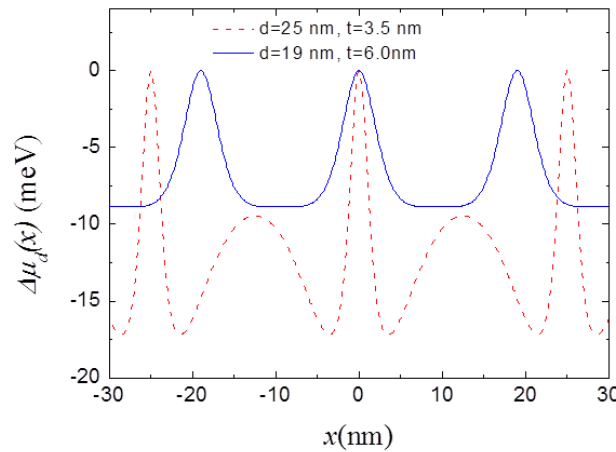
Figure 6.39: Modulation of the surface chemical potential corresponding to Figure 6.37.

It should also be noted that there exists a kinetic limitation for the vertical growth of the ridges: Once a ridge is formed, the rapid increase in surface curvature at that point causes competition between the surface energy, $\gamma\kappa(x)$, and strain energy, $w(x)$, in terms of the chemical potential, eventually hindering its vertical growth. This scenario drastically changes as the film surface moves further apart from the dislocation strain sources and the dislocation lines get closer, as exemplified by the 6-nm-thick film (Figure 6.39). The plot clearly shows that a thickness increase of 2.5nm results in nearly a 50% decrease in the amplitude of the fluctuation in $\Delta\mu_d(x)$. This effect

contributes to homogenization of the chemical potential throughout the surface, resulting in flatter films, in agreement with experimental observations presented in Figure 6.38. Therefore, the formation of terraces in the 3.5-nm-thick film, exhibiting a wider dispersion in *S* values, can be attributed to the overlapping of the strain field in regions with locally enhanced MD densities.

6.7.2. Impact of misfit dislocations on surface currents

The surface conduction properties of the films were analysed by C-AFM. Figure 6.40 shows the AFM images (a) and corresponding *I*(x,z) current map (b) for a 3.5-nm-thick film. Current enhancements are clearly seen as dark contrasts decorating surface steps, which are attributed to the extended tip-surface contact area along their ledges. Within the terraces, brighter lines of depressed current are also observed along the in-plane [100] directions. For the 6-nm-thick films, the topographic ridge/terrace pattern is no longer present (Figure 6.40(c)) and the corresponding current map still exhibits current depressions along lines parallel to the in-plane <100> directions, as seen in Figure 6.40(d). Both, topographic and conduction images are correlated with the underlying MD network, as the spacing between the brighter lines agrees with the spacing between the dislocations. For example, for 6-nm-thick films a line spacing of 22 nm was obtained from current map, which is similar that this measured from SEM images.

Figure 6.40: Topography (a)-(c) and simultaneous current map (b)-(d) for 3.5 and 6-nm-thick films, respectively. Dashed lines on the current map serve as a guide to highlight the impact of the dislocation network at the surface.

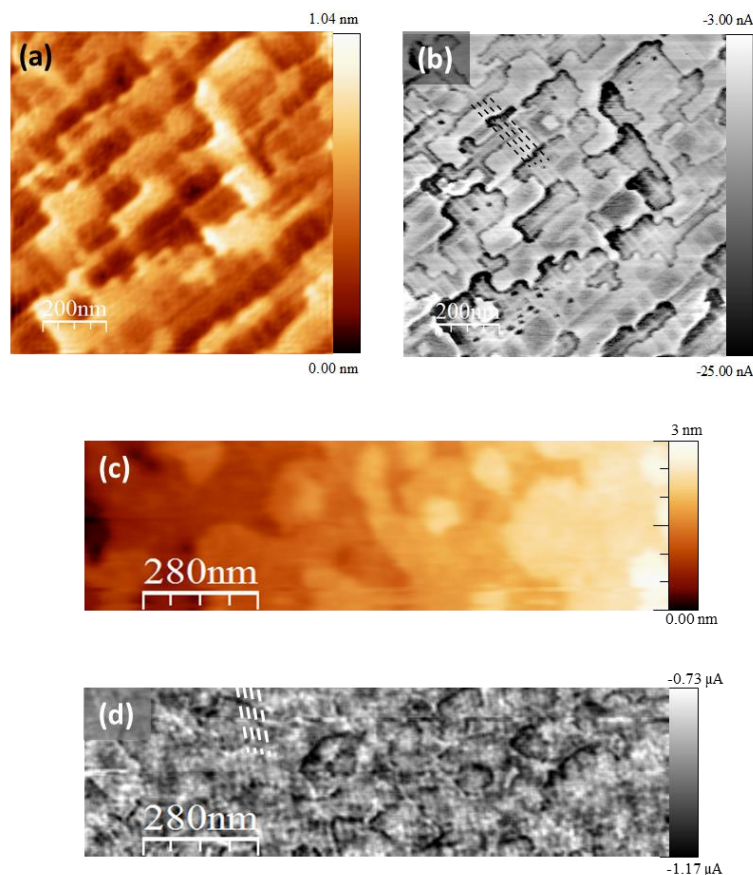The influence of strain on the magnetotransport properties of ABO_3 perovskite compounds is mediated through the relative modifications induced by the tilt and distortion processes of the MnO_6 octahedral framework. The <Mn-O-Mn> bond angle and the Mn-O bond length control the overlap integrals between the Mn $3d$ and the O $2p$ orbitals. An elongation of the Mn-O distances or a decrease of the <Mn-O-Mn> bond angle, would promote a reduction of the strength of double exchange ferromagnetic interactions and therefore, a reduction of the ferromagnetic Curie temperature, T_C, and an increase of electrical resistivity. On the contrary, the reduction of Mn-O distances or the straightening of the <Mn- O-Mn> bond angle promotes the strengthening of double exchange ferromagnetic interactions and a reduction of resistivity. Nevertheless, this scenario may be strongly affected by selective orbital occupancy and antiferromagnetic superexchange interactions. The balance between these competing effects is controlled by the ratio between perpendicular and in-plane lattice parameters c/a, reflecting the degree of tetragonal distortion of the structure [47]. In such a scenario, increasing c/a >1.0 works against the metallic ferromagnetic behaviour and promotes an increment of the resistivity. As was previously mentioned in section 6.4.2, the c/a ratio locally increases above the position of the dislocation core. This strong enhancement of c/a (tetragonal distortions) is fully consistent with the observed increase in electrical resistivity.

Overall, this analysis gives a view of partly relaxed LSMO/LAO thin films as a conducting compressed matrix, decorated with nanometric paths of less conducting material aligned in the in-plane [100] and [010] directions.

6.8. Conclusions

This chapter has examined the relaxation mechanism of LSMO films grown under compressive stress and the detailed structural and chemical features of dislocation core structures and their associated strain fields.

Misfit dislocations are formed at the interface between LSMO on LAO, above a critical thickness of about ~ 2.5 nm, as a relaxation mechanism to accommodate the misfit between them. The dislocation cores are dissociated, formed by two extra half planes. These planes leave a plane of AO composition, under a GP, which continues as a BO plane above the dislocation, or the contrary, depending on the GP and extra planes composition. The dislocation core is characterized by a tensile region above the GP and compression region below the GP. HAADF imaging and spectroscopic analysis of the dislocation core reveal a particular behaviour of ionic species around the dislocation cores. The HAADF images reveal the presence of La_{Mn}^x antisite defects in the tensile zone. The spectroscopic analysis show variations of the elemental concentrations related with the dislocations core: i) an increase of the La/Sr, ii) $V_O^{\cdot\cdot}$ accumulation, and iii) a reduction of Mn, in the tensile zone. The depletion of Sr, leading to a decrease in size of the average A-site cations in the tensile zone, is not compensated by any significant dilatation of the B-sites. This suggests that, the unique chemical expansion contributing to the relaxation of the tensile strain above the GP of the MD, comes from the formation of La_{Mn}^x antisite defects on the axial plane. The origin of this behaviour results from a

complex interplay between elastic and electrostatic energies, along with the thermodynamic driving force toward the formation of V$_O^{\cdot\cdot}$s in the tensile zone.

The particular procedure used for EDS data processing reveals that a best fit of the quantification results is obtained if the k- factors are calculated considering a single ((LSMO)$_x$(LAO)y) phase. In addition, the best fit is found when the interface plane of the supercell is considered to coincide with the glide plane.

Misfit dislocations exhibit a strong tendency toward self-organization on the interface plane in order to minimize elastic interactions between them. The MDs density increases as the films thicken, following a linear dependence with the reciprocal thickness, forming a highly ordered periodic crossed network of edge dislocations. The miniaturization limit imposed by misfit dislocation mechanisms is the equilibrium dislocation spacing for total relaxation, bx/ε; in the case studied here about 16nm, below the limits achieved by top-down approaches (about 80nm).

The strain field of MDs introduces a lateral modulation of the surface topography and the bandwidth-dependent properties at the free surface of the film. The two basic mechanisms leading to the formation of these ordered functional patterns at the surface of LSMO/LAO thin film are identified as: a) a lateral modulation of the surface chemical potential, leading to topographic patterning; and b) a lateral modulation of the tetragonal distortion, *c/a* ratio, leading to a surface current pattern.

This investigation demonstrates that the multiscale nature of dislocations holds great promise for the creation of spontaneous surface ordered functional nanostructures in complex oxide thin films.

Chapter 7

General conclusions and outlook

7.1. General Conclusions

The work reported in this thesis presents an exhaustive microstructural characterization of nanostructured heteroepitaxial films of functional oxide systems, focusing on the structure of the interfaces and strain-relieving defects. The characterization was performed by applying imaging and spectroscopic techniques using transmission electron microscopy. Two main different systems were investigated: a $LaMnO_3:MnO_x$ (LMO) nanocomposite epitaxial films grown on $SrTiO_3$ and $LaAlO_3$ substrates; and nanostructured $La_{0.7}Sr_{0.3}MnO_3$ (LSMO) epitaxial films with self-organized misfit relieving defects grown on $SrTiO_3$ and $LaAlO_3$ substrates.

In the case of LMO films, the growth kinetics promoted the segregation of secondary phases to compensate the chemical imbalance. In the case of LSMO films, the strain associated with the mismatch between the lattice parameters of film and the substrate, either tensile or compressive, as well as differences in shear angle, is relieved by the formation of self-organized twins domains or dislocations, respectively. From this point of view, all the systems studied may be regarded as nanostructured films.

The main conclusions obtained from each system are as follows:

In chapter 4 the spontaneous formation of regular vertically aligned nanoinclusions of a manganese oxide (MnO_x) embedded in an antiferromagnetic $LaMnO_3$ matrix was analysed in detail.

- The orthorhombic LMO matrix exhibits twin domains due to the Jahn-Teller transition occurring during cooling. The values of in-plane lattice parameters indicate that the LMO thin films are almost in a relaxed state.
- The spectroscopic analysis and HRTEM imaging suggest that the nanoinclusions are Mn_3O_4, accommodating the Mn^{2+} cations reduced under the employed growth conditions.
- The vertical Mn_3O_4 nanoinclusions present a wedge shape and their size and distribution are self-organized within the LMO matrix. The orientation relationship of the nanoinclusions, basically aligned with the main axes of the STO substrate and the LMO matrix, results from the accommodation of the cubic Mn_3O_4 spinel structure, which nucleated in cubic LMO matrix during the growth at elevated temperatures.

- An epitaxial La-rich Ruddlesden-Popper phase (La_2MnO_4) was identified close to the interface between the LMO and the substrate. The presence of this phase suggested that the stoichiometry imbalance generated by the nucleation of Mn_3O_4 inclusions is accommodated by the creation of this La-rich secondary phase.

In chapter 5, a microstructural study of epitaxial $La_{0.7}Sr_{0.3}MnO_3$ films grown on $SrTiO_3$, and therefore submitted to a tensile strain, was performed. This work consisted of a detailed analysis of the twin domain and the twin wall structure, as well as their implications on the film functional properties.

- Twin domains are distinguished in low-magnification TEM and STEM (MAADF-LAADF) images due to the contrast changes associated to the different orientations of the domains. However, in high resolution images (HRTEM and HAADF), the twin contrast is practically absent and their position was identified by the subtle tilt of atomic planes across the (100) or (010) twin walls.
- An increase of the twin angle was found in the vicinity of the twin wall. In cases where a twin domain was observed to disappear towards the substrate, the tilt angle is observed to decrease gradually. Apparently the TW does not reach the interface, but ends at an interfacial layer which very likely exhibits a different crystal structure.
- Surprisingly, the accurate strain analysis of the twin walls region revealed that, despite the overall biaxial tensile strain of the LSMO matrix, the twin wall is subject to a substantial uniaxial compression.
- An enhancement of the local electric conductivity and the strengthening of the magnetic interactions dereminated at the twin wall was associeted with this compressive state.
- Thus, it is postulated that these twinned LSMO films could be viewed as a self-organized nanostructure consisting of 1-nm-thick vertical sheets of strongly compressed LSMO material exhibiting different functional properties embedded in a matrix of tensile strained LSMO.

In chapter 6 the relaxation mechanisms of $La_{0.7}Sr_{0.3}MnO_3$ films grown under compressive stress on $LaAlO_3$ were examined. The local structure and chemical environment around the misfit dislocations was carefully analysed to conclude the following features:

- The formation of misfit dislocations at the LSMO-LAO interface was observed as a relaxation mechanism to accommodate the large compressive misfit between both materials.
- Misfit dislocations exhibit a strong tendency toward self-organization on the interface plane in order to minimize elastic interactions between them. Progressively, the MD density increases forming a periodic crossed network of edge dislocations with a highly ordered distribution. The miniaturization limit imposed by misfit dislocation mechanisms is the equilibrium dislocation spacing for total relaxation, b_x/ε: in the case studied here about 16nm.
- A detailed analysis of the dislocation core structure shows that those were in fact dissociated into two partial dislocations, formed by two extra half planes. The dislocation core is divided into a

tensile region above the glide plane and compressive region under the glide plane. A particular distribution of ionic species was found around the dislocation cores, which resulted from a complex interplay between elastic and electrostatic energies, along with the thermodynamic driving force toward the formation of $V_O^{\cdot\cdot}$s in the tensile zone.

- The strain field of MDs projected from their cores produced a lateral modulation of the chemical potential and the bandwidth-dependent properties at the free surface of the film, which is capable of a) modifying the local surface morphology above the MD lines, leading to a topographic pattern, as well as b) generating a lateral modulation of the tetragonal distortion (c/a ratio), leading to a surface current pattern.

- This investigation demonstrates that the dislocations hold great promise for the creation of spontaneous surface ordered functional nanostructures in complex oxide thin films.

Despite the fact that the mechanisms underscored in this work could be exclusive for LMO or LSMO epitaxial films and very likely limited to the specific constraints like: substrate mismatch, film thickness, and deposition conditions, it is envisaged that other heteroepitaxial structures combining complex perovskite oxides may show a similar hierarchical behaviour. The results shown in this work have evidenced how intricate the interplay could be between the structural, compositional and electronic features in locally distorted regions, which substantially deviate from a usually conceived lineal strain-versus structure standard models.

7.2. Outlook for future research

Self-organization of strain relieving defects in complex oxides is challenging as it needs control on strain relaxation mechanisms. In addition, the local effects in the film properties due to the presence of the defects are strongly linked to the defect structure and its associated strain field. In this regard, a detailed characterization of the defects and interfaces is essential to understand not only the relaxation mechanisms, but also the local effects in the film functional properties.

Given the continuous advances in transmission electron microscopy imaging and spectroscopy techniques it is envisaged that progressively more insight will be gained in film characterisation with higher resolution. This is the case of recent progress in annular bright field images, which permits acquisition of information about lighter oxygen positions. This will be an extraordinary tool to explore the complete structure of dislocation cores and twin walls, since most of the complex transition metal oxide features are determined by the oxygen coordination, octahedral rotations, oxygen vacancies, as well concomitant changes in transition metal oxidation state. In addition, EELS analyses with improved energy resolution as well as atomic-scale lateral resolution at the defect region and at the interfaces will provide information of the electronic structure and changes in the coordination of elements. In this respect, the exploration of O-K edges will be essential to complete the characterization of the defects and interfaces. In the case of LSMO/STO interfaces, the structural information presented in this work suggests that an interface in twinned films is different from those

obtained in non-twinned films (ultrathin films). These analyses will reveal the interface coupling mechanisms in each case.

Bibliography

[1] J.M. Rondinelli, N.A. Spaldin, Structure and Properties of Functional Oxide Thin Films: Insights From Electronic-Structure Calculations, Advanced Materials, 23 (2011) 3363-3381.

[2] P. Zubko, S. Gariglio, M. Gabay, P. Ghosez, J.-M. Triscone, Interface Physics in Complex Oxide Heterostructures, Annual Review of Condensed Matter Physics, 2 (2011) 141-165.

[3] H.Y. Hwang, Y. Iwasa, M. Kawasaki, B. Keimer, N. Nagaosa, Y. Tokura, Emergent phenomena at oxide interfaces, Nat Mater, 11 (2012) 103-113.

[4] A. Ohtomo, H.Y. Hwang, A high-mobility electron gas at the $LaAlO_3/SrTiO_3$ heterointerface, Nature, 427 (2004) 423-426.

[5] A. Gozar, G. Logvenov, L.F. Kourkoutis, A.T. Bollinger, L.A. Giannuzzi, D.A. Muller, I. Bozovic, High-temperature interface superconductivity between metallic and insulating copper oxides, Nature, 455 (2008) 782-785.

[6] N. Reyren, S. Thiel, A.D. Caviglia, L.F. Kourkoutis, G. Hammerl, C. Richter, C.W. Schneider, T. Kopp, A.-S. Rüetschi, D. Jaccard, M. Gabay, D.A. Muller, J.-M. Triscone, J. Mannhart, Superconducting Interfaces Between Insulating Oxides, Science, 317 (2007) 1196-1199.

[7] V. Garcia, M. Bibes, L. Bocher, S. Valencia, F. Kronast, A. Crassous, X. Moya, S. Enouz-Vedrenne, A. Gloter, D. Imhoff, C. Deranlot, N.D. Mathur, S. Fusil, K. Bouzehouane, A. Barthélémy, Ferroelectric Control of Spin Polarization, Science, 327 (2010) 1106-1110.

[8] V.M. Goldschmidt, Die Gesetze der Krystallochemie, Naturwissenschaften, 14 (1926) 477-485.

[9] J.M.D. Coey, M. Viret, S. von Molnár, Mixed-valence manganites, Advances in Physics, 48 (1999) 167-293.

[10] H.D. Megaw, Crystal Structures: A Working Approach, W.B. Saunders Co., Philadelphia, (1973).

[11] M.W. Lufaso, P.M. Woodward, Jahn-Teller distortions, cation ordering and octahedral tilting in perovskites, Acta Crystallographica Section B, 60 (2004) 10-20.

[12] P. Woodward, Octahedral Tilting in Perovskites. II. Structure Stabilizing Forces, Acta Crystallographica Section B, 53 (1997) 44-66.

[13] A. Glazer, The classification of tilted octahedra in perovskites, Acta Crystallographica Section B, 28 (1972) 3384-3392.

[14] A. Glazer, Simple ways of determining perovskite structures, Acta Crystallographica Section A, 31 (1975) 756-762.

[15] P. Woodward, Octahedral Tilting in Perovskites. I. Geometrical Considerations, Acta Crystallographica Section B, 53 (1997) 32-43.

[16] C.J. Howard, H.T. Stokes, Group-Theoretical Analysis of Octahedral Tilting in Perovskites, Acta Crystallographica Section B, 54 (1998) 782-789.

[17] J. Kanamori, Crystal Distortion in Magnetic Compounds, Journal of Applied Physics, 31 (1960) S14-S23.

[18] J.K. Burdett, Use of the Jahn-Teller theorem in inorganic chemistry Inorganic Chemistry, 20 (1981) 1959-1962.

[19] J.B. Goodenough, Jahn-Teller Phenomena in Solids, Annual Review of Materials Science, 28 (1998) 1-27.

[20] H.T. Stokes, E.H. Kisi, D.M. Hatch, C.J. Howard, Group-theoretical analysis of octahedral tilting in ferroelectric perovskites, Acta Crystallographica Section B, 58 (2002) 934-938.

[21] J.M. Rondinelli, A.S. Eidelson, N.A. Spaldin, Non-d⁰ Mn-driven ferroelectricity in antiferromagnetic $BaMnO_3$, Physical Review B, 79 (2009) 205119.

[22] S. Maekawa, T. Tohyama, S.E. Barnes, S. Ishihara, W. Koshibae, G. Khaliullin, Physics of Transition Metal Oxides, Springer-Verlag Berlin Heidelberg, 2004.

[23] H. Brune, M. Giovannini, K. Bromann, K. Kern, Self-organized growth of nanostructure arrays on strain-relief patterns, Nature, 394 (1998) 451-453.

[24] M. Abbate, F.M.F. de Groot, J.C. Fuggle, A. Fujimori, O. Strebel, F. Lopez, M. Domke, G. Kaindl, G.A. Sawatzky, M. Takano, Y. Takeda, H. Eisaki, S. Uchida, Controlled-valence properties of $La_{1-x}Sr_xFeO_3$ and $La_{1-x}Sr_xMnO_3$ studied by soft-x-ray absorption spectroscopy, Physical Review B, 46 (1992) 4511-4519.

[25] J. Stöhr, H.C. Siegmann, Magnetism. From Fundamentals to Nanoscale Dynamics, Springer-Verlag Berlin Heidelberg, 2006.

[26] A. Urushibara, Y. Moritomo, T. Arima, A. Asamitsu, G. Kido, Y. Tokura, Insulator-metal transition and giant magnetoresistance in $La_{1-x}Sr_xMnO_3$, Physical Review B, 51 (1995) 14103-14109.

[27] A. Szewczyk, M. Gutowska, B. Dabrowski, Specific heat and phase diagram of heavily doped $La_{1-x}Sr_xMnO_3$ (0,45< x<1), Physical Review B, 72 (2005) 224429.

[28] M. Ohring, Materials Science of Thin Films Second Edition ed., Academic Press, San Diego, 2002.

[29] H. Lüth, Solid Surfaces, Interfaces and Thin Films, 2010.

[30] L.W. Martin, Y.H. Chu, R. Ramesh, Advances in the growth and characterization of magnetic, ferroelectric, and multiferroic oxide thin films, Materials Science and Engineering R, 68 (2010) 89-133.

[31] P. Abellán, J. Zabaleta, J. Santiso, M.-J. Casanove, N. Dix, J. Aguiar, N.D. Browning, N. Mestres, T. Puig, X. Obradors, F. Sandiumenge, Interface structure governed by plastic and structural dissimilarity in perovskite $La_{0.7}Sr_{0.3}MnO_3$ nanodots on rock-salt MgO substrates, Applied Physics Letters, 100 (2012) 083104.

[32] J. Zabaleta, S. Valencia, F. Kronast, C. Moreno, P. Abellan, J. Gazquez, H. Sepehri-Amin, F. Sandiumenge, T. Puig, N. Mestres, X. Obradors, Photoemission electron microscopy study of sub-200 nm self-assembled $La_{0.7}Sr_{0.3}MnO_3$ epitaxial islands, Nanoscale, 5 (2013) 2990-2998.

[33] F. Sandiumenge, N. Bagués, J. Santiso, Interfaces and Nanostructures of Functional Oxide Octahedral Framework Structures, Frontiers in Materials, 1 (2014).

[34] M. Gibert, P. Abellán, A. Benedetti, T. Puig, F. Sandiumenge, A. García, X. Obradors, Self-Organized $Ce_{1-x}Gd_xO_{2-y}$ Nanowire Networks with Very Fast Coarsening Driven by Attractive Elastic Interactions, Small, 6 (2010) 2716-2724.

[35] A. Cavallaro, B. Ballesteros, R. Bachelet, J. Santiso, Heteroepitaxial orientation control of YSZ thin films by selective growth on SrO-, TiO_2-terminated $SrTiO_3$ crystal surfaces, CrystEngComm, 13 (2011) 1625-1631.

[36] F.C. Frank, J.H. van der Merwe, One-Dimensional Dislocations. I. Static Theory, Proceedings of the Royal Society of London. Series A. Mathematical and Physical Sciences, 198 (1949) 205-216.

[37] J.W. Matthews, A.E. Blakeslee, Defects in epitaxial multilayers, Journal of Crystal Growth, 29 (1975) 273-280.

[38] F.R.N. Nabarro, Dislocations in a simple cubic lattice, Proceedings of the Physical Society, 59 (1947) 256.

[39] S. Kishinû, M. Ogirima, K. Kurata, A Cross-Hatch Pattern in $GaAs_{1-x}P_x$ Epitaxially Grown on GaAs Substrate, Journal of The Electrochemical Society, 119 (1972) 617-622.

[40] Q.Y. Qiu, V. Nagarajan, S.P. Alpay, Film thickness versus misfit strain phase diagrams for epitaxial $PbTiO_3$ ultrathin ferroelectric films, Physical Review B, 78 (2008) 064117.

[41] C.J.M. Daumont, S. Farokhipoor, A. Ferri, J.C. Wojdeł, J. Íñiguez, B.J. Kooi, B. Noheda, Tuning the atomic and domain structure of epitaxial films of multiferroic $BiFeO_3$, Physical Review B, 81 (2010) 144115.

[42] C.J.M. Daumont, D. Mannix, V. Sriram, G. Catalan, D. Rubi, B.J. Kooi, J.T.M.D. Hosson, B. Noheda, Epitaxial $TbMnO_3$ thin films on $SrTiO_3$ substrates: a structural study, Journal of Physics: Condensed Matter, 21 (2009) 182001.

[43] F. Sandiumenge, J. Santiso, L. Balcells, Z. Konstantinovic, J. Roqueta, A. Pomar, J.P. Espinós, B. Martínez, Competing Misfit Relaxation Mechanisms in Epitaxial Correlated Oxides, Physical Review Letters, 110 (2013) 107206.

[44] J. Santiso, L. Balcells, Z. Konstantinovic, J. Roqueta, P. Ferrer, A. Pomar, B. Martinez, F. Sandiumenge, Thickness evolution of the twin structure and shear strain in LSMO films, CrystEngComm, 15 (2013) 3908-3918.

[45] P.W. Anderson, Antiferromagnetism. Theory of Superexchange Interaction, Physical Review, 79 (1950) 350-356.

[46] J.B. Goodenough, Theory of the Role of Covalence in the Perovskite-Type Manganites [La,*M*(II)] MnO_3, Physical Review, 100 (1955) 564-573.

[47] Z. Fang, I.V. Solovyev, K. Terakura, Phase Diagram of Tetragonal Manganites, Physical Review Letters, 84 (2000) 3169-3172.

[48] A. Tebano, C. Aruta, S. Sanna, P.G. Medaglia, G. Balestrino, A.A. Sidorenko, R. De Renzi, G. Ghiringhelli, L. Braicovich, V. Bisogni, N.B. Brookes, Evidence of Orbital Reconstruction at Interfaces in Ultrathin $La_{0.67}Sr_{0.33}MnO_{3-\delta}$ Films, Physical Review Letters, 100 (2008) 137401.

[49] D. Pesquera, G. Herranz, A. Barla, E. Pellegrin, F. Bondino, E. Magnano, F. Sánchez, J. Fontcuberta, Surface symmetry-breaking and strain effects on orbital occupancy in transition metal perovskite epitaxial films, Nature Communications, 3 (2012) 1189.

[50] N. Nakagawa, H.Y. Hwang, D.A. Muller, Why some interfaces cannot be sharp, Nat Mater, 5 (2006) 204-209.

[51] E. Dagotto, Playing with the geometry of oxide heterostructures., Physics and Chemistry of Minerals, (2009).

[52] T. Riedl, T. Gemming, K. Dörr, M. Luysberg, K. Wetzig, Mn Valency at $La_{0.7}Sr_{0.3}MnO_3/SrTiO_3$ (001) Thin Film Interfaces, Microscopy and Microanalysis, 15 (2009) 213-221.

[53] J.S. Lee, D.A. Arena, P. Yu, C.S. Nelson, R. Fan, C.J. Kinane, S. Langridge, M.D. Rossell, R. Ramesh, C.C. Kao, Hidden Magnetic Configuration in Epitaxial $La_{1-x}Sr_xMnO_3$ Films, Physical Review Letters, 105 (2010) 257204.

[54] C. Aruta, G. Ghiringhelli, A. Tebano, N.G. Boggio, N.B. Brookes, P.G. Medaglia, G. Balestrino, Strain induced x-ray absorption linear dichroism in $La_{0.7}Sr_{0.3}MnO_3$ thin films, Physical Review B, 73 (2006) 235121.

[55] H. Boschker, J. Verbeeck, R. Egoavil, S. Bals, G. van Tendeloo, M. Huijben, E.P. Houwman, G. Koster, D.H.A. Blank, G. Rijnders, Preventing the Reconstruction of the Polar Discontinuity at Oxide Heterointerfaces, Advanced Functional Materials, 22 (2012) 2235-2240.

[56] J.M. Rondinelli, S.J. May, J.W. Freeland, Control of octahedral connectivity in perovskite oxide heterostructures: An emerging route to multifunctional materials discovery, MRS Bulletin, 37 (2012) 261-270.

[57] E.J. Moon, P.V. Balachandran, B.J. Kirby, D.J. Keavney, R.J. Sichel-Tissot, C.M. Schlepütz, E. Karapetrova, X.M. Cheng, J.M. Rondinelli, S.J. May, Effect of Interfacial Octahedral Behavior in Ultrathin Manganite Films, Nano Letters, 14 (2014) 2509-2514.

[58] C.L. Jia, S.B. Mi, M. Faley, U. Poppe, J. Schubert, K. Urban, Oxygen octahedron reconstruction in the $SrTiO_3$/$LaAlO_3$ heterointerfaces investigated using aberration-corrected ultrahigh-resolution transmission electron microscopy, Physical Review B, 79 (2009) 081405.

[59] A. Borisevich, O.S. Ovchinnikov, H.J. Chang, M.P. Oxley, P. Yu, J. Seidel, E.A. Eliseev, A.N. Morozovska, R. Ramesh, S.J. Pennycook, S.V. Kalinin, Mapping Octahedral Tilts and Polarization Across a Domain Wall in $BiFeO_3$ from Z-Contrast Scanning Transmission Electron Microscopy Image Atomic Column Shape Analysis, ACS Nano, 4 (2010) 6071-6079.

[60] G. Catalan, J. Seidel, R. Ramesh, J.F. Scott, Domain wall nanoelectronics, Reviews of Modern Physics, 84 (2012) 119-156.

[61] S. Farokhipoor, C. Magen, S. Venkatesan, J. Iniguez, C.J.M. Daumont, D. Rubi, E. Snoeck, M. Mostovoy, C. de Graaf, A. Muller, M. Doblinger, C. Scheu, B. Noheda, Artificial chemical and magnetic structure at the domain walls of an epitaxial oxide, Nature, 515 (2014) 379-383.

[62] M. Arredondo, Q.M. Ramasse, M. Weyland, R. Mahjoub, I. Vrejoiu, D. Hesse, N.D. Browning, M. Alexe, P. Munroe, V. Nagarajan, Direct Evidence for Cation Non-Stoichiometry and Cottrell Atmospheres Around Dislocation Cores in Functional Oxide Interfaces, Advanced Materials, 22 (2010) 2430-2434.

[63] D. Hull, D. Bacon, Introduction to Dislocations, Fourth Edition ed., Butterworth-Heinemann, Oxford, 2001.

[64] D. Ruzmetov, Y. Seo, L.J. Belenky, D.M. Kim, X. Ke, H. Sun, V. Chandrasekhar, C.B. Eom, M.S. Rzchowski, X. Pan, Epitaxial Magnetic Perovskite Nanostructures, Advanced Materials, 17 (2005) 2869-2872.

[65] G. Stringfellow, Epitaxy, Reports on Progress in Physics, 45 (1982) 469.

[66] V. Moshnyaga, B. Damaschke, O. Shapoval, A. Belenchuk, J. Faupel, O.I. Lebedev, J. Verbeeck, G. van Tendeloo, M. Mucksch, V. Tsurkan, R. Tidecks, K. Samwer, Structural phase transition at the percolation threshold in epitaxial $(La_{0.7}Ca_{0.3}MnO_3)_{1-x}$:$(MgO)_x$ nanocomposite films, Nat Mater, 2 (2003) 247-252.

[67] H. Zheng, J. Wang, S.E. Lofland, Z. Ma, L. Mohaddes-Ardabili, T. Zhao, L. Salamanca-Riba, S.R. Shinde, S.B. Ogale, F. Bai, D. Viehland, Y. Jia, D.G. Schlom, M. Wuttig, A. Roytburd, R. Ramesh, Multiferroic $BaTiO_3$-$CoFe_2O_4$ Nanostructures, Science, 303 (2004) 661-663.

[68] C. Aiping, B. Zhenxing, H. Harshad, Z. Xinghang, S. Qing, C. Li, J. Quanxi, L.M.-D. Judith, W. Haiyan, Microstructure, magnetic, and low-field magnetotransport properties of self-assembled $(La_{0.7}Sr_{0.3}MnO_3)_{0.5}$:$(CeO_2)_{0.5}$ vertically aligned nanocomposite thin films, Nanotechnology, 22 (2011) 315712.

[69] A. Chen, Z. Bi, C.F. Tsai, J. Lee, Q. Su, X. Zhang, Q. Jia, J.L. MacManus-Driscoll, H. Wang, Tunable Low-Field Magnetoresistance in $(La_{0.7}Sr_{0.3}MnO_3)_{0.5}$:$(ZnO)_{0.5}$ Self-Assembled Vertically Aligned Nanocomposite Thin Films, Advanced Functional Materials, 21 (2011) 2423-2429.

[70] D.B. Williams, C.B. Carter, Transmission Electron Microscopy, Springer US, 2009.

[71] R.F. Egerton, Electron Energy-Loss Spectroscopy in the Electron Microscope, Springer 233 Spring Street, New York, NY 10013, USA, 2011.

[72] F. Krumeich, http://www.microscopy.ethz.ch, 2015.

[73] M. Varela, M.P. Oxley, W. Luo, J. Tao, M. Watanabe, A.R. Lupini, S.T. Pantelides, S.J. Pennycook, Atomic-resolution imaging of oxidation states in manganites, Physical Review B, 79 (2009) 085117.

[74] D.A. Muller, L.F. Kourkoutis, M. Murfitt, J.H. Song, H.Y. Hwang, J. Silcox, N. Dellby, O.L. Krivanek, Atomic-Scale Chemical Imaging of Composition and Bonding by Aberration-Corrected Microscopy, Science, 319 (2008) 1073-1076.

[75] A.J. D'Alfonso, B. Freitag, D. Klenov, L.J. Allen, Atomic-resolution chemical mapping using energy-dispersive x-ray spectroscopy, Physical Review B, 81 (2010) 100101.

[76] M.W. Chu, S.C. Liou, C.P. Chang, F.S. Choa, C.H. Chen, Emergent Chemical Mapping at Atomic-Column Resolution by Energy-Dispersive X-Ray Spectroscopy in an Aberration-Corrected Electron Microscope, Physical Review Letters, 104 (2010) 196101.

[77] P. Lu, J. Xiong, M.V. Benthem, Q. Jia, Atomic-scale chemical quantification of oxide interfaces using energy-dispersive X-ray spectroscopy, Applied Physics Letters, 102 (2013) 173111.

[78] P. Lu, E. Romero, S. Lee, J. MacManus-Driscoll, Q. Jia, Chemical Quantification of Atomic-Scale EDS Maps under Thin Specimen Conditions., Microscopy and Microanalysis, 20 (2014) 1782-1790.

[79] W.H. Bragg, W.L. Bragg, The Reflection of X-rays by Crystals, Proceedings of the Royal Society of London. Series A, 88 (1913) 428-438.

[80] J.A. Perez-Omil, in: University of Cadiz - Spain, University of Cadiz Spain, 1994

[81] S. Bernal, F.J. Botana, J.J. Calvino, C. López-Cartes, J.A. Pérez-Omil, J.M. Rodríguez-Izquierdo, The interpretation of HREM images of supported metal catalysts using image simulation: profile view images, Ultramicroscopy, 72 (1998) 135-164.

[82] R.T. Downs, M. Hall-Wallace, The American Mineralogist crystal structure database., American Mineralogist, 88(1) (2003) 247-250.

[83] M.J. Hÿtch, E. Snoeck, R. Kilaas, Quantitative measurement of displacement and strain fields from HREM micrographs, Ultramicroscopy, 74 (1998) 131-146.

[84] M.J. Hÿtch, J.L. Putaux, J. Thibault, Stress and strain around grain-boundary dislocations measured by high-resolution electron microscopy, Philosophical Magazine, 86 (2006) 4641-4656.

[85] M.J. Hytch, J.-L. Putaux, J.-M. Penisson, Measurement of the displacement field of dislocations to 0.03A by electron microscopy, Nature, 423 (2003) 270-273.

[86] M. Tyunina, L. Yao, D. Chvostova, A. Dejneka, T. Kocourek, M. Jelinek, V. Trepakov, S. van Dijken, Concurrent bandgap narrowing and polarization enhancement in epitaxial ferroelectric nanofilms, Science and Technology of Advanced Materials, 16 (2015) 026002.

[87] A.K. Gutakovskii, A.L. Chuvilin, S.A. Song, Application of high-resolution electron microscopy for visualization and quantitative analysis of strain fields in heterostructures, Bulletin of the Russian Academy of Sciences: Physics, 71 (2007) 1426-1432.

[88] M.J. Hytch, Analysis of Variations in Structure from High Resolution Electron Microscope Images by Combining Real Space and Fourier Space Information, Microsc. Microanal. Microstruct., 8 (1997) 41-57.

[89] J.P. Hirth and J. Lothe, Theory of Dislocations: second edition, Krieger, Malabar, Florida, , (1992).

[90] GPA for DigitalMicrograph, in: GPA Phase Manual, HREM Research Inc, 2015.

[91] S.J. Pennycook, D.E. Jesson, High-resolution incoherent imaging of crystals, Physical Review Letters, 64 (1990) 938-941.

[92] P.J. Phillips, M. De Graef, L. Kovarik, A. Agrawal, W. Windl, M.J. Mills, Atomic-resolution defect contrast in low angle annular dark-field STEM, Ultramicroscopy, 116 (2012) 47-55.

[93] L. Fitting, S. Thiel, A. Schmehl, J. Mannhart, D.A. Muller, Subtleties in ADF imaging and spatially resolved EELS: A case study of low-angle twist boundaries in $SrTiO_3$, Ultramicroscopy, 106 (2006) 1053-1061.

[94] S.R. Spurgeon, Y. Du, S.A. Chambers, Measurement Error in Atomic-Scale STEM-EDS Mapping of a Model Oxide Interface, eprint arXiv:1610.03432, (2016) 12.

[95] M.P. Oxley, M. Varela, T.J. Pennycook, K. van Benthem, S.D. Findlay, A.J. D'Alfonso, L.J. Allen, S.J. Pennycook, Interpreting atomic-resolution spectroscopic images, Physical Review B, 76 (2007) 064303.

[96] Leslie J. Allen, Adrian J. D'Alfonso, Bert Freitag, D.O. Klenov, Chemical mapping at atomic resolution using energy-dispersive x-ray spectroscopy, MRS Bulletin, 37 (2012).

[97] P. Wang, A.J. D'Alfonso, S.D. Findlay, L.J. Allen, A.L. Bleloch, Contrast reversal in atomic-resolution chemical mapping, Phys Rev Lett, 101 (2008) 236102.

[98] B.D. Forbes, A.J. D'Alfonso, R.E.A. Williams, R. Srinivasan, H.L. Fraser, D.W. McComb, B. Freitag, D.O. Klenov, L.J. Allen, Contribution of thermally scattered electrons to atomic resolution elemental maps, Physical Review B, 86 (2012) 024108.

[99] J. Scott, P.J. Thomas, M. MacKenzie, S. McFadzean, J. Wilbrink, A.J. Craven, W.A.P. Nicholson, Near-simultaneous dual energy range EELS spectrum imaging, Ultramicroscopy, 108 (2008) 1586-1594.

[100] J. Bobynko, I. MacLaren, A.J. Craven, Spectrum imaging of complex nanostructures using DualEELS: I. digital extraction replicas, Ultramicroscopy, 149 (2015) 9-20.

[101] P. Trebbia, N. Bonnet, EELS elemental mapping with unconventional methods I. Theoretical basis: Image analysis with multivariate statistics and entropy concepts, Ultramicroscopy, 34 (1990) 165-178.

[102] N. Bonnet, N. Brun, C. Colliex, Extracting information from sequences of spatially resolved EELS spectra using multivariate statistical analysis, Ultramicroscopy, 77 (1999) 97-112.

[103] M. Bosman, M. Watanabe, D.T.L. Alexander, V.J. Keast, Mapping chemical and bonding information using multivariate analysis of electron energy-loss spectrum images, Ultramicroscopy, 106 (2006) 1024-1032.

[104] G. Lucas, P. Burdet, M. Cantoni, C. Hébert, Multivariate statistical analysis as a tool for the segmentation of 3D spectral data, Micron, 52–53 (2013) 49-56.

[105] F. de la Peña, M.H. Berger, J.F. Hochepied, F. Dynys, O. Stephan, M. Walls, Mapping titanium and tin oxide phases using EELS: An application of independent component analysis, Ultramicroscopy, 111 (2011) 169-176.

[106] H. Kurata, C. Colliex, Electron-energy-loss core-edge structures in manganese oxides, Physical Review B, 48 (1993) 2102-2108.

[107] J.H. Rask, B.A. Miner, P.R. Buseck, Determination of manganese oxidation states in solids by electron energy-loss spectroscopy, Ultramicroscopy, 21 (1987) 321-326.

[108] G.A. Botton, C.C. Appel, A. Horsewell, W.M. Stobbs, Quantification of the EELS near-edge structures to study Mn doping in oxides, Journal of Microscopy, 180 (1995) 211-216.

136

[109] Z.L. Wang, J.S. Yin, Y.D. Jiang, EELS analysis of cation valence states and oxygen vacancies in magnetic oxides, Micron, 31 (2000) 571-580.

[110] H. Tan, J. Verbeeck, A. Abakumov, G. Van Tendeloo, Oxidation state and chemical shift investigation in transition metal oxides by EELS, Ultramicroscopy, 116 (2012) 24-33.

[111] R.D. Leapman, L.A. Grunes, Anomalous L3 L2 White-Line Ratios in the 3d Transition Metals, Physical Review Letters, 45 (1980) 397-401.

[112] T.G. Sparrow, B.G. Williams, C.N.R. Rao, J.M. Thomas, L3/L2 white-line intensity ratios in the electron energy-loss spectra of 3d transition-metal oxides, Chemical Physics Letters, 108 (1984) 547-550.

[113] T. Riedl, T. Gemming, W. Gruner, J. Acker, K. Wetzig, Determination of manganese valency in $La_{1-x}Sr_xMnO_3$ using ELNES in the (S)TEM, Micron, 38 (2007) 224-230.

[114] W.G. Waddington, P. Rez, I.P. Grant, C.J. Humphreys, White lines in the $L_{2,3}$ electron-energy-loss and x-ray absorption spectra of 3d transition metals, Physical Review B, 34 (1986) 1467-1473.

[115] D.H. Pearson, C.C. Ahn, B. Fultz, White lines and d-electron occupancies for the 3d and 4d transition metals, Physical Review B, 47 (1993) 8471-8478.

[116] C.P. Chang, M.W. Chu, H.T. Jeng, S.L. Cheng, J.G. Lin, J.R. Yang, C.H. Chen, Condensation of two-dimensional oxide-interfacial charges into one-dimensional electron chains by the misfit-dislocation strain field, Nature Communications, 5 (2014) 3522.

[117] E. Stavitski, F.M.F. de Groot, The CTM4XAS program for EELS and XAS spectral shape analysis of transition metal L edges, Micron, 41 (2010) 687-694.

[118] G. Cliff, G.W. Lorimer, The quantitative analysis of thin specimens, Journal of Microscopy, 103 (1975) 203-207.

[119] D.J. Prior, A.P. Boyle, F. Brenker, M.C. Cheadle, A. Day, G. Lopez, L. Peruzzi, G. Potts, S. Reddy, R. Spiess, N.E. Timms, P. Trimby, J. Wheeler, L. Zetterstrom, The application of electron backscatter diffraction and orientation contrast imaging in the SEM to textural problems in rocks, American Mineralogist, 84 (1999) 1741-1759.

[120] K. Wasa, M. Kitabatake, H. Adachi, 5 - Deposition of Compound Thin Films, in: Thin Film Materials Technology, William Andrew Publishing, Norwich, NY, 2004, pp. 191-403.

[121] B.E. Aufderheide, Sputtered Thin Film Coatings, in: A.A. Tracton (Ed.) Coatings Technology Handbook, Third Edition, Taylor & Francis Group, LLC, CRC Press, 2005.

[122] G. Regina, Spin-Dependent Transport in Oxide-Bades Tunnel Junctions, in: Physics Departament, Universitat Autònoma de Barcelona (UAB), Barcelona, 2015.

[123] M. Belyansky, 5 - Thin-Film Strain Engineering and Pattern Effects in Dielectrics CVD A2 - Seshan, Krishna, in: Handbook of Thin Film Deposition (Third Edition), William Andrew Publishing, Oxford, 2012, pp. 89-125.

[124] Z. Konstantinović, J. Santiso, D. Colson, A. Forget, L. Balcells, B. Martínez, Self-organization processes in highly epitaxial La2/3Sr1/3MnO3 thin films grown on SrTiO3 (001) substrates, Journal of Applied Physics, 105 (2009) 063919.

[125] D.B. Chrisey, G.K. Hubler, Pulsed Laser Deposition, 1994.

[126] A. Pomar, Z. Konstantinović, N. Bagués, J. Roqueta, L. López-Mir, L. Balcells, C. Frontera, N. Mestres, A. Gutiérrez-Llorente, M. Šćepanović, N. Lazarević, Z.V. Popović, F. Sandiumenge, B. Martínez, J. Santiso, Formation of Self-Organized Mn_3O_4 Nanoinclusions in $LaMnO_3$ Films, Frontiers in Physics, 4 (2016).

[127] J. Roqueta, A. Pomar, L. Balcells, C. Frontera, S. Valencia, R. Abrudan, B. Bozzo, Z. Konstantinović, J. Santiso, B. Martínez, Strain-Engineered Ferromagnetism in LaMnO$_3$ Thin Films, Crystal Growth & Design, 15 (2015) 5332-5337.

[128] L. Balcells, M. Paradinas, N. Baguès, N. Domingo, R. Moreno, R. Galceran, M. Walls, J. Santiso, Z. Konstantinovic, A. Pomar, M.-J. Casanove, C. Ocal, B. Martínez, F. Sandiumenge, Enhanced conduction and ferromagnetic order at (100)-type twin walls in La$_{0.7}$Sr$_{0.3}$MnO$_3$ thin films, Physical Review B, 92 (2015) 075111.

[129] J. Garcia-Barriocanal, F.Y. Bruno, A. Rivera-Calzada, Z. Sefrioui, N.M. Nemes, M. Garcia-Hernández, J. Rubio-Zuazo, G.R. Castro, M. Varela, S.J. Pennycook, C. Leon, J. Santamaria, "Charge Leakage" at LaMnO$_3$/SrTiO$_3$ Interfaces, Advanced Materials, 22 (2010) 627-632.

[130] A. Bhattacharya, S.J. May, S.G.E. te Velthuis, M. Warusawithana, X. Zhai, B. Jiang, J.M. Zuo, M.R. Fitzsimmons, S.D. Bader, J.N. Eckstein, Metal-Insulator Transition and Its Relation to Magnetic Structure in (LaMnO$_3$)$_{2n}$/ (SrMnO$_3$)$_n$ Superlattices, Physical Review Letters, 100 (2008) 257203.

[131] M. Gibert, P. Zubko, R. Scherwitzl, J. Íñiguez, J.-M. Triscone, Exchange bias in LaNiO3–LaMnO3 superlattices, Nat Mater, 11 (2012) 195-198.

[132] Q. Huang, A. Santoro, J.W. Lynn, R.W. Erwin, J.A. Borchers, J.L. Peng, R.L. Greene, Structure and magnetic order in undoped lanthanum manganite, Physical Review B, 55 (1997) 14987-14999.

[133] C. Ritter, M.R. Ibarra, J.M. De Teresa, P.A. Algarabel, C. Marquina, J. Blasco, J. García, S. Oseroff, S.W. Cheong, Influence of oxygen content on the structural, magnetotransport, and magnetic properties of LaMnO$_{3+\delta}$, Physical Review B, 56 (1997) 8902-8911.

[134] Z. Marton, S.S. A. Seo, T. Egami, H.N. Lee, Growth control of stoichiometry in LaMnO3 epitaxial thin films by pulsed laser deposition, Journal of Crystal Growth, 312 (2010) 2923-2927.

[135] I. Marozau, P.T. Das, M. Döbeli, J.G. Storey, M.A. Uribe-Laverde, S. Das, C. Wang, M. Rössle, C. Bernhard, Influence of La and Mn vacancies on the electronic and magnetic properties of LaMnO$_3$ thin films grown by pulsed laser deposition, Physical Review B, 89 (2014) 174422.

[136] C. Aruta, M. Angeloni, G. Balestrino, N.G. Boggio, P.G. Medaglia, A. Tebano, B. Davidson, M. Baldini, D. Di Castro, P. Postorino, P. Dore, A. Sidorenko, G. Allodi, R. De Renzi, Preparation and characterization of LaMnO3 thin films grown by pulsed laser deposition, Journal of Applied Physics, 100 (2006) 023910.

[137] W.S. Choi, Z. Marton, S.Y. Jang, S.J. Moon, B.C. Jeon, J.H. Shin, S.S.A. Seo, T.W. Noh, K. Myung-Whun, H.N. Lee, Y.S. Lee, Effects of oxygen-reducing atmosphere annealing on LaMnO$_3$ epitaxial thin films, Journal of Physics D: Applied Physics, 42 (2009) 165401.

[138] P. Orgiani, C. Aruta, R. Ciancio, A. Galdi, L. Maritato, Enhanced transport properties in La$_x$MnO$_{3-\delta}$ thin films epitaxially grown on SrTiO$_3$ substrates: The profound impact of the oxygen content, Applied Physics Letters, 95 (2009) 013510.

[139] H.S. Kim, H.M. Christen, Controlling the magnetic properties of LaMnO$_3$ thin films on SrTiO$_3$ (100) by deposition in a O$_2$/Ar gas mixture, Journal of Physics: Condensed Matter, 22 (2010) 146007.

[140] W.S. Choi, D.W. Jeong, S.Y. Jang, Z. Marton, S.S.A. Seo, H.N. Lee, Y.S. Lee, LaMnO$_3$ thin films grown by using pulsed laser deposition and their simple recovery to a stoichiometric phase by annealing, Journal - Korean Physical Society, (2011) Medium: X; Size: 569.

[141] J.L. MacManus-Driscoll, Self-Assembled Heteroepitaxial Oxide Nanocomposite Thin Film Structures: Designing Interface-Induced Functionality in Electronic Materials, Advanced Functional Materials, 20 (2010) 2035-2045.

[142] D. Mukherjee, N. Bingham, M. Hordagoda, M.-H. Phan, H. Srikanth, S. Witanachchi, P. Mukherjee, Influence of microstructure and interfacial strain on the magnetic properties of epitaxial

Mn3O4/La0.7Sr0.3MnO3 layered-composite thin films, Journal of Applied Physics, 112 (2012) 083910.

[143] H. Jian, Z. Zhang, Y. Wang, X. Tang, J. Yang, L. Hu, L. Chen, X. Zhu, Y. Sun, Preparation of $La_{0.7}Sr_{0.3}Mn_{1+x}O_y$ ($1 \leqslant x \leqslant 4$) thin films by chemical solution deposition: Dual epitaxy and possible spinodal growth, Journal of Alloys and Compounds, 561 (2013) 95-100.

[144] A.N. Grundy, M. Chen, L.J. Gauckler, B. Hallstedt, Assessment of the La-Mn-O system, Journal of Phase Equilibria and Diffusion, 26 (2005) 131-151.

[145] P.A. Joy, C.R. Sankar, S.K. Date, The limiting value of x in the ferromagnetic compositions $La_{1-x}MnO_3$, Journal of Physics: Condensed Matter, 14 (2002) L663.

[146] G. Dezanneau, M. Audier, H. Vincent, C. Meneghini, E. Djurado, Structural characterization of $La_{1-x}MnO_{3\pm\delta}$ by x-ray diffraction and x-ray absorption spectroscopy, Physical Review B, 69 (2004) 014412.

[147] A. Bosak, C. Dubourdieu, M. Audier, J.P. Sénateur, J. Pierre, Compositional effects on the structure and magnetotransport properties of lacunar $La_{1-x}MnO_{3-\delta}$ films (x>0) grown by MOCVD, Applied Physics A, 79 (2004) 1979-1984.

[148] J. Neerushana, L. Oleg, G. Isabelle, D. Catherine, T. Gustaaf Van, Structure and defect characterization of multiferroic $ReMnO_3$ films and multilayers by TEM, Nanotechnology, 21 (2010) 075705.

[149] I. Gélard, N. Jehanathan, H. Roussel, S. Gariglio, O.I. Lebedev, G. Van Tendeloo, C. Dubourdieu, Off-Stoichiometry Effects on the Crystalline and Defect Structure of Hexagonal Manganite $REMnO_3$ Films (RE = Y, Er, Dy), Chemistry of Materials, 23 (2011) 1232-1238.

[150] R. Wunderlich, C. Chiliotte, G. Bridoux, T. Maity, Ö. Kocabiyik, A. Setzer, M. Ziese, P. Esquinazi, Structural, magnetic and electric properties of $HoMnO_3$ films on $SrTiO_3$(001), Journal of Magnetism and Magnetic Materials, 324 (2012) 460-465.

[151] Z.-R. Tian, W. Tong, J.-Y. Wang, N.-G. Duan, V.V. Krishnan, S.L. Suib, Manganese Oxide Mesoporous Structures: Mixed-Valent Semiconducting Catalysts, Science, 276 (1997) 926-930.

[152] L. Zhang, Q. Zhou, Z. Liu, X. Hou, Y. Li, Y. Lv, Novel Mn3O4 Micro-octahedra: Promising Cataluminescence Sensing Material for Acetone, Chemistry of Materials, 21 (2009) 5066-5071.

[153] M.M. Najafpour, M. Hołyńska, S. Salimi, Applications of the "nano to bulk" Mn oxides: Mn oxide as a Swiss army knife, Coordination Chemistry Reviews, 285 (2015) 65-75.

[154] M.M. Najafpour, G. Renger, M. Hołyńska, A.N. Moghaddam, E.-M. Aro, R. Carpentier, H. Nishihara, J.J. Eaton-Rye, J.-R. Shen, S.I. Allakhverdiev, Manganese Compounds as Water-Oxidizing Catalysts: From the Natural Water-Oxidizing Complex to Nanosized Manganese Oxide Structures, Chemical Reviews, 116 (2016) 2886-2936.

[155] R.E. Pacalo, E.K. Graham, Pressure and temperature dependence of the elastic properties of synthetic MnO, Physics and Chemistry of Minerals, 18 (1991) 69-80.

[156] G. J, Structure cristalline de la manganite Comptes Rendus Hebdomadaires des Seances de l'Academie des Sciences 200 Structure cristalline de la manganite (1935) 69-71.

[157] Geller S, Structures of alpha-Mn2O3, $(Mn_{0.983}Fe_{0.017})_2O_3$ and $(Mn_{0.37}Fe_{0.63})_2O_3$ and relation to magnetic ordering, Acta Crystallographica, B27 (1971) 821-828

[158] Zachariasen W, Untersuchungen ueber die Kristallstruktur von Sesquioxyden und Verbindungen ABO3, Skrifter utgitt av det Norske Videnskaps-Akademi i Oslo 1(1928) 1-165

[159] R.D.C. Ross C R, Paris E, Rietveld refinement of the high-pressure polymorph of Mn3O4 American Mineralogist 75 (1990) 1249-1252.

[160] A. G, Ueber die Kristallstruktur von Hausmannit (Mn Mn2 O4). Zeitschrift fur Kristallographie 64 (1926) 475-490.

[161] V. Baron, J. Gutzmer, H. Rundlof, R. Tellgren, The influence of iron substitution in the magnetic properties of hausmannite, $Mn^{2+} (Fe,Mn)^{3+}_2 O_4$, American Mineralogist, 83 (1998) 786-793.

[162] J.E. Post, D.L. Bish, Rietveld refinement of the todorokite structure, American Mineralogist, 73 (1988) 861-869.

[163] J.E. Post, P.J. Heaney, Neutron and synchrotron X-ray diffraction study of the structures and dehydration behaviors of ramsdellite and "groutellite", American Mineralogist, 89 (2004) 969-975.

[164] Z.A.I. Kondrashev Y D, The structure of the modifications of manganese oxide, Izvestiya Akademii Nauk SSSR 15 (1951) 179-186.

[165] K. Momma, F. Izumi, VESTA 3 for three-dimensional visualization of crystal, volumetric and morphology data, Journal of Applied Crystallography, 44 (2011) 1272-1276.

[166] J. Rodríguez-Carvajal, M. Hennion, F. Moussa, A.H. Moudden, L. Pinsard, A. Revcolevschi, Neutron-diffraction study of the Jahn-Teller transition in stoichiometric $LaMnO_3$, Physical Review B, 57 (1998) R3189-R3192.

[167] M.J. Radler, J.B. Cohen, G.P. Sykora, T. Mason, D.E. Ellis, J. Faber, The defect structures of $Mn_{1-x}O$, Journal of Physics and Chemistry of Solids, 53 (1992) 141-154.

[168] S.H.C. Kim, S. J.; , G.H. Lee, S.J. Oh, B. Kim, H.C. Choi, J. Park, Y. Chang, Ferrimagnetism in γ-493 manganese sesquioxide (γ-Mn2O3) nanoparticles, Journal of the Korean Physical Society, 46(4) (2005) 941. 494.

[169] H. Kurata, E. Lefèvre, C. Colliex, R. Brydson, Electron-energy-loss near-edge structures in the oxygen *K*-edge spectra of transition-metal oxides, Physical Review B, 47 (1993) 13763-13768.

[170] F.M.F. de Groot, M. Grioni, J.C. Fuggle, J. Ghijsen, G.A. Sawatzky, H. Petersen, Oxygen 1s x-ray-absorption edges of transition-metal oxides, Physical Review B, 40 (1989) 5715-5723.

[171] L.A. Grunes, R.D. Leapman, C.N. Wilker, R. Hoffmann, A.B. Kunz, Oxygen K near-edge fine structure: An electron-energy-loss investigation with comparisons to new theory for selected 3d Transition-metal oxides, Physical Review B, 25 (1982) 7157-7173.

[172] A.M. I. Davoli, A. Bianconi, M. Tomellini, and M. Fanfoni, Phys. Rev. B, 33 (1986).

[173] C. Moreno, P. Abellán, A. Hassini, A. Ruyter, A.P. del Pino, F. Sandiumenge, M.-J. Casanove, J. Santiso, T. Puig, X. Obradors, Spontaneous Outcropping of Self-Assembled Insulating Nanodots in Solution-Derived Metallic Ferromagnetic La0.7Sr0.3MnO3 Films, Advanced Functional Materials, 19 (2009) 2139-2146.

[174] P. Abellán, C. Moreno, F. Sandiumenge, X. Obradors, M.-J. Casanove, Misfit relaxation of $La_{0.7}Sr_{0.3}MnO_3$ thin films by a nanodot segregation mechanism, Applied Physics Letters, 98 (2011) 041903.

[175] C. Moreno, P. Abellán, F. Sandiumenge, M.-J. Casanove, X. Obradors, Nanocomposite lanthanum strontium manganite thin films formed by using a chemical solution deposition, Applied Physics Letters, 100 (2012) 023103.

[176] P. Orgiani, A. Galdi, C. Aruta, V. Cataudella, G. De Filippis, C.A. Perroni, V. Marigliano Ramaglia, R. Ciancio, N.B. Brookes, M. Moretti Sala, G. Ghiringhelli, L. Maritato, Multiple double-exchange mechanism by Mn^{2+}-doping in manganite compounds, Physical Review B, 82 (2010) 205122.

[177] P. Orgiani, C. Aruta, R. Ciancio, A. Galdi, L. Maritato, Synthesis and properties of highly metallic orbital-ordered A-site manganites, Journal of Nanoparticle Research, 15 (2013) 1655.

140

[178] P.G. Radaelli, G. Iannone, M. Marezio, H.Y. Hwang, S.W. Cheong, J.D. Jorgensen, D.N. Argyriou, Structural effects on the magnetic and transport properties of perovskite $A_{1-x}A_x'MnO_3$ (x=0.25, 0.30), Physical Review B, 56 (1997) 8265-8276.

[179] A.E. Romanov, A. Vojta, W. Pompe, M.J. Lefevre, J.S. Speck, Domain Patterns in (111) Oriented Tetragonal Ferroelectric Films, physica status solidi (a), 172 (1999) 225-253.

[180] T.W. Darling, A. Migliori, E.G. Moshopoulou, S.A. Trugman, J.J. Neumeier, J.L. Sarrao, A.R. Bishop, J.D. Thompson, Measurement of the elastic tensor of a single crystal of $La_{0.83}Sr_{0.17}MnO_3$ and its response to magnetic fields, Physical Review B, 57 (1998) 5093-5097.

[181] P. Abellan, S. Felip, C. Moreno, M.-J. Casanove, T. Puig, X. Obradors, Strain Relaxation of Self-nanostructured Solution Derived $La_{0.7}Sr_{0.3}MnO_3$ Films, in: MRS Proceedings, Cambridge University Press, New York, USA, 2009.

[182] J.L. Maurice, F. Pailloux, A. Barthélémy, O. Durand, D. Imhoff, R. Lyonnet, A. Rocher, J.P. Contour, Strain relaxation in the epitaxy of $La_{2/3}Sr_{1/3}MnO_3$ grown by pulsed-laser deposition on $SrTiO_3$(001), Philosophical Magazine, 83 (2003) 3201-3224.

[183] N. Farag, M. Bobeth, W. Pompe, A.E. Romanov, J.S. Speck, Modeling of twinning in epitaxial (001)-oriented La0.67Sr0.33MnO3 thin films, Journal of Applied Physics, 97 (2005) 113516.

[184] Y.L. Zhu, X.L. Ma, M. Zhang, D.X. Li, H.B. Lu, Z.H. Chen, G.Z. Yang, Structure and microstructural characteristics in the thin films of La1−xSrxMnO3 (x = 0.1, 0.2, 0.3), Materials Letters, 58 (2004) 1485-1489.

[185] O.I. Lebedev, G. Van Tendeloo, S. Amelinckx, Misfit accommodation of epitaxial $La_{1-x}A_xMnO_3$ (A=Ca, Sr) thin films, The International Journal of Inorganic Materials, 3 (2001) 1331-1337.

[186] O.I. Lebedev, G. van Tendeloo, Phase transitions: an alternative for stress accommodation in CMR manganate films, Zeitschrift für Metallkunde, 95 (2004) 244-246.

[187] J. Sapriel, Domain-wall orientations in ferroelastics, Physical Review B, 12 (1975) 5128-5140.

[188] C.W. Haas, W.F. Jaep, Domain wall model for ferroelastics, Physics Letters A, 49 (1974) 77-78.

[189] J. Seidel, G. Singh-Bhalla, Q. He, S.-Y. Yang, Y.-H. Chu, R. Ramesh, Domain wall functionality in BiFeO3, Phase Transitions, 86 (2013) 53-66.

[190] P. Zubko, G. Catalan, A. Buckley, P.R.L. Welche, J.F. Scott, Strain-Gradient-Induced Polarization in $SrTiO_3$ Single Crystals, Physical Review Letters, 99 (2007) 167601.

[191] A. Alison, K.H.S. Ekhard, Sheet superconductivity in twin walls: experimental evidence of WO_{3-x}, Journal of Physics: Condensed Matter, 10 (1998) L377.

[192] S.a.T. Van Aert, Stuart and Delville, Rémi and Schryvers, Dominique and Van Tendeloo, Gustaaf and Salje, Ekhard K. H., Direct observation of ferrielectricity at ferroelastic domain boundaries in CaTiO3 by electron microscopy, Advanced Materials, 24 (2012).

[193] J. Seidel, L.W. Martin, Q. He, Q. Zhan, Y.H. Chu, A. Rother, M.E. Hawkridge, P. Maksymovych, P. Yu, M. Gajek, N. Balke, S.V. Kalinin, S. Gemming, F. Wang, G. Catalan, J.F. Scott, N.A. Spaldin, J. Orenstein, R. Ramesh, Conduction at domain walls in oxide multiferroics, Nat Mater, 8 (2009) 229-234.

[194] S. Farokhipoor, B. Noheda, Conduction through 71º Domain Walls in BiFeO3 Thin Films, Physical Review Letters, 107 (2011) 127601.

[195] T. Choi, Y. Horibe, H.T. Yi, Y.J. Choi, W. Wu, S.W. Cheong, Insulating interlocked ferroelectric and structural antiphase domain walls in multiferroic YMnO3, Nat Mater, 9 (2010) 253-258.

[196] T. Sluka, A.K. Tagantsev, P. Bednyakov, N. Setter, Free-electron gas at charged domain walls in insulating BaTiO3, Nature Communications, 4 (2013) 1808.

[197] N.M. Nemes, M.J. Calderón, J.I. Beltrán, F.Y. Bruno, J. García-Barriocanal, Z. Sefrioui, C. León, M. García-Hernández, M.C. Muñoz, L. Brey, J. Santamaría, Signatures of a Two-Dimensional Ferromagnetic Electron Gas at the $La_{0.7}Sr_{0.3}MnO_3/SrTiO_3$ Interface Arising From Orbital Reconstruction, Advanced Materials, 26 (2014) 7516-7520.

[198] H. Jalili, J.W. Han, Y. Kuru, Z. Cai, B. Yildiz, New Insights into the Strain Coupling to Surface Chemistry, Electronic Structure, and Reactivity of $La_{0.7}Sr_{0.3}MnO_3$, The Journal of Physical Chemistry Letters, 2 (2011) 801-807.

[199] W. Lee, J.W. Han, Y. Chen, Z. Cai, B. Yildiz, Cation Size Mismatch and Charge Interactions Drive Dopant Segregation at the Surfaces of Manganite Perovskites, Journal of the American Chemical Society, 135 (2013) 7909-7925.

[200] R. Herger, P.R. Willmott, C.M. Schlepütz, M. Björck, S.A. Pauli, D. Martoccia, B.D. Patterson, D. Kumah, R. Clarke, Y. Yacoby, M. Döbeli, Structure determination of monolayer-by-monolayer grown $La_{1-x}Sr_xMnO_3$ thin films and the onset of magnetoresistance, Physical Review B, 77 (2008) 085401.

[201] H. Dulli, P.A. Dowben, S.H. Liou, E.W. Plummer, Surface segregation and restructuring of colossal-magnetoresistant manganese perovskites $La_{0.65}Sr_{0.35}MnO_3$, Physical Review B, 62 (2000) R14629-R14632.

[202] L. Peña, L. Garzón, R. Galceran, A. Pomar, B. Bozzo, Z. Konstantinovic, F. Sandiumenge, L. Balcells, C. Ocal, B. Martinez, Macroscopic evidence of nanoscale resistive switching in $La_{2/3}Sr_{1/3}MnO_3$ micro-fabricated bridges, Journal of Physics: Condensed Matter, 26 (2014) 395010.

[203] H.D. Megaw, C.N.W. Darlington, Geometrical and structural relations in the rhombohedral perovskites, Acta Crystallographica Section A, 31 (1975) 161-173.

[204] J.F. Mitchell, D.N. Argyriou, C.D. Potter, D.G. Hinks, J.D. Jorgensen, S.D. Bader, Structural phase diagram of $La_{1-x}Sr_xMnO_{3+\delta}$: Relationship to magnetic and transport properties, Physical Review B, 54 (1996) 6172-6183.

[205] M. Medarde, J. Mesot, P. Lacorre, S. Rosenkranz, P. Fischer, K. Gobrecht, High-pressure neutron-diffraction study of the metallization process in $PrNiO_3$, Physical Review B, 52 (1995) 9248-9258.

[206] A. Mukherjee, W.S. Cole, P. Woodward, M. Randeria, N. Trivedi, Theory of Strain-Controlled Magnetotransport and Stabilization of the Ferromagnetic Insulating Phase in Manganite Thin Films, Physical Review Letters, 110 (2013) 157201.

[207] D.P. Kozlenko, I.N. Goncharenko, B.N. Savenko, V.I. Voronin, High pressure effects on the crystal and magnetic structure of La 0.7 Sr 0.3 MnO 3, Journal of Physics: Condensed Matter, 16 (2004) 6755.

[208] J.S. Speck, W. Pompe, Domain configurations due to multiple misfit relaxation mechanisms in epitaxial ferroelectric thin films. I. Theory, Journal of Applied Physics, 76 (1994) 466-476.

[209] F. Sánchez, M.V. García-Cuenca, C. Ferrater, M. Varela, G. Herranz, B. Martínez, J. Fontcuberta, Transition from three- to two-dimensional growth in strained SrRuO3 films on SrTiO3(001), Applied Physics Letters, 83 (2003) 902-904.

[210] S.G. Kim, Y. Wang, I.-W. Chen, Strain relaxation in buried $SrRuO_3$ layer in $(Ca_{1-x}Sr_x)(Zr_{1-x}Ru_x)O_3$ ∕ $SrRuO_3$ ∕ $SrTiO_3$ system, Applied Physics Letters, 89 (2006) 031905.

[211] Z.-H. Wang, O.I. Lebedev, G. Van Tendeloo, G. Cristiani, H.U. Habermeier, Crosshatching on $La_{0.5}Ca_{0.5}MnO_3$ ultrathin films epitaxially grown on $SrTiO_3$ (100), Physical Review B, 77 (2008) 115330.

[212] H.P. Sun, W. Tian, X.Q. Pan, J.H. Haeni, D.G. Schlom, Evolution of dislocation arrays in epitaxial $BaTiO_3$ thin films grown on (100) $SrTiO_3$, Applied Physics Letters, 84 (2004) 3298-3300.

[213] Y.B. Chen, M.B. Katz, X.Q. Pan, C.M. Folkman, R.R. Das, C.B. Eom, Microstructure and strain relaxation of epitaxial $PrScO_3$ thin films grown on (001) $SrTiO_3$ substrates, Applied Physics Letters, 91 (2007) 031902.

[214] O.I. Lebedev, G.V. Tendeloo, S. Amelinckx, H.L. Ju, K.M. Krishnan, High-resolution electron microscopy study of strained epitaxial $La_{0.7}Sr_{0.3}MnO_3$ thin films, Philosophical Magazine A, 80 (2000) 673-691.

[215] L. Lymperakis, J. Neugebauer, M. Albrecht, T. Remmele, H.P. Strunk, Strain Induced Deep Electronic States around Threading Dislocations in GaN, Physical Review Letters, 93 (2004) 196401.

[216] A. Lubk, M.D. Rossell, J. Seidel, Y.H. Chu, R. Ramesh, M.J. Hÿtch, E. Snoeck, Electromechanical Coupling among Edge Dislocations, Domain Walls, and Nanodomains in $BiFeO_3$ Revealed by Unit-Cell-Wise Strain and Polarization Maps, Nano Letters, 13 (2013) 1410-1415.

[217] Z. Zhang, W. Sigle, M. Rühle, Atomic and electronic characterization of the a[100] dislocation core in $SrTiO_3$, Physical Review B, 66 (2002) 094108.

[218] C.L. Jia, A. Thust, K. Urban, Atomic-Scale Analysis of the Oxygen Configuration at a $SrTiO_3$ Dislocation Core, Physical Review Letters, 95 (2005) 225506.

[219] H. Du, C.-L. Jia, L. Houben, V. Metlenko, R.A. De Souza, R. Waser, J. Mayer, Atomic structure and chemistry of dislocation cores at low-angle tilt grain boundary in $SrTiO_3$ bicrystals, Acta Materialia, 89 (2015) 344-351.

[220] K. Szot, W. Speier, G. Bihlmayer, R. Waser, Switching the electrical resistance of individual dislocations in single-crystalline $SrTiO_3$, Nat Mater, 5 (2006) 312-320.

[221] M. Kuzmina, M. Herbig, D. Ponge, S. Sandlöbes, D. Raabe, Linear complexions: Confined chemical and structural states at dislocations, Science, 349 (2015) 1080-1083.

[222] G. Springholz, K. Wiesauer, Nanoscale Dislocation Patterning in PbTe/PbSe(001) Lattice-Mismatched Heteroepitaxy, Physical Review Letters, 88 (2001) 015507.

[223] S.Y. Shiryaev, F. Jensen, J.L. Hansen, J.W. Petersen, A.N. Larsen, Nanoscale Structuring by Misfit Dislocations in $Si_{1-x}Ge_x$SiEpitaxial Systems, Physical Review Letters, 78 (1997) 503-506.

[224] K. Häusler, K. Eberl, F. Noll, A. Trampert, Strong alignment of self-assembling InP quantum dots, Physical Review B, 54 (1996) 4913-4918.

[225] J. Santiso, J. Roqueta, N. Bagués, C. Frontera, Z. Konstantinovic, Q. Lu, B. Yildiz, B. Martínez, A. Pomar, L. Balcells, F. Sandiumenge, Self-Arranged Misfit Dislocation Network Formation upon Strain Release in $La_{0.7}Sr_{0.3}MnO_3$/LaAlO$_3$(100) Epitaxial Films under Compressive Strain, ACS Applied Materials & Interfaces, 8 (2016) 16823-16832.

[226] Z. Wang, M. Saito, K.P. McKenna, Y. Ikuhara, Polymorphism of dislocation core structures at the atomic scale, Nature Communications, 5 (2014) 3239.

[227] F. Ernst, A. Rečnik, P.A. Langjahr, P.D. Nellist, M. Rühle, Atomistic structure of misfit dislocations in SrZrO3/SrTiO3 interfaces, Acta Materialia, 47 (1998) 183-198.

[228] F.A. Kröger, H.J. Vink, Relations between the Concentrations of Imperfections in Crystalline Solids, Solid State Physics, 3 (1956) 307-435.

[229] R. Shannon, Revised effective ionic radii and systematic studies of interatomic distances in halides and chalcogenides, Acta Crystallographica Section A, 32 (1976) 751-767.

[230] F. Sandiumenge, N. Bagués, J. Santiso, M. Paradinas, A. Pomar, Z. Konstantinovic, C. Ocal, L. Balcells, M.-J. Casanove, B. Martínez, Misfit Dislocation Guided Topographic and Conduction Patterning in Complex Oxide Epitaxial Thin Films, Advanced Materials Interfaces, 3 (2016) 1600106-n/a.

[231] L. Sun, D. Marrocchelli, B. Yildiz, Edge dislocation slows down oxide ion diffusion in doped CeO2 by segregation of charged defects, Nature Communications, 6 (2015) 6294.

[232] D. Marrocchelli, L. Sun, B. Yildiz, Dislocations in SrTiO3: Easy To Reduce but Not so Fast for Oxygen Transport, Journal of the American Chemical Society, 137 (2015) 4735-4748.

[233] U. Aschauer, R. Pfenninger, S.M. Selbach, T. Grande, N.A. Spaldin, Strain-controlled oxygen vacancy formation and ordering in $CaMnO_3$, Physical Review B, 88 (2013) 054111.

[234] U. Aschauer, N.A. Spaldin, Interplay between strain, defect charge state, and functionality in complex oxides, Applied Physics Letters, 109 (2016) 031901.

[235] R. Colby, L. Qiao, K.H.L. Zhang, V. Shutthanandan, J. Ciston, B. Kabius, S.A. Chambers, Cation intermixing and electronic deviations at the insulating $LaCrO_3/SrTiO_3$(001) interface, Physical Review B, 88 (2013) 155325.

[236] S.-Y. Choi, S.-D. Kim, M. Choi, H.-S. Lee, J. Ryu, N. Shibata, T. Mizoguchi, E. Tochigi, T. Yamamoto, S.-J.L. Kang, Y. Ikuhara, Assessment of Strain-Generated Oxygen Vacancies Using SrTiO3 Bicrystals, Nano Letters, 15 (2015) 4129-4134.

[237] N. F. Mott, F. R. N. Nabarro, An attemot to estimate the degree of precipitation hardening, with a simple model, Proceedings of the Physical Society, 52 (1940) 86-89.

[238] H. Yamada, G.R. Miller, Point defects in reduced strontium titanate, Journal of Solid State Chemistry, 6 (1973) 169-177.

[239] W. Gong, H. Yun, Y.B. Ning, J.E. Greedan, W.R. Datars, C.V. Stager, Oxygen-deficient $SrTiO_{3-x}$, x = 0.28, 0.17, and 0.08. Crystal growth, crystal structure, magnetic, and transport properties, Journal of Solid State Chemistry, 90 (1991) 320-330.

[240] G. MacPherson, R. Beanland, P.J. Goodhew, On the development of misfit dislocation distributions in strained epitaxial layer interfaces, Scripta Metallurgica et Materialia, 33 (1995) 123-128.

[241] J.W.B. Matthews, A. E. , Defects in Epitaxial Multilayers: I. Misfit Dislocations, Journal of Crystal Growth, 27 (1974) 118–125.

[242] L.B. Freund, Dislocation Mechanisms of Relaxation in Strained Epitaxial Films, MRS Bulletin, 17 (1992) 52–60.

[243] J.C.B. R. Hull, Crit. Rev. Solid State Mater. Sci. , 17 (1992).

[244] G. Springholz, Strain contrast in scanning tunneling microscopy imaging of subsurface dislocations in lattice-mismatched heteroepitaxy, Applied Surface Science, 112 (1997) 12-22.

[245] D.J. Srolovitz, On the stability of surfaces of stressed solids, Acta Metallurgica, 37 (1989) 621-625.

[246] G. Springholz, G. Bauer, V. Holy, Scanning-tunneling-microscopy observation of stress-driven surface diffusion due to localized strain fields of misfit dislocations in heteroepitaxy, Physical Review B, 54 (1996) 4500-4503.

[247] L. Yao, S. Majumdar, L. Äkäslompolo, S. Inkinen, Q.H. Qin, S. van Dijken, Electron-Beam-Induced Perovskite–Brownmillerite–Perovskite Structural Phase Transitions in Epitaxial $La_{2/3}Sr_{1/3}MnO_3$ Films, Advanced Materials, 26 (2014) 2789-2793.

[248] M. Nord, P.E. Vullum, I. Hallsteinsen, T. Tybell, R. Holmestad, Assessing electron beam sensitivity for $SrTiO_3$ and $La_{0.7}Sr_{0.3}MnO_3$ using electron energy loss spectroscopy, Ultramicroscopy, 169 (2016) 98-106.

Appendix

A. Lattice parameters obtained from HTREM images

The values of the unit cell lattice parameters presented in sections 5.3 were obtained by a procedure based on the analysis of the FFT obtained from a single atomic row in the HRTEM image. A typical FFT procedure to measure the interplanar distances uses all the image or specific large area, giving the parameter values of these areas. In contrast, the procedure followed here only gives information of a specific atomic row in the HRTEM image.

Thus, there were two basic steps: (i) selection of the intensity profile from the atomic row of interest and (ii) performing the corresponding FFT. The first step was performed in the Digital Micrograph environment using the profile routine. An intensity profile was performed across the atomic row of interest, selecting a specific number of atoms in the row and integrating all the width of the atomic row in the HRTEM image. This profile was then processed using the routines available in the Origin software in order to obtain the FFT. The basic steps performed were (1) plotting and interpolation of the raw data, (2) performing the FFT, and (3) fitting a Gaussian peak to the FFT intensity distribution of first peak (the most intense), corresponding to the interplanar periodicity.

In sections 5.3, this procedure was used in order to obtain average values of the in-plane and out-of-plane lattice parameters of the domains and interface layer. The atomic row profiles were obtained from these two regions of the LSMO film. The atomic row profiles were formed by 5 atoms and they were integrated in three different zones for each region.

B. Assessment of specimen damage during TEM sample preparation

As these films present a low roughness surface, possible changes in thickness observed in planar view specimens could result from a preferential attack during TEM sample preparation. Secondary electron (SE) SEM images of a planar view TEM sample were acquired from the substrate side, which is the attacked part by the ion beam during the TEM sample preparation, to observe possible variations in thickness due to a preferential attack.

Figure B shows a SE-SEM image (a) and the bright (b) and dark (c) field TEM images acquired in the SEM from the same zone of the substrate. The TEM images show the contrast results from the presence of MD, as can be observed in the inset enlarged of Figure B1 (a) and (b). In the SE-SEM image, besides the typical undulations produced by the ion attacks during TEM sample preparation, no other changes in contrast are observed indicating that there are no topography effects due to a preferential attack related with the MD during the sample preparation.
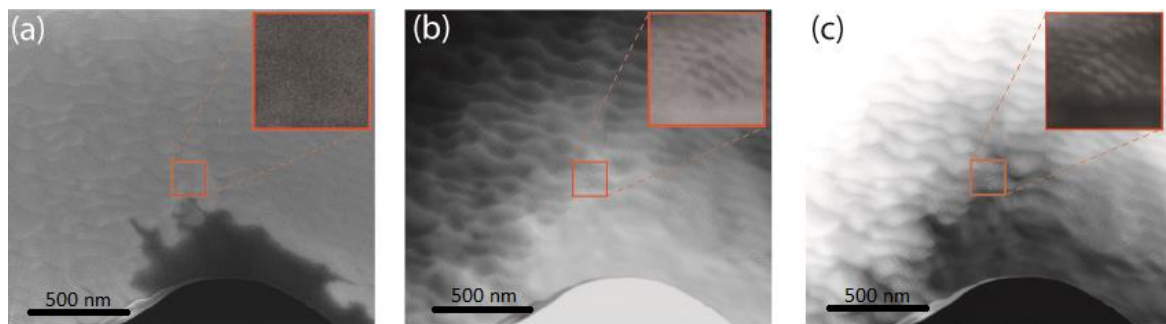

Figure B: (a) Secondary electron SEM image obtained from the substrate side of a planar view TEM sample of a 6-nm-thick film and the corresponding (b) bright and (c) dark filed TEM images acquired in the same SEM microscope. The red square marks the enlarged inset.

C. Example of k-factor calculations considering La₀.₇Sr₀.₃MnO₃ and LAO₃ as different phases

As an example, a profile obtained from a large map between dislocations, away from the dislocations is shown in Figure C. The intensity elemental profile was obtained by integrating the area of the EDS-SI in the horizontal direction. This profile was used to calculate the k-factor.

Firstly, the k-factors were calculated in the film and the substrate away from the interface as shown in the image in Figure C, assuming that these positions followed the La₀.₇Sr₀.₃MnO₃ stoichiometry for the film and LaAlO₃ stoichiometry for the substrate. The resulting concentration profile is shown in Figure C(a). The conversion of La and O counts to atomic% was calculated using the k-factors obtained from LSMO and LAO. Thus, the La concentration was measured with the k-factors obtained from the film (k_{La-Sr}) and the substrate (K_{La-Al}), and as a result, two La concentrations curves were obtained (inset in Figure C(a)). The point where these curves intersect was used to establish the cut-off of the curve obtained from the k-factors of the film and connected from this point with the curve obtained from the k-factors of the substrate.
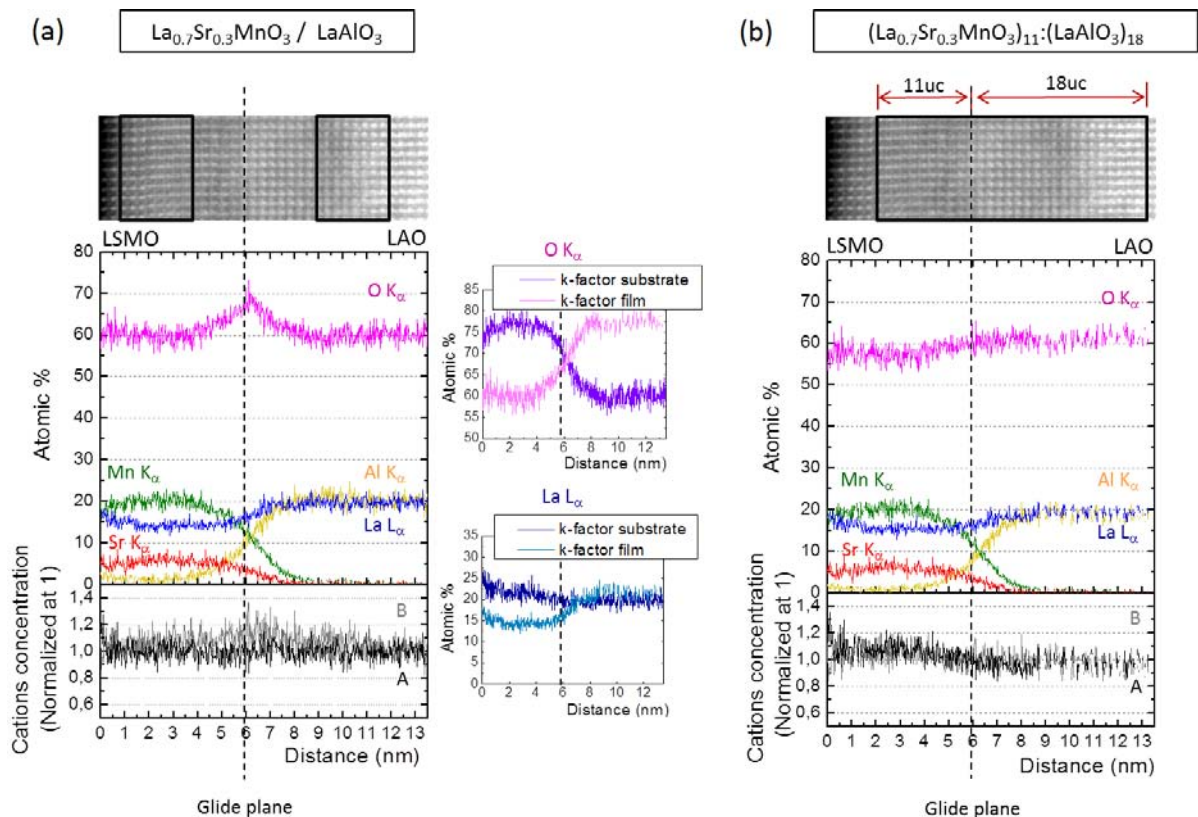

Figure C: (a) and (b) elemental concentration profiles obtained by using the k-factors considering the references separately for the substrates and the films (LSMO/LAO) and considering one supercell ((LSMO)₁₁(LAO)₁₈), respectively.

However, as can be seen in Figure C(a), if the criterion used for obtaining the La concentration curve is applied to O, the O concentration at the interface is not well resolved. The resulting O concentration curve shows and increment of the oxygen of 10at% at the intersection point. Moreover, by this procedure it is not possible to extract any information about Al-Mn intermixing in the film, where the Mn and Al curves intersect above 10at% resulting in an unrealistic excess of B cations, as can be seen in the profile of the A and B cation concentration presented in Figure C (a). Thus, the interface is not well resolved by this procedure.

In order to resolve the interface region, k-factors were calculated considering a supercell $(LSMO)_X(LAO)_Y$, combining a number of film (x unit cells) and substrate (y unit cells) along a vertical profile. In the case shown in Figure C(b), k-factors were calculated by integrating a total of 11unit cells of LSMO and 18unit cells of LAO, considering the GP as an interface plane. The resulting concentration profiles can be seen in Figure C(b).

D. Beam damage effects on the La$_{0.7}$Sr$_{0.3}$MnO$_3$ structure

During the development of the TEM experiments, some sample damage and phase transitions were observed. They were observed in LSMO films, both on STO and on LAO, and also in the LAO substrate.

In the case of LSMO, a change in the HRTEM contrast pattern was observed during the observation. A dilatation of the out-of-plane lattice direction was distinguished, as shown the image in figure D (a). This phase may correspond to a brownmillerite-type phase. The transition from LSMO perovskite to brownmillerite under beam irradiation has been previously reported in LSMO films on STO [247]. The appearance of this phase is attributed to the ordering of oxygen vacancies [247].
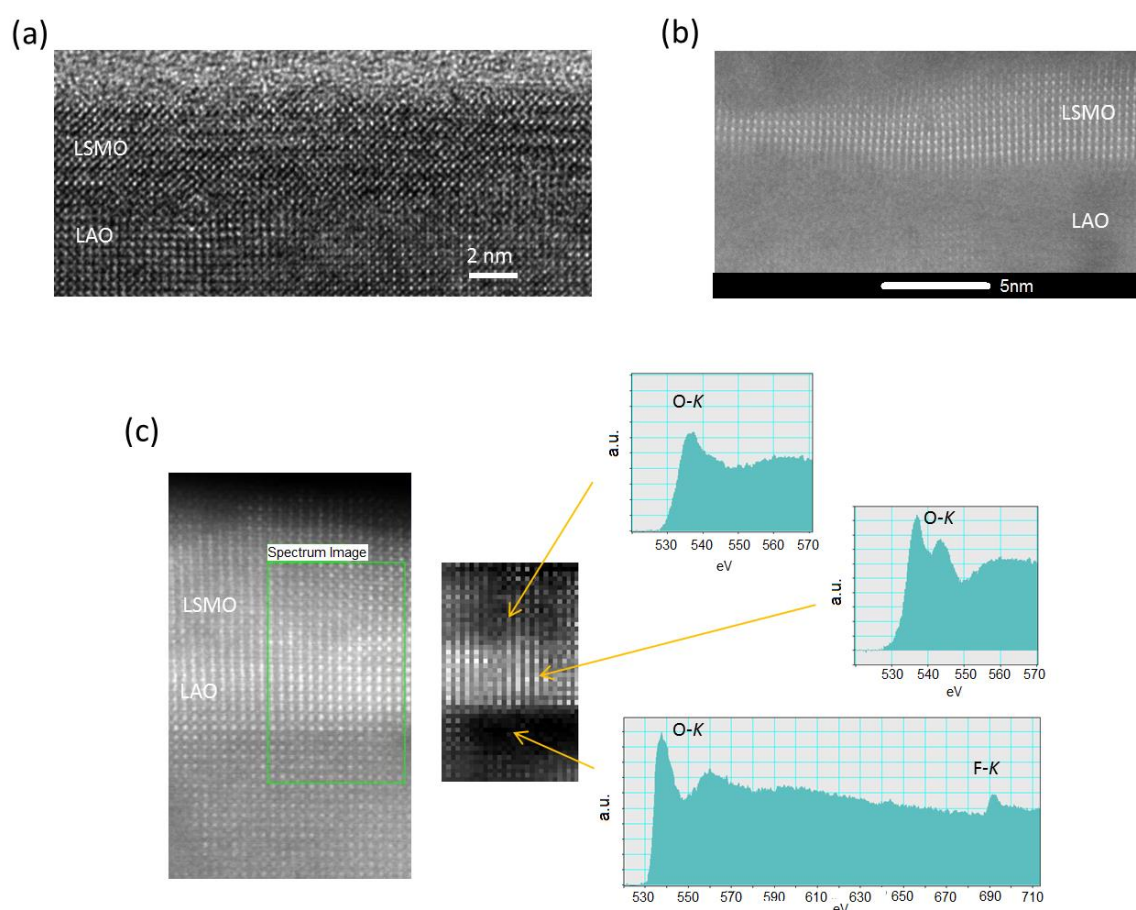

Figure D: (a) HRTEM image showing the dilatation of the out-of-plane lattice direction. (b) HAADF showing the loss of high resolution pattern in the LSMO (top-left corner) and in the LAO as beam damage. (c) EELS-SI of LSMO-LAO where the image left indicates the integrated area (green box) and the central image correspond to the HAADF image obtained simultaneously with the spectres. The spectres correspond at regions in the HAADF indicated with arrows (top – to LSMO, medium – to upper part of LAO, and bottom – to bulk LAO).

Other damage observed in LSMO is the loss of atomic resolution, probably due to amorphization or the deposition of carbon on top of the sample. Besides this apparent, effects excessive beam exposure as well as probe current, may produce some damage in LSMO that is not observed directly in the HAADF images and is only detected by EELS [248]. In this work, this type of damage was observed in the O-K as the loss of the third peak (previously denoted as a ***c*** peak), probably due to the larger beam exposure time during EDS and EELS analysis, as can be seen in figure D (c) in the top spectrum.

In the case of LAO, some damage was also observed as the disappearance of the atomic pattern under an over radiation, as can be seen in Figure D (b). Notice that only the region close to the interface with the LSMO, the structure is preserved, suggesting that the strained zone is more resistant to beam damage. In addition, the EELS shows the disappearance of the secondary peaks in the O-K edge typically observed in LAO, leading to only one peak, as shown in figure D (c), and which highlights the presence of flour in these damage areas.

These observations were used to minimize errors in the interpretation of the results.

E. List of publications and contributions

Journal Articles

Publications derived from the work depicted in this thesis:

N. Bagués, J. Santiso, R. E. A. Williams, B. Esser, D. W. McComb, Z. Konstantinovic, Ll. Balcells and F. Sandiumenge, *The misfit dislocation core phase in complex oxide heteroepitaxy* (in preparation).

A. Pomar, Z. Konstantinovic, N. Bagués, J. Roqueta, L. López-Mir, Ll. Balcells, C. Frontera, N. Mestres, A. Gutiérrez-Llorente, M. Ščepanovic, N. Lazarevic, Z.V. Popovic, F. Sandiumenge, B. Martínez and J. Santiso, *Spontaneous Formation of LaMnO3:Mn3O4 Nanostructures*, Frontiers in Physics, **4** (2016) 41. doi: 10.3389/fphy.2016.00041

J. Santiso, J. Roqueta, N. Bagués, C. Frontera, Z. Konstantinovic, L. Qiyang, Y. Bilge, B. Martínez, A. Pomar, Ll. Balcells and F. Sandiumenge*, Self-Arranged Misfit Dislocation Network Formation upon Strain Release in $La_{0.7}Sr_{0.3}MnO_3/LaAlO_3(100)$ Epitaxial Films under Compressive Strain*, ACS Applied Materials & Interfaces, **8** (2016) 16823-16832. doi:10.1021/acsami.6b02896

F. Sandiumenge, N. Bagués, J. Santiso, M. Paradinas, A. Pomar, Z. Konstantinović, C. Ocal, Ll. Balcells, M.-J.Casanove and B. Martínez, *Misfit Dislocation Guided Topographic and Conduction Patterning in Complex Oxide Epitaxial Thin Films*, Advanced Materials Interfaces; **3** (2016) 1600106-n/a. doi: 10.1002/admi.201600106.

Ll. Balcells, M. Paradinas, N. Bagués, N. Domingo, R. Moreno, R. Galceran, M. Walls, J. Santiso, Z. Konstantinovic, A. Pomar, M-J. Casanove, C. Ocal, B. Martínez F. Sandiumenge, *Enhanced conduction and ferromagnetic order at (100)-type twin walls in $La_{0.7}Sr_{0.3}MnO_3$ thin films*, Physical Review B, **92** (2015) 075111. doi: 10.1103/PhysRevB.92.075111

F. Sandiumenge, N. Bagués, J. Santiso, *Interfaces and nanostructures of functional oxide octahedral framework structures*, Frontiers in Materials, **1** (2014).

Other publications developed during the thesis period:

Ll. Balcells, C. Martínez-Boubeta, J. Cisneros-Fernández, K. Simeonidis, B. Bozzo, J. Oro-Sole, N. Bagués, J. Arbiol, N. Mestres and B. Martínez, *One-Step Route to Iron Oxide Hollow Nanocuboids by Cluster Condensation: Implementation in Water Remediation Technology*, ACS Appl Mater Interfaces **8** (2016) 28599-28606. doi: 10.1021/acsami.6b08709

R. Galceran, Ll. Balcells, A. Pomar, Z. Konstantinović, N. Bagués, F. Sandiumenge, B. Martínez, *Tunneling anisotropic magnetoresistance in $La_{2/3}Sr_{1/3}MnO_3/LaAlO_3/Pt$ tunnel junctions*, AIP Advances **6** (2016) 4, 045305. doi:10.1063/1.4946851

N. Domingo, N. Bagués, J. Santiso, and G. Catalan*, Persistence of ferroelectricity above the Curie temperature at the surface of Pb(Z n1/3 N b2/3) O3-12%PbTi O3*, Physical Review B **91** (2015)**,** 9, 094111. doi 10.1103/PhysRevB.91.094111

R. Galceran, C. Frontera, Ll. Balcells, J. Cisneros-Fernández, L. López-Mir, J. Roqueta, J. Santiso, N. Bagués, B. Bozzo, A. Pomar, F. Sandiumenge, B. Martínez, *Engineering the microstructure and magnetism of La_2CoMnO_{6-d} by tailoring oxygen stoichiometry*, Applied Physics Letters **105** (2014) 242401. doi: 10.1063/1.4904410

R. Moreno, J. Zapata, J. Roqueta, N. Bagués and J. Santiso. *Chemical strain and oxidation-reduction kinetics of epitaxial thin films of mixed ionic-electronic conducting oxides determined by x-ray diffraction*, Journal of The Electrochemical Society **161** (2014) F3046-F3051. doi 10.11149/2.009141jes

Conference contributions

Oral contribution: *Misfit Dislocation Structure and Guided Topographic and Conduction Pattering in Complex Oxide Epitaxial Thin Films*. N. Bagués, J. Santiso, M. Paradinas, Z. Konstantinovic, A. Pomar, Ll. Balcells, C. Ocal, B. Esser, D. McComb, B. Martínez and F. Sandiumenge, **Conference of the Condensed Matter Division of the European Physical Society (CMD26)**, Groningen (Nertherlands), Septembe, 2016

Poster: *Structural, chemical and strain features of misfit dislocation cores in ultrathin $La_{0.7}Sr_{0.3}MnO_3$ epitaxial films deposited on $LaAlO_3$*. N. Bagués, J. Santiso B. Esser, R. Williams, D. McComb Z. Konstantinovic, A. Pomar, Ll. Balcells and F. Sandiumenge, The 16th European Microscopy Congress 2016, **EMC2016**, Lyon (France), August-September 2016

Oral contribution: *Misfit Dislocation Guided Topographic and Conduction Patterning in Complex Oxide Epitaxial Thin Films,* N. Bagués **SELF2016,** Self-assembly at ICMAB, Barcelona (Spain), June 2016.

Oral contribution: *Strategies for guided self-assembly in oxide thin films,* A. Pomar, Z. Konstantinović, Ll. Balcells, C. Frontera, B. Bozzo, L. López-Mir, N. Bagués, J. Santiso, F. Sandiumenge, B. Martínez **SELF2016,** Self-assembly at ICMAB, Barcelona (Spain), June 2016.

Oral contribution: *Chemical and structural characterization of misfit dislocation cores in ultrathin La0.7Sr0.3MnO3 epitaxial films on LaAlO3.* N. Bagués, B. Esser, Z. Konstantinović, R. Williams, D. McComb, J. Santiso, Ll. Balcells, B. Martinez, F. Sandiumenge **Nanoselect NOE- Annual Meeting**, St Feliu de Guíxols (Spain), June 2016.

Oral contribution: *Modulation of surface strain and altered currents by misfit relieving defects in epitaxial complex oxide*s. N. Bagués, J. Santiso, M. Paradinas, Z. Konstantinovic, A. Pomar, Ll. Balcells, C. Ocal, B. Esser, D.-W. McComb, M.-J. Casanove, and F. Sandiumenge. **2nd Funtioal Oxide Thin Films for Advanced Energy and Information Technology Conference**, Cancún (Mexico), March 2016.

Poster: *Influence of strain on the magnetic properties of LaMnO$_3$ thin films.* A. Pomar, J. Roqueta, J. Santiso, Ll. Balcells, C. Frontera, B. Bozzo, Z. Konstantinović ,N.Bagués, F.Sandiumenge, B. Martínez. **20th International Conference on Magnetism**, Barcelona (Spain), July 2015.

Oral contribution: *Intrinsic High Conductivity and Magnetization at Twin Wall in LSMO Thin Films.* Balcells, M. Paradinas, R. Glaceran, N. Bagués**,** Z. Konstantinovic, A. Pomar, R. Moreno, J. Santiso, N. Domingo, M.-J. Casanove, M. Walls, C. Ocal, B. Martínez and F. Sandiumenge. **MRS Fall Meeting (MRS)-2014 ,** Boston (USA), November-December 2014.

Poster: Disentangling Interfacial Stress from Polarity in the Relaxation Behaviour of Epitaxial Octahedral Framework Structures of Strongly Correlated Oxides. N. Bagués, J. Roqueta, J. Santiso, Ll. Balcells, Z. Konstantinović, A. Pomar, S. Valencia, MJ. Casanove, B. Martínez, F. Sandiumenge. **Materials Research Society MRS Spring Meeting**, San Francisco, CA (USA), April 2014.

Poster: *High Conductivity at twin boundaries in LSMO thin films.* Ll. Balcells, M. Paradinas, R. Galceran, N. Bagués, Z. Konstantinović, A. Pomar, R. Moreno, J. Santiso, N. Domingo, F. Sandiumenge, C. Ocal, B. Martínez. **Materials Research Society MRS Spring Meeting, San Francisco**, CA (USA), April 2014.